

---

# Investigations into the Effect of Temperature on the Flotation of Galena, Sphalerite, and Pyrite

---

Dzmitry Pashkevich

Department of Mining and Materials Engineering,  
McGill University



November 2024

A thesis submitted to McGill University in partial fulfillment of the  
requirements for the degree of Doctor in Engineering in the Department of  
Mining and Materials Engineering

© Dzmitry Pashkevich 2024

---

## Abstract

Temperature variations could potentially impact flotation performance, leading to operational and economic issues. Several historical and currently operating plants across Canada have reported seasonal metal losses as one of the major challenges. Improvements in flotation efficiency at cold temperatures are important for the sustainable development of the industry, especially in view of expanding mining operations to the North, and an increasing impact of climate change-originated weather extremes on mining operations. To better understand the driving mechanisms of seasonal metallurgical variations, and the degree of vulnerability of froth flotation to fluctuations in temperature, as well as to develop recommendations addressing seasonally driven losses, a series of laboratory experiments at different levels were conducted (adsorption experiments with UV-VIS, microflotation, Denver cell mono-mineral flotation, Denver cell ore flotation, foam stability, and froth stability investigations). Experimental findings were supported by numerical simulations.

Selective flotation of lead-zinc ores is a process with many variables and a delicate balance of external (such as temperature) and internal factors (reagent concentrations, surface alterations). Theoretical calculations assist in explaining observed variations in adsorption and microflotation results with temperature. Other statistically significant parameters explaining adsorption performance were xanthate concentration, copper sulfate dosage, and pH. Adsorption selectivity calculations were performed on individual mineral responses, which gives some insights into potential trends in the separation of galena, sphalerite, and pyrite. Adsorption results also confirmed current perceptions of the adsorption mechanism of dextrin. It has been shown that xanthate adsorption and, hence, sulfide flotation is an entropy-driven process with the highest performance observed for galena among the three tested minerals. Scanning electron microscopy and EDS results reveal a potential mechanism contributing to sphalerite depression at 45 °C. Inverse gas chromatography provided surface energy heterogeneity maps of the minerals, which were generally in line with microflotation performance. Higher surface energy heterogeneity was observed for galena at 5 °C and for sphalerite at 45 °C. The role and variations in dissolved oxygen and lime dosages with temperature were also discussed with regard to flotation performance.

On a Denver batch flotation scale for monomineralic samples, the flotation results followed the same trends: higher recovery and slower kinetics at lower temperatures, and lower recoveries and faster

---

kinetics at higher temperatures. Following the results of the flotation tests, foam height, and stability were investigated at different temperatures to explain the observed variations. A high correlation between changes in mono-mineral flotation behavior and foam properties with temperature was revealed. Further investigations in froth stability with VMS ore demonstrated similar trends – higher yields and thicker, more stable froth at lower temperatures. SEDEX ore flotation experiments resulted in the highest variability for sphalerite, which corresponds well with the literature. Since sphalerite flotation represents one of a few sulfide recovery systems that experience significant variations in seasonal performance, cases from several zinc mines across the world were analyzed to show the correlation between temperature and plant performance. Too high or too low temperatures were seen to provoke fluctuations in the metallurgical performance of zinc flotation. The efficiencies of such flotation modifiers as lime, copper sulfate pentahydrate, and zinc sulfate heptahydrate have been studied in a selective flotation circuit for SEDEX ore types using the central composite design of the experiment. The results showed variations in the recovery kinetics, bubble size on the froth surface, concentrate grade, yield, and water recovery with temperature. Higher yields and water recoveries originating from more stable froth were observed at colder temperatures, presumably explaining the observed lower concentration grades. Recommendations on the mitigation of temperature-driven discrepancies in the sulfide flotation performance were developed.

---

## Résumé

Les variations de température pourraient potentiellement avoir un impact sur les performances de flottation, entraînant des problèmes opérationnels et économiques. Plusieurs usines historiques et actuellement en activité à travers le Canada ont signalé les pertes saisonnières de métaux comme l'un des défis majeurs. L'amélioration de l'efficacité de la flottation à des températures froides est importante pour le développement durable de l'industrie, en particulier compte tenu de l'expansion des opérations minières vers le Nord et de l'impact croissant des phénomènes météorologiques extrêmes provoqués par le changement climatique sur les opérations minières. Pour mieux comprendre les mécanismes déterminants de la variation métallurgique saisonnière et le degré de vulnérabilité de la flottation des mousses aux fluctuations de température, ainsi que pour élaborer des recommandations concernant les pertes saisonnières, une série d'expériences en laboratoire à différents niveaux ont été menées (expériences d'adsorption avec UV-VIS, microflottation, flottation mono-minérale de Denver, flottation du minerai de Denver, stabilité de la mousse et enquêtes sur la stabilité de la mousse). Les résultats expérimentaux ont été étayés par des simulations numériques.

La flottation sélective des minerais de plomb et de zinc est un processus comportant de nombreuses variables et un équilibre délicat entre des facteurs externes (tels que la température) et internes (concentrations de réactifs, altérations de surface). Les calculs théoriques aident à expliquer les variations observées dans les résultats d'adsorption et de microflottation avec la température. D'autres paramètres statistiquement significatifs expliquant les performances d'adsorption étaient la concentration en xanthate, le dosage en sulfate de cuivre et le pH. Des calculs de sélectivité d'adsorption ont été effectués sur les réponses minérales individuelles, ce qui donne un aperçu des tendances potentielles dans la séparation de la galène, de la sphalérite et de la pyrite. Les résultats de l'adsorption ont également confirmé les perceptions actuelles du mécanisme d'adsorption de la dextrine. Il a été démontré que l'adsorption du xanthate et, par conséquent, la flottation des sulfures sont un processus piloté par l'entropie, avec les performances les plus élevées observées pour la galène parmi les trois minéraux testés. Les résultats de la microscopie électronique à balayage et de l'EDS ont permis de révéler un mécanisme potentiel contribuant à la dépression de la sphalérite à 45 °C. La chromatographie gazeuse inverse a fourni des cartes d'hétérogénéité d'énergie de surface des minéraux. Les valeurs d'énergie de surface étaient généralement conformes aux performances de microflottation. Une plus grande hétérogénéité d'énergie de surface a été observée pour la galène à



---

5 °C et pour la sphalérite à 45 °C. Le rôle et les variations des dosages d'oxygène dissous et de chaux en fonction de la température ont également été discutés en ce qui concerne les performances de flottation.

Sur une échelle de flottation par lots de Denver pour les échantillons monominéraux, les résultats de flottation ont suivi les mêmes tendances: une récupération plus élevée et une cinétique plus lente à des températures plus basses, et des récupérations plus faibles et une cinétique plus rapide à des températures plus élevées. Suite aux résultats des tests de flottation, la hauteur de mousse et la stabilité ont été étudiées à différentes températures pour expliquer les variations observées. Une forte corrélation entre les changements dans le comportement de flottation des mono-minéraux et les propriétés de la mousse avec la température a été révélée. Des recherches plus approfondies sur la stabilité de la mousse avec le minerai VMS ont démontré des tendances similaires : des rendements plus élevés et une mousse plus épaisse et plus stable à des températures plus basses. Les expériences de flottation du minerai SEDEX ont abouti à la variabilité la plus élevée pour la sphalérite, ce qui correspond bien à la littérature. Étant donné que la flottation de la sphalérite représente l'un des rares systèmes de récupération des sulfures dont les performances saisonnières varient considérablement, des cas provenant de plusieurs mines de zinc à travers le monde ont été analysés pour montrer la corrélation entre la température et les performances de l'usine. Des températures trop élevées ou trop basses ont provoqué des fluctuations dans les performances métallurgiques de la flottation du zinc. L'efficacité de modificateurs de flottation tels que la chaux, le sulfate de cuivre pentahydraté et le sulfate de zinc heptahydraté a été étudiée dans un circuit de flottation sélectif pour les types de minerais SEDEX en utilisant le plan composite central de l'expérience. Les résultats ont montré des variations dans la cinétique de récupération, la taille des bulles à la surface de la mousse, la qualité du concentré, le rendement et la récupération de l'eau en fonction de la température. Des rendements plus élevés et des récupérations d'eau provenant d'une mousse plus stable ont été observés à des températures plus froides, expliquant probablement les concentrations plus faibles observées. Des recommandations sur l'atténuation des écarts liés à la température dans les performances de flottation des sulfures ont été élaborées.

---

## Acknowledgements

I would like to express my deepest gratitude to Professor Kristian Waters for his invaluable guidance, unwavering support, and the opportunity to pursue a PhD within the best Mineral Processing Group in the world! I am extremely grateful to you for taking me to conferences in Cape Town, Vancouver, and Liverpool, where I not only expanded my knowledge but also broadened my professional network and met my old friends. Your mentorship just not only helped me professionally but also made me a better version of myself throughout my research journey. I appreciate your insightful ideas, your encouragement, and your ability to support my laboratory work without distraction. Moreover, I am grateful for your kindness and generosity. You have not only been an exceptional supervisor but also a wonderful person. I am also thankful for the opportunities you provided, such as putting me in contact with industry professionals and for providing me with the opportunity to gain teaching assistantship experience under your supervision. I am truly fortunate to have had you as my supervisor, and I am immensely grateful for everything you have done for me.

I am also thankful for the McGill Engineering Doctoral Award (MEDA) from the Faculty of Engineering at McGill University and the support from the Fonds de recherche du Québec–Nature et technologies (FRQNT). Also, I would like to express my gratitude for the financial support provided by the Natural Sciences and Engineering Research Council of Canada (NSERC), Teck Resources Limited, COREM, SGS Canada Inc., and Flottec.

I extend my deepest appreciation to Ray Langlois, the Godfather of MinPro labs, for the countless insightful conversations we had, and for teaching me the importance of tidiness and organization in our work environment. The Denver cell with cooling/heating jacket that you have constructed for me still works like a charm, because it was made with love. I am also grateful for the wonderful summer BBQs you organized, and the endless supply of jokes and humor that you brought to the lab.

I did not have a sister before I started my PhD, but at McGill I met Sofi, who luckily didn't have a brother. Thank you for being not only my best friend, but also my sister. Your constant moral support has been a source of strength during the challenging times in my life. I am grateful to you for introducing me to your dog, Jordi, and for helping me overcome my fear of dogs. Furthermore, I want to thank you for always being there to cheer me up. Your encouragement and friendship have meant the world to me!

---

I am also grateful to Ozzy for introducing me to the world of design of experiment and for his insightful advice, whether it was about research methodologies or firing up the BBQ. I would also like to express my sincere appreciation to Shiva for her unwavering kindness and support. I am especially thankful to you for your assistance in the lab, which greatly contributed to the progress of my research.

I would like to extend my sincere gratitude to my Canadian brothers, Jeff, Mark, Ronghao, and Justin for their friendship and support throughout my doctoral journey. I will always cherish my trips with Jeff to Costco, countless insane table tennis games we played with Mark, delightful Chinese restaurant lunches with Ronghao, and enjoyable French conversations with Justin. I am also thankful to Luis, Jeff, and Mark for their invaluable assistance during our trip to a mineral processing plant.

Ahmed, Collins, Arian, Mandy, Elmira, Ahila, Bailee, Ebuka, Helmi, Frank, Heekang, Islom, Leader, Young, Zolboo, Tian, Rana, and Teddy, I consider each of you my friend, and I am incredibly grateful for your companionship and involvement in various activities outside of academia. I would also like to thank Alia, Dima, Kolya, Nastya, Lucas, Alan, Ivan, and Lior for being my good friends outside of the university. You helped me to stay sane, especially during the pandemic.

Last but certainly not least, I want to express my deepest gratitude to my family, Larysa, Aliaksandr, Tanya, and my big brother, Eugene, for their unwavering support, love, and belief in me. Mom, Dad, thank you for giving your best so that I could pursue my dreams. Your encouragement and love have been my driving force.

*In loving memory of my grandmother, Galina, who ignited my curiosity and passion for the wonders of science*

---

## Foreword

This PhD research has been presented in a traditional thesis format. A part of the material presented in Chapters 2, 4, 5, and 6 has either been published/submitted or is under review in a peer-reviewed journal. The published data has been re-arranged into the thesis Chapters for a clear and consistent explanation of the topic starting from simple systems and finishing with more complex processes. The research was conducted in the Mining and Materials Engineering Department of McGill University in the MinPro Group under the supervision of Prof. Kristian E. Waters. Prof. Waters was the principal investigator and administrator of the thesis project. The contribution and assistance of various co-investigators involved with this research is given below:

**Chapter 3:** The candidate has performed sample preparation. XRD and PSA analyses were run with the help of Mr. Ronghao Li. Raw data processing (modeling, and Rietveld refinement) were performed by the candidate.

**Chapter 4:** The candidate has developed the methodology and has confirmed the objectives with Prof. Waters. The candidate has performed thermodynamic calculations, 3D-printed set-up parts, and constructed/assembled microflotation and continuous reagent adsorption setups. Then the candidate ran the tests and analyzed the results. The Inverse Gas Chromatography, XPS, and BET tests with produced by the candidate microflotation samples were run by Dr. Shiva Mohammadi-Jam. The candidate analyzed the results and provided a discussion with the help of Dr. Shiva Mohammadi-Jam and Prof. Waters. SEM-EDS tests were run with the assistance of Ms. Sofi Buzukashvili. The analysis of the results and preparation of the associated discussions were performed by the candidate in conjunction with Prof. Waters.

**Chapter 5:** The candidate has prepared the designs of the experiment for the foam/froth stability tests with the assistance of Dr. Ozan Kökkılıç and Prof. Waters. The candidate has constructed set-ups for foam stability measurements, froth stability tests, and ran the tests. The candidate has analyzed bubble size distribution from the videos with the help of Mr. Lucas Pereira. The candidate has analyzed and modeled the rest of the data by himself. The main ideas for the discussion sections were confirmed with Dr. Ozan Kökkılıç and Prof. Waters.

**Chapter 6:** The candidate has prepared the designs of the experiment for Denver flotation tests with the assistance of Dr. Ozan Kökkılıç and Prof. Waters. The candidate has assembled the set-ups for

---

flotation tests. Mr. Ray Langlois has assisted in equipping the flotation cell with a heating/cooling jacket. The candidate ran the tests, and together with Mr. Ranjan Roy analyzed the samples using ICP-OES. Then the candidate modeled and processed the results, and, in conjunction with Dr. Ozan Kökkılıç and Prof. Waters, prepared discussions.

**Chapter 7:** The candidate has extracted the data from the literature, synthesized it, written a code in R, performed an exploratory investigation of the data, and prepared the discussions with the help of Prof. Waters

---

## Table of Contents

Abstract .....	i
Résumé.....	iii
Acknowledgements.....	v
Foreword .....	vii
Table of Contents.....	ix
List of Symbols .....	xiv
List of Acronyms .....	xxiv
List of Figures .....	xxvi
List of Tables .....	xxxiv
Chapter 1. Introduction .....	1
1.1. Geo-Technological Characterization of Lead-Zinc Ores .....	2
1.2. Mineral Processing of Lead-Zinc Ores .....	7
1.2.1. Comminution and Classification.....	7
1.2.2. Non-Flotation Processing Techniques .....	8
1.2.3. Lead-Zinc Ore Flotation .....	11
1.3. Thesis Motivation, Objectives, and Organization.....	17
Chapter 2. Literature Review on Temperature Effects in Flotation .....	21
2.1. Introduction.....	21
2.2. Temperature Impact on Processing Units Surrounding Flotation.....	22
2.3. Temperature Effects on Flotation.....	22
2.3.1. Flotation Medium: Water and Gas Properties.....	22
2.3.2. Primary Concentration: Flotation Thermodynamics and Particle Transport .....	30
2.3.3. Secondary Concentration: Foam and Froth Stability.....	32
2.4. Sulfide Flotation at Different Temperatures .....	34

---

2.4.1. Efficiency of Collectors .....	37
2.4.2. Efficiency of Flotation Modifiers .....	40
2.4.3. Mineral Surface Properties .....	45
2.5. Non-Sulfide Flotation at Different Temperatures .....	47
2.5.1. Oxides .....	47
2.5.2. Sulfates and carbonates .....	50
2.5.3. Halides .....	52
2.5.4. Phosphates .....	57
2.5.5. Tungstates .....	59
2.5.6. Rare-Earth Multi-Anion Minerals .....	60
2.5.7. Lithium Silicates .....	62
2.5.8. Carbonaceous Materials .....	63
2.6. Summary .....	65
Chapter 3. Materials and Methods .....	68
3.1. Sample Description .....	68
3.1.1. Monomineralic Samples .....	68
3.1.2. Lead-Zinc Ore Samples .....	68
3.2. Sample Preparation .....	68
3.2.1. Monomineralic Sample .....	68
3.2.2. Lead-Zinc Ore Sample .....	69
3.3. Sample Characterization .....	69
3.3.1. Surface Characterization .....	70
3.3.2. Analysis of Bulk Composition .....	72
3.4. Methodology of Testing Reagent Adsorption .....	76
3.5. Foam/Froth Stability Measurements .....	78

---

---

3.5.1. Foam Stability Tests.....	78
3.5.2. Froth Stability: Bubble Size in Monomineralic System .....	80
3.5.3. Froth Stability: Absolute Froth Height in VMS Ore System .....	81
3.5.4. Froth Stability: Stability Factor and Air recovery in SEDEX Ore System.....	82
3.6. Flotation Methodology.....	85
3.6.1. Micro-Flotation Set-Up.....	85
3.6.2. Denver Set-Up for Monomineralic Flotation.....	86
3.6.3. Denver Set-Up for Lead-Zinc Ore Flotation.....	89
3.7. Methodology of Numerical Simulations and Data Processing .....	90
3.7.1. Primary Concentration: Thermodynamic Calculations .....	90
3.7.2. Secondary Concentration: Froth Drainage Simulation .....	98
3.7.3. Analysis of Correlations between Flotation Responses and Foam Stability.....	101
3.7.4. Analysis of Plant Data.....	102
Chapter 4. Temperature Effect on Primary Concentration: Surface Chemistry of Galena, Sphalerite, and Pyrite .....	103
4.1. Introduction.....	103
4.2. Thermodynamic Models of Hydrophobization at Different Temperatures.....	106
4.3. Temperature-constrained Reagent Adsorption.....	109
4.4. True Flotation Recovery and Surface Energy at Varying Temperatures .....	118
4.5. Discussions .....	129
4.6. Conclusions.....	135
Chapter 5. Assessment of Temperature Impact on Secondary Concentration: Foam and Froth Stability Issues .....	137
5.1. Introduction.....	137
5.2. Foam Stability at Different Temperatures.....	137

---



---

5.3. Temperature Effects on Froth Properties .....	141
5.3.1. Bubble Size in the Monomineralic Froth.....	142
5.3.2. Froth Depth in Ore Flotation.....	142
5.3.3. Froth Stability in Ore Flotation.....	143
5.4. Numerical Simulation of Froth Drainage .....	145
5.5. Discussions .....	147
5.5.1. Foam Stability.....	147
5.5.2. Froth Stability .....	149
5.6. Conclusions.....	151
Chapter 6. Variations in the Overall Lab-Scale Flotation Performance with Temperature .....	153
6.1. Introduction.....	153
6.2. Monomineralic Flotation of Galena, Sphalerite, and Pyrite .....	153
6.2.1. Galena Responses .....	155
6.2.2. Pyrite Responses .....	157
6.2.3. Sphalerite Responses .....	159
6.2.4. Correlation of Monomineralic Flotation Performance to Foam Stability.....	161
6.3. Lead-Zinc Ore Flotation .....	163
6.4. Discussions .....	168
6.4.1. Monomineralic Flotation Performance .....	168
6.4.2. Lead-Zinc Ore Flotation Performance .....	169
6.5. Conclusions.....	170
Chapter 7. Temperature Contribution to Plant-Scale Variations in Sulfide Flotation.....	171
7.1. Description of Ores and Flowsheets .....	172
7.2. Correlations Between Metallurgical Performance and Meteorological Data .....	177
7.3. Discussions .....	189

---

---

7.4. Conclusions.....	191
Chapter 8. Global Discussions and Conclusions .....	192
8.1. Global Discussions.....	192
8.2. Contributions to the Original Knowledge.....	199
8.3. Global Conclusions.....	201
8.4. Recommendations for Future Work .....	202
References.....	203
APPENDIXES .....	253
APPENDIX A: Summary of recommended flotation temperatures for different minerals .....	253
APPENDIX B: XRD diffractograms for: pyrite (a), galena (b), sphalerite (c) .....	259
APPENDIX C: Detailed Scheme of Denver Flotation Set-Up with Automatic Level Control..	261
APPENDIX D: Calculations of the moments of inertia of the atoms of iPX molecules adsorbed on galena, sphalerite, and pyrite .....	262
APPENDIX E: iPX molecule on sphalerite (a), galena (b) and pyrite (c) surfaces (110) .....	264
APPENDIX F: Experimental results of adsorption tests for pyrite, sphalerite, and galena .....	265
APPENDIX G: Foam stability central composite design results.....	266
APPENDIX H: Statistical significance of models of froth stability parameters in SEDEX ore flotation .....	268
APPENDIX I: Responses of galena, pyrite, and sphalerite flotation systems under the investigated general factorial design. ....	269
APPENDIX J: A detailed numerical example of the thermodynamic calculations. ....	270
APPENDIX K: Bubble size on the top of the froth at different temperatures.....	271

## List of Symbols

### Latin Symbols

Symbol	Description	Units	Equations
$A$	is cross-sectional area of the froth phase	$\text{dm}^2$	(2-25)
$A$	is a coefficient, dependent on changes in thermodynamic characteristics of minerals		(2-38)
$\mathbf{A}$	is a matrix of elemental contents of the mineral phases		(3-2)
$\mathbf{A}$	is the covariance matrix		(3-62)
$A$	is the cross-sectional area of the cell	$\text{cm}^2$	(3-13)
$A$	is froth plateau border cross-section	$\text{m}^2$	(3-52, 3-53)
$A$	is the specific surface area of a mineral sample	$\text{m}^2/\text{g}$	(3-4)
$A_r$	is the atomic mass of an element in the molecule	$\text{amu}$	(3-45)
$a$	the activity of the reaction product and reactants		(2-20)
$a$	is a liquid-specific constant	$\text{Pa}\cdot\text{s}$	(3-55)
$a, b$	are beta distribution shape parameters		(3-10)
$a, b$	are constants		(2-3)
$a$ and $b$	are liquid-specific constants		(2-13)
$a, b$ , and $c$	are constants		(2-40)
$B$	is a coefficient characterizing an incremental value of required xanthate concentration with pH increase		(2-38)
$Bo$	is the Boussinesq number		(3-59, 3-60)
$B_r$	is the bubble bursting rate	$1/\text{s}$	(3-13)
$b$	is a liquid-specific constant	$\text{K}$	(3-55)
$b$	Temkin heat of sorption constant	$\text{J/mol}$	Table 4-2
$\vec{b}$	is a vector of sample assays		(3-2)
$b_0$	is an intercept		(3-7)
$b_i$	is the equation linear term coefficient		(3-7)
$b_{ii}$	is the equation cubic term coefficient		(3-7)
$b_{ij}$	is the cross-product coefficient		(3-7)

Symbol	Description	Units	Equations	
$C$	is a constant	dyn	(2-11)	
$C$	is the surfactant concentration	mol/l	(2-8, 2-39)	
$C_0$	is the initial concentration of a xanthate before adsorption	μmol/l	(3-4)	
$C_e$	is equilibrium concentration	mol/l	Table 4-2	
$C_f$	is the froth coefficient		(2-41)	
$C_p$	is heat capacity at constant pressure	J/(mol K)	(3-33)	
$C_t$	is the concentration of xanthate at time $t$ (s)	μmol/l	(3-4)	
$C^\ominus$	is a concentration of a component in aqueous phase at standard temperature (25 °C)	mol/l	(3-50)	
$CC$	is the concentration criteria		(1-1)	(1)
$c$	is a liquid-specific constant	K	(3-55)	
$c$	is a froth parameter		(2-30)	
$c_0$ and $c$	is a reference and actual frother concentrations	mol/l	(2-9)	
$cov_{\vec{X},\vec{Y}}$	is the covariance for $\vec{X}$ and $\vec{Y}$ (a pair of variable/response vectors)		(3-61)	
$D$ and $J$	are the coefficients		(2-10)	
$D_{32}$	is the Sauter mean bubble diameter	mm	(2-4, 2-12)	
$D_b^{max}(t)$	is the diameter of the top bubble on the froth surface	dm	(3-10)	
$D_{b(eq)}^{max}$	is an “equilibrium” top bubble size in the plateau area of the “Bathtub” curve	dm	(3-10)	
$d$	is the foam height decay constant		(3-8)	
$d_{avg}$	is the average bubble diameter	cm	(3-13)	
$d_p$	is particle diameter	mm	(2-5)	
$d_b$	is bubble diameter	mm	(2-5, 2-6)	
$d_{l-f}$	is the distance from the laser to the froth surface	cm	(3-11)	
$d_{l-c}$	is the distance from the laser to the cell lip	cm	(3-11)	
$E_a$	is the activation energy/activation energy of adsorption	J/mol	(2-18, 3-5)	
$E_c$	is collision efficiency		(2-5, 2-6)	
$E_a$	is attachment efficiency		(2-6)	
$E_d$	is detachment efficiency		(2-6)	

Symbol	Description	Units	Equations
$E_{col}$	is collection efficiency		(2-6)
$\Delta E$	is mineral surface potential in relation to a zero charge	V	(2-39)
$e_0$	is the elementary charge ( $1.602 \times 10^{-19}$ )	Coulombs	(2-39)
$e_G$	is a gangue material constant		(2-21)
$e_M$	is the entrainment factor for the mineral of interest		(2-22)
$F(t)$	the failure distribution function		(3-9)
$F_h(t)$	is foam height at time $t$	mm	(3-8)
$F_{h(eq)}$	is equilibrium foam height	mm	(3-8)
$F_s$	is the froth stability factor	s	(3-14)
$f_X(x), f_Y(y),$ $f_{X,Y}(x, y)$	are density functions		(3-66)
$\Delta G_{T_\ominus}$	is change in Gibbs free energy at standard temperature	J/mol	(3-38, 3-39)
$\Delta G(H)$	is the function of the energy barrier for bubble attachment depending on liquid layer thickness $H$		(4-3)
$\Delta G, \Delta G^0$	is a change in the Gibbs free energy	J/mol	(2-15, 2-20, 2-36, 4-2)
$g$	is gravity acceleration (9.8)	m/s <sup>2</sup>	(3-52)
$H^0$	is absorbed heat in the evaporation of 1 mol of gas	J/mol	(2-2)
$H_f$	is froth (foam) height	dm	(2-24, 2-25)
$\Delta H$	is enthalpy change	J/mol	(2-17)
$\Delta H^\ddagger$	is the enthalpy of activation	J/mol	(3-6)
$\Delta_{sol}H$	is solution enthalpy	J/mol	(3-51)
$h$	is the liquid film thickness	m	(2-27)
$h$	is Planck's constant ( $6.626 \cdot 10^{-34}$ )	J·s	(3-6, 3-44)
$h_{lip}$	is the froth height over the lip	cm	(3-14)
$I$	is the identity matrix		(3-62)
$I, I_\varphi$	is a moment of inertia of adsorbed xanthate ions around any principal axis ( $\varphi$ ), e.g. X, Y, or Z	kg·m <sup>2</sup>	(3-44, 3-45)

Symbol	Description	Units	Equations
$J_g$	is the superficial gas velocity	cm/s	(2-6, 3-11)
$J_{het}$	is the heterogeneous nucleation rate	1/(cm <sup>3</sup> s)	(2-37)
$J_b$	is bubble bursting flux	cm/s	(3-11, 3-12)
$K$	is the individual gas constant	atm/mol	(2-2)
$K$	is Eotvos-Ramsay Coefficient	J/(K·mol) <sup>2/3</sup>	(2-14)
$K_F$	is Freundlich coefficient	(mol <sup>1-n</sup> · l <sup>n</sup> )/m <sup>2</sup>	Table 4-2
$K_m$	is Temkin equilibrium binding constant	L/mol	Table 4-2
$K_L$	is Langmiur constant for adsorption energy	L/mol	Table 4-2
$K_c$	is Henry's constant	atm/mol	(2-1)
$K_T$	is solubility constant at the investigated temperature		(3-40)
$K_{T\ominus}$	is solubility constant at standard temperature (25 °C)		(3-30)
$K_w$	is solubility constant for water		(3-31, 3-49)
$K_d, K$	is an equilibrium dissociation constant	mol/L	(2-17, 2-20)
$K, a, \text{ and } b$	are coefficients		(2-4)
$k$	is the reaction rate constant		(2-18)
$k_a$	the apparent adsorption rate constant	nmol/(m <sup>2</sup> ·s)	(3-3)
$k, k_B$	is the Boltzmann constant	J/K	(2-37, 2-39, 3-6)
$k, K$	is the flotation rate constant		(2-28, 3-15)
$k_0$	is a constant that depends on the continuous phase viscosity and surface tension		(2-12)
$k_{max}$	is the reaction rate constant at $E_a=0$		(2-18)
$k_n$	is Arrhenius rate constant		(2-9)
$k_H^\ominus$	is Henry's constant at standard conditions	mol/atm	(3-50, 3-51)
$k_H^T$	is Henry's constant at a temperature of interest	mol/atm	(3-51)
$l$	is a length of a cell lip	cm	(3-11)
$M$	the molar mass of the liquid	kg/mol	(2-14)

Symbol	Description	Units	Equations
$M$	is a gas molar concentration in a liter of a solution	mol/l	(2-1)
$M$	is $\text{MgCl}_2$ concentration	%	(2-40)
$\mathbf{M}$	is a matrix with standardized original data		(3-62)
$MI(X, Y)$	is mutual information of $X$ and $Y$		(3-66)
$M_r$	is a molecular mass	<i>amu</i>	(3-46)
$m$	is foam height reduction after reaching a peak at the beginning of the test (difference between $F_h(t)$ and $F_{h(eq)}$ )	mm	(3-8)
$m$	is the sample mass	g	(3-4)
$m$	is a mass of xanthate ion	kg	(3-43)
$N$	is a number of points		(3-61)
$N_b$	is the number of bubbles		(3-13)
$n$	is the number of variables		(3-7)
$n$	proportionality coefficient		(2-5)
$n$	is the number of carbon atoms in a collector radical group		(2-39)
$P$	is the partial pressure of the gas above the solution	atm	(2-1)
$P$	is ore floatability parameter		(2-29)
$P$	is atmospheric pressure	atm	(3-49)
$\Delta P$	is the difference between hydrostatic pressure and disjoining pressure	N/m <sup>2</sup>	(2-27)
$p$	is the shape factor of Gamma distribution		(3-15, 3-16)
$p_g$	is a partial pressure of a component in a gas phase above the aqueous phase	atm	(3-50)
$dp/ dz$	is the pressure gradient	Pa/m	(3-59)
$Q_a$	is the rate of air flow passing though the froth zone	l/min	(2-24, 2-25)
$Q_o$	is Langmuir constant for adsorbed capacity	mol/m	Table 4-2
$Q, Q_{tr}, Q_r$	is a partition function (translational and rotational)		(3-42 - 3-44)
$q_t$	is the quantity of xanthate adsorbed on a mineral surface at time $t(s)$	$\mu\text{mol/m}^2$	(3-3)
$q_e$	is the quantity of the xanthate adsorbed at equilibrium	$\mu\text{mol/m}^2$	(3-3)

Symbol	Description	Units	Equations
$R$	is the universal gas constant (equals 8.3145)	J/(mol·K)	(2-2, 2-17, 2-18, 2-20, 3-5, 3-40, 3-51)
$\vec{R}$	is a vector of residuals		(3-2)
$R_G$	is the recovery of fine gangue		(2-21)
$R_w$	is water recovery		(2-21, 2-22)
$R_{ind}$	is the model's extrapolated intercept on the recovery axis		(2-22)
$R_{cw}$	is water recovery from pulp zone to froth zone		(2-23)
$R_f$	is froth recovery		(2-29)
$R_{fw}$	is water recovery from froth phase to the concentrate		(2-23, 2-24)
$\hat{R}(t)$	is modeled recovery at time $t$ (min)		(3-16, 3-17)
$R(t)$	is experimental recovery value at time $t$ (min)		(3-16, 3-17)
$R_\infty$	is infinite recovery		(3-16)
$r$	is bubble radius	m	(2-27)
$r$	is the Plateau border radius	m	(3-53, 3-54)
$r_b$	is froth bubble radius	m	(3-54)
$r_p^{max}$	is the maximum radius of a floatable particle	cm	(2-11)
$r_{Pearson}$	is Pearson's correlation coefficient		(3-65)
$S$	is the supersaturation state		(2-37)
$S$	is total salinity (NaCl + KCl)	%	(2-40)
$S_f$	is froth stability	s	(2-41)
$S_b$	is bubble surface area flux	s <sup>-1</sup>	(2-6, 2-29)
$S_{AD}$	is a total entropy of adsorbed species	J/(mol·K)	(3-41)
$S_v$	is vibrational entropy	J/(mol·K)	(3-41)
$S_r$	rotational entropy	J/(mol·K)	(3-41)
$S_{tr}$	is translational entropy	J/(mol·K)	(3-41)



Symbol	Description	Units	Equations
$S_{\ominus}^o$	the entropy of the formation of substance at standard temperature (25 °C)	J/(mol·K)	(3-47, 3-48)
$\Delta S_{T_{\ominus}}$	is a change in the entropy at standard temperature (25 °C)	J/(mol·K)	(3-48)
$\Delta S_{T_{\ominus}}$	is change in the entropy at standard temperature	J/(mol·K)	(3-37-3-40)
$\Delta S^{\ddagger}$	is the entropy of activation	J/(mol·K)	(3-6)
$SG_{heavy\ mineral}$	is the specific gravity of heavier mineral		(1-1)
$SG_{light\ mineral}$	is the specific gravity of lighter mineral in the separation process		(1-1)
$SG_{media}$	is the specific gravity of media where separation takes place		(1-1)
$T$	is the dissolution temperature of sylvite	°C	(2-40)
$T$	is a water temperature	°C	(2-3, 2-9, 3-58)
$T_c$	is the critical temperature	K	(2-13)
$T, T_2, T_1$	is the absolute temperature	K	(2-2, 2-8, 2-17, 2-18, 2-20, 2-37, 3-40, 3-51)
$T_{\ominus}$	is the standard temperature (298.15)	K	(3-37-3-40)
$t_{1/2}$	is froth half-life	s	(2-30)
$V$	is water drainage rate	m/s	(2-26, 2-27)
$V$	is the volume of the solution	l	(3-4)
$\mathbf{V}$	is a matrix of eigenvectors		(3-62)
$V_f$	is froth volume	cm <sup>3</sup>	(2-41)
$V_m$	is the molecular volume		(2-37)
$V_t$	is theoretical froth drainage	m/s	(3-52)
$V_t^P$	is a function of drainage velocity of a single Plateau border		(3-59)
$\vec{v}_i$	are eigenvectors		(3-62)
$v_b$	is the bubble rise velocity	cm/s	(2-11)
$v_f$	is the froth velocity towards flotation cell lip	cm/s	(3-11)

---

Symbol	Description	Units	Equations
$\Delta W_a$	is the energy of association for each CH <sub>2</sub> group	J	(2-39)
$[X^-]$	xanthate concentration	mol/l	(2-38)
$\vec{X}$ and $\vec{Y}$	is a pair of variable/response vectors		(3-61)
$x$	is association degree of liquid		(2-14)
$\vec{x}$	is a vector of mineral grades in a sample		(3-2)
$(x \cdot y)$	is xanthate ion area	m <sup>2</sup>	(3-43)
$x_i$ and $x_j$	are the variables		(3-7)
$x_i$ and $y_i$	are $i^{th}$ observations from compared arrays $X$ and $Y$		(3-65)
$\bar{x}$ and $\bar{y}$	are average values of the arrays $X$ and $Y$		(3-65)
$y$	is the $k^{th}$ response		(3-7)
$Z$	is a matrix with scores		(3-62)
$z$	is the valence of adsorbent		(2-39)

## Greek symbols

Symbol	Description	Units	Equations
$\alpha$	is the fraction of the froth that reports to the concentrate (air recovery)		(2-26, 3-11, 3-12)
$\alpha$	is a superficial fraction of lamella that is covered with solids		(2-12)
$\beta$	is geometrical shape factor		(2-37)
$\beta$	is the Weibull slope (shape parameter)		(3-9)
$B()$	is beta distribution of Weibull shape parameter		(3-10)
$\Gamma$	is surfactant adsorption density	mol/m <sup>2</sup>	(2-8, 2-39, 4-14)
$\Gamma(p)$	is Euler's gamma function		(3-15)
$\gamma$	is the surface tension	N/m	(2-8, 2-13, 2-14)
$\gamma$	is surface tension	dyn/cm	(2-11)
$\gamma$	is interfacial energy (subscripts $l, s, c$ , refer to liquid, solid and critical nucleus respectively)		(2-37)

Symbol	Description	Units	Equations
$\gamma$	is the thermal expansion coefficient	1/°C	(3-57)
$\gamma_{LG}(H)$	is a function of surface tension of liquid–gas interface depending on liquid layer thickness $H$		(4-3)
$\gamma_r$	is the shear rate	1/s	(2-12)
$\gamma_g$	is galena flotation yield		Table 5-1
$\gamma_p$	is pyrite flotation yield		Table 5-1
$\gamma_s$	is sphalerite flotation yield		Table 5-1
$\gamma_g^w$	is water recovery during galena flotation		Table 5-1
$\gamma_p^w$	is water recovery during pyrite flotation		Table 5-1
$\gamma_s^w$	is water recovery during sphalerite flotation		Table 5-1
$\gamma^d$	is dispersive component of surface energy	mJ/m <sup>2</sup>	Figure 4-12
$\gamma^{ab}$	is specific component of surface energy	mJ/m <sup>2</sup>	Figure 4-12
$\gamma_{VL}, \gamma_{SV}, \gamma_{SL}$	are the surface tensions at vapor-liquid, solid-vapor, and solid-liquid interfaces respectively	N/m	(2-15, 2-16, 4-2, 4-3)
$\varepsilon$	foam/froth liquid fraction		(3-54)
$\varepsilon$	is a residual (error)		(3-7)
$\varepsilon_f$	is the volume fraction of air		(2-12)
$\varepsilon_f$	is air holdup		(2-24, 2-25)
$\eta$	is dynamic viscosity	cP	(2-3)
$\eta$	is characteristic life (scale factor)		(3-9)
$\eta$	is pulp viscosity	μPa·s	(2-4)
$\eta_f$	is apparent froth viscosity	mPa·s	(2-12)
$\eta_{20}$	is pulp viscosity at a reference temperature (20 °C)	μPa·s	(2-4)
$\theta$	is the contact angle	°	(2-11)
$\theta_0$	is intercept at zero froth height		(2-28)
$\theta_1$	is the gradient of the flotation rate constant versus froth height plot		(2-28)
$\lambda$	is the scale factor		(3-15, 3-16)

---

Symbol	Description	Units	Equations
$\lambda_i$	are eigenvalues		(3-62)
$\mu$	is continuous phase dynamic viscosity	Pa · s	(2-27)
$\mu (T)$	is dynamic viscosity at temperature T	Pa·s	(3-55)
$\mu (\varphi)$	is dynamic viscosity at the pulp solids volume $\varphi$	Pa·s	(3-56)
$\mu_s$	is a surface shear viscosity	Pa·s	(3-60)
$\mu_X$ and $\mu_Y$	are the mean values, and $X_i$ and $Y_i$		(3-61)
$\rho$	is a media density	g/cm <sup>3</sup>	(2-11)
$\rho$	is liquid density	kg/m <sup>3</sup>	(2-14)
$\rho$	is continuous phase density	kg/m <sup>3</sup>	(3-52)
$\rho_T$	is the density of the substance at temperature $T$	kg/m <sup>3</sup>	(3-57)
$\rho_0$	is the initial substance density at standard temperature	kg/m <sup>3</sup>	(3-57)
$\rho_w(T)$	is a function of water density depending on temperature		(3-58)
$\tau_i$	is the induction time	μsec	(2-10)
$\tau_f$	is the residence time	(min)	(2-25)
$\varphi(K)$	is the probability density function of flotation rate constant distribution		(3-15)

---

## List of Acronyms

AFM	Atomic force microscopy
ANOVA	Analysis of variance
BET	Brunauer-Emmett-Teller surface area analysis
BHA	Benzohydroxamic acid
CCC	Critical Coalescence Concentration
CCD	Central composite design
CMC	Carboxymethyl cellulose
DDA	Dodecylamine
DDM	Dodecyl morpholine
DIBD	Diisobutyl dithiophosphate
DO	Dissolved oxygen
DoE	Design of Experiment
DoG	Differences of Gaussian
EDS	Energy dispersive X-ray spectroscopy
FTIR	Fourier Transform Infrared Spectroscopy
GOK	Gorno-Obogatitelny Kombinat (Ore mining and processing plant)
HBMS	Hudson Bay Mining and Smelting
HIGmill	High-intensity grinding mill
IGC	Inverse Gas Chromatography
IOCG	Iron oxide copper-gold deposit (ore)
JCI	Johannesburg Consolidated Investment Co. Ltd.
JSC	Joint-stock company
KEX (PEX)	Potassium ethyl xanthate
MGS	Multi-gravity separator
MIBC	Methyl Isobutyl Carbinol
MVT	Mississippi Valley-type deposit (ore)
NaOl	Sodium oleate
PAX	Potassium amyl xanthate collector
PCA	Principal component analysis

---

PGE	Propylene Glycol Ether
PNIPAM	Poly(N-isopropyl acrylamide) (flocculant/collector)
PPG	Polypropylene glycol
PSD	Particle size distribution
RE	Rare-earth
SBX	Sodium butyl xanthate collector
SDS	Sodium dodecyl sulfate
SEDEX	Sedimentary exhalative deposit (ore)
SEM	Scanning electron microscopy
SIBX	Sodium isobutyl xanthate collector
SIPX	Sodium isopropyl xanthate collector
SMD	Stirred media detritor
TEB	Triethoxy butane frother
UV-VIS	Ultraviolet–visible spectroscopy
VMS	Volcanogenic Massive Sulfide deposit (ore)

---

## List of Figures

Figure 1-1. Thesis structure .....	20
Figure 2-1. (a) DO solubility in distilled water at different temperatures, adapted from (Radtke <i>et al.</i> , 1998); (b) effect of temperature on water viscosity and bubble size, adapted from (Zhang, 2014)...	23
Figure 2-2. Zinc concentrate grade fluctuations at Matagami concentrator, adapted from (Nesset <i>et al.</i> , 2002) .....	25
Figure 2-3. Monthly pyrite production on a flotation plant in South Africa relative to temperature, adapted from (O'Connor <i>et al.</i> , 1984).....	27
Figure 2-4. (a) Concentrate quality depending on froth rheological properties; (b) changes in water and pyrite pulp viscosities, and water surface tension as a function of temperature. Adapted from (Kaye and Laby, 1962; O'Connor <i>et al.</i> , 1984).....	28
Figure 2-5. Flotation recovery of selected sulfide minerals in relation to liquid-vapor surface tension, adapted from (Yarar and Kaona, 1983).....	29
Figure 2-6. Examples of seasonal drop: (a) in gold recovery on Hudson Bay Mining and Smelting, 2000-2003; (b) in Cu+Ni grade on Clarabelle mill, adapted from (Levanaho <i>et al.</i> , 2005; Xu and Wilson, 2000).....	30
Figure 2-7. Laboratory results of zinc rougher flotation, adapted from (Roberts <i>et al.</i> , 2008) .....	36
Figure 2-8. Zinc recovery at the Neves-Corvo zinc plant in relation to the daily temperature, adapted from (Fernandes, 2016).....	37
Figure 2-9. Interaction scheme of xanthates with sulfide surface in aerated pulp, adapted from (Avdohin, 1996), where $E_v$ is the location of the energy level of the valence band “ceiling”, and $E_c$ is the location of the energy level of the conductivity band “bottom” .....	39
Figure 2-10. (a) Butyl xanthate adsorption on pyritic surface, adapted from (Liu <i>et al.</i> , 2019); (b) change of butyl xanthate concentration in the pulp ( $C/C_0$ ) with time during adsorption onto chalcopyrite, adapted from (Mhonde <i>et al.</i> , 2020).....	40
Figure 2-11. Areas of pH and concentration stabilities of copper species at different temperatures, adapted from (Albrecht <i>et al.</i> , 2016).....	41

---

---

Figure 2-12. Critical cyanide concentrations in captive bubble tests for combinations of activator and collector at different pH and under varying temperature conditions: (a) chalcopyrite (25 mg/l KEX), (b) sphalerite (150 mg/l Cu-vitriol), (c) pyrite, adapted from (Wark and Cox, 1938).....	45
Figure 2-13. Schematic representation of PNIPAM hematite flotation steps, with results compared with sodium oleate flotation, adapted from (Ng <i>et al.</i> , 2015).....	49
Figure 2-14. Seasonal variations of niobium recovery at Niobec facilities, adapted from (Marois <i>et al.</i> , 2018): months with negative recovery shift has blue bars, with positive shift having red bars, months with close to zero shift (<1%) has yellow bars or no bars. The zero point is mean summer recovery.....	50
Figure 2-15. Effect of flotation temperature on fluorite grade and recovery at pH 9 with oleic acid, adapted from (Li <i>et al.</i> , 2020) .....	52
Figure 2-16. Fluorite recovery as a function of pulp temperature and collector type, adapted from (Corpas-Martínez <i>et al.</i> , 2020).....	54
Figure 2-17. Solubility surfaces for (a) halite and (b) sylvite as a function of MgCl <sub>2</sub> and temperature (in a system with NaCl : KCl ratio of 1:1), adapted from (Bodnar <i>et al.</i> , 1997) .....	56
Figure 2-18. Comparison of a commercial fatty acid collector composition from Zheng <i>et al.</i> tests with EV-1, plotted using data from (Zheng <i>et al.</i> , 2016) .....	58
Figure 2-19. Recovery and grade of lithium concentrate at different temperatures of the flotation pulp, adapted from (Menéndez <i>et al.</i> , 2004) .....	62
Figure 2-20. A concept of “flotation rectangular” demonstrating seasonal triggers sphere of influence and flotation system components interactions .....	66
Figure 3-1. Sample preparation procedure for sphalerite, galena, and pyrite samples. ....	69
Figure 3-2. Particle size distributions for galena (Gn), pyrite (Py), and sphalerite (Sph) samples. ...	70
Figure 3-3. Graphical representation of determination of dispersive and specific surface energies (a) (adapted from (Mohammadi-Jam, 2017)), the diagram of typical surface energy heterogeneity profiles (b).....	71
Figure 3-4. Simplified explanation of the working principle of XPS analysis.....	72

---



Figure 4-1. Solubility constants at different temperatures for: (a) different lead species, (b) different zinc species, (c) different iron species, (d) different calcium and carbonate species, gasses, and copper-xanthate complex .....	107
Figure 4-2. Theoretically estimated minimum isopropyl xanthate concentration required for pyrite, sphalerite, galena and activated sphalerite flotation at different pH (a); and temperature (at pH 9) (b) .....	109
Figure 4-3. Standardized effects of model parameters: a – adsorption rate constant on pyrite, b – equilibrium adsorption capacity of pyrite surface, c - adsorption rate constant on sphalerite, d - equilibrium adsorption capacity of sphalerite surface, e - adsorption rate constant on galena, f - equilibrium adsorption capacity of galena surface. Non-significant factors are gray bars, significant factors are green (positive effect) and blue (negative effect) bars .....	111
Figure 4-4. Contour plots of $k$ (apparent adsorption rate constant in $\text{nmol}\cdot\text{m}^{-2}\cdot\text{s}^{-1}$ ) (a-c) at different temperatures and pH: a - for pyrite, b - for sphalerite, c - for galena; contour plots of apparent equilibrium adsorption capacity in collector dosage – temperature coordinates: d – for pyrite, e – for sphalerite, f – for galena.....	112
Figure 4-5. Temkin adsorption isotherms for pyrite, sphalerite, and galena (pH 10, 25 °C, 40 $\mu\text{mol/l}$ dextrin, 80 $\mu\text{mol/l}$ copper sulfate).....	114
Figure 4-6. Optimal pH for largest selectivity of adsorption kinetics on galena and sphalerite compared to pyrite at different temperatures (a), optimal initial collector dosage for highest selectivity in adsorption capacity against pyrite, depending on temperature (b), overlaid contour plot showing optimal conditions for the highest selectivity in adsorption kinetics between galena and sphalerite (c), overlaid contour plot showing optimal conditions for the highest selectivity in adsorption capacity between galena and sphalerite (d).....	115
Figure 4-7. Overlaid contour plots showing the change of the feasible area in coordinates of copper sulfate concentration and pH that allows to achieve maximum adsorption selectivity between sphalerite and pyrite at different temperature scenarios: (a) 5 °C, (b) 15 °C, (c) 25 °C, (d) 35 °C, (e) 45 °C .....	116

---

Figure 4-8. Graphical estimation of apparent activation energies for adsorption of SIPX on pyrite, galena, and sphalerite at pH 10 in the temperature range 5-45 °C (a); graphical estimation of entropy and enthalpy of activation (b) .....	117
Figure 4-9. Microflotation results for galena (pH 9), sphalerite (pH 11), and pyrite (pH 9 and 11) .....	118
Figure 4-10. XPS results for feed samples: galena (a), sphalerite (b), pyrite (c).....	119
Figure 4-11. Mineral yield versus xanthate supply/demand ratio for the tested monomineralic samples (galena, sphalerite, and pyrite) and for industrial plants (data from (Abramov, 2010)) .....	120
Figure 4-12. Dispersive (blue bars) and specific (orange bars) components of the surface energy of the microflotation products (at 5% coverage): a – galena and sphalerite, b – pyrite.....	121
Figure 4-13. Surface energy heterogeneity profiles of galena after conditioning with SIPX at different temperatures: 5 °C (a), 25 °C (b), and 45 °C (c); $\gamma^d$ , $\gamma^{ab}$ – represent dispersive and specific surface energy, respectively. ....	123
Figure 4-14. Surface energy heterogeneity profiles of sphalerite after conditioning at 5 °C (a), 25 °C (b), and 45 °C (c); $\gamma^d$ , $\gamma^{ab}$ – represent dispersive and specific surface energy, respectively .....	124
Figure 4-15. Specific surface energy distributions galena conditioned at 5, 25, and 45 °C (a) and dispersive surface energy distributions of sphalerite conditioned at 5, 25, and 45 °C (b).....	125
Figure 4-16. Scanning electron microscopy image of a sphalerite grain in micro-flotation tails (45 °C test): (a) sphalerite grain image and EDS point analysis of precipitate on a mineral surface, (b) EDS mapping of the grain .....	126
Figure 4-17. XPS results for sphalerite tailing sample (before and after conditioning and flotation at 45 °C): general spectrum (a), detailed calcium scan after conditioning (b) .....	127
Figure 4-18. Dynamics of dissolved oxygen concentration with temperature at different microflotation stages.....	128
Figure 4-19. Lime consumption at different pH and temperatures.....	128
Figure 5-1. Pareto chart of standardized effects of model terms on: (a) foam height; (b) foam half-life time. ....	139

---

Figure 5-2. Contour plots of foam half-life time in: (a) temperature versus aeration coordinates; (b) temperature versus pH coordinates; (c) temperature versus MIBC coordinates. ....	140
Figure 5-3. Contour plots of foam height in: (a) temperature versus aeration coordinates; (b) temperature versus pH coordinates; (c) temperature versus MIBC coordinates. ....	141
Figure 5-4. Top froth maximum bubble size versus flotation time for at 10 °C and 30 °C for: (a) galena; (b) pyrite; (c) sphalerite. ....	142
Figure 5-5. Froth depth depending versus temperature (a), water recovery (b), and solids yield (c) .....	143
Figure 5-6. Contour plots of the horizontal froth speed (a), froth height over the lip (b) and air recovery (c) as a function of temperature and copper sulfate (activator) dosages.....	144
Figure 5-7. Contour plots of bubble burst rate (a) and froth stability factor (c) as a function of temperature and copper-sulfate dosage; Box and Whisker plot of bubble size with temperature (middle line represents median, the box covers upper and lower quartile, the vertical line expands until extreme values) (b) .....	145
Figure 5-8. Results of Monte-Carlo simulation of a froth drainage in SEDEX ore flotation for a single plateau border.....	146
Figure 5-9. Froth drainage simulation with SDS, MIBC and PPG/PGE frothers used at concentrations in the flotation range (below 50 ppm).....	147
Figure 5-10. Graphical representation of the variation in bubble size at low and high temperature at low solids content (red arrows represent turbulent flows, blue arrows represent drainage, brown dots with yellow rim represent particles.....	150
Figure 6-1. Flotation responses of galena, sphalerite, and pyrite at pH 9, 10 °C, and 30 °C: (a) kinetic yield curves; (b) distributions of flotation rate constants.....	153
Figure 6-2. Distributions of flotation rate constants at 10 °C and 30 °C for pH 9 and 11: (a) galena; (b) pyrite; (c) sphalerite. ....	154
Figure 6-3. Galena flotation main effects and interaction plots: (a) main effects plot for galena recovery; (b) interaction plot for galena recovery; (c) main effects plot for water recovery; (d) interaction plot for water recovery (error bars represent $\pm 1$ standard deviation). ....	156

Figure 6-4. (a) Pareto chart for galena ( $\gamma g$ ) and water yields ( $\gamma gw$ ); (b) water recovery versus galena yield at different pH and temperatures.....	157
Figure 6-5. Pyrite flotation main effects and interaction plots: (a) main effects plot for pyrite recovery; (b) interaction plot for pyrite recovery; (c) main effects plot for water recovery; (d) interaction plot for water recovery (error bars represent $\pm 1$ standard deviation).....	158
Figure 6-6. (a) Pareto chart for pyrite ( $\gamma p$ ) and water yields ( $\gamma pw$ ); (b) water recovery versus pyrite yield at different pH and temperatures.....	159
Figure 6-7. Sphalerite flotation main effects and interaction plots: (a) main effects plot for sphalerite recovery; (b) interaction plot for sphalerite recovery; (c) main effects plot for water recovery; (d) interaction plot for water recovery (error bars represent $\pm 1$ standard deviation). ....	160
Figure 6-8. (a) The Pareto chart for sphalerite ( $\gamma s$ ) and water yields ( $\gamma sw$ ); (b) water recovery versus sphalerite yield at different pH and temperatures. ....	161
Figure 6-9. Loading plots for foam stability responses, temperature, and pH, and flotation responses of: (a) galena; (b) pyrite; (c) sphalerite. ....	162
Figure 6-10. Modified Pareto charts, showing statistical significance of the factors (combinations of factors) on metallurgical performance of sphalerite (a – grade, b – recovery), quartz (c – grade, d – recovery), and baryte (e – grade, f – recovery).....	164
Figure 6-11. Contour plots of statistically significant models for the first flotation stage (Pb stage) of SEDEX ore in the coordinates of temperature-depressant dosage for sphalerite recovery (a), quartz recovery (b), and baryte recovery (c) (all values are given as relative numbers to a central point).165	
Figure 6-12. Modified Pareto charts showing an importance of factors for flotation of sphalerite (a – grade, b – recovery), quartz (c – grade, d – recovery), and baryte (e – grade, f – recovery).....	166
Figure 6-13. Changes in sphalerite concentrate zinc grade with temperature and activator dosage	167
Figure 6-14. Flotation rate constant distributions at 15 °C (blue lines) and 35 °C (red lines) for: sphalerite (a), galena (b), quartz (c), and baryte (d).....	167
Figure 6-15. Linear regression between sphalerite grade change and air recovery (a), and forth stability factor (b).....	168

---

Figure 7-1. Selected zinc mines on a world climate map. Main climates: A – equatorial, B – arid, C – warm, D – snow, E – polar. Precipitation: W – desert, S – steppe, f – fully humid, s – summer dry, w – winter dry, m – monsoonal. Temperature: h – hot arid, k – cold arid, a – hot summer, b – warm winter, c – cool summer, d – extremely continental, F – polar frost, T – polar tundra (adapted from (Kottek <i>et al.</i> , 2006)).....	171
Figure 7-2. Simplified flotation flowsheet of Red Dog Concentrator (based on (Krolak <i>et al.</i> , 2017)) .....	173
Figure 7-3. Simplified flowsheet of zinc flotation section of Matagami Concentrator (adapted from (Hamel <i>et al.</i> , 2001)).....	174
Figure 7-4. Simplified flotation flowsheet for Caribou Concentrator (adapted from (Côté and Adante, 2009)).....	175
Figure 7-5. Simplified flowsheet of Neves Corvo zinc circuit of a plant (based on (He <i>et al.</i> , 2008)) .....	176
Figure 7-6. Historical performance of Caribou processing plant for zinc recovery and grade .....	177
Figure 7-7. Regression analysis of zinc concentrate grade and recovery in relation to temperature (built using the data from (Jensen <i>et al.</i> , 2018)).....	178
Figure 7-8. Regression analysis of zinc concentrate grade at Matagami Mine (data for analysis retrieved from (Nesset <i>et al.</i> , 2002)).....	181
Figure 7-9. Regression models for zinc recovery with temperature at Neves-Corvo plant: (a) 2012 to 2015 data, (b) data from 2015 only (the data for the plots was taken from (Fernandes, 2016)) .....	182
Figure 7-10. Relation between zinc recovery and atmospheric precipitation in Neves-Corvo Mine in 2015 (plotted using data published in (Fernandes, 2016)).....	184
Figure 7-11. Dosages of flotation reagents compared to maximum temperature in Neves-Corvo mine: (a) lime dosage, (b) copper sulfate dosage, (c) potassium amyl xanthate dosage (constructed using the data reported in (Fernandes, 2016)) .....	185
Figure 7-12. Improvement in sphalerite and galena recovery after introduction of Jameson cells on the plant (red dots and red trend line represent plant performance before installation of Jameson cells, the	

---

---

blue dots and blue trend line shows plant performance after installation of the cells) (adapted from (Smith <i>et al.</i> , 2008)).....	186
Figure 7-13. Rejection of sphalerite and galena before installation of Jameson cells (a and b), and after installation of Jameson cells (c and d), plotted based on the data published in (Smith <i>et al.</i> , 2008)	187
Figure 7-14. Sensitivity of laboratory investigations and plant performances in terms of sphalerite recovery (a) and sphalerite concentrate grade (b).....	188

---

## List of Tables

Table 1-1. CC for different pairs of minerals constituting typical Pb-Zn ore .....	9
Table 3-1. Characteristics of monomineralic samples used in this research.....	70
Table 3-2. Mineralogical composition of pyrite, galena, and sphalerite samples. ....	73
Table 3-3. Central composite design of experimental levels. ....	79
Table 3-4. Solubility constants of reactions used for thermodynamic calculations.....	92
Table 3-5. Entropy values for ionic species used in thermodynamic calculations .....	95
Table 3-6 Surface shear viscosity of solutions with different surfactants.....	100
Table 4-1. Characteristics of the models for pyrite, sphalerite, and galena adsorption tests .....	110
Table 4-2. Adsorption isotherms for SIPX adsorption on pyrite, sphalerite, and galena.....	113
Table 4-3. Results of calculations of apparent activation parameters for iPX adsorption .....	118
Table 5-1. Summary of CCD models' goodness of fit and ANOVA. ....	138
Table 6-1. General full factorial model summary for galena flotation responses (summary of ANOVA for regression galena flotation model). ....	155
Table 6-2. General full factorial model summary for pyrite flotation responses (summary of ANOVA for regression pyrite flotation model). ....	157
Table 6-3. General full factorial model summary for pyrite flotation responses (summary of ANOVA for regression pyrite flotation model). ....	159
Table 6-4. Characteristics of the models for galena, sphalerite, quartz and baryte flotation to the first (Pb) concentrate .....	163
Table 6-5. Characteristics of the models for galena, sphalerite, quartz and baryte flotation to the second (Zn) concentrate .....	165
Table 7-1. Pearson's correlation coefficients for the metallurgical plant performance and meteorological data (calculated based on data from (Jensen <i>et al.</i> , 2018)) .....	179

---

Table 7-2. Partial correlation coefficients for precipitation and throughput (built using the data from (Jensen <i>et al.</i> , 2018)).....	179
Table 7-3. Ranking of external factors based on maximum information coefficient (built using the data from (Jensen <i>et al.</i> , 2018)).....	180
Table 7-4. Correlation coefficients for zinc concentrate grade and some external factors at Matagami Mine (calculated based on the data in (Nesset <i>et al.</i> , 2002)).....	182
Table 7-5. Pearson's correlation coefficients of zinc recovery and different meteorological and process parameters (calculated based on (Fernandes, 2016)).....	183
Table 7-6. Maximum information coefficient of natural and process factors affecting zinc recovery in Neves-Corvo plant in 2015 (calculated based on data in (Fernandes, 2016)) .....	184
Table 7-7. Pearson's coefficients for Red Dog mine pre-flotation circuit performance versus meteorological data before and after reconstruction (based on data in (Smith <i>et al.</i> , 2008)).....	188



---

## Chapter 1. Introduction

Zinc and lead are among the longest mined metals with important applications across different sectors of the economy (Christie and Brathwaite, 1995; Mohr *et al.*, 2018). Despite being found together in different mineral deposits these two metals have different properties, which determine different areas of their application (Mohr *et al.*, 2018).

Zinc is one of the most crucial elements for the sustainable development of modern construction, metallurgical, and energy sectors among others (Kania and Saturnus, 2023). It is recognized as one of the fundamental drivers of the green energy transition (Liesbet *et al.*, 2022). Through galvanization, zinc substantially contributes to a circular economy by extending the service life of products in numerous industries including wind and solar applications (International Zinc Association, 2017). Despite its economic importance recognized by the European Commission, low supply risk rendered zinc non-critical for the European market (European Commission, 2020). Nevertheless, critical raw material lists of such countries as, *e.g.*, Canada, Australia, the U.S., and South Africa in 2021 and 2022 included zinc as a critical metal, outlining its importance for clean technologies and advanced manufacturing (Natural Resources Canada, 2022; U.S. Geological Survey, 2022).

Lead is categorized as an essential metal by the International Lead Association (Binks, 2023). The metal was included in the critical mineral and metal lists of countries including South Africa and South Korea (Australian Government: Australian Trade and Investment Commission, 2023; Department of Mineral Resources and Energy of the Republic of South Africa, 2022). Moreover, lead was categorized as a commodity with high economic vulnerability for the U.S. market (Nassar and Fortier, 2021). A substantial amount of lead produced is used in the production of batteries (industrial and automotive), cable coverings, ammunition, and construction materials, as well as for various applications in the chemical industry (Klochko, 2018).

For both metals, an increase in price is forecasted during the decades ahead, related to a decline in the ore grades and an increase in the extraction cost (Sverdrup *et al.*, 2019). More efficient resource utilization is one of the challenges modern extractive industries are facing. It requires a comprehensive understanding of the mechanisms underlying discrepancies in the recovery

processes, which may be triggered internally (*e.g.* declining ore quality) and externally (by temperature, process water quality, reagents, *etc.*) (Kawatra, 2009).

### 1.1. Geo-Technological Characterization of Lead-Zinc Ores

Approximately 70% of zinc and less than 50% of lead were mined from primary sources in 2019 and 2015 respectively (International Zinc Association, 2019; Keating, 2015). Zinc is never found and mined from nature as pure metal (BCS Inc., 2002), but is found in 295 minerals (Mindat.org) with approximately 55 classified as zinc minerals (Thompson, 2006). From these 55 minerals the most industrially important are sphalerite ((Zn,Fe)S), zincite (ZnO), franklinite (ZnO(Fe,Mn)<sub>2</sub>O<sub>3</sub>), calamine (Zn<sub>2</sub>(OH)<sub>2</sub>SiO<sub>3</sub>), and smithsonite (ZnCO<sub>3</sub>) (Ray *et al.*, 2014). Zinc production predominantly relies on sphalerite extraction (more than 85% of world primary production) (Abkhoshk *et al.*, 2014; Balarini *et al.*, 2008; Gilg *et al.*, 2008) from sulfide deposits. Sphalerite is frequently associated with lead, copper, and silver minerals (BCS Inc., 2002). Lead is rarely found in metallic form in nature (Indian Bureau of Mines, 2020), rather in more than 600 minerals (Mindat.org) with 144 classified as lead minerals (Pol'kin and Adamov, 1975). The principal industrial lead minerals are galena (PbS), cerussite (PbCO<sub>3</sub>), and anglesite (PbSO<sub>4</sub>) (Wang, 2016a). Similar to zinc, lead is abundantly found in sulfidic form with galena being the most widespread and the most economically important lead mineral (Indian Bureau of Mines, 2020). Galena may contain such accessory elements as silver, copper, zinc, bismuth, arsenic, antimony, molybdenum, and manganese (Mitrofanov, 1966). From a mineralogical perspective, lead and zinc ores may be classified into oxide, mixed, and sulfide types depending on their degree of oxidation (Indian Bureau of Mines, 2020). In oxide lead-zinc ores more than 50% of lead and zinc is found in minerals with oxygen in the crystal lattice. The sulfide ore type has less than 15 and 10% of lead and zinc presented in oxide minerals respectively (State Commission for Mineral Reserves, 2007). Currently, sulfide deposits have the most economic importance as they serve as the main source of lead and zinc (Indian Bureau of Mines, 2020).

There are 8 main genetic types of deposits with lead and zinc, namely: Sediment-hosted, Volcanogenic Massive Sulfide (VMS), Skarn, Epithermal, Porphyry, Manto-type, Iron oxide copper-gold (IOCG), Orogenic gold and mesothermal veins (Mudd *et al.*, 2017). Sediment-hosted,

VMS, Skarn, and Epithermal deposits account for more than 90% of the world's zinc mining production (Redmond, 2023).

Sediment-hosted Pb-Zn deposits are the most important source of lead and zinc. The deposits are responsible for approximately 50% of the world's primary lead-zinc production (Bulatovic, 2007; Redmond, 2023). These deposits form at lower temperatures, compared to VMS deposits, as they are not directly related to igneous activity (Leach *et al.*, 2005). The main ore minerals of these deposits are galena and sphalerite. The host rocks typically went through weak dolomitization, baritization, and silicification (State Commission for Mineral Reserves, 2007). The processability (floatability) of these ores varies significantly. Generally, they are classified as difficult to treat (Bulatovic, 2007). It is related to sphalerite and galena being frequently finely disseminated in the deposits. The presence of secondary copper minerals in some deposits of this type creates selectivity problems between galena and sphalerite due to uncontrollable natural activation (Bulatovic, 2007). Additionally, a range of sediment-hosted deposits contain carbonaceous pyrite (contaminated with graphitic or organic carbon), and arsenopyrite which further complicates the selective extraction of galena and sphalerite.

There are two types of sediment-hosted deposits: sedimentary exhalative (SEDEX), and Mississippi Valley-type (MVT). SEDEX deposits form when hydrothermal fluids replace sediments at the seafloor with secondary minerals. Ore of this sub-type may be hosted by carbonaceous-terrigenous strata, carbonate rocks, and tuff-terrigenous strata (State Commission for Mineral Reserves, 2007). Baryte may be present in large (for Phanerozoic age deposits), small (for Proterozoic age) quantities, or even none. Iron sulfide content is also highly variable (Lydon, 1995). MVT forms with low-temperature fluids at the sedimentary basins during diagenesis (Robb, 2020). This subtype is particularly interesting because of the relatively low contents of pyrite and pyrrhotite compared to other lead-zinc deposits (Vikentiev, 2023). The MVT deposits' main minerals are galena, sphalerite, baryte, and fluorite, which fill secondary porosity in carbonate rocks (limestone and/or dolomite) (Kesler and Simon, 1994). Apart from their simple mineralogical composition, these ores are also known as easy to treat, with high grades achieved even with a simple flotation scheme (Bulatovic, 2007).

VMS deposits are the second most important source of zinc. The deposits were estimated to be responsible for approximately 22% and 10% of the world's primary production of zinc and lead

respectively (Mills, 2022; Redmond, 2023). Moreover, approximately 18% of zinc resources are found in VMS deposits (Redmond, 2023). VMS deposits are also formed in the sub-marine environment as a result of volcanic activity (Galley and Koski, 1999). In the raw VMS→SEDEX→MVT the contribution of volcanism and the temperature of ore formation decrease, while the salinity of ore-forming hydrothermal fluids increases (Vikentiev, 2023). These deposits have two compositional sub-groups: copper-zinc deposits, and copper-lead-zinc deposits (Franklin *et al.*, 2005). The main minerals of these deposits are sphalerite, galena, pyrite, pyrrhotite, chalcopyrite, and baryte (State Commission for Mineral Reserves, 2007), with host rocks represented by volcanic rocks or sedimentary strata (Franklin *et al.*, 2005). In some deposits of this group the pyrite content may reach up to 90% (Lydon, 1995). As for SEDEX ores, the floatability of the ores varies significantly. The main challenges in processing these ores arise from high contents of soluble salts (which decreases conventional flotation reagents efficiency), the presence of acidic gangue in some deposits (which increases pH modifier consumption in flotation), as well as high clay content in some deposits (which negatively impacts all aspects of flotation) (Bulatovic, 2007).

Based on the environment of the formation, 3 sub-types of VMS deposits may be identified: Cyprus, Kuroko, and Besshi types. Cyprus sub-type deposits are small to medium in size and are typically rich in copper and zinc. These deposits are characterized by the presence of massive pyrite underlain by quartz-sulfide veins, that are rich in copper (Singer, 1986a). Kuroko deposits, in contrast to Cyprus-type, can be very large. They also have higher grades of zinc, lead, silver, and antimony, compared to Cyprus deposits. These deposits are known for typical coarse sulfide mineralization (Singer, 1986b). The Besshi-type deposits are found in a mixed sedimentary-volcanogenic environment, characterized as highly variable ores. These deposits are known to be rich in copper (poor in lead), and, unlike the previous 2 sub-types of VMS, form thin sheets of massive sulfide rocks predominantly composed of iron sulfides (pyrite and/or pyrrhotite) (Taylor *et al.*, 1996).

SEDEX and VMS deposits formed under conditions of rapid cooling of hydrothermal fluids resulting from contact with cold marine water have finely disseminated ore minerals. It is challenging to separate the valuable minerals in such ores from gangue, which renders these ores hard to process (Ghazi and Millette, 1964). Deposits that were formed in a slow cooling

environment, and/or experienced metamorphism/recrystallization have larger ore mineral grain size and are classified as easy-to-process deposits (Ghazi and Millette, 1964).

Skarns are epithermal deposits that are also an important source of zinc (Dawson, 1995) responsible for approximately 18% of primary production and 14% of world resources (Redmond, 2023). The skarns are predominantly represented by calcium and magnesium silicates (Dawson, 1995) hosted in carbonate strata (State Commission for Mineral Reserves, 2007). These deposits are formed as a result of the interaction of hydrothermal fluids from magmatic intrusions with country rocks (limestones) (Einaudi and Burt, 1982). The regional and thermal metamorphism and metasomatic replacements are primarily responsible for the formation of these deposits. The metamorphic events followed by recrystallization improved the quality of the ore for mineral processing/metallurgical recovery through an increase in grain size. Most large zinc skarns contain rich and poor skarn zones (Dawson, 1995). These ores are closely associated with pyroxenes, areas of silicification and chloritization, and, sometimes, quartz-ankerite metasomatites. The most important minerals found in these deposits are galena, sphalerite, chalcopyrite, pyrrhotite, and arsenopyrite (State Commission for Mineral Reserves, 2007).

Epithermal deposits are formed by hydrothermal fluid circulation driven by magmatic heat at a depth <1.5 km below the local water table (Simmons *et al.*, 2005). The main resources of epithermal deposits in most cases are gold and silver. Nevertheless, they may also contain Cu, Pb, Zn, As, Sb, and Sn (Simmons *et al.*, 2005). Epithermal deposits with low to intermediate sulfidation frequently contain Pb-Zn mineralization (Sillitoe *et al.*, 1998). Subvolcanic types of epithermal deposits have notably simple mineralogic composition dominated by quartz. Other gangue mineralogy may include carbonates, sericite, chlorite, and micas. The sulfide minerals are closely associated with quartz and are typically represented by a pyrite-pyrrhotite-arsenopyrite complex with high-iron sphalerite. The deep volcanogenic type is formed in andesites and rhyodacite host rocks. They are known for the tennantite-tetrahedrite-chalcopyrite ore complex with associated low-iron sphalerite and rhodochrosite and anhydrite gangue (Sidorov *et al.*, 2015).

Bulatovic (Bulatovic, 2007) grouped lead-zinc ores into 6 categories based on the processability:

1. Coarse-grained ores with low-to-medium iron content. This type typically includes MVT deposits. They have relatively simple mineralogical composition and coarse liberation sizes

of galena and sphalerite (above 100  $\mu\text{m}$ ). Treatment of such ores requires a simple reagent scheme.

2. Relatively coarse-grained unoxidized massive sulfide ores. Zinc minerals in such deposits are typically rich in iron (*e.g.* marmatite).
3. Finely disseminated massive sulfide ores. These ores may/may not contain carbonaceous gangue. The mineralogy is relatively complex, with iron sulfide (pyrite, pyrrhotite) content between 15 and 60%. Other gangue may be represented by baryte and clay minerals.
4. Finely disseminated refractory ores. Characterized by extremely fine dissemination of ore minerals (liberation size below 10  $\mu\text{m}$ ). Iron sulfide content varies between 10 and 90%.
5. Oxidized and altered ores. Known for the high content of acidic gangue. Therefore, these ores are treated by bulk sulfide flotation or selective flotation scheme with prior ore washing.
6. Silver-rich ores. The ores contain lead and zinc minerals, but the processes are focused on silver recovery as a primary commodity. Silver content may reach up to 500 g/t.

The main challenges in the mineral processing of lead-zinc ores, demonstrated by the examples from Canada and Australia (Mudd *et al.*, 2017), are the historically declining grades of the processed ores, as well as processing increasingly complex (refractory) ores, which, as a rule, leads to lower recovery, grades, and higher operating costs (Mudd *et al.*, 2017). The depletion of high-quality ores and limited success in the exploration of new deposits in the last 20 years raises concerns about potential long-term zinc supply shortfall (Redmond, 2023). The overall increase in zinc demand and an increasing demand for high-quality zinc concentrates are additional challenges the industry is facing. Some forecasts suggest that in order to meet the forecasted zinc demand for 2040 every year three new zinc mines should be opened (240 kt of new production per year) (Wojcik, 2023).

Only the development of new technologies allowed the commercial exploitation of some refractory ore deposits that were previously considered untreatable (Mudd *et al.*, 2017). Therefore, the potential shortfall of zinc supply should be tackled just not only by increased investment into the exploration of new deposits but also by improvement of the efficiency of current processing plants, which should allow increased recovery, and decelerate the acuity of zinc resource availability. From the mineralogical point of view, Weiss outlined four main ore factors controlling zinc

flotation efficiency: the degree of ore oxidation, the presence of copper minerals in the ore, the content of iron sulfides, and the acidity/basicity of the gangue matrix (Weiss, 1985). However, apart from such internal factors as the nature of the ore and the efficiency of the processing method, sphalerite flotation may be also impacted by external triggers. In view of climate change and the development of deposits at locations with increasingly degrading climate conditions, temperature adds another dimension to the criticality of zinc ores extraction and processing.

## **1.2. Mineral Processing of Lead-Zinc Ores**

Zinc ores typically contain 5-15% zinc (Wang, 2016a) while rich lead ores typically have a grade between 3 and 8% (Davidson *et al.*, 2014). Therefore, to be economically extracted, the ores have to be pre-concentrated by mineral processing to separate the minerals with a metal of interest from low economic value material prior to the metallurgical extraction (Wang, 2016a). Moreover, it is important to produce high-grade concentrates, as the costs of downstream metallurgical processes (*e.g.* electrolysis, smelting in a blast furnace) rise steeply with a decrease in concentrate grade (Bhatti *et al.*, 2016). Usually, the lowest quality of zinc and lead concentrates accepted by metallurgical facilities is 40 wt. % of metal (State Commission for Mineral Reserves, 2007).

Until the discovery of selective flotation, magnetic and gravity separations were the most common methods utilized for beneficiating lead-zinc ores (Gunther, 1909). Nowadays, a common challenge for the processing of lead-zinc ores is complex mineralogy with fine liberation size of valuable minerals, which requires fine grinding and flotation (Nayak *et al.*, 2021).

### **1.2.1. Comminution and Classification**

Typical comminution steps for lead-zinc ores include crushing (with jaw and/or cone crushers) followed by milling (in rod and/or ball mills) (Pease *et al.*, 2010; Wei and Sandenbergh, 2007). In the case of fine ore dissemination, in order to achieve liberation size and produce a concentrate of required quality the fineness of grinding may be required to go below 10  $\mu\text{m}$  (*e.g.* McArthur River mine in Canada, Mount Isa Mine in Australia) (Pease *et al.*, 2010). For ultrafine grinding purposes, Isa Mills are frequently used (Côté and Adante, 2009). Isa Mills utilizes inert grinding media which results in relatively clean mineral surfaces that improve sulfide floatability (Bulatovic, 2007; Gao *et al.*, 2002). Some other alternatives to Isa Mills in ultrafine grinding are the stirred media detritor (SMD) and high intensity grinding mill (HIGmill). One of the most

important drawbacks of these three ultrafine grinding machines is the production of de-oxygenated pulps, which decelerates pyrite oxidation. Unoxidized pyrite floats well and contaminates the concentrates of valuable base metals (Greet, 2023).

After grinding, classification takes place to separate fine particles from coarse particles, with coarse material recirculated to the mill and fines pumped to flotation. It is usually accomplished by hydrocyclones (Ejtemaei *et al.*, 2011). For some lead-zinc ores with high clay content hydrocycloning is extremely important for ultra-fines removal to minimize slime coating of sphalerite and galena surfaces, as well as avoiding increased reagent consumption by fines (Ejtemaei *et al.*, 2011). Water-injection cyclones can further improve the efficiency of material classification. Thus, in tests with lead-zinc ores water injection into the cyclone helped to displace fines from cyclone underflow to overflow, which eventually increased flowsheet recovery (Udaya Bhaskar *et al.*, 2005). Moreover, desliming can even decrease the content of gangue minerals, such as quartz or gypsum (Rashchi *et al.*, 2005).

### **1.2.2. Non-Flotation Processing Techniques**

Nowadays magnetic and gravity separations are gaining more attention, mostly as processing techniques complimentary to flotation (Nayak *et al.*, 2021). For ores with coarse galena, the processing schemes include gravitational recovery of coarse galena particles upstream and subsequent flotation recovery of fine galena downstream (Pol'kin and Adamov, 1975). Application of shaking tables and heavy-media cyclones can help to process coarse-grained lead-zinc ores (Abere *et al.*, 2018). Contrarily, the application of conventional gravity separation methods has demonstrated a complete ineffectiveness for pre-concentration of fine-grained disseminated lead-zinc sulfide ores (Kohad, 1998). In order to separate valuable minerals from such ores they should be finely ground; however, gravity alone is not enough to create sufficient differential mobility between fine and ultrafine gangue and ore particles (Sarkar *et al.*, 2007). For a quick assessment of amenability to conventional gravity separation of minerals concentration criterion (CC) can be used (Gupta and Yan, 2016):

$$CC = \frac{SG_{heavy\ mineral} - SG_{media}}{SG_{light\ mineral} - SG_{media}} \quad (1-1)$$



where  $SG_{\text{heavy mineral}}$  is the specific gravity of heavier mineral,  $SG_{\text{light mineral}}$  is the specific gravity of lighter mineral in the separation process, and  $SG_{\text{media}}$  is the specific gravity of media where separation takes place (taken as water). When assuming the following specific gravities, CC for different pairs of minerals constituting typical Pb-Zn ore may be estimated: 7.6 for galena, 5.0 for pyrite, 4.5 for baryte, 4.1 for sphalerite, and 2.7 for quartz (Robie and Bethke, 1962) (Table 1-1).

Table 1-1. CC for different pairs of minerals constituting typical Pb-Zn ore

	Galena	Pyrite	Baryte	Sphalerite	Quartz
Galena					
Pyrite	1.65				
Baryte	1.90	1.15			
Sphalerite	2.16	1.31	1.14		
Quartz	4.00	2.42	2.11	2.11	

	CC < 1.25 (impossible at any size with conventional gravity methods)
	1.25 < CC < 1.50 (gravity separation is possible down to 6.35 mm)
	1.50 < CC < 1.75 (gravity separation is possible down to 1.70 mm)
	1.75 < CC < 2.50 (gravity separation is possible down to 150 $\mu\text{m}$ )
	CC > 2.50 (gravity separation is easy down to 75 $\mu\text{m}$ )

As seen in Table 1-1, the best separability with conventional gravity methods may be obtained with galena and quartz (separation is easily achievable down to 75  $\mu\text{m}$  size). The criterion between 2.5 and 1.75 (for galena-sphalerite, galena-baryte, pyrite-quartz, baryte-quartz, and sphalerite-quartz) indicates a possibility of gravity separation of this mineral pairs down to 150  $\mu\text{m}$  particle size. Based on CC for galena-pyrite and pyrite-sphalerite it could be assumed that their separation is possible with particle sizes down to 1.7 mm and 6.35 mm respectively. Baryte-pyrite and baryte-sphalerite separation according to CC is impossible at any particle size.

As can be determined from these simple calculations, conventional gravity separation can be considered as a pre-concentration method, mainly for the elimination of light gangue, like, *e.g.*, quartz, or for recovery of coarse galena at the head of the process. Application of gravity-flotation flowsheets was reported at some lead-zinc plants with coarse ore mineralogy and oxide minerals

(Oladunni Oyelola *et al.*, 2016; Önal *et al.*, 2005). Conventional gravity separation may be also improved by utilizing separation media other than water (*e.g.* heavy media suspensions) (Pol'kin and Adamov, 1975).

To increase particle momentum (settling characteristics), additional forces and conditions may be introduced to a gravity separation system (advanced gravity separation), such as *e.g.* centrifugal acceleration (*e.g.* enhanced gravity separators: Knelson, Falcon, Kelsey jig, Multi-Gravity Separator, *etc.*), modifications of separation medium viscosity and density via fluidization (*e.g.* counter flow fluidized separators: Floatex separator, Reflux classifier, Crossflow separator, Allflux separator, *etc.*) (Das and Sarkar, 2018; Sarkar *et al.*, 2007). Thus, for example, the successful application of advanced gravity separators was reported for lead-zinc ores with Falcon and Multi-Gravity Separator (MGS) (Göktepe, 2005; Nayak *et al.*, 2021; Sarkar *et al.*, 2007). The MGS was reported to be a particularly suitable processing unit for graphite rejection from lead concentrates (Udaya Bhaskar *et al.*, 2002). In another study, MGS was able to achieve an upgrade ratio close to 3 with lead flotation tailings with a particle size below 106  $\mu\text{m}$  (Göktepe, 2005). Counterflow fluidized separators can also be used for more complete recovery of valuables from lead-zinc ore, as has been demonstrated with reflux classifier (additional separation of baryte and pyrite products from a lead-zinc ore) (Hu *et al.*, 2024).

Some of the disadvantages of the advanced gravity separators compared to flotation are that it is hard to reject ultrafine clay particles (Honaker and Reed, 1995), they have relatively low capacities (Luttrell *et al.*, 1995), and, in some cases, lower recoveries are achieved (Erkan *et al.*, 2022). Additionally, for mineral combinations of low-density contrast (*e.g.* baryte and sphalerite), the application of any gravity-based technique would be less efficient than in the case of mineral surface-based methods, such as flotation. Thus, some rich baryte mines produce gravity concentrates with SG that coincide with sphalerite SG of 4.1 (Johnson *et al.*, 2017). It has been emphasized in the review by Nayak *et al.* (Nayak *et al.*, 2021) that achieving satisfactory grades and recoveries is challenging in the case of lead-zinc ores by using gravity separation techniques alone. They have suggested that gravity separation may have a potential application in lead-zinc ore processing by applying multi-stage cleaning with advanced gravity separation equipment or as a part of a flowsheet that starts with gravity pre-concentration followed by flotation (Nayak *et al.*, 2021).

Historically, depending on the iron content of sphalerite, magnetic separation has been used for pre-concentration of this mineral (after or before roasting). Magnetic separation has been also applied for the separation of sphalerite and siderite (often after magnetizing roasting) (Plotnikova *et al.*, 2019). Pure sphalerite, like galena, is diamagnetic (Plotnikova *et al.*, 2019). However, with an increase in iron and manganese content the magnetic susceptibility of sphalerite increases. (Ryabeva and Dobrovol'skaja, 1978). Nevertheless, even in sphalerite with 20% isomorphous iron the magnetic susceptibility only slightly increases (Plotnikova *et al.*, 2019). Therefore, iron substitution alone is not sufficient for sphalerite recovery using magnetic methods. Higher magnetic susceptibilities reported for natural sphalerite samples are related to the inclusions of finely disseminated highly magnetic minerals, such as pyrrhotite. Depending on mineral associations sphalerite samples may expose different paramagnetic properties by having inclusions of such iron minerals as siderite, pyrite, pyrrhotite, or even magnetite (Plotnikova *et al.*, 2019; Ye *et al.*, 2011).

Magnetic separation for lead zinc ores has demonstrated some promising results in the case of sphalerite pre-concentration with a high-intensity magnetic separator (0.65 T for iron-rich sphalerite and 0.85 T for iron-poor sphalerite). Magnetic pre-concentration allowed for improved flotation efficiency downstream (Jeong and Kim, 2018). Another reported application of magnetic separation for lead-zinc ores is the removal of sphalerite from galena concentrate using a high-intensity magnetic separator (1.1 T). It should be noted that sphalerite in the tested ore samples was closely associated with magnetic minerals: pyrrhotite, pyrite, and siderite (Plotnikova and Bragin, 2018). With all the advantages of magnetic separation for lead-zinc ore processing, under current technological development, it is inferior in many respects to flotation and may be considered only as an additional operation to the main flotation processing route (Plotnikova *et al.*, 2019).

### **1.2.3. Lead-Zinc Ore Flotation**

As an industrial process for zinc-lead minerals recovery from sulfide ores, froth flotation was developed at the beginning of the 19<sup>th</sup> century (Fuerstenau *et al.*, 2007). It remains the most widely used method for lead-zinc ore processing (Fuerstenau *et al.*, 2007).

Galena may be efficiently floated by sulfhydryl and oxyhydryl collectors. However, because oxyhydryl collectors also tend to float gangue minerals, sulfhydryl collectors found widespread

application in galena flotation practice (Glembotskij and Klassen, 1981). Some of the accessory elements in the galena structure can modify its flotation properties. Thus, *e.g.*, silver, bismuth, and copper can improve galena floatability. Contrarily, the presence of zinc, manganese, iron, and antimony makes galena less active for flotation with xanthates, which are the main sulfhydryl collectors used for galena flotation (Mitrofanov, 1966). Thus, galena shows excellent floatability with ethyl xanthate in the pH range of 3-10.5. At pH above 10.5 lead carbonate and hydroxide are less soluble and form stable compounds on the mineral surface (Fuerstenau *et al.*, 2007). In cases of strongly oxidized galena or in deposits with mixed oxide-sulfide ore composition, sulfidization (with sodium sulfide) is applied before flotation. The excess of sodium sulfide leads to galena depression, whereas too low a concentration does not fully activate non-sulfidic lead minerals (Pol'kin and Adamov, 1975).

Cyanides and zinc salts, as a rule, do not depress galena flotation, while copper sulfate usually does not activate galena. The optimum flotation pH in many cases is around 9. Since lime depresses galena flotation, soda ash is considered to be a preferable pH modifier (Glembotskij and Klassen, 1981). Galena is known to be depressed by salts of chromic acid (*e.g.*  $K_2Cr_2O_7$  or  $K_2CrO_4$ ) which form hydrophilic lead chromate compounds on the mineral surface (Pol'kin and Adamov, 1975). Additionally, for copper-lead-zinc ores galena can be depressed by sodium phosphates. Thus, there is an opportunity for galena–sphalerite separation using sodium phosphate when sphalerite is sufficiently activated by copper ions (Dudnikov *et al.*, 1969). Disulfite ferrite ions ( $[Fe(SO_3)_2]^{2-}$ ) are also known to depress galena as well as other minerals (including sphalerite and pyrite). However, having been depressed by disulfite ferrite ions, galena can be re-activated by the addition of cyanide or sodium dicarbonate cuprite ( $Na_2[Cu(CO_3)_2]$ ) (Konev, 1985).

Another reported depressant for galena is dextrin, which has found an application in the separation of bulk copper-lead concentrates (Bulatovic, 2007). Some commercial short-chain dextrans were also successfully used for carbonaceous pyrite depression at the Mount-Isa copper concentrator (Grano, 1991). Tannins are also known to depress galena (Dudnikov *et al.*, 1969). Therefore, galena and carbonaceous pyrite can be also successfully depressed by mixing them with dextrin (Agent G4) (Bulatovic, 2007). However, by combining Agent G4 with cyanide, this mixture can efficiently depress sphalerite and pyrite while preserving galena floatability (Bulatovic, 2007).

Sphalerite flotation properties are strongly determined by its composition. Iron in sphalerite may substitute for zinc in the crystal lattice or be found as micro-inclusions of pyrrhotite (Glembotskij and Klassen, 1981). Depending on the iron content, sphalerite may be called cleiophane (low on iron), marmatite (up to 20% Fe), or christophite (with a maximum iron content of approximately 26%) (Crundwell, 2021; Glembotskij and Klassen, 1981). Copper in sphalerite, like pyrrhotite, may be found as micro-inclusions (chalcopyrite disease). Cadmium, indium, and gallium are frequently found in sphalerite, which increases the value of sphalerite concentrate. An important property of sphalerite is its depressibility by cyanides, sulfites, hyposulfites, and sodium sulfide (Glembotskij and Klassen, 1981). The largest effect is achieved by the combination of cyanides and zinc sulfate (Glembotskij and Klassen, 1981).

Other sphalerite depressants include ammonium sulfate (Fuerstenau *et al.*, 2007), ferrous sulfate (Xia *et al.*, 2017), and zincates (*e.g.*  $\text{Na}_2\text{Zn}(\text{OH})_4$  (Wang *et al.*, 2023)). Since sphalerite normally does not float well at alkali pH with sulfhydryl collectors, this property is actively used in the industry for selective separation of sphalerite from other valuable minerals, such as, *e.g.* galena, chalcopyrite, chalcocite, *etc.* Then, to float sphalerite, its surface should be activated by metal ions that form more active sites for xanthate adsorption, such as copper ions (cupric and cuprous) (Glembotskij and Klassen, 1981). Other ions suitable for sphalerite activation include silver, lead, cadmium, antimony and mercury (mercuric and mercurous). The most common sphalerite activator is copper sulfate, which renders sphalerite properties similar to those of copper sulfides (Fuerstenau *et al.*, 2007). For sphalerite separation from pyrite, lime is most frequently used (Bulatovic, 2007), which could be even further improved by mixing it with sodium humate (Wei *et al.*, 2021). Alternatively, dextrin has also demonstrated satisfactory selectivity in sphalerite-pyrite separation at pH 7-9 (Sun *et al.*, 2022).

Galena, sphalerite, and iron sulfides (pyrite and pyrrhotite) are also known to be depressed by potassium permanganate ( $\text{KMnO}_4$ ) (Xiang, 2015). However, by combining it with sodium alginate ( $\text{NaC}_6\text{H}_7\text{O}_6$ ) a selective depression of sphalerite is achievable (Feng *et al.*, 2021). For galena and sphalerite flotation, the most important industrially applied collectors are xanthates (*e.g.* SIPX, PAX, KEX, SIBX, *etc.*), and dithiophosphates (*e.g.* R208, R242, AF242, *etc.*) being added as secondary collectors in some cases (Bulatovic, 2007; Cytec Industries Inc., 2010). Commercial reagents based on mercaptobenzothiazole and their mixtures with dithiophosphate

and dithiocarbamate were also reported as efficient flotation promoters (Cytec Industries Inc., 2010; Noirant *et al.*, 2019). Low-carbon xanthates are generally more efficient in weakly alkali environments created by soda ash, while xanthates with higher carbon numbers (C<sub>4</sub>-C<sub>5</sub>) have higher efficiency at strong alkali conditions created by lime (Mitrofanov, 1966). To improve the separation of sulfide minerals from non-sulfide gangue some plants additionally use water glass (Pol'kin and Adamov, 1975).

Flotation of lead-zinc ores can be performed using bulk and selective schemes. In bulk flotation, all sulfides are floated, and the produced concentrate is further selectively separated into minerals of interest (Glembotskij and Klassen, 1981). Higher floatability and lower grades of galena compared to sphalerite explain why in selective flotation this mineral is floated first. The main flotation approaches for the direct selective flotation of lead-zinc ores are the Sheridan-Griswold regime, the Hellstrand method, and the Pallanch process among others (Glembotskij and Klassen, 1981).

The Sheridan-Griswold regime facilitates lead recovery by depressing sphalerite and pyrite with cyanide (Sheridan and Griswold, 1922) (from 40 to 200 g/t) and zinc sulfate (120-500 g/t) in a mild alkali environment created by soda ash. According to this method, subsequent re-activation of sphalerite by copper sulfate (400-800 g/t) in strongly alkali conditions (created by lime to depress pyrite) allows for the production of a zinc concentrate. This method is widely used by numerous plants as one of the most efficient (Abramov and Forssberg, 2005; Glembotskij and Klassen, 1981; Guo *et al.*, 2014). The biggest disadvantages of this method are free gold losses (dissolved by cyanides) and toxicity of cyanides. In some cases, when an ore contains sphalerite with low floatability only zinc sulfate is used without cyanide. From the perspective of seasonal variation in flotation, considering that cyanide (Wark and Cox, 1938) efficiency changes with temperature (increase), this method is less robust to temperature fluctuations.

The Hellstrand method is based on the application of sodium sulfide for sphalerite depression. The recommended dosage of Na<sub>2</sub>S is between 500 g/t to 3.5 kg/t, which should be added preferably to the mill. Initially, Hellstrand suggested using cresylic acid or pine oil as frothers, and coal tar creosote as the collector to recover any lead and/or copper minerals presented. From a temperature perspective, this method has a significant drawback as for an efficient selective flotation under the suggested reagent regime low pulp temperatures are preferred. Sphalerite

flotation on the second flotation step was suggested to be proceed either in an alkali or acidic environment, with prior activation of zinc mineral. For an acidic regime, Hellstrand suggested heating the pulp up to 35 °C for increased efficiency (Hellstrand, 1923). The efficiency of conditioning with Na<sub>2</sub>S for the cases of sulfidization in flotation was reported to be temperature dependent. Thus, in a temperature range of 20 to 60 °C the performance of the reagent increases. At temperatures below 20 °C the reagent efficiency is low due to the endothermic character of the adsorption reactions (Fa *et al.*, 2005).

The Pallanch process suggests sphalerite depression by sodium sulfite (Na<sub>2</sub>SO<sub>3</sub>), hyposulfite (Na<sub>2</sub>S<sub>2</sub>O<sub>3</sub>), or sulfur dioxide gas applied together with zinc sulfate. Pallach also successfully used calcium sulfite for sphalerite depression; however, because of low calcium reagent solubility, the preference has been given to sodium sulfite. The reported dosages applied in the industrial setting were from 125 g/t to 250 g/t. After the flotation of galena with xanthates, like in Hellstrand and Sheridan-Griswold flotation regimes, sphalerite is activated with copper sulfate. In the zinc flotation circuit sodium sulfite is believed to combine with copper sulfate to produce copper sulfite, which improves flotation selectivity between sphalerite and pyrite with xanthate (Pallanch, 1928). For lead-zinc ores with copper Pallanch additionally suggested the addition of zinc sulfate for prevention of sphalerite activation, while for ores rich in pyrite addition of sodium sulfide or cyanide was suggested (Pallanch, 1936).

The Anderson-Norman method suggests recovery of sphalerite on the first step by depressing lead minerals with chromic acid, or sodium/potassium chromate. Since lead has strong floatability, flotation of zinc is suggested with a relatively weak collector, such as ammonium dibutyl dithiophosphate. Again, copper sulfate was suggested as an activator of sphalerite flotation. Flotation of galena in the second step was achieved by activating lead sulfide with ferrous sulfate, the addition of acids (hydrochloric, sulfuric), a mixture of acids with sodium chloride or sodium hydrosulfite, or addition of sodium bisulfite (Anderson and Hedley, 1939). The drawback of this method is that it was tested on a sample deficient in pyrite. The presence of iron sulfide will require additional flotation modifiers to be added. Additionally, low lead recoveries were obtained using this method (Anderson and Hedley, 1939).

The choice of appropriate processing regime strongly depends on ore characteristics. Thus, Bulatovic has summarized processing approaches based on his technological classification of lead-zinc ores, presented in Section 1.1. (Bulatovic, 2007).

The coarse-grained ores category usually does not contain pre-activated sphalerite; therefore, in some cases, no depressants may be used. Primarily, these ores are treated using the Sheridan-Griswold regime with some variations from the classical process. Thus, due to the generally low pyrite content, zinc flotation is usually conducted at neutral to mildly alkali pH, as sphalerite floats better under such conditions (Pattison, 1981) and contamination of the concentrate with pyrite is low. Numerous plants that treat this ore type use cyanide with zinc sulfate, although in some cases only zinc sulfate is applied (Bulatovic, 2007). The coarse character of the ore motivated some plants to introduce flash flotation (coarse particle flotation) (Gorain, 2013; Sutherland *et al.*, 2019) of lead in the grinding circuit to avoid sliming and potential losses of the mineral downstream.

Relatively coarse-grained unoxidized massive sulfide ores require more intensive utilization of depressants at higher dosages compared to the coarse-grained ores low on sulfides. The abundance of iron sulfides requires an increase in pH (Fuerstenau *et al.*, 2007). The pH is increased either with soda ash or lime (the majority of plants use lime for both: lead and zinc circuits, especially at high pyrite content) (Fuerstenau, 1962; Zanin *et al.*, 2019). Particularly for zinc circuits, the reported pH range for flotation of this ore type is between 10.5 and 11.8 (Bulatovic, 2007). The natural pH of ores goes down to 5-5.5; however, on a few plants where it exceeds 8 pH modifiers are not used in the lead circuit (Bulatovic, 2007). These ores also contain sphalerite with a higher iron content (marmatite), which negatively impacts the process through lower flotation kinetics, lower stability of marmatite in cleaner circuits (increased losses in zinc flotation cleaners), higher copper sulfate demand (Bulatovic, 2007), and lower selectivity against pyrite (Dávila-Pulido and Uribe-Salas, 2014; Deng *et al.*, 2013). The unoxidized coarse sulfide ores are mainly treated either by a collective flotation scheme or directly by the Sheridan-Griswold method with cyanide and zinc sulfate dosages varying across different plants (Bulatovic, 2007).

Finely disseminated massive sulfide ores are treated by conventional flotation techniques described for coarse ore treatment with some modifications in the reagent regime and flowsheet (Bulatovic, 2007). Thus, because of the increased ore complexity, some plants produce 3 products: lead concentrate, zinc concentrate, and bulk lead-zinc concentrate (Tolcin, 2022). The liberation



size in such ores generally varies from 15 to 40  $\mu\text{m}$  (Bulatovic, 2007). In the first flotation step, the ore is typically floated at a particle size coarser than the liberation size. Therefore, the produced rougher concentrates are typically lead-zinc bulk concentrates. The upgrade of the concentrates is achieved after re-grinding. Additionally, these ores are known to have surface contaminations with Cu, Cd, and carbonaceous gangue (Barton and Bethke, 1987; Gredelj *et al.*, 2009; Taylor *et al.*, 1996).

Besides the Sheridan-Griswold regime and collective flotation schemes, the flowsheets may have the following adjustments: zinc concentrate de-leading, and reverse flotation of iron sulfides from lead concentrate and zinc concentrate (Bulatovic, 2007). De-leading of the zinc concentrate can be achieved either by reverse flotation approach with depression of sphalerite with zinc sulfate/cyanide and galena flotation at a pH around 9 (Boeke and Gunther, 1952). Alternatively, the Anderson-Norman method with direct flotation of sphalerite and galena depression with dichromate is applied. For reverse iron sulfide flotation from zinc concentrates Hellstrand method is successfully applied (Bulatovic, 2007). Moreover, regimes with  $\text{Na}_2\text{S}+\text{NaHS}+\text{ZnSO}_4$  have proven to be more effective compared to  $\text{Na}_2\text{S}+\text{Na}_2\text{CO}_3+\text{ZnSO}_4$ , and  $\text{Na}_2\text{S}+\text{ZnSO}_4$  in terms of sphalerite depression (Shun-Ming and Jian-Tao, 2018).

As seen from a wide variety of applied methods, approaches, and chemicals, they are ore-specific and target particular challenges arising from the ore characteristics. Some of them also exhibit vulnerability to variations in temperature. Moreover, all discussed schemes share one thing in common: in later flotation stages there is a copper activation for sphalerite flotation, which is known to be a temperature-sensitive process (Albrecht *et al.*, 2016).

### **1.3. Thesis Motivation, Objectives, and Organization**

An increased complexity of the ores and a decrease in the major metal reserves has led to the mining and processing of low-grade ores with fine dissemination of the valuable component (Calvo *et al.*, 2016; Rötzer and Schmidt, 2018; The Mining Association of Canada, 2019), which requires loss minimization and process improvement. From the point of view of climate-induced challenges, several mineral processing plants across Canada have reported seasonally attributed metal losses during flotation (Levanaho *et al.*, 2005; Malafarina and Deredin, 2021; Nasset *et al.*, 2002; Xu and Wilson, 2000). Historically, similar fluctuations resulted in revenue loss accounting

for millions of dollars with JCI plants in South Africa taken as an example (Lin, 1989; O'Connor *et al.*, 1984). Therefore, it is vital to investigate temperature effects to develop forecasting models and flexible flotation solutions for securing mining businesses, maintaining mining competitiveness, and expanding resource-efficient practices in the Arctic, Subarctic, and mountainous regions (Natural Resources Canada, 2019). This is particularly important for Canada's development of Arctic and Sub-arctic regions, supported by Quebec's "Plan Nord" strategy, Chinese mining expansions in mountainous Tibet, or new mining projects in Fenno-Scandinavia (Boyd *et al.*, 2016; Gouvernement du Quebec, 2011; Palace, 2014).

Investigations into more stable and environmentally friendly methods could be a pivotal point in the development of territories with drastic temperature fluctuations. For example, in Canada, mines can experience temperature variations from below -40 °C during arctic winters to above +30 °C during hot summers (for example, Raglan mine experiences a temperature swing of more than 30 °C over the calendar year) (Mekis *et al.*, 2015). To fully account for temperature effects in flotation, an investigation of individual flotation factors and their contribution to seasonal metallurgical patterns is vital. This would help to develop technical solutions improving the performances of plants subjected to rigid climatic conditions and assisting in understanding fluctuations' driving mechanisms.

Despite wide application and a long history of innovation in froth flotation, some aspects of the process are still not completely understood (Brito-Parada *et al.*, 2012; Fuerstenau *et al.*, 2007). Moreover, the degree of impact of temperature on different flotation aspects has not been systematically investigated in the frameworks of the sulfide flotation system, which makes this thesis the first comprehensive quantitative-based research of temperature-induced variations in primary and secondary concentration of sulfide minerals in the context of lead-zinc flotation.

Moreover, the necessity of this research is dictated by an expected increase in the impact of Climate Change on the mining and metallurgical domain (through more frequent and intense manifestations of climate extremes). A strategy developed for combating Climate Change involves the Clean Energy Transition, which heavily relies on the sustainable production of required minerals and metals (Delevingne *et al.*, 2020) making this research particularly useful for consulting the industrial flotation practices and laboratory-scale investigations.

To summarize, the main objectives of the thesis are:

1. A comprehensive investigation of all flotation components under different temperatures (from reagent adsorption to froth stability issues)
2. Identification of the main mechanisms responsible for temperature-driven process discrepancies
3. Development of indicators and forecasting tools for deviations in metallurgical performance with temperature
4. Development of guidelines for the mitigation of temperature-induced fluctuations

This research is presented in the form of a monograph thesis with 8 chapters (Figure 1-1). The first chapter introduces the lead-zinc extraction business and provides descriptions of geo-technological characteristics of available primary materials, industrially applied processing methods, and related challenges. The second chapter broadly reviews temperature effects on flotation components, sulfide, and non-sulfide flotation. It also highlights some of the approaches historically applied to handle temperature-induced fluctuations. Chapter 3 describes the methodology applied in this thesis including materials, analytical techniques, and constructed experimental set-ups. The fourth chapter focuses on theoretically and practically revealed fluctuations in the primary concentration of sulfide minerals as a function of temperature. Chapter 5 is devoted to foam and froth stability issues and explains their implications for the secondary concentration. Chapter 6 shows the overall flotation performance for simple (monomineralic) and complex (multi-mineral) systems at different temperatures. Monomineralic tests aim at demonstrating temperature effects on individual minerals as well as potential cleaner flotation operations, while tests with ore (multi-mineral system) were to give an idea of rougher-scavenger flotation performance. Chapter 7 is based on openly available data. It contains analysis of the performance of different plants at different temperatures. It also attempts to bridge the observed laboratory-scale results with industrially observed trends. The last chapter of this thesis (Chapter 8) gives a general overview of the main findings and addresses knowledge gaps by new discoveries reported in this thesis. It also identifies the most promising directions for further research in the field of seasonal metallurgy.

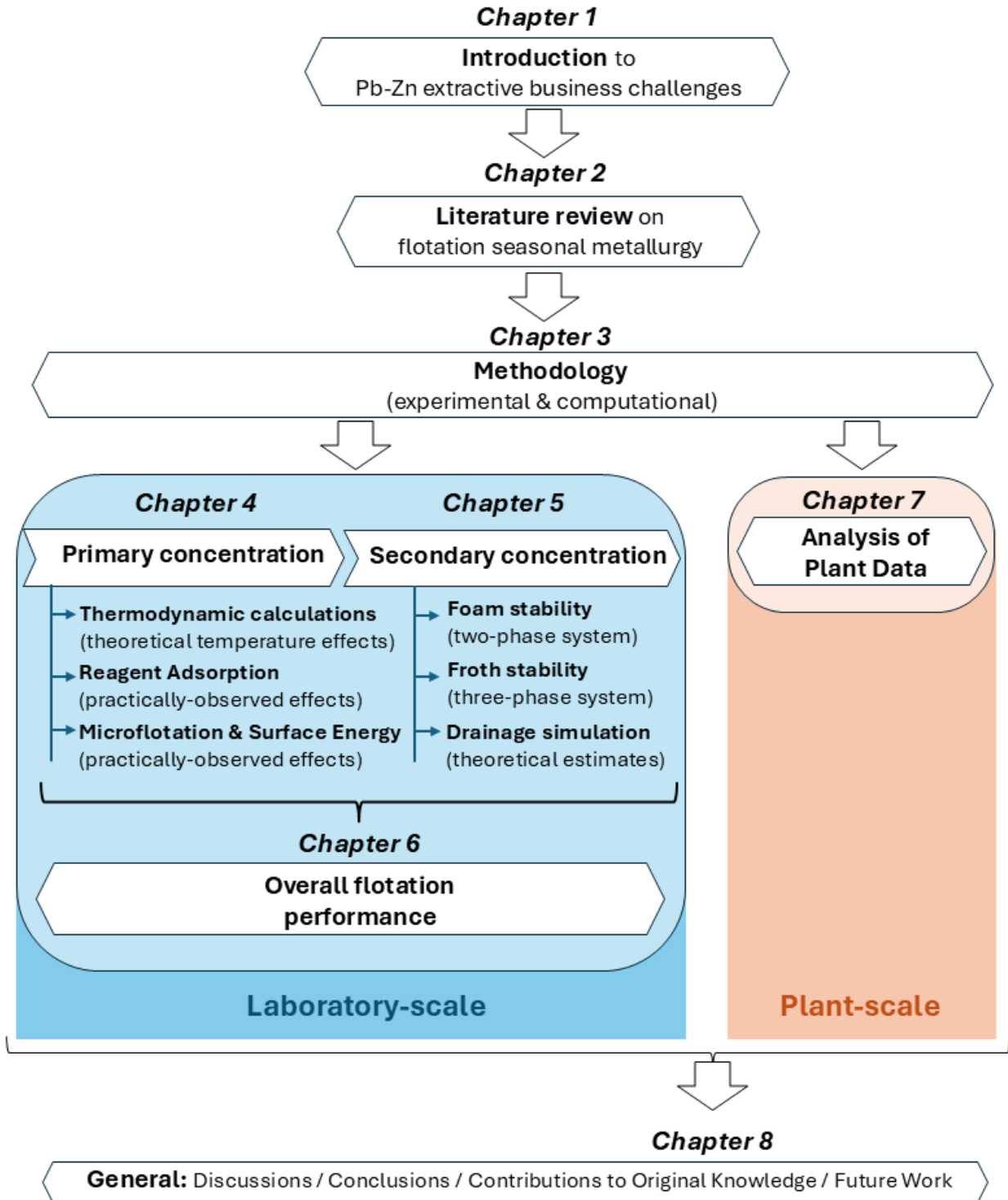


Figure 1-1. Thesis structure

---

## Chapter 2. Literature Review on Temperature Effects in Flotation

### 2.1. Introduction

Froth flotation is a complex process that has been utilized in mineral processing for more than a century (Fuerstenau *et al.*, 2007). It has one of the largest tonnage capacities among separation technologies (Brito-Parada *et al.*, 2012). The process is a cornerstone of numerous industries, such as wastewater treatment (*e.g.* sewage treatment and water purification), the energy sector (*e.g.* bitumen recovery from tar sands and coal desulfurization), recycling (*e.g.* plastics separation (Wang *et al.*, 2019) and paper deinking), and mining and metallurgical domain (around 1 billion tons of ore is treated by froth flotation worldwide annually) (Yarar, 2000). Numerous flotation research highlighted temperature and climate being important parameters for wastewater flotation (Hughes *et al.*, 2021; Kyzas and Matis, 2018), oil sands and coal flotation (Bhattacharya and Pascoe, 2005; Choung *et al.*, 2008; Schramm *et al.*, 2003), plastics recycling flotation (Kökkılıç *et al.*, 2022; Wang *et al.*, 2018; Wang *et al.*, 2019), and deinking flotation (Abdel Khalek, 2011; Downing, 1984). For mineral froth flotation in most of the cases, temperature effects were studied in relation to concentrate grade and recovery variations (De Oliveira Balduino *et al.*, 2012; Levanaho *et al.*, 2005). However, apart from the decrease in grade and recovery under varying temperatures, seasonal impacts are also known to raise the following challenges:

- Discrepancies in flotation selectivity: *e.g.* a less efficient sphalerite-chalcopyrite separation was observed in summer at the Prieska Copper Mines concentrator in South Africa (Marais, 1980).
- Changes in slurry viscosity: higher slurry viscosity was recorded during winter at South African mines including Daggafontein, Vaal Reefs, and Welkom (Marais, 1980). These changes have implications on entrainment, froth drainage issues, and bubble size (Choung *et al.*, 2008; Delahaije *et al.*, 2019; Zhang, 2014), ultimately affecting concentrate quality.
- Fluctuations in flotation kinetics: for example, a kinetics study into sulfide flotation showed that the flotation rate constant increases with temperature (Laskowski, 1989)
- Deterioration of reagent efficiencies: *e.g.* an increase in the required dosages of depressants on plants in Finland, Sweden, and Norway (Marais, 1980).

## 2.2. Temperature Impact on Processing Units Surrounding Flotation

Temperature changes influence the output of other mineral processing units “serving” flotation circuits, namely: grinding, classification (such as hydrocyclones), and thickening (water recycling). Increased water viscosity due to a seasonal temperature drop in milling leads to less efficient grinding. Theoretically, this produces fewer fines in a mill discharge and reduces milling capacity (Lin, 1989). Regarding classification, slurry viscosity changes the hydrocyclone cut point during the summer. A comparison of a hydrocyclone cut point for iron ore at 3.3 °C and 20 °C revealed coarser output in cold water: 25 µm as opposed to 20 µm (Kawatra *et al.*, 1988). The result of sending coarser material to the flotation circuit is that flotation performance will be negatively impacted due to poorer mineral liberation and a coarser feed (Lin, 1989).

Another possible seasonal issue is grinding media, which contaminates the pulp with iron and plays a critical role in sulfide flotation depression, especially for fine fractions through iron hydroxide coverage on mineral particles (Peng and Grano, 2010). Iron dissolution takes place more readily at elevated oxygen levels in the pulp (at lower temperatures) (McNeill, 2000), through a cathodic reaction (Rao and Natarajan, 1988). Thus, for marmatite, it has been reported that iron (III) hydroxide from grinding media adsorbed on the copper-activated surface hinders collector adsorption (Long *et al.*, 2020).

Regarding thickener efficiency, a drop from 29 °C to 13 °C has the potential to increase residence time by 33% as a consequence of decreased settling rate in more viscous pulps (Lin, 1989). Such seasonal changes should be taken into consideration in the plant design stage as recycling the finest material back to the flotation could render the whole process inefficient.

## 2.3. Temperature Effects on Flotation

Flotation systems and individual components can be (and have been) investigated by measuring such parameters as water hardness, dissolved oxygen level, pH, suspended fines, viscosity, surface tension, *etc.* All these parameters have been shown to be influenced by temperature variations (Dinçer and Zamfirescu, 2015), leading to cyclicity in flotation performance (Lin, 1989).

### 2.3.1. Flotation Medium: Water and Gas Properties

Significant inter-seasonal temperature changes (of more than 10 °C) could have a pronounced effect on dissolved oxygen (DO) content and slurry viscosity (Lin, 1989). Oxygen is an important

component for the oxidation of mineral surfaces and flotation chemicals. DO has temperature-dependent solubility (Figure 2-1a), affecting flotation pulp pH and Eh. Gas dissolution in water can be described by Henri's law and Van't Hoff-type equations (Dassey and Theegala, 2012; Faust and Aly, 1998):

$$M = \frac{P}{K_c} \quad (2-1)$$

$$\log(K_c) = \frac{-H^0}{2.3RT} + K \quad (2-2)$$

where  $M$  is a gas molar concentration in a liter of a solution (mol/l),  $P$  is the partial pressure of the gas above the solution in atm,  $K_c$  is Henry's constant in l·atm/mol,  $H^0$  is absorbed heat in the evaporation of 1 mol of gas in J/mol,  $K$  is the individual gas constant in l·atm/mol. From these equations, it can be observed that an increase in temperature decreases Henry's constant, and subsequently the molar gas concentrations, which could lead to a DO deficit in flotation pulps.

Another important water-related flotation parameter is viscosity, which impacts the entrainment rate of gangue minerals leading to poor flotation selectivity (Xu and Wilson, 2000). Viscosity is believed to change turbulence, energy dissipation, and bubble-particle interaction patterns in a flotation cell (Manouchehri *et al.*, 2012).

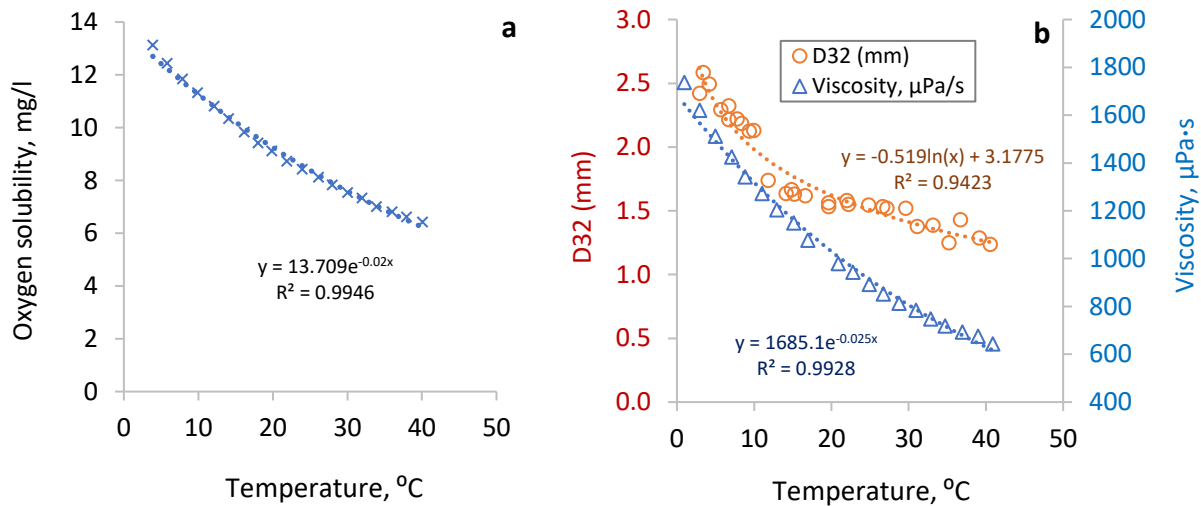


Figure 2-1. (a) DO solubility in distilled water at different temperatures, adapted from (Radtke *et al.*, 1998); (b) effect of temperature on water viscosity and bubble size, adapted from (Zhang, 2014)

The change of viscosity in a liquid system with respect to temperature (Figure 2-1b) may be described by Barrier's equation:

$$\log (\eta) = a + \frac{b}{T} \quad (2-3)$$

where  $a$  and  $b$  are constants,  $\eta$  is dynamic viscosity in centipoise (1 cP = 1 mPa·s) and  $T$  is temperature (K) (Kaye and Laby, 1962). In the example of the Canatuan Cu-Zn plant in the Philippines, a decrease in viscosity at elevated temperatures was believed to improve flotation selectivity (Umipig *et al.*, 2012). Moreover, in the case of viscous pulps, any temperature-driven viscosity changes will impact collector emulsification and, as a result, attachment to mineral particles. For example, molybdenite recovery on the Climax plant in the USA was increased by flotation pulp heating and the application of emulsification additives (Gray *et al.*, 1990).

Viscosity also has been shown to have a strong impact on bubble size (Equation 2-4) (Zhang, 2014). Bubble diameter ( $d_b$ , in mm) is one of the key controllers of the flotation rate constant through collision efficiency ( $E_c$ ) (Schulze, 1989) and bubble surface area flux ( $S_b$ , in s<sup>-1</sup>). The flotation rate constant is directly proportional to recovery ( $R$ ), as shown in Equation 2-7 (Cho, 2001; Leite, 1992; Wills and Finch, 2016):

$$D_{32} = K \left( \frac{\eta}{\eta_{20}} \right)^x = -a \lg(T) + b \quad (2-4)$$

$$E_c \propto \left( \frac{d_p}{d_b} \right)^n \quad (2-5)$$

$$k = S_b P R_f \propto \frac{J_g}{d_b} E_c E_a (1 - E_d) \propto S_b E_{col} \quad (2-6)$$

$$R = 1 - e^{-kt} \quad (2-7)$$

where  $D_{32}$  is the Sauter mean bubble diameter (in mm);  $\eta$  is pulp viscosity in  $\mu\text{Pa}\cdot\text{s}$ ,  $\eta_{20}$  is pulp viscosity at a reference temperature (20 °C) in  $\mu\text{Pa}\cdot\text{s}$ ;  $K$ ,  $a$ , and  $b$  are coefficients;  $J_g$  is the superficial gas velocity in cm/s;  $d_p$  is particle diameter in mm;  $E_c$  is collision efficiency;  $E_a$  is attachment efficiency;  $E_d$  is detachment efficiency;  $E_{col}$  is collection efficiency,  $t$  is flotation time in s, and  $T$  is a water temperature (°C). A seasonality study of zinc grades at the Matagami



concentrator (Canada) attempted to link seasonal metallurgy with bubble size variations. It was found that in summer the zinc grade was on average 2.5% higher and the bubble size was approximately two times larger compared to winter (Figure 2-2) (Nesset *et al.*, 2002).

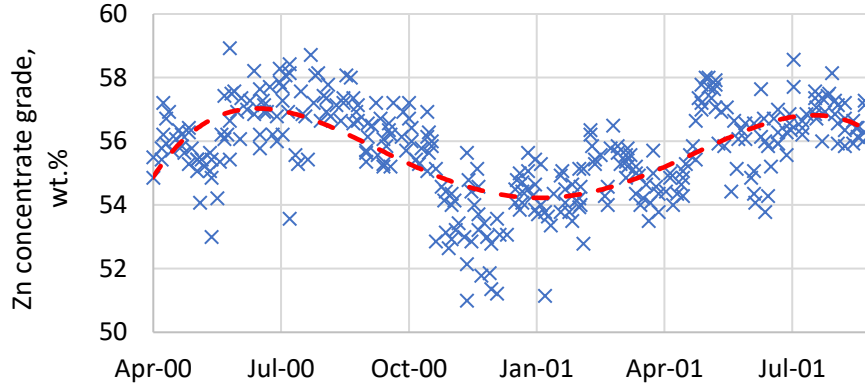


Figure 2-2. Zinc concentrate grade fluctuations at Matagami concentrator, adapted from (Nesset *et al.*, 2002)

Nesset *et al.* proposed the following explanation (Nesset *et al.*, 2002): an increase in the water recovery (and hence entrained gangue minerals) by smaller bubbles in winter, and higher froth stability caused by smaller bubbles/increased water viscosity (and hence poorer water drainage). Another explanation could be the changes in frother concentrations due to high evaporation rates in summer (Barton, 1988; Fuerstenau *et al.*, 2007).

Frother adsorption at the water-gas interface is also temperature dependent and is closely linked to the surface tension ( $\gamma$ , in N/m) by Gibbs' adsorption equation (Sutherland and Wark, 1955):

$$\Gamma = -\frac{C}{RT} \times \frac{d\gamma}{dC} \quad (2-8)$$

where  $\Gamma$  is surfactant adsorption in mol/m<sup>2</sup>,  $C$  is the surfactant concentration in mol/m<sup>3</sup>,  $T$  is the temperature (K). Drzymala reported (at laboratory scale) the use of frother concentration as an incentive parameter in an Arrhenius-type equation to describe the kinetics of collectorless chalcopyrite flotation from copper shales (Drzymala, 2018):

$$k_n = A_n e^{-\frac{E_a}{kT}} \ln\left(\frac{c}{c_0}\right) \quad (2-9)$$

where  $k_n$  is a rate constant,  $c_0$  and  $c$  is a reference and actual frother concentrations respectively, expressed in the same units (*e.g.* mol/l). The response of frothers to temperature changes is revealed by increased froth stability and height in cold environments (Choung *et al.*, 2008). Liu *et al.* studied the temperature effect on pyrite flotation with SBX as the collector and “# 2 oil” (alcohol group frother with general formula ROH), showing that at 23 °C, the dosage of frother required to reach maximum recovery was 5 mg/l, compared to 10 mg/l at 0 °C (Liu *et al.*, 2019).

From the perspective of even smaller bubbles, recent investigations with a Pb-Zn ore from Gorevskoye mill (Russia) showed that nanobubbles formed on ore mineral surfaces after sharp temperature fluctuations have the potential to improve recovery. Mikhlin *et al.* noted that this factor should be considered when analyzing plant performance in winter when heated milling discharge is mixed with cold process waters (Mikhlin *et al.*, 2020). The formation of nanobubbles on a mineral surface will hydrophobize it and facilitate more efficient collection by larger bubbles.

Collection efficiency (Fuerstenau *et al.*, 2007) from Equation 2-6 could be also seen as a parameter controlled by temperature-dependent induction time ( $\tau_i$ , in  $\mu$ s): particle-bubble attachment time reduces with increasing temperature as a result of increased water fluidity, facilitating the extrusion of a water layer between a mineral and a bubble (Laskowski, 1989):

$$\log \tau_i = \frac{D}{T} + J \quad (2-10)$$

where  $D$  and  $J$  are constants. Increased collection of quartz through improved bubble-particle collision has been also found when increasing temperature from 20 °C up to 40 °C (Laskowski, 1989). The bubble rise velocity ( $v_b$ ) increased by approximately 40%, increasing bubble kinetic energy and reducing the size of the largest particle feasible to float ( $r_p^{max}$ , in cm) (Equation 2-11, (Scheludko *et al.*, 1976)):

$$r_p^{max} = \frac{3C\gamma(1 - \cos\theta)}{\rho v_b^2} \quad (2-11)$$

where  $C$  is a constant in dyn,  $\gamma$  is surface tension in dyn/cm,  $\theta$  is the contact angle in degrees,  $\rho$  is a media density in g/cm<sup>3</sup>, and  $v_b$  is the bubble rise velocity in cm/s. Bubble rise velocity could explain certain variations in flotation performance. For example, He *et al.* suggested it as one possible explanation for reduced galena recovery in cold pulps. They blamed low pulp

temperatures and the associated increase in slurry viscosity for reduced bubble rise velocity and lower collision efficiency between bubbles and particles (He *et al.*, 2020). The slow bubble rise velocity hypothesis has been also used by O'Connor *et al.* (O'Connor *et al.*, 1984) to explain a reduction of pyrite mass transfer from the pulp to the froth, leading to a decreased pyrite flotation performance in winter months on a pyrite flotation plant in South Africa (Figure 2-3).

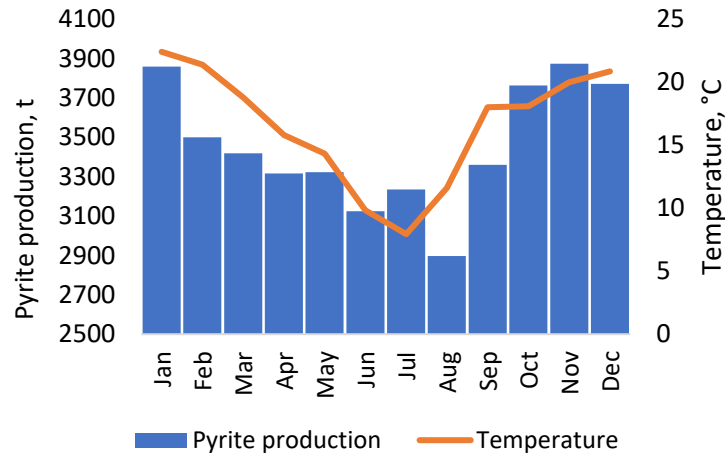


Figure 2-3. Monthly pyrite production on a flotation plant in South Africa relative to temperature, adapted from (O'Connor *et al.*, 1984)

Another effect of altered pulp viscosity is a change in froth rheology. A relationship between bubble size and pulp viscosity with froth properties may be described through Equation 2-12 (Princen and Kiss, 1989; Wang and Li, 2020):

$$\eta_f = \frac{\varepsilon_f - 0.73}{\sqrt{\frac{D_{32}\gamma_r}{k_0\alpha}}} \quad (2-12)$$

where  $\eta_f$  is apparent froth viscosity in mPa·s,  $\varepsilon_f$  is the volume fraction of air,  $D_{32}$  is the Sauter mean bubble diameter in mm,  $\gamma_r$  is the shear rate in  $s^{-1}$ ,  $k_0$  is a constant that depends on the continuous phase viscosity and surface tension,  $\alpha$  is a superficial fraction of lamella that is covered with solids. Increased froth viscosity has been reported to increase copper grade, which was explained by increased residence and froth drainage times (Li *et al.*, 2016; Shi and Zheng, 2003; Wang and Li, 2020) (Figure 2-4.).

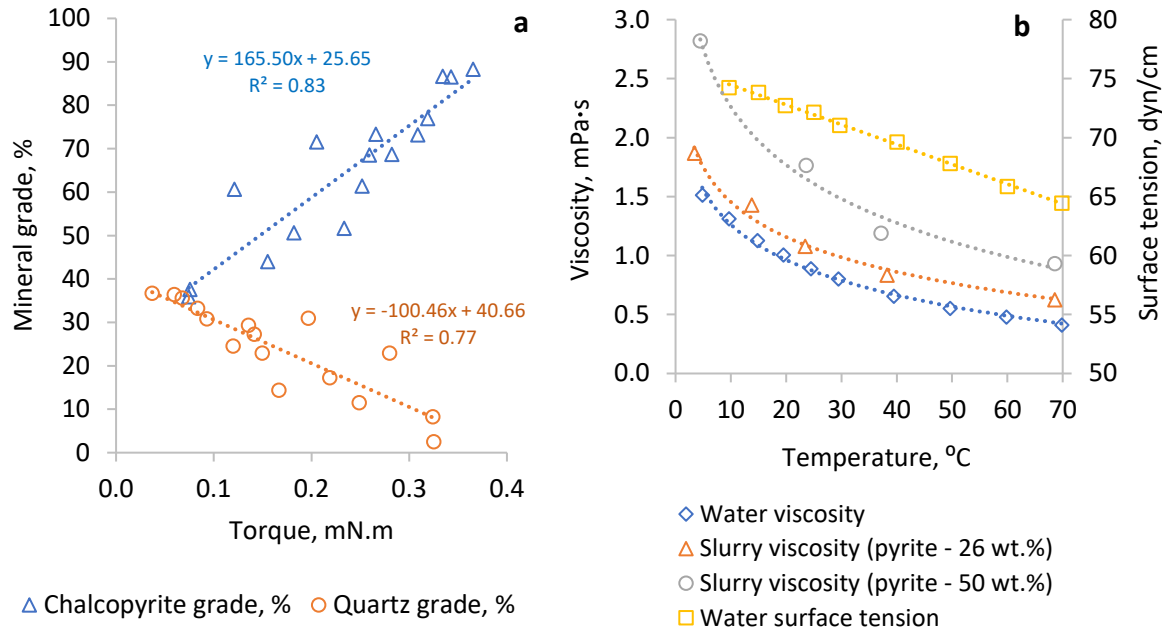


Figure 2-4. (a) Concentrate quality depending on froth rheological properties; (b) changes in water and pyrite pulp viscosities, and water surface tension as a function of temperature. Adapted from (Kaye and Laby, 1962; O'Connor *et al.*, 1984)

Surface tension is another parameter, closely related to viscosity (Equation 2-13) (Silverman and Roseveare, 1932), which shows a similar trend as a function of temperature, while the best fit described in the literature was achieved with the Ramsay-Shields Equation (2-14) (Shaw, 1992):

$$\gamma = a^4 \sqrt[4]{\eta} + b \quad (2-13)$$

$$\gamma = \frac{K(T_c - T - 6)^3 \sqrt[3]{\rho^2}}{\sqrt[3]{M^2 x^2}} \quad (2-14)$$

where  $\gamma$  is surface tension in N/m,  $a$  and  $b$  are liquid-specific constants,  $T_c$  is the critical temperature (K),  $T$  is the actual temperature (K),  $\rho$  is liquid density in kg/m<sup>3</sup>,  $M$  is the molar mass of the liquid in kg/mol,  $x$  is association degree of liquid,  $K$  is Eotvos-Ramsay coefficient in J/(K·mol)<sup>2/3</sup>. Some laboratory investigations into the collectorless flotation of sulfides (Yarar and Kaona, 1983) have discovered that different minerals have a certain optimum surface tension range where the highest recoveries are achieved (Figure 2-5.). Moreover, above a critical surface tension, stable wetting layers form, which increases the induction time for particle-bubble attachment (Fox and Zisman, 1950; Yörük *et al.*, 1987).

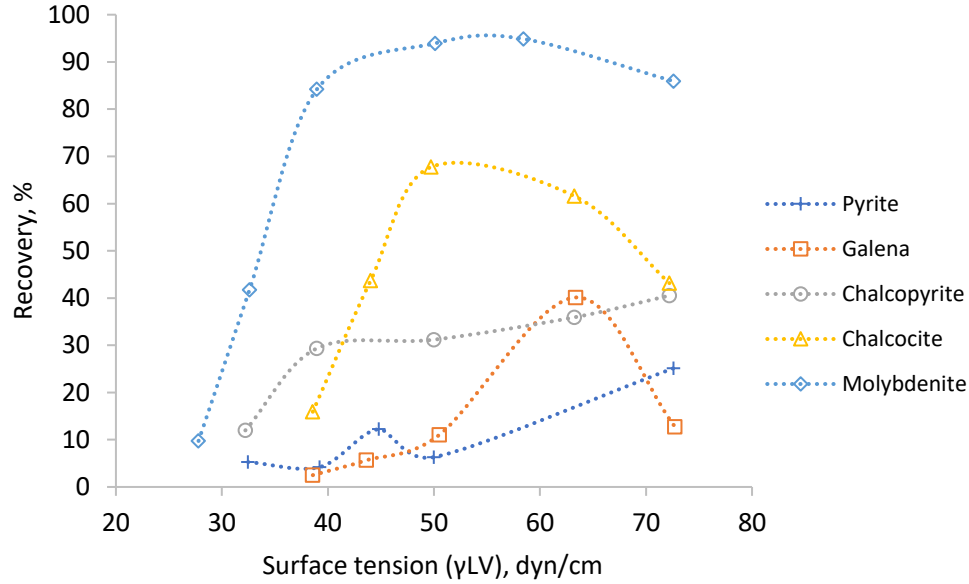


Figure 2-5. Flotation recovery of selected sulfide minerals in relation to liquid-vapor surface tension, adapted from (Yarar and Kaona, 1983)

As the contact angle depends on surface tension (Bhattacharya and Pascoe, 2005), it could be concluded that the angle is also a temperature-dependent parameter, and could be used to determine the free energy of the system (Equation 2-15). Young's equation (2-16) describes the contact angle-surface tension relationship:

$$\Delta G = \gamma_{VL}(\cos\theta - 1) \quad (2-15)$$

$$\cos\theta = \frac{\gamma_{SV} - \gamma_{SL}}{\gamma_{VL}} \quad (2-16)$$

where  $\gamma_{VL}$ ,  $\gamma_{SV}$ ,  $\gamma_{SL}$ , are the surface tensions at vapor-liquid, solid-vapor, and solid-liquid interfaces respectively. Similar to mineral recovery at different surface tensions, a contact angle measured for copper-activated sphalerite, and galena conditioned with potassium amyl xanthate (PAX), have indicated an optimal temperature (Gayle and Smelley, 1960). The largest contact angle (floatability) was found in the range 30-35 °C for both tested minerals. An and Zhang (An and Zhang, 2020) showed that for chalcopyrite conditioned with PAX, the contact angle steadily increased over the temperature range 25-60 °C.

### 2.3.2. Primary Concentration: Flotation Thermodynamics and Particle Transport

From the point of view of climate-induced challenges, several mineral processing plants across Canada have reported seasonally-attributed metal losses during flotation (Levanaho *et al.*, 2005; Malafarina and Deredin, 2021; Nesset *et al.*, 2002; Xu and Wilson, 2000), with examples of seasonal variations in flotation for two Canadian processing plants given in Figure 2-6.

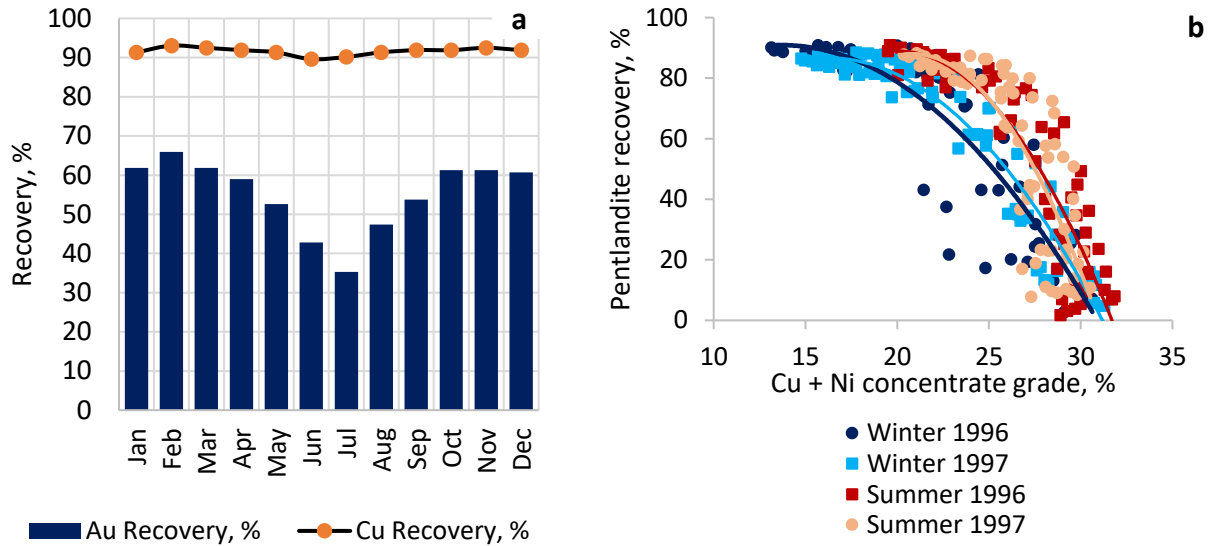


Figure 2-6. Examples of seasonal drop: (a) in gold recovery on Hudson Bay Mining and Smelting, 2000-2003; (b) in Cu+Ni grade on Clarabelle mill, adapted from (Levanaho *et al.*, 2005; Xu and Wilson, 2000)

Froth flotation combines chemical reactions (reagent adsorption, or conditioning) and physical separation (particle transport to the concentrate with bubbles) steps (Yianatos, 2003). From the chemical perspective, Van't Hoff Equation (2-17) (Hoff, 1887), relates flotation reaction equilibrium constants to temperature:

$$\ln\left(\frac{K_{d_2}}{K_{d_1}}\right) = -\frac{\Delta H}{R}\left(\frac{1}{T_2} - \frac{1}{T_1}\right) \quad (2-17)$$

where  $\Delta H$  is enthalpy (temperature effect of a chemical reaction) in J/mol,  $R$  is the universal gas constant (8.3145 J/mol·K),  $T$  is the temperature (K), and  $K_d$  is an equilibrium dissociation constant. Collector adsorption through physisorption is normally achieved at negative enthalpy values, while

chemisorption increases with temperature (Rao, 2004). The importance of the adsorption mechanism may be demonstrated by fluorite flotation/adsorption tests, which revealed that at room temperature, fluorite recovery with oleic acid was lower than that at higher temperatures. Investigations of collector adsorption on the mineral surface at room temperature revealed that it was washed off more easily from the surface compared to higher temperatures. These observations led to the conclusion that at a higher temperature, a change in the adsorption mechanism from physisorption to chemisorption of some part of the collector allowed the production of a more stable hydrophobic layer, which improved flotation (Cook and Last, 1950; Rao, 2004).

The adsorption process could be characterized by its speed (adsorption kinetics) and completeness (adsorption equilibrium capacity). The adsorption kinetics of flotation reagents depends on temperature, and may be described through the Arrhenius equation (2-18) (Arrhenius, 1889):

$$k = k_{max} e^{\frac{-E_a}{RT}} \quad (2-18)$$

where  $E_a$  is the activation energy in J/mol required to trigger the reaction (*i.e.* to overcome electron repulsive forces, as well as weakening bonds of reactants),  $k_{max}$  is the reaction rate constant at  $E_a=0$ ,  $k$  is the reaction rate constant, and  $T$  is the temperature in K.

Low temperatures and high activation energies could result in no pronounced interaction of reactants even when thermodynamic criteria are satisfied (Mingulina *et al.*, 1990). Favorable conditions for collector adsorption are found when the total energy of the mineral-collector aggregate is lower than the sum of collector and mineral surface energies (Xu *et al.*, 2016b).

After nano-scale processes of conditioning and reagent adsorption on a mineral surface, hydrophobized particles should be collected by bubbles and rise to the froth zone. The micro-scale description of the flotation process can also be summarized by temperature-dependent equations, where bubble (B) and particle (p) “react” to produce flotula (particle-bubble aggregate - pB), as illustrated in Equations 2-19 and 2-20 (Drzymala *et al.*, 2021):



$$\ln K = \ln \left( \frac{a_{pB}}{a_p a_B} \right) = - \frac{\Delta G^0}{RT} \quad (2-20)$$

where  $a$  denotes the activity of the reaction product and reactants,  $\Delta G^0$  is Gibbs free energy in J/mol (characterizes direction and limits of flotation reaction, it is negative for adsorption reactions (Du *et al.*, 2018)).

Overall, the current understanding of seasonal variations in flotation is heavily based on the established thermodynamic perceptions, some of which are adapted to describe flotation specifics. Combating the adverse effects of seasonal triggers on flotation performance follows two main methods: through controlled temperature manipulations, and/or by expanding (optimizing) the nomenclature of chemicals used (*e.g.* collectors, modifiers).

### 2.3.3. Secondary Concentration: Foam and Froth Stability

O'Connor *et al.* found that in pyrite flotation the increased froth stability at temperatures below 10 °C promoted excessive gangue entrainment, leading to poorer concentrate grades (O'Connor *et al.*, 1984). According to Equation 2-21, entrainment is proportional to the water recovery in the concentrate (Warren, 1985):

$$R_G = e_G \cdot R_w \quad (2-21)$$

where  $R_G$  is the recovery of fine gangue,  $e_G$  is a gangue material constant (dependent on particle size and specific gravity), and  $R_w$  is water recovery. As for the total recovery of a mineral of interest (hydrophobized mineral particles)  $R_M$ , it consists of two main parts: water recovery-controlled, and water recovery-independent, as described by Equation 2-22:

$$R_M = R_{ind} + e_M \cdot R_w \quad (2-22)$$

where  $R_{ind}$  is the model's extrapolated intercept on the recovery axis and  $e_M$  is the entrainment factor for the mineral of interest. Water recovery ( $R_w$ ), as shown in Equation 2-23, is a parameter that depends on two steps: water recovery from the pulp zone to the froth zone ( $R_{cw}$ ) and water recovery from the froth phase to the concentrate ( $R_{fw}$ ). The latter is largely affected by froth height  $H_f$  (dm) and residence time  $\tau_f$  (min), as shown in Equations (2-24)–(2-26) (Zheng *et al.*, 2006):

$$R_w = \frac{R_{cw} \cdot R_{fw}}{1 - R_{cw} + R_{cw} \cdot R_{fw}} \quad (2-23)$$



$$R_{fw}(H_f) = e^{\frac{-V \cdot \varepsilon_f \cdot A \cdot H_f}{Q_a}} \quad (2-24)$$

$$\tau_f = \frac{\varepsilon_f \cdot A \cdot H_f}{Q_a} \quad (2-25)$$

$$R_{fw} = \alpha e^{-V \cdot \tau_f} \quad (2-26)$$

where  $\varepsilon_f$  is air holdup,  $A$  is the cross-sectional area of the froth phase ( $\text{dm}^2$ ),  $Q_a$  is the rate of airflow ( $\text{L/min}$ ) passing through the froth zone,  $\alpha$  is the fraction of the froth that reports to the concentrate, and  $V$  is water drainage rate ( $\text{m/s}$ ). Liquid drainage and gas disproportionation constitute two major macroscopic processes destabilizing foams (Damodaran, 2006).

Coalescence is another important destabilizing mechanism that occurs due to the drainage from inter-bubble liquid film, leading to lamella film thinning and rupture. Therefore, this mechanism, with lamella rupture and a subsequent reduction in foam height, also originates from the drainage macro process (Monsalve and Schechter, 1984; Yu and Damodaran, 1991). The rate of liquid drainage (Damodaran, 2006) (also known as Reynolds drainage) depends on continuous phase viscosity (Equation 2-27), which renders it a temperature-dependent parameter when considering Barrier's equation (Equation 2-3) (Kaye and Laby, 1962):

$$V = \frac{2h^3 \cdot \Delta P}{3\mu \cdot r^2} \quad (2-27)$$

where  $h$  is the liquid film thickness ( $\text{m}$ ),  $\Delta P$  is the difference between hydrostatic pressure and disjoining pressure ( $\text{N/m}^2$ ),  $\mu$  is continuous phase dynamic viscosity ( $\text{Pa} \cdot \text{s}$ ),  $r$  is bubble radius ( $\text{m}$ ).

Stabilization of foams may be achieved by increasing continuous phase viscosity, increasing disjoining pressure (by developing osmotic pressure with the help of surfactants) (Damodaran, 2006), and attaching mineral particles to the bubbles (mechanically preventing bubble convergence) (Glembotskij and Klassen, 1981; Wills and Finch, 2016). Flotation froth should satisfy two principal criteria: it should be stable enough to allow valuable mineral recovery while possessing flexibility for gangue drainage (Bhondayi, 2014; Glembotskij and Klassen, 1981).

Bhondayi summarized different attempts for froth stability assessment (Bhondayi, 2014), such as froth half-life time measurements (Iglesias *et al.*, 1995), recording froth height at equilibrium (Barbian *et al.*, 2005; Barbian *et al.*, 2003; Pugh, 2016), froth phase bubble size measurements (Ata *et al.*, 2003; Oetjen *et al.*, 2014), among others. Froth height was found to have a linear negative impact on the flotation rate constant  $k$  (Feteris *et al.*, 1987):

$$k = \theta_0 - \theta_1 \cdot H_f \quad (2-28)$$

where  $\theta_0$  is the intercept at zero froth height and  $\theta_1$  is the gradient of the flotation rate constant versus the froth height. Froth recovery is another important parameter affecting the flotation rate constant (Gorain *et al.*, 1998), which depends on froth half-life time, as per Equation 2-30 (Zanin *et al.*, 2008):

$$k = P \cdot S_b \cdot R_f \quad (2-29)$$

$$R_f = e^{-c \cdot \left(\frac{\tau_f}{t_{1/2}}\right)} \quad (2-30)$$

where  $P$  is ore floatability parameter,  $S_b$  is bubble surface area flux ( $\text{s}^{-1}$ ),  $R_f$  is froth recovery,  $c$  is a froth parameter, and  $t_{1/2}$  is froth half-life (s).

The froth stability mechanism was suggested by Nasset *et al.* to explain the observed variations in zinc concentrate grade at the Matagami plant (Canada). The proposed explanation was that smaller bubbles observed during flotation in winter decrease water drainage from the froth phase, leading to higher water recoveries and associated increased gangue entrainment (Nasset *et al.*, 2002).

## 2.4. Sulfide Flotation at Different Temperatures

Seasonal variations are an important factor in most sulfide flotation circuits, with temperature changes impacting numerous flotation plants (Dunne *et al.*, 2019), or being manipulated to improve process selectivity (Glembotsky and Klassen, 1981; Twidle and Engelbrecht, 1984). Dunne *et al.* outlined that temperature regulation has limited potential for sulfide plants with heating operations being impractical, and noted limited industrial application – mostly for molybdenite separation from copper minerals or in sphalerite flotation (Dunne *et al.*, 2019). In the

separation of molybdenite from copper minerals, pulp heating is used to decelerate  $\text{Na}_2\text{S}$  degradation, which improves the depression of copper minerals (Plaksa, 1970).

Nevertheless, it does not negate the fact that cyclicity in sulfide flotation within annual operation cycles (between summer and winter seasons), and even on a daily production scale (between day and night) has been observed worldwide (Lin, 1989). Research from South African sulfide flotation plants revealed that seasonal variations were responsible for losses equal to millions of US dollars every year (Lin, 1989; O'Connor *et al.*, 1984). The acuity of the seasonality problem correlates well with territories characterized by significant seasonal temperature fluctuations. For example, the Uchalinskaja Cu-Zn plant in the Russian Urals introduced thermal treatment of the pulp in winter to improve zinc concentrate grade and recovery which, however, requires treatment of the pulp with steam at 140-150 °C to increase the pulp temperature to 25-30 °C (Arustamjan, 2004).

Zinc flotation without pulp heating has higher seasonally induced risks. For example, the Chinese Fankou Zn-Pb plant reported a seasonal drop in both Zn recovery and grade by 0.7% and 0.4% respectively at lower temperature slurries (22-28 °C), when compared to the results at 31-39 °C (Zheng *et al.*, 2005). Historical data from a German zinc operation in Meggen with pulp temperatures similar to the ones in the Fankou plant in winter indicated a greater inter-seasonal contrast in concentrate grades (Weise *et al.*, 1978), attributed to increased winter losses triggered by pH fluctuations.

Other historical operating data on differential polymetallic flotation showed that zinc-lead separation may be facilitated by low temperatures. Thus, Base Metals Mining Corp. in the USA reported better separation efficiency in the lead cleaner at 16 °C resulting from low sphalerite floatability in cold pulps. For related reasons, zinc cleaners on the same plant were reported to be heated up to 32 °C. Bolivian Potosi Mine historical data has also indicated increased winter zinc losses, where the zinc concentrate was found to have higher concentrations of iron minerals during the cold season (Taggart, 1945). Investigations at Brunswick Mine concentrator (Canada) also reported similar results: a strong dependence of zinc grade and recovery on pulp temperature was confirmed by a series of tests (Figure 2-7), where cold pulps were found to enhance pyrite flotation instead of sphalerite (Roberts *et al.*, 2008).

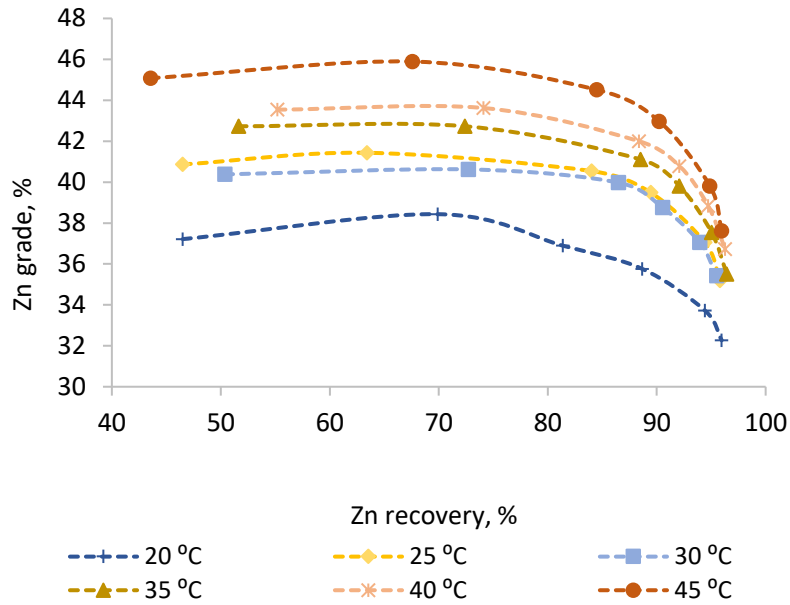


Figure 2-7. Laboratory results of zinc rougher flotation, adapted from (Roberts *et al.*, 2008)

Under significantly colder winter conditions the operations may experience more drastic performance fluctuations. For example, many pyrite flotation plants in Tibet and Yunnan (China) were reported to experience winter shutdowns due to a significant decrease in production output (Liu *et al.*, 2019). Even for naturally hydrophobic molybdenite, cold temperatures in winter may cause a decrease in recovery. As Zhao noted with an example of a molybdenite operation in Northeastern China, there is an inter-seasonal drop in molybdenite recovery by 1-2% when cold and hot seasons are compared (Zhao, 1991). Boliden Cu-Pb-Zn plants in Sweden also experienced winter recovery issues, which were particularly acute at temperatures below 12 °C. A winter decline for the Boliden plants could be explained by poorer sphalerite depression in the copper-lead circuit and less efficient copper activation in the zinc circuit (Albrecht *et al.*, 2010). Isshiki has also found for Zn-Pb-Cu flotation systems that the grades of these base metals increase in the respective concentrates as the temperature rises (Isshiki, 1961).

The flotation performance of sulfide ores also declines if the temperature is too high. For example, it has been observed at the Neves-Corvo zinc plant (Portugal) that the highest losses were recorded during traditionally hot summers with slurry temperatures after milling reaching above 50 °C (Fernandes, 2016). Fernandes has also mentioned that the hottest days were usually accompanied by sphalerite recovery drop at the plant (Figure 2-8)

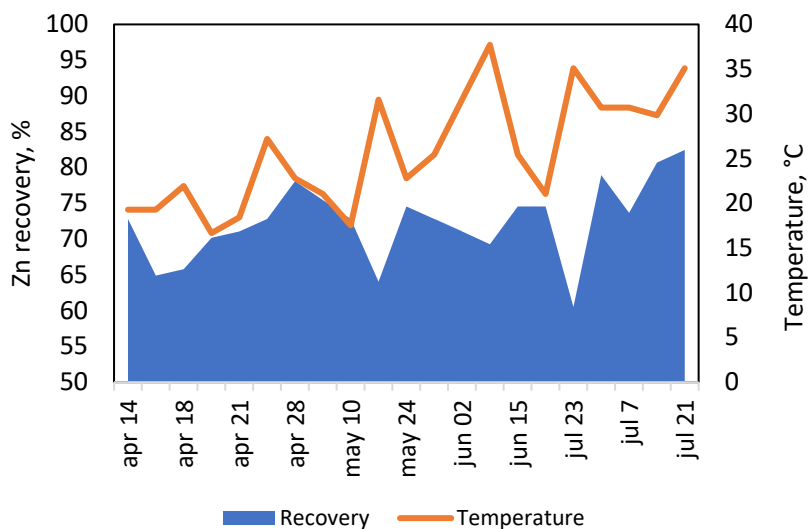


Figure 2-8. Zinc recovery at the Neves-Corvo zinc plant in relation to the daily temperature, adapted from (Fernandes, 2016)

Another example of decreased performance in summer is the processing of polymetallic ores of Hudson Bay Mining and Smelting (HBMS, currently known as Hudbay Minerals Inc.) in Canada, where recovery degradation was amplified after the plant transitioned to recycled water. The fluctuations at HBMS facilities demonstrated correlations with temperature, conductivity, Eh, as well as thiosulphate and calcium concentration in the pulp (Levanaho *et al.*, 2005). A decrease in performance at hot and cold conditions suggests that there is an optimal temperature range for sulfide flotation that maximizes a plant's performance.

#### 2.4.1. Efficiency of Collectors

The sensitivity of flotation with xanthates to temperature changes was found to increase significantly with decreasing collector dosage (Levanaho *et al.*, 2005). Moreover, for the example of Almalujskaja, Zyryanovskaja, and Belousovskaja plants in Central Asia it has been shown that maximum copper, lead, and zinc recovery was achieved when the ratio between dosed and required (to maximize recovery) concentration of xanthate is close to 1 (Abramov, 2005). Several mechanisms were suggested to explain the fall in recovery from xanthate excess in the pulp, namely partial desorption of copper activating ions from the sphalerite surface by xanthates and an increase in slime production as a result of xanthates reacting with dissolved metal ions in the pulp. Reductions in temperature decrease xanthate demand, which will increase the ratio between

dosed and required xanthate concentration from around 1 at 15 °C to above 2 at 10 °C (Abramov, 2005) ultimately affecting flotation. He *et al.* studied the effect of temperature on galena flotation using SBX as collector and MIBC as frother, showing that at a low temperature (5 °C) the recovery was reduced by 7% compared to that at 20 °C. FTIR results suggested that the chemicals adsorbed on the mineral surface were not affected by temperature. Zeta potential and XPS analysis suggested that lower temperatures would reduce the surface oxidation of galena, which could reduce the number of adsorption sites, and therefore reduce the adsorption of SBX (He *et al.*, 2020).

Another important temperature-driven aspect of xanthate adsorption is an analysis of a Krafft point or a temperature at which collector solubility reaches a level of critical micelle concentration. Tests with alkyl xanthates series revealed that with an increase in the hydrocarbon chain, the Krafft point increases as well (Hamilton and Woods, 1986; Klevens, 1953).

Research on the flotation behavior of monomineralic samples of chalcopyrite, pentlandite, and pyrrhotite at 10, 20, 50, and 70 °C revealed that there is an increased demand on xanthates observed with increased temperature (Abramov, 2012). Thus, in the case of pyrrhotite flotation, an increase in pulp temperature from 10 to 50 °C led to an increase in butyl xanthate consumption by 10% at pH 10, 36% at pH 11, and 49% at pH 12. For chalcopyrite, collector consumption increased even more drastically: 64% at pH 11.5 and 73% at pH 12.5. Pentlandite showed the largest temperature-induced changes in collector consumption (177% at pH 10.5 and 166% at pH 11.5) (Abramov, 2012).

To achieve efficient sulfide flotation, both types of collector adsorption mechanisms should be present on the surface: physisorbed dixanthogen and chemisorbed xanthates (Abramov, 2013). The presence of both types of adsorption masks the polar bonds of a surface more effectively, increasing the chances of a liquid film rupture between a particle and a bubble, as well as a more stable bubble-particle aggregate. Dixanthogen physisorption is believed to derive from the partial oxidation of xanthates by involving superficially adsorbed oxygen taking an electron from the conductivity zone. The reaction is catalyzed by the presence of copper ions on a sulfidic surface (Pomianowski and Leja, 1963). The temperature has the potential to change the availability of both ingredients: oxygen and copper (Hidmi and Edwards, 1999; Radtke *et al.*, 1998). Xanthate adsorption and oxidation on a mineral surface may be summarized in Figure 2-9.

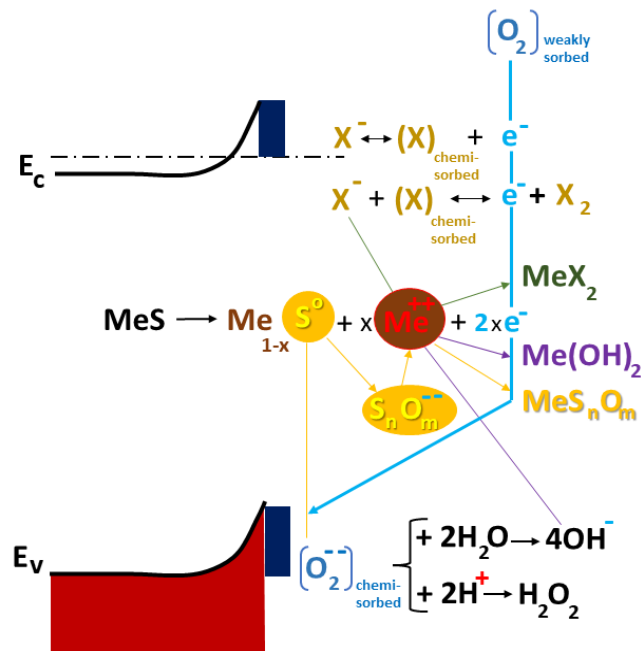


Figure 2-9. Interaction scheme of xanthates with sulfide surface in aerated pulp, adapted from (Avdohin, 1996), where  $E_v$  is the location of the energy level of the valence band “ceiling”, and  $E_c$  is the location of the energy level of the conductivity band “bottom”

For dioxanthogen adsorption on pyrite, it has been shown that enthalpy decreases from approximately 250 kJ/mole at pH 4.5 down to approximately 105 kJ/mole at pH 12 (Haung and Miller, 1978). The morphology of dioxanthogen adsorption is another important parameter. Thus, in a laboratory investigation of xanthate adsorption on chalcopyrite, hydrophobicity increased with temperature owing to the low melting point of dioxanthogen (30 °C), which caused the irregular shape of dioxanthogen aggregates leading to a larger surface coverage at elevated temperatures (An and Zhang, 2020). Conversely, excessive increases in temperature (up to 65 °C) in iron-containing pulps induce a 20-fold increase in dioxanthogen dissolution from the surface (Bocharov, 1996).

Xanthate adsorption on a mineral surface also requires certain potential values. Surface potential determines the probability of collector adsorption and depends on numerous factors including initial mineral hydrophobicity, size of non-polar collector radical, concentration and structure of a collector, *etc.* (Abramov, 2010). Xanthate adsorption on sulfide minerals increases with temperature, which has been shown with pyrite (Liu *et al.*, 2019) and chalcopyrite (Mhonde *et al.*, 2020) in different temperature ranges (Figure 2-10).

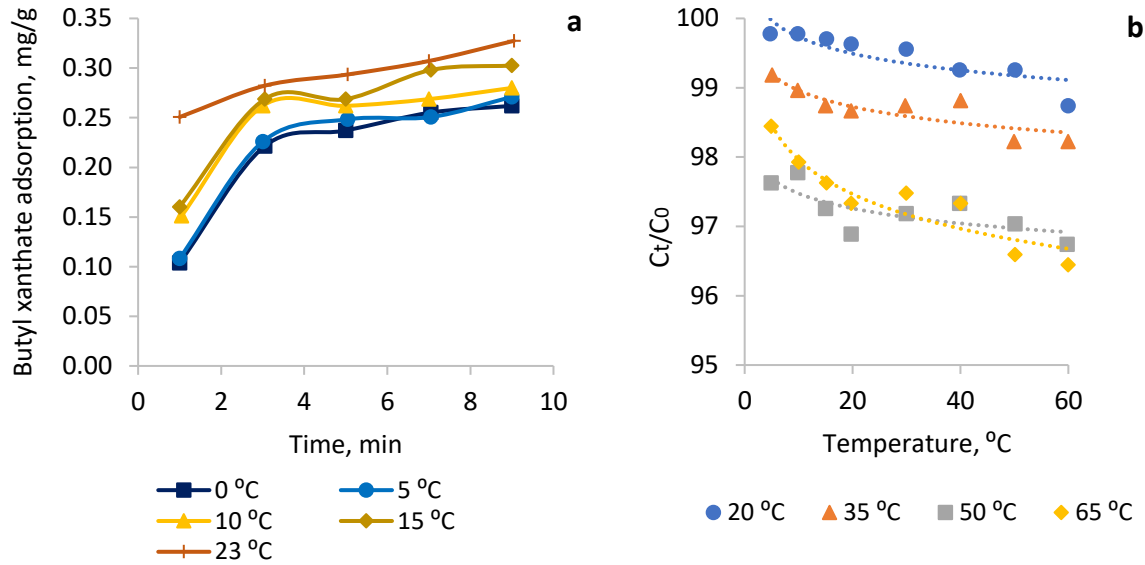


Figure 2-10. (a) Butyl xanthate adsorption on pyritic surface, adapted from (Liu *et al.*, 2019); (b) change of butyl xanthate concentration in the pulp ( $C_t/C_0$ ) with time during adsorption onto chalcopyrite, adapted from (Mhonde *et al.*, 2020)

Xanthate oxidation to dixanthogen (Figure 2-9) occurs for most sulfide minerals at potential values around +0.2 V, while the desorption of the dixanthogen layer was found between +0.5 V and +0.8 V. Formation of chemisorbed xanthate species occurs at negative potential values (-0.2 to -0.1 V). There are some exceptions, for example, it is thermodynamically impossible to produce dixanthogen on non-activated sphalerite surfaces (Abramov, 2013).

#### 2.4.2. Efficiency of Flotation Modifiers

Copper activation is a method commonly used in sulfide flotation for minerals such as sphalerite and pyrite among others (Bulatovic, 2007). The aim of copper activation is to lower the Fermi level of a mineral surface with a broad band gap (*e.g.* 3.7 eV for sphalerite), which allows xanthate to oxidize and form dixanthogen on a mineral surface (Abramov, 2013). From a temperature perspective, it has been determined that the limiting concentration (a value of concentration before precipitation) of aqueous copper in solution increases with pulp temperature. The limiting concentration has been shown to be a good indicator of conditions with the highest sphalerite recovery during collectorless flotation (Albrecht *et al.*, 2016). Aqueous copper stability borders shift to lower pH values and higher copper concentrations as temperature rises. Lower



temperatures result in poorer copper dissolution, which decreases the amount of aqueous metal species available for sphalerite activation, as indicated by Figure 2-11.

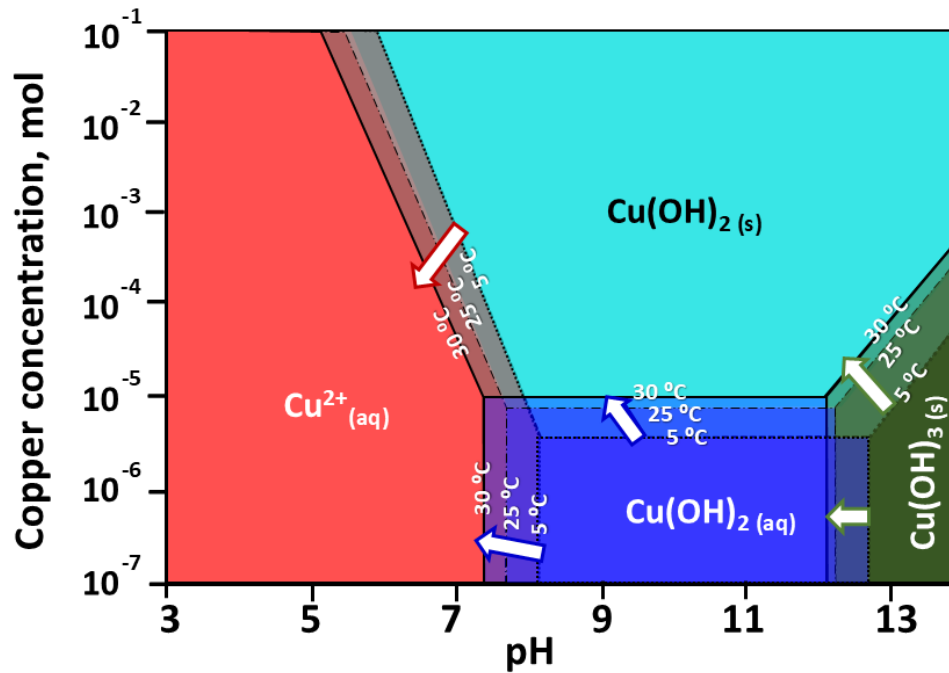
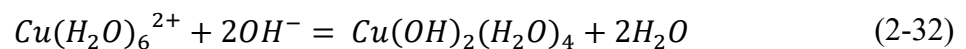
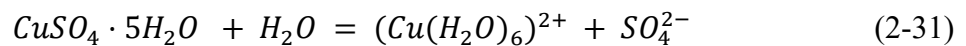
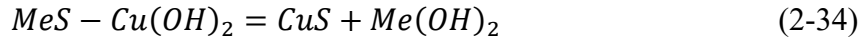
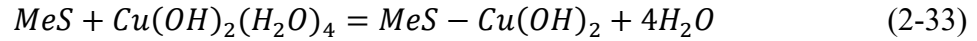


Figure 2-11. Areas of pH and concentration stabilities of copper species at different temperatures, adapted from (Albrecht *et al.*, 2016)

It has been commonly agreed that copper activation proceeds in two steps: fast (abstraction of copper by ZnS, concentration-dependent step) and slow (diffusion of copper inwards and of zinc outwards of the surface, temperature-dependent) (Siva Reddy and Konda Reddy, 1988).

Albrecht *et al.* showed that increasing temperature from 5 to 20 °C led to an increase in Zn recovery of approximately 15% and a 5-fold improvement in sphalerite flotation kinetics (Albrecht *et al.*, 2016). This improvement at higher temperatures was attributed to the acceleration of the multi-step copper activation process, with copper-zinc displacement not being affected, and copper deposition on the zinc surface being temperature sensitive (Albrecht *et al.*, 2016). Copper activation could be described by Equations (2-31) – (2-35) (Bailey, 2015; Knockhardy, 2015; Ryan and Norris, 2014):





There is a critical temperature of 10 °C which has been established by Manouchehri *et al.* for the collectorless flotation of copper-activated sphalerite. Below this temperature, a drastic decrease in recovery was observed (Manouchehri *et al.*, 2012). To compensate for this loss in recovery, increasing the copper dosage was found to be effective. Tests on the Garpenberg ore (Sweden) revealed that by decreasing pulp temperature during activation and during flotation, the grade and recovery values were impacted, with temperature during conditioning (activation) having a slightly higher impact on recovery (Manouchehri *et al.*, 2012).

Copper hydroxide precipitation on the mineral surface plays an important role in copper activation (Equation 2-33). It has been shown to be a temperature-dependent parameter (Hidmi and Edwards, 1999): aqueous copper concentration ( $Cu^{2+}$ ) in solution was found to be approximately 3 times larger at 4.2 °C than at 23.6 °C under neutral pH conditions. To achieve an efficient copper activation, a temperature-dependent ratio between copper and zinc ions in the solution should be favorable (which means a predominance of copper ions), as per Equation 2-36 (Zheng *et al.*, 2005):

$$\frac{c(Cu^{2+})}{c(Zn^{2+})} = e^{\frac{\Delta G^0}{RT}} \quad (2-36)$$

It has been suggested that the optimal temperature range for copper activation from the perspective of Zn grade and recovery using sodium butyl xanthate as the collector is between 25 and 40 °C, but not higher than 50 °C (Zheng *et al.*, 2005).

Lime is a widely used modifier in sulfide flotation, being an important reagent for low-cost iron sulfide depression (Zanin *et al.*, 2019). Changing concentrations of dissolved oxygen due to temperature fluctuations might have an impact on pH and lime consumption at a plant. In research conducted on the ore from the Neves-Corvo mine (Portugal), it was noted that the required lime dosage for pH adjustment increased with temperature (Fernandes, 2016). One suggested reason was the reduced solubility of lime at elevated temperatures – according to chemical handbook data,

it has a negative linear relationship with temperature: from 0.14 g/l at 40 °C up to 0.17 g/l at 10 °C (Rabinovich and Havin, 1978).

Lime also serves as a source of calcium ions in the flotation pulp. In the case of galena flotation, some studies recorded a depressive effect (up to 15% Pb loss) when the calcium ion concentration was below 0.5 g/l, with a more pronounced effect at concentrations higher than 0.5 g/l (up to 30% Pb loss). The depressive effect of calcium could be linked to the formation of hydrophilic calcium compounds on the sulfide surface (Ikumapayi, 2010). Ikumapayi and Rao performed flotation tests with Renström Zn ore (New Boliden, Sweden), in simulated (synthetic process) water, based on  $\text{Ca}^{2+}$  and  $\text{SO}_4^{2-}$  ion balances at different temperatures (Ikumapayi and Rao, 2015). It was found that  $\text{Ca}^{2+}$  consumption (due to adsorption on mineral surfaces and/or precipitation as calcium carbonate) at 4 °C was lower than at 11 and 22 °C, while the concentrate grade in pulps with low  $\text{Ca}^{2+}$  concentrations was showing a decreasing trend with temperature (Ikumapayi and Rao, 2015). In another example of sulfide flotation, Grano *et al.* investigated the Hilton concentrator (Australia) and proposed that galena depression originated from calcium thiosulfate and calcium sulfate precipitation on the lead mineral surface (Grano *et al.*, 1997a). The rate of such heterogeneous nucleation may be described by Equation 2-37 (Wu and Nancollas, 1996):

$$J_{het} = Ae^{\left(-\frac{\beta V_m(\gamma_{cl})^2(\gamma_{sc}-(\gamma_{cl}+\gamma_{sl}))}{k^3 T^3 \ln^2 S}\right)} \quad (2-37)$$

where  $J_{het}$  is the heterogeneous nucleation rate ( $\text{cm}^{-3} \text{ s}^{-1}$ ),  $A$  is pre-exponential factor,  $\beta$  is geometrical shape factor,  $V_m$  is the molecular volume,  $\gamma$  is interfacial energy (subscripts  $l$ ,  $s$ ,  $c$ , refer to liquid, solid and critical nucleus respectively),  $k$  is the Boltzmann constant in J/K,  $S$  is the supersaturation states, and  $T$  is temperature (K).

For different minerals, there is a critical pH level that prevents particle-bubble attachment as a result of the prevention of collector adsorption on the mineral surface (Wark and Cox, 1932). For galena, the critical pH was found to be around 9.7 at 35 °C, which increased to 10.8 at 10 °C (Wark and Cox, 1938). This means that under certain conditions galena flotation may well improve during the cold season.

Cyanides are effective depressants for sulfides. They are used extensively for the selective separation of base metals, mainly as a depressant for iron sulfides (*e.g.* pyrite), or sphalerite (Guo *et al.*, 2014). Research conducted on zinc ore (Umipig *et al.*, 2012) noted that the cyanide reagent

scheme was temperature sensitive, as hydrogen cyanide gas (HCN) is more likely to form at elevated temperatures. The detrimental influence of cyanide at high temperatures has been also shown in flotation research of a polymetallic ore from the Belousovskaja plant in Kazakhstan. It was noted that the optimal plant temperature range was between 18 °C and 20 °C, as lower temperatures led to decreased mineral floatabilities, while higher temperatures sharply increased cyanide activity, which depressed some copper sulfides in addition to the targeted pyrite (Abramov, 2005).

Laboratory captive bubble tests (Wark and Cox, 1938) have revealed that there is a general increase in the required cyanide concentration that prevents mineral-bubble contact with temperature. In the case of a pyritic surface, the required cyanide concentration appears to be in a power relationship with temperatures up to 35 °C. The tests were conducted at pH 9 with 150 mg/l of  $\text{CuSO}_4 \cdot 5\text{H}_2\text{O}$ , and 25 mg/l of KEX (Figure 2-12). After achieving a peak at around 40 °C, the required cyanide concentration dropped by approximately 14 % as the temperature reached 60 °C. For pyrite and chalcopyrite at pH > 10 without activation, an increase in the temperature from 10 °C to 35 °C resulted in a decrease of critical cyanide concentration, almost a 7-fold drop for chalcopyrite (from 0.87 to 0.13 mg/l) and 2 fold decrease for pyrite (from 0.08 to 0.04) (Wark and Cox, 1938).

Strathcona copper-nickel operations in Canada have also reported the temperature sensitivity of the cyanide scheme. Chalcopyrite and nickel minerals (pentlandite and millerite) separation was experiencing seasonal effects described by poor selectivity during the cold season (poor nickel depression). As an alternative, Glencore investigated dextrin as a substitute for sodium cyanide, which demonstrated better selectivity at cold temperatures in laboratory trials (Malafarina and Deredin, 2021).

Sulfide flotation in alkali media may generally be seen as a balance between 2 types of reagents: increasing hydrophobicity through the use of an activator (*e.g.* copper sulfate) and collector (*e.g.* xanthates) on one side, and depressant (*e.g.* cyanide) and pH modifier on the other side (increasing  $\text{OH}^-$  groups tends to hydrophilize mineral surfaces). Temperature may be interpreted as an external factor shifting the equilibrium depending on mineral and reagent properties.

Wark and Cox (Wark and Cox, 1938) noted that in the case of non-activated pyrite, activated and non-activated chalcopyrite, a temperature increase decreases cyanide concentration required for

mineral depression. For activated sphalerite, higher temperatures led to an increased hydrophobicity. Increasing collector concentration, as reported by McCreedy and Honeywell (McCreedy and Honeywell, 1966) retards the cyanide dissolution processes (depression), as shown in Figure 2-12.

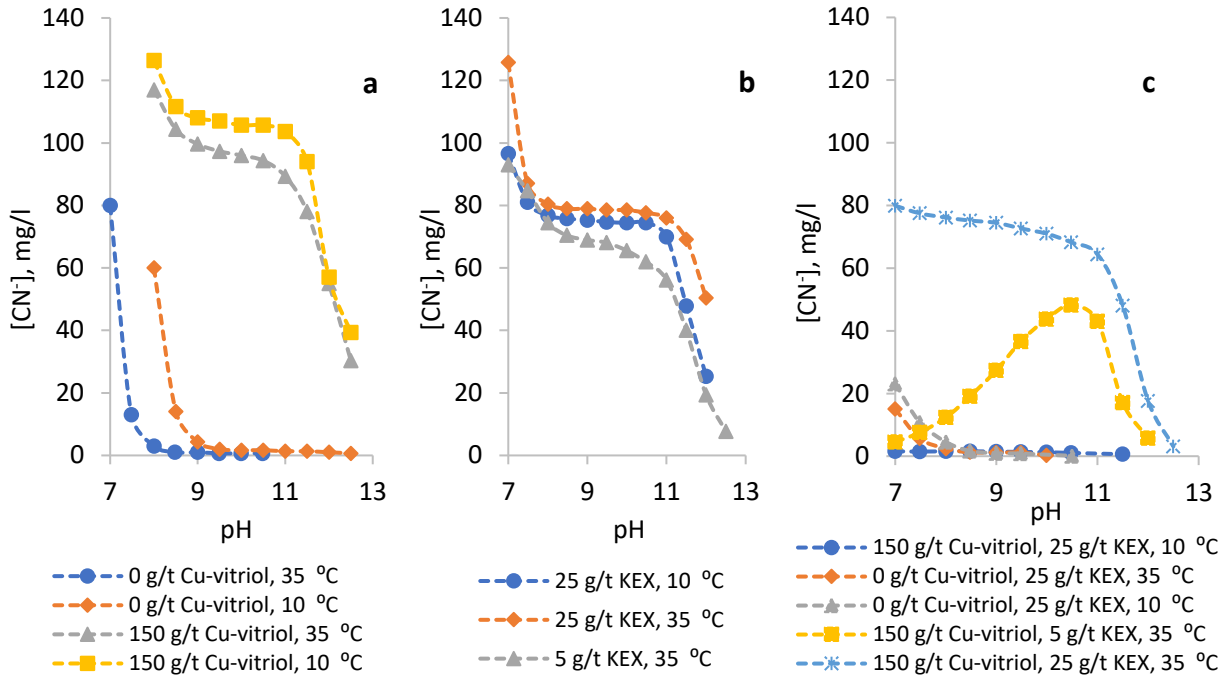


Figure 2-12. Critical cyanide concentrations in captive bubble tests for combinations of activator and collector at different pH and under varying temperature conditions: (a) chalcopyrite (25 mg/l KEX), (b) sphalerite (150 mg/l Cu-vitriol), (c) pyrite, adapted from (Wark and Cox, 1938).

### 2.4.3. Mineral Surface Properties

The change in ore surface properties with temperature is mainly related to different oxidation rates and the change in oxidation mechanism. Increased oxidation processes require higher collector dosages. The required xanthate concentration is linked to mineral thermodynamic parameters through Equation 2-38 (Abramov, 2012):

$$\log[X^-] = A + B \text{ pH} \quad (2-38)$$

where  $A$  is a coefficient, dependent on changes in thermodynamic characteristics of minerals as temperature rises, and  $B$  is a coefficient characterizing an incremental value of required xanthate concentration with pH increase (Abramov, 2012). Temperature is a factor that controls thiosalt

oxidation. Thiosulfates ( $\text{S}_2\text{O}_3^{2-}$ ), trithionates ( $\text{S}_3\text{O}_6^{2-}$ ), and intermediate products of sulfide minerals' oxidation are considered important flotation parameters (Xu and Wilson, 2000).

As an example, it has been found for iron sulfides that  $B$  from Equation 2-38 does not change over the temperature range 15-70 °C, which is a consequence of the unchanging mechanism of mineral oxidation (predominant sulfur oxidation product remains  $\text{S}_2\text{O}_3^{2-}$ ) (Abramov, 2013). Thus, only an increase in parameter  $A$  was observed with temperature. Analysis of chalcopyrite revealed changes in both  $A$  and  $B$  as oxidation at ambient conditions to  $\text{SO}_3^{2-}$  was substituted by the formation of  $\text{S}_2\text{O}_3^{2-}$  with increasing temperature (up to 50 °C) and pH (up to 13). Consequently, a shift from  $\text{SO}_3^{2-}$  to  $\text{S}_2\text{O}_3^{2-}$  led to increased xanthate demand (Abramov, 2012). In the case of galena flotation, sulfate ions ( $\text{SO}_4^{2-}$ ) were believed to decrease the recovery in cold pulps through surface coverage with sulfoxy complexes (Ikumapayi, 2010). Such complexes might be considered to be one of the reasons for galena's 20% recovery drop in winter reported for the Belousovskaja plant (Kazakhstan) (Abramov, 2005). Historical data from Brunswick concentrator (Canada) also indicates seasonal metallurgical fluctuations correlating with thiosulfate concentrations in process water (Wills and Finch, 2016).

In addition to thiosulfates, the concentration of dissolved metal cations rises when heating the pulp above room temperature: up to 3 times when the temperature reaches 65 °C (Bocharov, 1996). In sphalerite flotation, it has been demonstrated that an increase in pH and temperature creates favorable conditions for the stability of the zinc hydroxide complex on the mineral surface (Manouchehri *et al.*, 2012). In the Somincor plant (Portugal), significant (25%) seasonal fluctuations in zinc recovery were attributed to collector desorption from the mineral surface at pulp temperatures above 60 °C, whereas sphalerite surfaces were found to be covered by zinc hydroxide species. Research conducted by Oriti resulted in similar flotation responses: the recovery of sphalerite gradually decreased with temperature up to 50 °C (Oriti, 1961). Moreover, at 80 °C, floatabilities of chalcopyrite, pyrite, and sphalerite were significantly reduced. Historical data from bornite flotation in the USA Magma concentrator revealed that too high temperature after milling also caused drops in copper recovery as a result of overoxidation of the mineral (Taggart, 1945).

Kuroko concentrator (Japan) (Lukio Co. Ltd., 2005) and Broken Hill concentrator (South Africa) (Twiddle and Engelbrecht, 1984) attempted to benefit from the oxidation phenomenon: they applied differential oxidation by heating (60-70 °C) for galena depression in copper-lead concentrate

separation circuits. Kubota *et al.* reached similar conclusions: flotation of galena with n-BAF was found to be depressed when the temperature was increased from 20 to 60 °C. This was justified by increased hydrophilicity on the galena surface due to oxidation and desorption of collectors (Kubota *et al.*, 1974).

## 2.5. Non-Sulfide Flotation at Different Temperatures

Apart from the main sulfide minerals, like galena and sphalerite, polymetallic mineral deposits may have up to 100 other mineral species, represented by silicates, sulfates, carbonates, *etc.* (Plotnikova *et al.*, 2019). Reviewing changes in flotation characteristics of other mineral groups with temperature is vital for understanding general flotation mechanisms in action at different temperatures, and for benchmarking the approaches applied industrially and on a laboratory scale to combat temperature-induced inefficiencies.

### 2.5.1. Oxides

Seasonal changes in oxide ore flotation are frequently associated with collector efficiency, particularly in terms of solubility and selectivity under low (winter) temperatures. Cationic collector efficiency at different temperatures is dependent on the dissolution (diffusion) rate and adsorption density, along with other factors. Collector adsorption density ( $\Gamma$ ) increases with temperature and can be represented through an Arrhenius-type equation (Abramov, 2012; Mitrofanov, 1966; Schubert and Schneider, 1969):

$$\Gamma = 2rCe^{\frac{-(ze_0\Delta E + n\Delta W_a + W_x)}{kT}} \quad (2-39)$$

where  $\Gamma$  is adsorption density in mol/m<sup>2</sup>,  $r$  is the collector's polar group radius in m,  $C$  is the concentration of collector molecules mol/m<sup>3</sup>,  $z$  is the valence of adsorbent,  $e_0$  is the elementary charge ( $1.602 \times 10^{-19}$  C),  $\Delta E$  is mineral surface potential in relation to a zero charge in volts,  $n$  is the number of carbon atoms in a collector radical group,  $\Delta W_a$  is the energy of association for each CH<sub>2</sub> group (J),  $\Delta W_x$  is the energy of non-electrostatic interaction between a polar group of a collector and a mineral surface (J),  $k$  is the Boltzmann constant, and  $T$  is the temperature (K). Data from JSC “Mihajlovsky GOK” in Russia shows seasonality-related issues in the reverse flotation of quartz when cleaning the magnetite concentrate, which is related to low temperatures: as the pulp temperature dropped below 10-12 °C between November and March, there was a 2-3%

decrease in grade and recovery of the final product (Ignatova and Shelepov, 2011). In the Lanping Pb-Zn oxide mine located in the Hengduan Mountains (China), Zhang *et al.* reported that the flotation pulp, which used octadecyl amine as a collector, needed to be heated up to 25-30 °C to achieve good zinc recovery (Zhang *et al.*, 2003).

Kulkarni and Somasundaran (Kulkarni and Somasundaran, 1980) conducted adsorption and flotation tests using oleic acid as a collector for hematite flotation. They demonstrated that temperature was important for facilitating molecular transport and increasing the solubility of oleic acid by increasing the soluble oleate ( $R^-$ ) and acid-soap ( $R_2H^-$ ) ions. The prevalence of ionic species ensures faster adsorption kinetics. A lower adsorption density, but with stronger bonding was achieved, compared to a regime dominated by oleic acid ( $RH$ ) and associated non-solvated droplets adsorption. Consequently, higher temperatures provided better hematite recovery (Kulkarni and Somasundaran, 1980). Reverse flotation of quartz from hematite ores using RA-915 (fatty acid collector, composition not disclosed) was studied by Li and Hui, who found that iron recovery and grade in the cleaner stage were both reduced if the slurry temperature in the rougher stage was increased. When the cleaner stage temperature dropped from 30 to 22 °C, the iron grade was reduced by 3%. It was suggested that the flotation temperature should be kept between 30-35 °C, while the temperature difference between the rougher and cleaner stages should not be too large (Li and Hui, 2013).

Work by Cooke *et al.* on iron ore flotation showed that at pH 6, hematite recovery improves with temperature, while calcium-activated quartz recovery drops. Moreover, out of fatty acids such as linolenic, linoleic, oleic, elaidic, and stearic acids, the last one was found to be most heavily dependent on temperature. It was speculated that in such systems, temperature-assisted collector diffusion rate plays a decisive role in flotation performance through induction time control (Cooke *et al.*, 1960). Improvements to long-chain fatty acid solubility and collection efficiency at low temperatures (down to 10 °C) have been demonstrated through collector modification targeting  $\alpha$ -carbon position with amino and hydroxyl groups (Guo *et al.*, 2020). In general, improvements to flotation with fatty acids in cold pulps are achievable through mixtures with non-ionic reagents, or through collector modification (sulfonation, halogenation, nitration, *etc.*).

Pyrolusite flotation with oleic acid between 23-60 °C also indicated recovery improvements (from 40 to nearly 100 %) (Parrent, 2012). For ilmenite fatty acid flotation, it has been demonstrated that



the temperature of the flotation stage is more important than the conditioning temperature. Ilmenite recovery increased with temperature, while the quality of the concentrate deteriorated owing to increased collector adsorption on some gangue (feldspars). It was also noted that collector physisorption on feldspars increased at pH 8, whereas at pH 9.5, such trends were not observed (Parkins, 1975).

Depressants are also vital in improving the selectivity of oxide flotation. The depressing effect of starch at different temperatures was investigated in the context of quartz reverse flotation in Brazilian iron ore processing. Successful applications of starch in flotation require gelatinization by NaOH addition or increased temperature. For the regular non-modified cornstarch used in the work by Carlos Silva *et al.*, it was shown that the minimum temperature allowing gelatinization without NaOH addition was 65 °C, indicating an increase in the depressive effect with increasing temperature (Carlos Silva *et al.*, 2017).

Within the frameworks of flotation modifiers and flotation temperature, a novel approach to hematite fines recovery is the application of thermo-responsive polymers (*e.g.* PNIPAM) (Ng *et al.*, 2015). This is the next step of profiting from temperature changes in flotation, where PNIPAM is utilized as a multitasking reagent. According to Ng *et al.*, the ore was first conditioned with PNIPAM at 20 °C, which allowed hematite flocculation, with subsequent flotation at elevated pulp temperature (50 °C) at which PNIPAM demonstrates hydrophobic properties and acts like a collector. The PNIPAM results appear promising when compared to sodium oleate tests for +20 µm samples (see Figure 2-13).

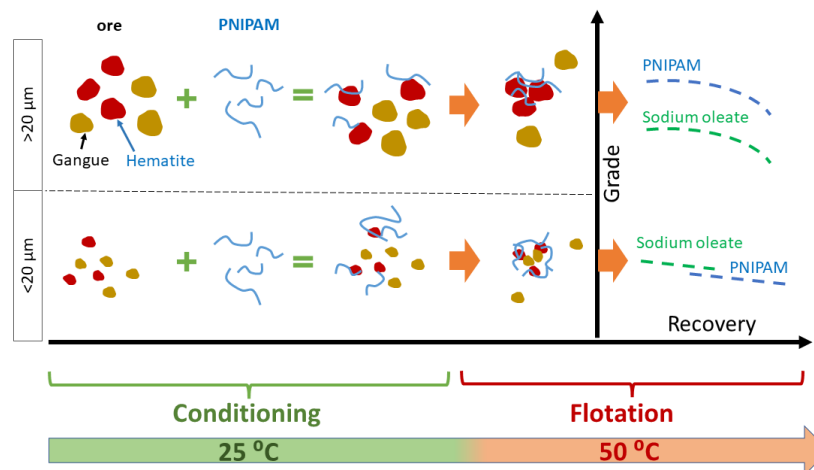


Figure 2-13. Schematic representation of PNIPAM hematite flotation steps, with results compared with sodium oleate flotation, adapted from (Ng *et al.*, 2015)

Another potential reason for possible seasonal variation in oxide flotation lies in the process water quality. For example, Niobec (Canada) reported a mean 4 % niobium (pyrochlore) recovery decrease in winter, which was related to a decrease in the preceding carbonate flotation efficiency (Figure 2-14.). A 4-fold increase in tall fatty acid consumption has been found during the cold season. An investigation of the discrepancy trigger revealed that process waters contained more phosphates during winter as algae activity in cold seasons was suppressed (Marois *et al.*, 2018).

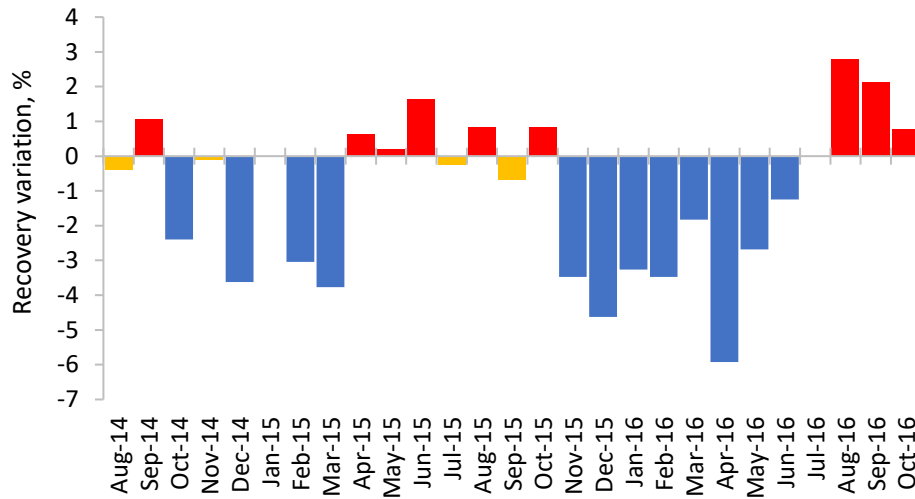


Figure 2-14. Seasonal variations of niobium recovery at Niobec facilities, adapted from (Marois *et al.*, 2018): months with negative recovery shift has blue bars, with positive shift having red bars, months with close to zero shift (<1%) has yellow bars or no bars. The zero point is mean summer recovery

### 2.5.2. Sulfates and carbonates

For non-sulfide base metal ores, sulfidation with subsequent xanthate flotation is often employed (Cai *et al.*, 2021). As highlighted by Tyushkova *et al.*, this process is also temperature dependent: large lead losses were registered when the process temperature decreased from 24 to 15 °C. Thus, conditioning at elevated temperatures was included in the flowsheet of the pre-production trials (Tyushkova *et al.*, 2012). In another example, smithsonite (a zinc carbonate mineral) sulfidation was enhanced by heating the pulp from 20 up to 60 °C, which resulted in a flotation recovery increase of 30% (Cai *et al.*, 2021).

The flotation of magnesium and calcium carbonates is strongly dependent on mineral dissolution. Thus, in laboratory experiments of magnesite flotation from dolomite, it has been shown that the

largest selectivity was achieved at 15 °C. Dissolution of cations from the surface of magnesite was maximum at 25 °C, while for dolomite it was 15 °C at pH 11 and in the presence of oleic acid. Consequently, the largest ratio between dissolved cations from dolomite and magnesite was found at 15 °C, which resulted in more metal cation adsorption sites on magnesite compared to dolomite (Yin *et al.*, 2019). Further research into magnesite and dolomite dissolution at different temperatures by Li *et al.* identified that dissolution generally decreases for both minerals with increasing pH (up to 11). A decrease in the mineral solubility was demonstrated to be beneficial for flotation with dodecylamine (DDA) as a collector. When the pH was greater than 11 (*i.e.*, at 12) the solubility increased drastically. This was explained by the formation of  $\text{Mg}(\text{OH})_2$  which is more stable than  $\text{MgCO}_3$  (Li *et al.*, 2011).

In alunite flotation, oleic acid as a collector shows improvements as the temperature increases, allowing for reagent savings. In the temperature range from 20 and 80 °C, the largest savings of the collector were observed by increasing temperature from 35 to 50 °C. Above 50 °C, an increase in temperature did not yield further substantial improvements in reagent savings (Miller and Ackerman, 1980). In addition to collector efficiency, sulfate and carbonate flotation practice relies heavily on depressants. Celestite laboratory flotation tests revealed that at low concentrations of depressant in a quebracho-oleic acid-celestite system at neutral to mildly alkali pH conditions, a temperature increase shifts the equilibrium towards surface hydrophobization; however, high collector dosages masked the temperature effects (De Castro and Borrego, 1996). In tests on calcite, which is a common gangue in celestite ores, flotation recovery was maximum at high collector dosages and with increased temperature: from below 10% at 20 °C to approximately 95% at 50 °C. The depressing effect of the quebracho on calcite during the tests increased with temperature in the same tested ranges: the recovery of calcite dropped from 95% to 5-10% (De Castro and Borrego, 1996).

In order to improve selectivity, magnesite processing plants apply and test different combinations of depressants, carboxymethyl cellulose (CMC) being a common one (Baranovskii, 1968, 1980). Unlike most magnesite collectors, CMC solubility is considered good at both cold and warm temperatures. However, when considering a plant operation with a recycled water system, seasonal triggering of biodegradation of the chemical should be taken into account (Batelaan *et al.*, 1992).

A study on Nigerian baryte flotation by Ofor and Nwoko using oleate showed decreased reagent adsorption density at temperatures above 40 °C, which was accompanied by a decrease in recovery. The authors explained this through changes in the adsorption mechanism and dissociation of the chemisorbed collector from the baryte surface (Ofor and Nwoko, 1997).

### 2.5.3. Halides

Laboratory tests by Li *et al.* on a fluorite ore from Hebei (China) revealed that an increase in temperature from 13 to 27 °C improved flotation performance considerably (10% recovery increase), which was accompanied by a slight grade decrease of 0.8% (Figure 2-15). A similar effect was found in tests that varied the oleic acid collector dosage. To achieve optimal flotation performance, it was suggested to decrease the collector dosage when the temperature rises (Li *et al.*, 2020). In Chinese fluorite flotation plants, it is common to heat the pulp to 40 °C to improve the flotation performance of oleic acid through improved dispersing conditions (Zhang, 1995). Consequently, some fluorite mines in northern China were reported to experience significant energy costs in winter (Kienko *et al.*, 2010). Laboratory scale tests demonstrated that by using a GY-2 collector at 10 °C, it was possible to achieve similar flotation results as with oleic acid at 35 °C (Zhang, 1995).

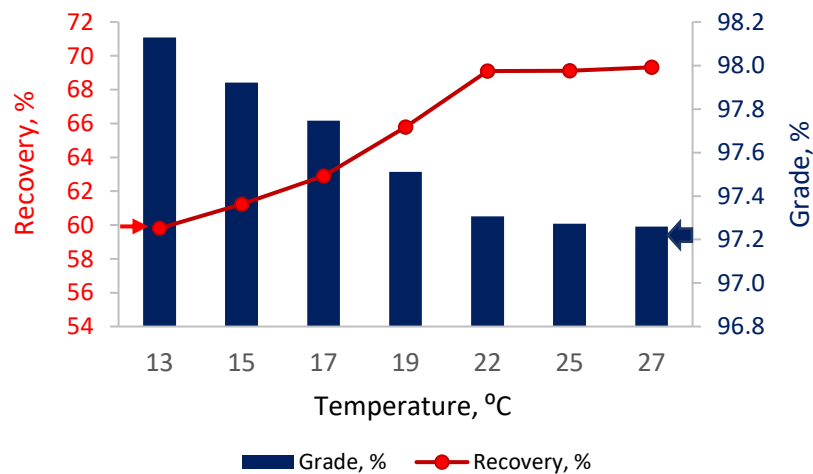


Figure 2-15. Effect of flotation temperature on fluorite grade and recovery at pH 9 with oleic acid, adapted from (Li *et al.*, 2020)

At JSC “Jaroslavsky GOK” in the Russian Far East, decreasing ore quality and low winter temperatures challenged the sustainable production of fluorite through flotation, which was

addressed by the addition of organic thermoregulatory modifiers. It was found that the application of oxyethylated compounds allowed fluorite flotation at 12 °C (Kienko *et al.*, 2010). Moreover, laboratory pre-emulsification trials of fatty acids of tall oils were found to be efficient. For example, pre-emulsification with oxyethylated fatty acids showed the potential to exclude costly pulp heating in winter for the Mongolian Bor-Undur GOK flotation plant (Vigdergauz *et al.*, 2000).

Cold winter conditions were also blamed for the decrease in efficiency of industrial trials on the Jaroslavsky GOK plant with mixed collectors (Asparal F and fatty acids of tall oils) (Samatova *et al.*, 2007). Consequently, the degradation of selectivity associated with cold winter temperatures was addressed by introducing a more selective and temperature-resistant mixture of collectors and activators: sodium fluorite, a mixture of diphosphonic acids and tetra-sodium salt of modified aspartic acid (Kienko, 2008).

Chen *et al.* also noted that due to the low solubility and poor dispersity of oleates under low temperatures, good fluorite flotation performance could be achieved only by heating the pulp to above 30 °C, or by using new reagent systems (Chen *et al.*, 2020). They investigated the use of petroleum sodium sulfonate in fluorite flotation rather than conventional sodium oleate systems. A sulfonate collector (PSK-13) was investigated at different temperatures with Na<sub>2</sub>CO<sub>3</sub> as a pH modifier and Na<sub>2</sub>SiO<sub>3</sub> as a depressant. PSK-13 is an anionic surfactant, mainly composed of sulfonates (37%) with a general structure RSO<sub>3</sub>Na, where R is an alkyl group. Closed circuit flotation studies showed that the CaF<sub>2</sub> grade gradually increased by decreasing the temperature: 97.9% (30 °C), 97.8% (20 °C), 98.3% (10 °C), and 98.6% (5 °C). In the same tests the recovery dropped with the temperature: 88.1% (30 °C), 84.4% (20 °C), 79.5% (10 °C), and 75% (5 °C). The decreased recovery might be due to lower adsorption of PSK-13 on fluorite. Adsorption tests indicated that when temperature was below 15 °C the adsorption of oleate on fluorite decreased rapidly, whereas the adsorption of PSK-13 decreased slowly with the temperature drop in the ranges of 5-30 °C. Generally, the adsorption of PSK-13 was significantly higher than that of oleate, which explained the better efficiency (Chen *et al.*, 2020).

Corpas-Martínez *et al.* also demonstrated that at temperatures below 30 °C, oleates and oleic acid led to a significant decrease in fluorite recovery (Figure 2-16.). They suggested utilizing new collectors (DP-I and DP-II), which consist of a mixture of oleic, linoleic, and rosin acids. These

mixed collectors did not demonstrate a sharp decrease in recovery below 30 °C (Corpas-Martínez *et al.*, 2020).

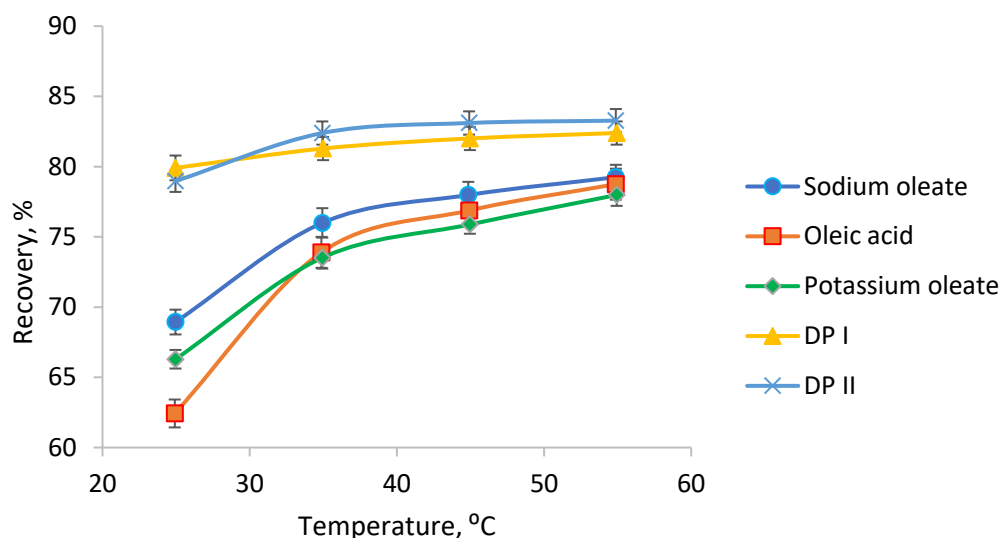


Figure 2-16. Fluorite recovery as a function of pulp temperature and collector type, adapted from (Corpas-Martínez *et al.*, 2020)

Another attempt to improve the oleic acid flotation of fluorite at low temperatures using “boosters” was by Zhou and Lu (Zhou and Lu, 1995). At 10 °C, the tested boosters improved recovery, especially B700 and B724 (composition not revealed). When the oleic acid concentration was  $10^{-5}$  mol/l, just 1% of a booster recovered almost all of the fluorite. With the presence of 1% B710 or 1% B724, a temperature decrease from 25 °C to 5 °C led to less than 5% drop in recovery. Compared to saponified oleic acid and sonicated oleic acid, oleic acid mixed with boosters could reduce the collector dosage by approximately 50% in low-temperature flotation conditions (Zhou and Lu, 1995).

Deng *et al.* also studied methods of improving fluorite flotation with oleic acid at temperatures below 15 °C, which was considered as a threshold for effective oleic acid flotation. Tests at 8-9 °C confirmed that applying only sonication as an emulsification method was not sufficient. They developed an approach of adding 20-30% diesel, and 10% sodium dodecyl sulfate, coupled with sonication, which yielded high fluorite recovery and grade (85.3% and 98.4% respectively) (Deng *et al.*, 1993). Reasonable fluorite recoveries at low pulp temperatures were also obtained using the EV-1 collector synthesized from *EvodiaeFructus* oil. Pulp temperature still significantly affected

flotation results: at 6.5 °C CaF<sub>2</sub> recovery was around 80%, while at 30 °C it reached almost 97% (Jong *et al.*, 2020).

Unlike most other ore types, sylvite flotation generally decreases at elevated temperatures. The first reason is an increased adsorption of the amine collector to slime particles (Oliazadeh *et al.*, 2012). Seasonal summer drops in potash flotation recovery from Solikamsk ores (JSC “Sylvinite” plant) in Russia were reported when the pulp temperature reached 35-37 °C (Aliferova, 2007). Pulp temperatures between 32-37 °C caused weak amine adsorption on coarse sylvite particles, revealed through higher losses of the coarse fraction in summer, compared to the flotation performance in winter (pulp temperature between 20-25°C) (Aliferova, 2007). Lower sylvite recoveries were also reported at JSC “Belaruskali” in Belarus during the summer months with the temperature reaching 36-39 °C. Lower recoveries were explained by increased adsorption of amine collector on NaCl and clay minerals (Turko *et al.*, 2014).

For larger particles amines with longer hydrocarbon chains should be used, which is realized through collector mixtures (Oliazadeh *et al.*, 2012). Aliferova also determined that amine collector mixtures possess 2-3 times lower viscosity compared to individual collectors (Aliferova, 2007). By increasing the temperature above 25 °C it has been reported that the solubility of shorter chain amines increases, disturbing the mixture balance and decreasing sylvite recovery (Oliazadeh *et al.*, 2012). Consequently, longer chain amines are generally used in summer (recommended above 32 °C), while shorter chain amines are preferred in winter (recommended below 15 °C) (Essilfie, 2014).

Another possible reason for lower flotation performance during summer is connected with ores extracted from deep mines leading to higher brine temperatures, causing increased KCl surface hydration and a decrease in amine adsorption (Oliazadeh *et al.*, 2012). Additionally, the solubility of magnesium salts also has a depressing effect on sylvite, which increases with temperature (Mehri *et al.*, 2019). A concentration of magnesium ions in the brine greater than 4% has the potential to negatively impact sylvite flotation through increased viscosity (Perucca, 2000), even though increased magnesium concentrations would theoretically decrease sylvite dissolution by rising KCl dissolution temperature (Figure 2-17, and Equation 2-40).

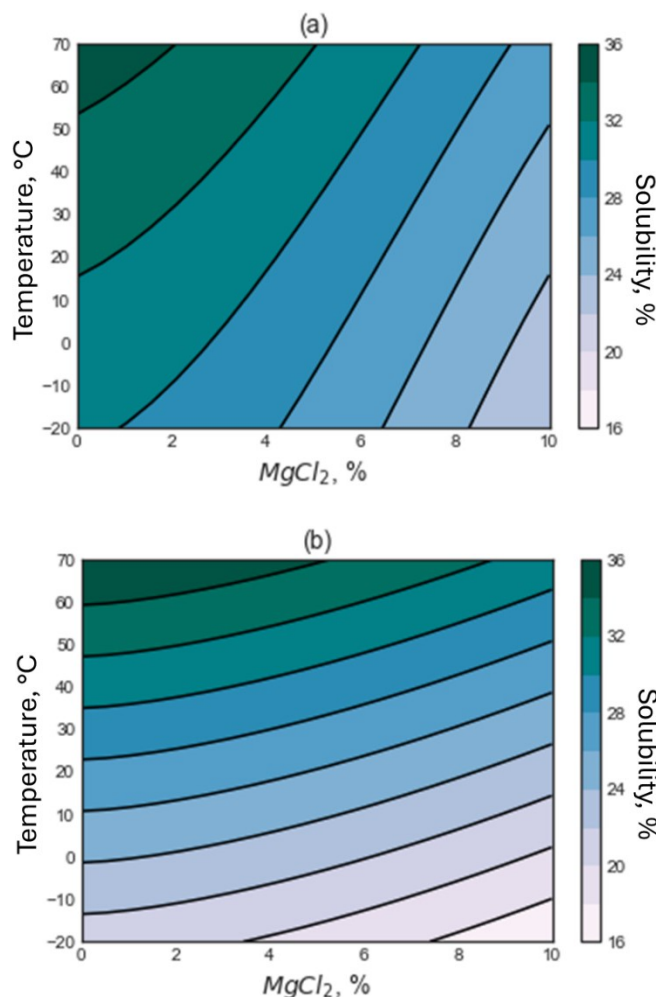


Figure 2-17. Solubility surfaces for (a) halite and (b) sylvite as a function of  $MgCl_2$  and temperature (in a system with NaCl : KCl ratio of 1:1), adapted from (Bodnar *et al.*, 1997)

$$S = a + bM^{1.5} + cT \quad (2-40)$$

where  $S$  is total salinity (NaCl + KCl, in wt.%),  $T$  is the dissolution temperature of sylvite,  $M$  is  $MgCl_2$  concentration in wt.%, while  $a$ ,  $b$ , and  $c$  are constants. Regarding NaCl flotation, Abu-Hamatteh and Al-Amr investigated carnallite reverse flotation at different temperatures (Abu-Hamatteh and Al-Amr, 2008). A sharp decrease in NaCl removal efficiency (related to the halite recovery to froth) was observed when the temperature increased from 20 to 50 °C (Abu-Hamatteh and Al-Amr, 2008), which might be related to increased mineral dissolution.

Cold temperatures have also been reported to degrade potash recovery, such as in Saskatchewan, Canada. Essilfie attributed the negative impact on flotation at cold temperatures to lower transport kinetics of sylvite as a result of increased viscosity and associated lower bubble velocities and



bubble-particle transport (Essilfie, 2014). Another mechanism related to viscosity issues is that at too low a temperature, there is an increase in viscosity which triggers sylvite surface hydration by increased contact with magnesium ions coming from slimes (Oliazadeh *et al.*, 2012). Some laboratory tests have also demonstrated a decreased desliming efficiency by dropping the temperature from 45 to approximately 15 °C (Vahrushev, 2014). Thus, optimal potash flotation was reported by some sources to be at approximately 21 °C (Oliazadeh *et al.*, 2012). Essilfie claims an optimal temperature for sylvite flotation to be 20-32 °C, with temperatures below 15 °C leading to an increased viscosity, which degrades flotation through poor amine dispersion (Essilfie, 2014).

Wang *et al.* found that poor collector efficiency in cold pulps was the main reason behind the Chinese Qinghai Avic Resources Ltd plant's annual scheduled shutdowns from November to March, as well as some other plants in the Chaerhan area of China, with winter temperatures below 10 °C (Wang *et al.*, 2014). A suggested solution by Cheng *et al.* is an increase in amine dispersion through the application of a mixed amine collector scheme (Cheng *et al.*, 2012). Another Chinese producer, Qinghai Salt Lake Group Co., mitigated the negative winter impact by using reverse flotation technology, floating NaCl from carnallite with a more temperature-robust DDM collector (Wang *et al.*, 2014).

#### **2.5.4. Phosphates**

Phosphorus minerals' flotation is also challenged by the low efficiency and low thermal robustness of collectors, especially when it concerns separation from silicate gangue. For example, investigations of possible cyclicities related to daily temperature fluctuations during amine flotation of Peruvian Bayovar phosphate ores using seawater revealed that the temperature robust regime is found between 25 to 40 °C (De Oliveira Balduino *et al.*, 2012). Possible methods of dealing with efficiency issues are: mixing reagents, using boosters, and modifying the properties of fatty acids and soaps. For example, to improve flotation, some alternative collectors have been suggested, which have better miscibility at room temperature, *e.g.* cottonseed oil (Ruan *et al.*, 2017). Furthermore, Li *et al.* investigated the impact of boosters on phosphate rock flotation with soapstock of cottonseed oil as the collector. It was found that anionic and non-ionic surfactants could be used as low-temperature boosters. At 7-12 °C, the addition of 5% sodium dodecyl sulfate (SDS) to the soapstock resulted in a recovery increase of 30.7%. Tests with only soapstock suffered from larger temperature impacts compared to the tests with a booster (Li *et al.*, 2010).

In other research, Zhang and Li studied low-temperature (13-15 °C) phosphate ore flotation using cotton soap as the main collector, mixed with different surfactants. It was found that cotton soap mixed with 10% SDS and a polar organic compound (exact composition not reported) could achieve the highest  $P_2O_5$  recovery (89.9%) among all studied chemicals. This boosting mechanism was explained by lowering the surface tension of the polar organic compound. Adding SDS and this polar organic compound could decrease the surface tension and therefore improve the solubility and dispersibility of cotton soap in water (Zhang and Li, 2007).

Another collector system has been suggested by Zheng *et al.*, who synthesized a new apatite flotation collector (EV-1) out of evodiae fructus oil using saponification, sulfation, and amidation. Compared to the traditionally used commercial collector (also a mixture of organic compounds), EV-1 gave 73.4%  $P_2O_5$  recovery at 5 °C, versus 64.6% recovery using a commercial alternative. At 12 °C, the recoveries for traditional and EV-1 were 74.9% and 86.5% respectively. The reason for EV-1's better performance at low temperatures was attributed to the content of fatty acids and their low melting points (as shown in Figure 2-18). For example, the content of  $C_{17}H_{29}COONa$  and  $C_{17}H_{29}CONH_2$  (which have melting temperatures as low as -11 °C) is 10.9% in EV-1, compared to only 1.9% in the traditional collector. Consequently, the solubility and flotation performance at low temperatures were improved (Zheng *et al.*, 2016).

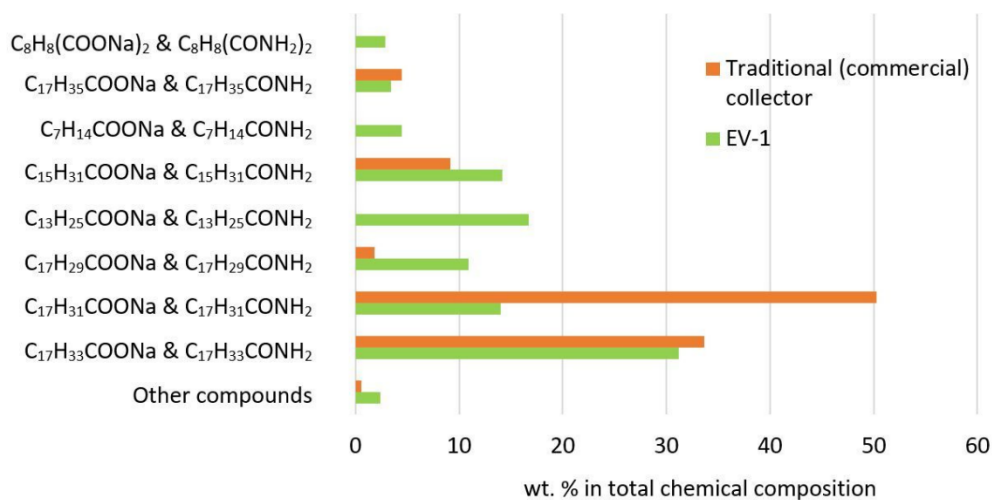


Figure 2-18. Comparison of a commercial fatty acid collector composition from Zheng *et al.* tests with EV-1, plotted using data from (Zheng *et al.*, 2016)

Recovery of phosphorus minerals has challenges under conditions with significantly lower temperatures, especially in Arctic regions. Thus, at the JSC “Apatity” plant in Russia, it has been

demonstrated that winter water temperature (10 °C after mixing with recycled water) was below the ideal temperature for apatite flotation (16-20 °C) under the reagent scheme used (mixture of different tall oils with sulfonate) (Ivanova *et al.*, 2005). This resulted in poor selectivity, increased consumption of reagents, decreased recovery, and excessive frothing. Consequently, the plant was forced to heat the pulp to maintain plant operations during the 8 month long Arctic winter. The possibility of operating without heating has been demonstrated at a laboratory scale using different combinations of oils and resin acids (Ivanova and Mitrofanova, 2009; Ivanova *et al.*, 2005). Located in the Arctic Circle, the Swedish iron company LKAB used an Atrac collector for reverse flotation of apatite. In laboratory tests, it was found that apatite flotation kinetics, even when using this non-conventional collector, was subject to variations with temperature in the range of 10 to 30 °C (Smolko-Schvarzmayr *et al.*, 2017; Su *et al.*, 1998). In addition to temperature, apatite flotation is sensitive to water quality, specifically to the presence of ions such as  $\text{Ca}^{2+}$ ,  $\text{CO}_3^{2-}$ , and  $\text{HCO}_3^-$ . Thus, research on Siilinjärvi concentrator (Finland) sampling data revealed seasonal and daily variations in pH and the above-mentioned ions, potentially contributing to fluctuations in flotation efficiency (Stén *et al.*, 2003).

To overcome low-temperature issues, Xu studied new collectors at 8-9 °C for phosphate flotation. In the case study of the PA-808A collector (composition not revealed) at Xinpu (China) phosphate flotation plant, under low temperatures (7-9 °C), low mass pull and low recoveries were observed in a cleaner stage. Xu tested the PA-900B collector (composition not revealed) and concluded that it could be used as a phosphate flotation collector, without pulp heating throughout the year provided that there are seasonal adjustments to the reagent dosage (Xu, 2005).

#### **2.5.5. Tungstates**

Cold winters can also cause problems for different scheelite flotation plants (Kupka and Rudolph, 2018). Samatova *et al.* investigated the Primorskaja plant in Russia; it was noted that a temperature drop leads to poorer collector solubility and an increased concentration of micelles with a shortage of ionic species for adsorption on mineral surfaces (Samatova *et al.*, 2015). To expand the “window” of operable collector dosages under conditions of lowering the critical micelle concentration with temperature, mixed chemistry may be applied, *e.g.* mixtures of fatty acids with non-polar surfactants (polyoxyethylene ether) (Zhu *et al.*, 2016). Thus, Chen *et al.* investigated the effect of the addition of a non-ionic polyoxyethylene ether (JFC-5) to scheelite flotation with

sodium oleate (NaOl). It was found that at 10 °C, the recovery of scheelite could be increased from 22% to 85% in the presence of JFC-5 with a mass ratio of 20% at pH 10. This was attributed to the reduced electrostatic repulsion between the oleate ions by JFC-5, which resulted in enhanced NaOl adsorption on the scheelite surface (Chen *et al.*, 2018).

Seasonality effects may also be attributed to the water quality and associated changes in chemistry. For example, the Luanchuan flotation plant (China) was experiencing a 5-8% recovery drop in winter, associated with fluctuations of water glass in process waters. It was found that winter process water contained more than 500 mg/l Si, which created an excess of reagent in the system and depressed the scheelite (Kang *et al.*, 2017; Kang *et al.*, 2018). As a solution to a seasonal (from late autumn to early spring) degradation of the scheelite concentration index at a Hunan copper-tungsten separation plant, similar to the Primorskaja plant, a special mixture of collectors that exhibits resistance to low temperatures (down to 10 °C) has been suggested, where the ratio of the reagents is adjustable depending on pulp temperature (Li *et al.*, 2014). Some laboratory investigations of scheelite flotation determined that at a temperature of 10 °C mineral recovery was improved by a sodium oleate – TX15 (a collector based on octaphenyl polyoxyethylenes) mixture at a ratio of 5:1 (Chen *et al.*, 2017). In another study by Zhu *et al.*, oleate collector efficiency for cold pulps was enhanced by adding MOA-9 (lauryl alcohol polyoxyethylene ether), where a synergistic effect with the non-ionic reagent was explained by screening of electrostatic repulsions between the polar anionic groups (Zhu *et al.*, 2016).

Adsorption and flotation studies by Meng *et al.* at elevated temperatures conducted on wolframite fines using sodium oleate demonstrated that higher pulp temperatures improved ionization of oleate species intensifying chemisorption and flotation performance (Meng *et al.*, 2018).

#### **2.5.6. Rare-Earth Multi-Anion Minerals**

Flotation of RE minerals and associated gangue is highly influenced by temperature variations. Using the Mountain Pass Mine (USA) as an example, bastnaesite flotation from calcite and baryte is a system consisting of semi-soluble minerals. This semi-solubility amplifies flotation variability with temperature. Improvement in flotation selectivity through surface cleaning and selective collector adsorption was facilitated on the plant through pulp heating. It has been found that temperature has no effect on depression using lignin sulfonate, while collector adsorption was the most optimal at approximately 70 °C for oleic acid and 85 °C for tests with alkyl hydroxamic acid

(Pradip, 1981; Pradip and Fuerstenau, 1991; Schriener, 2016). High pulp temperatures were also applied in a series of industrial-scale tests conducted on the RE concentrator at 60 to 65 °C (Yang, 2005).

For the largest RE mine in China, Bayan Obo, it has been confirmed on an industrial scale that bastnaesite grade and recovery increase in the temperature range of 25-75 °C, with more than 80% of the growth observed by increasing the temperature up to 50 °C (Li *et al.*, 2018). Further investigations revealed a decrease in collector adsorption density with temperature, which was, however, accompanied by a larger amount of characteristic (-C(=O)N-) bonds indicating stronger adsorption (Li *et al.*, 2018). Similar conclusions of higher differences in adsorption free energies between gangue minerals and bastnaesite have been demonstrated in experiments on the Mountain Pass ore (Pradip and Fuerstenau, 1991). It has been suggested that an easily detachable physisorbed collector layer becomes chemisorbed with a temperature increase, promoting the growth of chelate complexes (Li *et al.*, 2018). Using L102 and L108 collectors (salicylhydroxamic acid based and ethoxylate based respectively), for the example of the tailings from the Baotou (China) concentrator, a possible optimal operation at lower temperatures (35-45 °C) has been demonstrated (Xu *et al.*, 2006). Research conducted on Wei Shan (China) ore (Zanin *et al.*, 2019) and the middlings of Baotou mineral processing plant (Ren and Hu, 1996) came to a similar conclusion indicating an optimal temperature range being 40-43 °C. It has been demonstrated that the selectivity index is poor at pulp temperatures below 32 °C, and above 44 °C, and the poor efficiency at a higher temperature was associated with collector decomposition (Zanin *et al.*, 2019). Studies on mixed collector systems on ores from Sichuan and Hubei RE mines were assumed to be more robust in relation to normal temperature fluctuations (Li and Zeng, 1999).

Sodium metasilicate acts as a typical depressant in RE mineral flotation systems. Its solubility and dissolution rate increase substantially with temperature (PQ Corporation, 2009). Pradip and Fuerstenau investigated monazite flotation from rutile-zircon mixtures, revealing that with a temperature rise in systems with oleic acid or potassium octyl hydroxamate collectors accompanied by sodium metasilicate or sodium sulfide depressants, there is a clear trend of improved selectivity (Pradip and Fuerstenau, 1991). Tests with the commercial hydroxamic acid-based Flotisor V3759 collector demonstrated a selectivity loss with increased temperature, as the collector showed an increase in collection effectiveness with temperature, which increased greater

than the depressive ability of sodium metasilicate and sodium sulfide (Pavez and Peres, 1993). Another commercial collector from the Flotisor series, Flotisor V3579, doubled the amount adsorbed on bastnaesite surfaces as the temperature increased from 25 to 80 °C (Anderson, 2015). Moreover, in the flotation of bastnaesite and xenotime, it was found that the free surface energy of the hydroxamate collector increases with temperature, providing a rise in the recovery of floated minerals (Anderson, 2015; Zhang, 2016).

### 2.5.7. Lithium Silicates

Spodumene ( $\text{LiAl}(\text{SiO}_3)_2$ ) is reported to be floated using anionic collectors, known to be sensitive to temperature variations. Laboratory testing of ore from Vilatuxe (Spain) by Menéndez *et al.* revealed that an increase in temperature above 33 °C resulted in higher recoveries, while an abrupt selectivity loss was observed above 50 °C. Consequently, the best results for the ore under the investigated reagent scheme were achieved at 15 °C (Menéndez *et al.*, 2004) (Figure 2-19. ). Xu *et al.* studied spodumene and feldspar flotation, showing that by using solely oleic acid as a collector, there was a dramatic decrease in recovery for both minerals below 30 °C, while a mixture of oleic acid with dodecyl trimethyl ammonium chloride reduced the negative impact of temperature drop for spodumene, while not significantly changing the recovery profile of feldspar (Xu *et al.*, 2016a), providing a greater degree of freedom for selective separation.

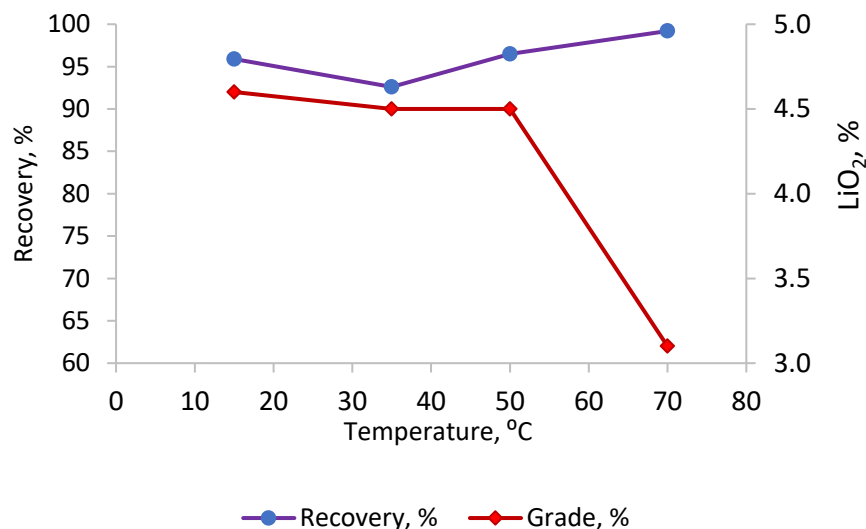


Figure 2-19. Recovery and grade of lithium concentrate at different temperatures of the flotation pulp, adapted from (Menéndez *et al.*, 2004)

Recovery of another lithium mineral, lepidolite, from Yichun Tantalum Niobium Mine (China) tailings was accomplished with cocoamine, which resulted in significant winter losses. Poor concentrate quality and recovery were associated with the low crystallization point (17 °C) of coco amine. To address such poor efficiency, it was recommended to apply a more complex reagent scheme involving primary alkyl amine, mixed alkyl alcohols, and alkali metal salts (Liu *et al.*, 2011).

#### **2.5.8. Carbonaceous Materials**

Carbonaceous materials, such as coal or graphite, are known for their natural hydrophobicity (Honaker, 1992). In the context of temperature variations, the effect of preferential nucleation of nano-bubbles on hydrophobic mineral surfaces should be considered (Zhou *et al.*, 2020). Arising from the rapid increase in temperature, nanobubbles promote attraction between hydrophobic mineral particles and increase their recovery to the concentrate (Zhou *et al.*, 2020). From the perspective of flotation recovery, laboratory tests with graphite, anthracite, and coal at 10, 22, and 40 °C revealed a some detrimental temperature effect on the maximum recovery (*ca.* 2% decrease per 30 °C temperature rise for all three tested carbonaceous materials) with no evident effect on flotation kinetics (Drzymala *et al.*, 2021). Such effects are in line with a hypothesis linking recovery decrease for carbonaceous material with froth stability issues (Sun and Chao, 1966).

Non-polar reagents are the principal collectors of naturally hydrophobic minerals, and it has been reported that their strength increases with viscosity (Glembotsky *et al.*, 1968). Thus, for the flotation of carbonaceous materials, it can be suggested that reagent efficiency will be dependent on viscosity and dispersibility. Generally, as non-polar reagent viscosity rises, the temperature required to maintain the same level of dispersibility also increases. When the collector dispersion level is too high and the non-polar reagent droplet size is less than 5 µm, there is insufficient kinetic energy for droplet-particle collisions. Therefore, an excessive temperature rise may decrease coal flotation efficiency (Klassen and Plaksin, 1954). Moreover, from adsorption studies with different hydrocarbons, it was found that the temperature-induced viscosity decrease correlates with contact angle values, implying a decrease in reagent adhesion to mineral (Glembotsky *et al.*, 1968).

Temperature also controls coal surface oxidation, which impacts recovery. Research by Gayle *et al.* on a low volatile bituminous coal and an alcohol-type frother demonstrated a decrease in recovery due to increased coal surface oxidation because of increased conditioning time at room

temperature. Applying a mixture of kerosene and pine oil translated into consistent recovery values as a result of being more robust toward coal oxidation (Gayle *et al.*, 1965).

Another mechanism contributing to seasonal variations suggested for coal flotation plants in northern China was the formation of nanobubbles on mineral surfaces in winter. For nano-bubble formation, a temperature gradient is required, which could be obtained when a slurry is transported from the cold outside to the warm interior part of the process plant (Li *et al.*, 2020). Laboratory tests confirmed an improvement in coal flotation efficiency when nano-bubbles were formed on the surface (Chang *et al.*, 2020).

Frother properties and efficiency also play a critical role in coal flotation. Froth volume was reduced by half when the temperature dropped from 25 °C to 10 °C when pine oil was used (Sun, 1952), and a more stable froth was produced. Higher solubility and lower media viscosity at elevated temperatures provide better efficiency of air dispersion, reflected through finer bubbles and greater recovery (Bhattacharya and Pascoe, 2005).

There is also a hypothesis explaining the decrease of coal recovery at temperatures above 40 °C, observed in tests with Barnesboro (USA) coal plant rejects, through the frothing coefficient (FC). The FC is believed to be in a direct relationship with coal recovery (Sun and Chao, 1966), as can be seen from Equation 2-41:

$$C_f = V_f \times S_f \quad (2-41)$$

where  $C_f$  is the froth coefficient,  $V_f$  is froth volume (cm<sup>3</sup>), and  $S_f$  is froth stability in seconds. The frothing coefficient is seen to decrease for elevated temperatures, leading to lower coal recoveries (Sun and Chao, 1966). Investigations into laboratory coal flotation accompanied by contact angle measurements at different temperatures concluded that coal flotation variation is heavily dependent on physical factors rather than chemical (Gayle and Eddy, 1961).

Flotation studies with coal samples taken from the Karbomet Mining Coal Washing Plant in Turkey also confirmed the existence of an optimal flotation temperature range between 25 and 50 °C, where low recovery at higher temperatures was explained by decreased froth stability and increased bubble bursting rate (Hacifazlıoğlu and Gerdan, 2016). Bailey and Whelan (Bailey and Whelan, 1953) obtained a slightly different optimal flotation temperature range for weakly



hydrophobic coals (from 20 to 40 °C), while for strongly hydrophobic coal flotation, the impact of temperature was insignificant (Bhattacharya and Pascoe, 2005). Similar results were also obtained in laboratory flotation trials with anthracite, graphite, and coking coal, where the flotation rate constant was found to have a non-linear behavior with temperature (modeled with a second-degree polynomial) (Drzymala *et al.*, 2021).

## **2.6. Summary**

For most minerals, there is an optimal flotation temperature range that maximizes its performance. Seasonal variations could result in increased energy costs for pulp heating, decreased mineral recovery, and even shutdowns. Many sources reported the most feasible method of dealing with seasonal variations is through modifications of the reagent regime. For fatty acid flotation, most efforts have been on collector modification, while in sulfide flotation it is generally agreed that xanthates are quite resistant to temperature fluctuations. In sulfide flotation, most seasonal discrepancies reported were related to polymetallic and zinc flotation systems, where copper activation was often considered the main trigger of low performance in winter. It is observed in the reviewed research that not only temperature but also water quality is an important factor causing recovery seasonality issues. Extreme pulp temperature conditions are seen to depress sulfide flotation by an increased surface oxidation and collector desorption mechanisms at high temperatures, and by reduced reaction kinetics, increased viscosity, and reagent efficiency at low temperatures. Non-sulfidic flotation systems demonstrated increased collector and mineral solubilities at elevated temperatures, which were more sensitive to winter temperature drops. Different sources reported optimal conditioning for flotation to be close to room temperature for most ore types (Appendix A).

Temperatures above 40-50 °C, depending on the ore and operating parameters, may indicate an upper limit of optimal operating conditions, while 10-12 °C is seen as a lower optimal temperature limit. A rough generalization could be made by stating that temperature-driven changes are more impactful on non-sulfide ores where the most common issues are increased pulp viscosity and poor reagent dispersion. Sulfide flotation systems are more temperature resistant; however, for the case of polymetallic ores and the application of several modifiers, significant changes in flotation

performance could also be observed. Water quality variation is also a factor that is seen as important for both discussed flotation systems.

Different dissolution rates, precipitation, and adsorption of ions in the pulp driven by altered interactions and properties of water, mineral surfaces, reagents, and air suggest expanding the concept of the flotation system as a “flotation triangle” previously developed by Kawatra (Kawatra, 2009) to a multi-domain “flotation rectangle”, Figure 2-20.

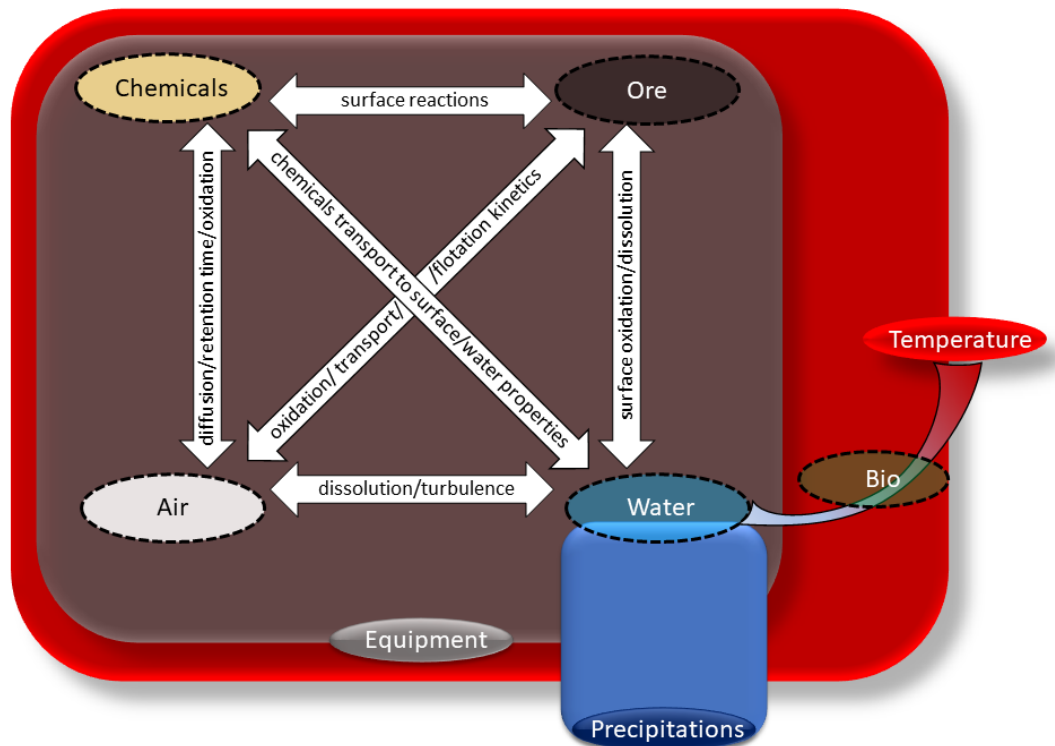


Figure 2-20. A concept of “flotation rectangular” demonstrating seasonal triggers sphere of influence and flotation system components interactions

As depicted in Figure 2-20, temperature has the potential to trigger changes in all four major flotation components, by altering interactions between them, and impacting the efficiency of the equipment domain, hosting above mentioned interactions. Atmospheric precipitation is seen as another external trigger, that supplies fresh water to a system, predominantly impacting the water component in flotation. Increased precipitation, as a rule, leads to improvements in water quality, especially on plants with a high rate of process water recirculation, ultimately improving flotation performance. A biological sub-trigger is activated by temperature and precipitations. It also has a strong impact on a water component and its interactions. As for the chemicals domain, because

different reagents have varying power at different temperatures, plants operating at starvation regimes, or at lower bounds of chemical dosages, have higher risks of being shifted to sub-optimal areas as a result of seasonal shifts in reagents efficiency. Recirculation of process waters complicates, even more, the seasonally based choice of optimal reagent dosage. The air domain has been expressed through seasonal bubble size deviations, nano-bubbles, and dissolved gas contents, which are all important parameters to consider when analyzing seasonal discrepancies in flotation.

Such a comprehensive understanding of flotation components' response to external climate-induced triggers is of great importance, as the era of black-box flotation models goes down in history in connection with the new challenges that lie ahead of the industry, such as even larger fluctuations in weather conditions triggered by climate change, continuous deterioration of ore quality, scarcity of freshwater resources, increased environmental restrictions, and increased demand on minerals and metals. To successfully cope with the above-mentioned problems, the flotation process should be more deeply investigated which would assist in more accurate production forecasts, developing flexible flotation solutions, and understanding of the required properties for new flotation reagents. The investigations of new chemistries are one of the most important directions for sustainable flotation development, especially in view of the development of temperature-robust chemicals. Additionally, implementation of artificial intelligence in the decision-making process at the plants would be another important step toward linking flotation performance with weather forecasts on the way to developing sustainable flotation production.

---

## **Chapter 3. Materials and Methods**

### **3.1. Sample Description**

#### **3.1.1. Monomineralic Samples**

Galena (Morocco), sphalerite (Pierdes Verdes, Chihuahua, Mexico), and pyrite (Huanzala, Peru) samples were all purchased from Ward's Science (Rochester, NY, USA) and arrived in 1 kg bulk packs with specimen sizes up to 15 cm. Galena samples were relatively pure with some contamination with quartz. Pyrite samples have also been predominantly monomineralic with some inclusions of chalcopyrite. The sphalerite sample had the poorest quality, contaminated with galena, quartz, green garnet, pyrite, pyroxenes, and minor chalcopyrite. Because of the relatively complex mineralogy of a sphalerite sample, and the fine intergrowth of some minerals, this sample was upgraded with additional sorting, classification, gravity pre-concentration, and comminution methods before conducting flotation experiments.

#### **3.1.2. Lead-Zinc Ore Samples**

Ore samples used in the froth stability and flotation tests in this research originate from VMS and SEDEX deposits. Both ore samples were taken after primary crushing with a maximum particle size of *ca.* 300 mm. The VMS ore sample contained sphalerite, galena, and a minor amount of chalcopyrite as ore minerals. Pyrite, magnetite, siderite, quartz, chlorite, and stilpnomelane were the gangue. The SEDEX ore consisted of sphalerite and galena as ore minerals, while baryte and quartz were almost exclusively the gangue minerals. Some minor iron sulfides were also observed in the SEDEX ore.

### **3.2. Sample Preparation**

#### **3.2.1. Monomineralic Sample**

Galena, sphalerite, and pyrite samples were crushed, hand-sorted, and dry-milled. Galena and pyrite only required hand sorting, whereas the sphalerite was additionally purified using a Mozley table. The detailed sample preparation procedure is shown in Figure 3-1.

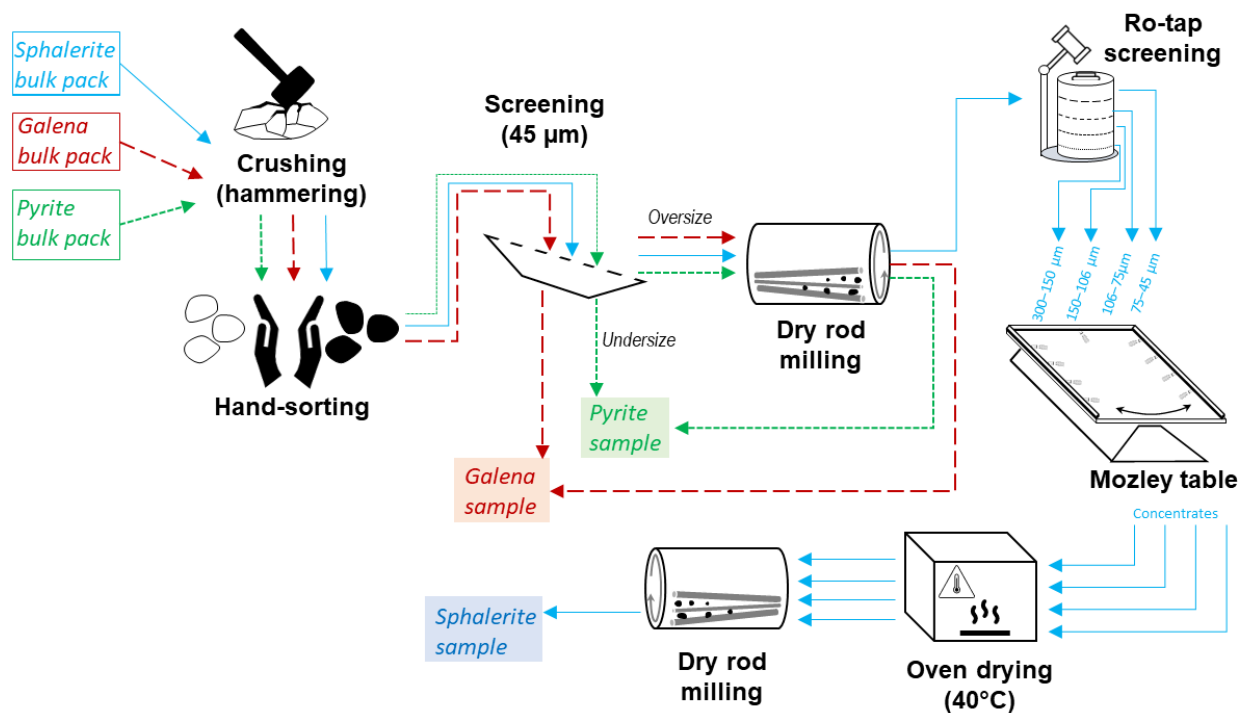


Figure 3-1. Sample preparation procedure for sphalerite, galena, and pyrite samples.

### 3.2.2. Lead-Zinc Ore Sample

Lead-zinc ore samples were crushed (using a jaw crusher) in 4 steps with gradual reduction of crusher opening, and screened (Sweco Screen) at 3.35 mm. The <3.35 mm product was representatively split using a rotary splitter before the final comminution step in a rod mill.

### 3.3. Sample Characterization

For particle size analysis of monomineralic samples ATS Scientific Microtrac Sync Size and Shape Particle Analyzer (ATS Scientific Inc., Burlington, Canada) was used. The particle size distribution (PSD) was obtained by dispersing diluted slurry with ultrasound, and by combining the data from laser light and high-speed camera. The PSD was fitted to the Rosin–Rammler model (Figure 3-2).

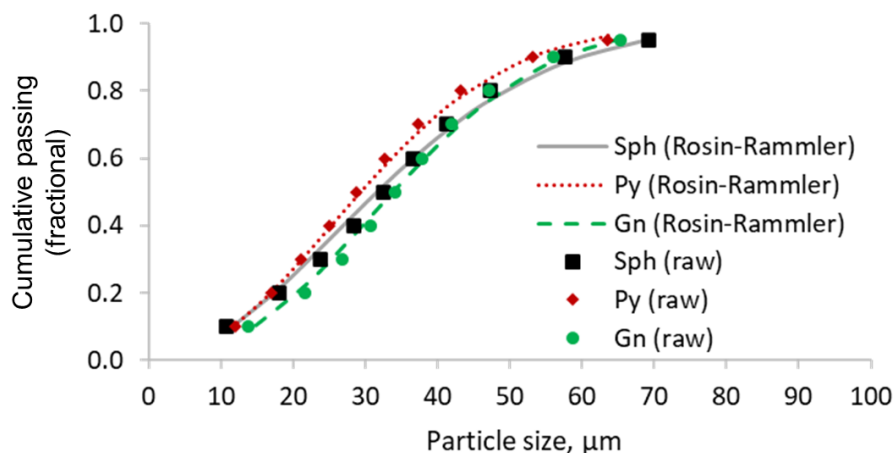


Figure 3-2. Particle size distributions for galena (Gn), pyrite (Py), and sphalerite (Sph) samples.

### 3.3.1. Surface Characterization

Surface characterization consisted of three steps: characterization of sample surface area using Brunauer-Emmett-Teller (BET) analysis (Table 3-1), characterization of sample surface energy by the inverse gas chromatography (IGC), and X-ray Photoelectron Spectroscopy (XPS) surface characterization. For BET surface area analysis, a Micromeritics TriStar 3000 Surface Area and Porosity Analyzer (Micromeritics Instrument Corporation, GA, USA) was used. Prior to analysis, samples were degassed with N<sub>2</sub>. Calculation of specific surface area was based on the nitrogen gas adsorption isotherms measured at 77 K.

Table 3-1. Characteristics of monomineralic samples used in this research

Mineral	BET surface area in (m <sup>2</sup> /g)	D <sub>80</sub> particle size (μm)
Galena	0.6	47
Sphalerite	0.7	47
Pyrite	2.5	43

The surface energy of the minerals was determined by the inverse gas chromatography (IGC) technique using a Surface Energy Analyzer, SEA (Surface Measurements System Ltd., UK). The data were analyzed using the Advanced SEA Analysis Software. Samples were packed into individual IGC pre-silanized glass columns with 6 mm outer diameter, 4 mm inner diameter, and 30 cm length. Methane, helium, and hydrogen gases were purchased from Megs Specialty Gases Inc. (Canada). The samples were run with nonpolar (heptane, octane, nonane, and decane) and

polar (toluene and dichloromethane) probes. The IGC measurements were conducted at 30 °C and 0% RH using a 10 sccm total flow rate of helium as inert carrier gas. Methane was used for dead volume corrections. Prior to IGC experiments, each sample column was preconditioned for 60 min with the carrier gas at 30 °C and 0% RH to remove any physisorbed water/reagents. For the analysis of the IGC data, the Schultz method was applied for dispersive components (Figure 3-3a) and specific surface energy components were determined based on the van Oss methodology using the Della Volpe scale (Mohammadi-Jam and Waters, 2014; Volpe and Siboni, 1997). Surface energy heterogeneity was determined through the injection of the probe vapors at different surface coverages (Figure 3-3b).

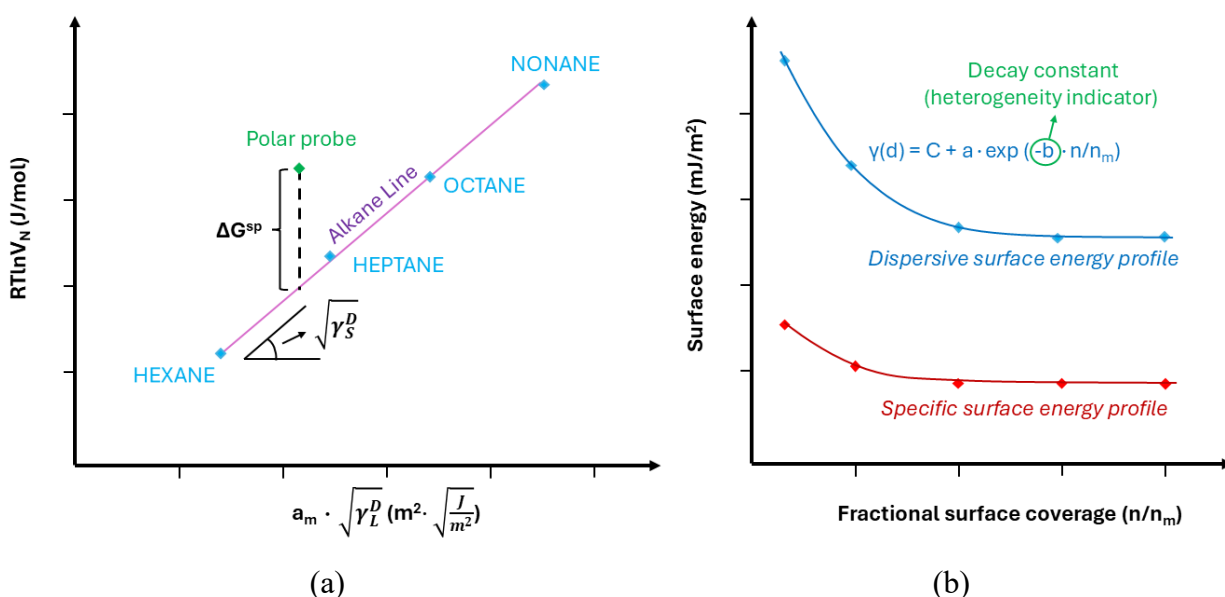


Figure 3-3. Graphical representation of determination of dispersive and specific surface energies (a) (adapted from (Mohammadi-Jam, 2017)), the diagram of typical surface energy heterogeneity profiles (b)

XPS measurements were conducted using a Thermo Scientific K-Alpha Monochromatic X-ray Photoelectron Spectrometer (Thermo Fisher Scientific Inc., USA) to study the chemical composition of the mineral surfaces under high vacuum conditions. The XPS instrument was equipped with an Al K $\alpha$  X-ray source (1486.6 eV, 0.834 nm). The analysis was carried out by applying a 400  $\mu$ m spot size, 50.0 eV pass energy, and 0.100 eV energy step size. A flood gun was used to shoot the samples with low-energy electrons to avoid charging on the surface. The collected data was processed using Avantage Data Processing software (Thermo Fisher Scientific Inc.,

USA). The binding energy (Figure 3-4) was calibrated using the background hydrocarbon C 1s binding energy (284.8 eV).

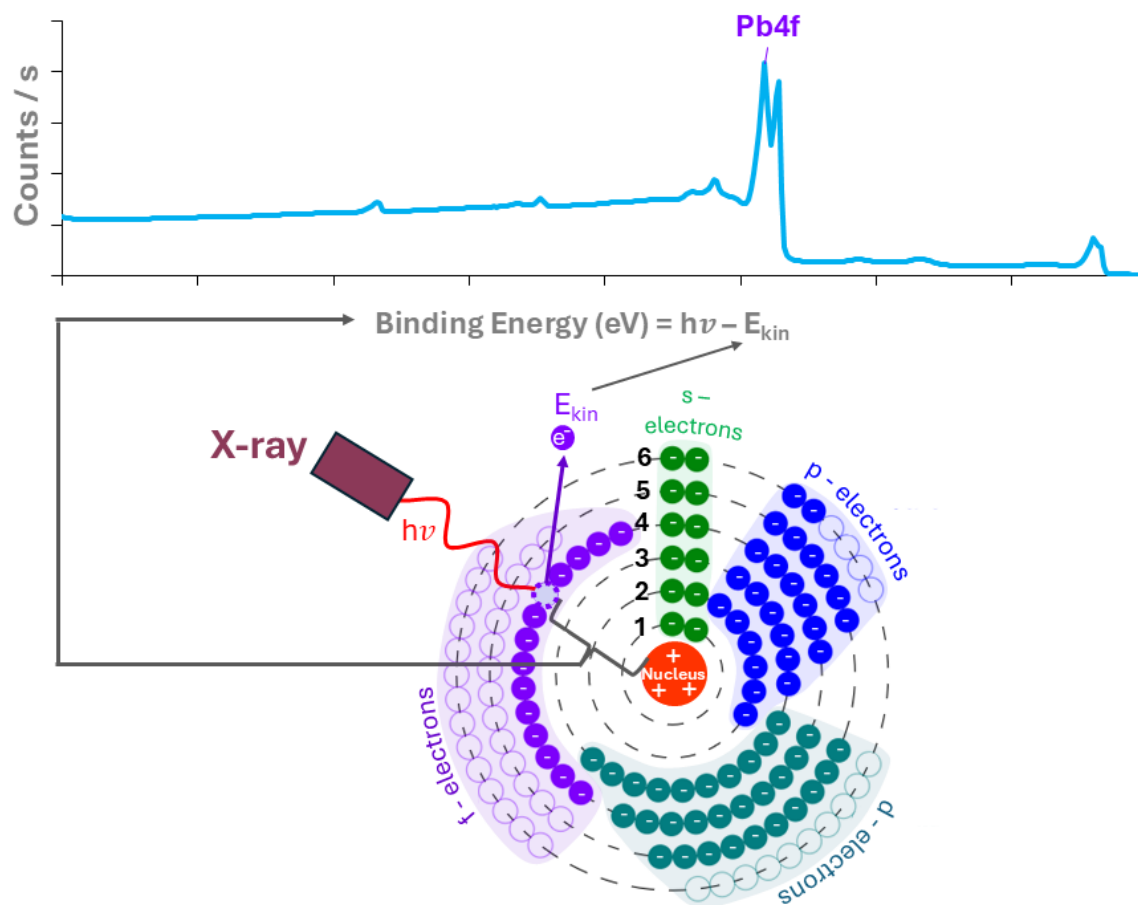


Figure 3-4. Simplified explanation of the working principle of XPS analysis

### 3.3.2. Analysis of Bulk Composition

The monomineralic and ore samples were analyzed by Bruker D8 Discovery X-Ray Diffractometer (XRD) (Co  $K\alpha$  source,  $\lambda = 1.79 \text{ \AA}$ ) (Bruker AXS GmbH, Karlsruhe, Germany). Rietveld refinement was carried out using Materials Analysis Using Diffraction (MAUD) Java program (version 2.992) (Lutterotti *et al.*, 1999).

The produced monomineralic samples were more than 90% composed of one mineral phase, which permits them to be termed “monomineralic” (Guilbert and Park, 1986). The pyrite sample, based on the mineralogical composition of the deposit, XRD results, and mineral matching using “Match!” software (version 3.0), was identified to contain pyrite, hematite, Al-phase (corundum),



and marcasite. The galena sample was found to contain some cerussite and fluorite, while the sphalerite sample after pre-concentration still contained some galena, quartz, and calcite, as shown in Table 3-2. The diffractograms of monomineralic samples are given in Appendix B.

Table 3-2. Mineralogical composition of pyrite, galena, and sphalerite samples.

Pyrite Sample		Galena Sample		Sphalerite Sample	
Mineral	wt.%	Mineral	wt.%	Mineral	wt.%
Pyrite	94.2	Galena	95.4	Sphalerite	92.0
Corundum	1.0	Fluorite	0.7	Galena	2.4
Hematite	1.1	Cerussite	3.8	Albite	2.5
Marcasite	1.4			Calcite	1.6
Anatase	2.3			Quartz	1.5

The mineralogical composition of SEDEX ore sample was the following: sphalerite, galena, quartz, baryte, and iron sulfides. The sample is dominated by quartz and baryte (more than half of the sample content), with substantial sphalerite presence (approximately 20%), Figure 3-5.

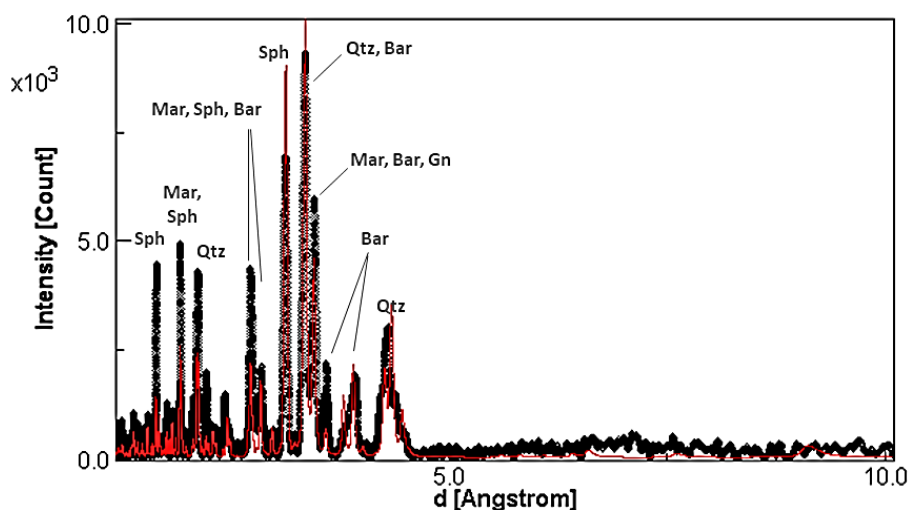


Figure 3-5. Diffractogram of a SEDEX ore sample (Sph – sphalerite, Qtz – quartz, Bar – baryte, Mar – marcasite, Gn – galena)

The elemental composition of the samples was analyzed using ICP-OES (ICAP-6500DV, Thermo Fisher Scientific Inc., USA). For that, first, samples were digested in the Nieka E1 fusion machine

(Materiaux Nieka Inc., Quebec City, Canada) using a lithium tetraborate flux fusion/nitric acid dissolution (15% HNO<sub>3</sub>) procedure.

XRD-based ore composition was compared to the composition derived from ICP-OES assays using element-to-mineral conversion (EMC) (Figure 3-6). Element-to-mineral conversion was performed by solving Equation 3-1 for  $\vec{x}$  (Lamberg *et al.*, 1997):

$$\mathbf{A} \vec{x} = \vec{b} \quad (3-1)$$

where  $\mathbf{A}$  is a matrix of elemental contents of the mineral phases,  $\vec{b}$  is a vector of sample assays,  $\vec{x}$  is a vector of mineral grades in a sample. The  $\vec{x}$  is found by using a non-negative least square approach:

$$\vec{R} = |\vec{b} - \mathbf{A} \vec{x}| \quad (3-2)$$

where  $\vec{R}$  is a vector of residuals that has to be minimized.

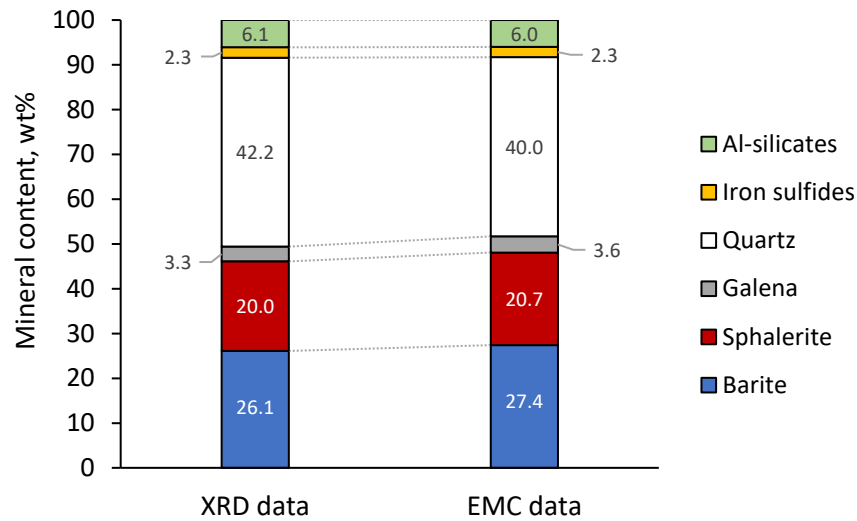


Figure 3-6. Comparison of XRD-based mineralogical composition of SEDEX ore sample with Element-to-Mineral conversion results

The VMS sample was mainly composed of pyrite (more than half of the sample) and silicate/aluminosilicate gangue (*ca.* 30%). The ore minerals were less abundant compared to SEDEX ore: roughly 7% sphalerite and approximately 2% galena (Figure 3-7 and Figure 3-8).

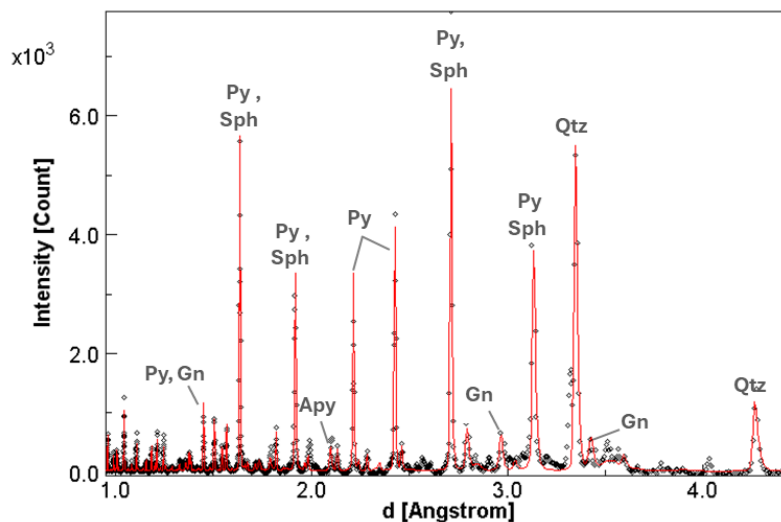


Figure 3-7. Diffractogram of a VMS ore sample (Sph – sphalerite, Qtz – quartz, Bar – baryte, Mar – marcasite, Gn – galena)

XRD results satisfactorily correspond to element-to-mineral conversion results (Figure 3-8), with some variations most probably caused by nonstoichiometric composition of some of the minerals, mineral alterations, as well as instrumental and sampling errors.

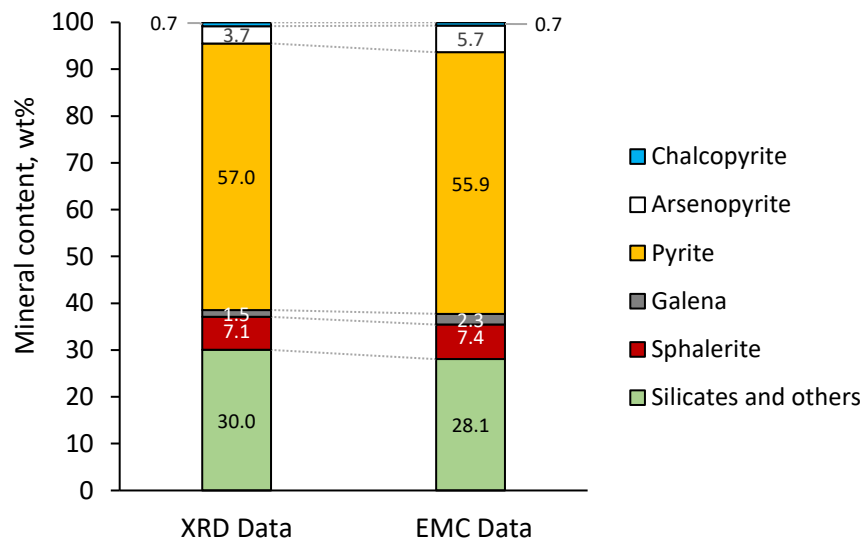


Figure 3-8. Comparison of XRD-based mineralogical composition of VMS ore sample with Element-to-Mineral conversion results

### 3.4. Methodology of Testing Reagent Adsorption

Flotation/adsorption reagents used in the tests included methyl isobutyl carbinol (98% pure, Sigma-Aldrich, USA), sodium isopropyl xanthate (SIPX, 90% pure, SNF Flomin Inc., China), copper sulfate pentahydrate (98% pure, Fischer Scientific, Canada), dextrin (sulfated ash  $\leq 0.5\%$ , Acros Organics™, USA), calcium hydroxide ( $>95\%$  pure, Fischer Scientific, USA), and sodium hydroxide (99.2% pure, Fischer Scientific, USA).

The conditioning process in the adsorption tests started with solids mixing with flotation modifiers. Sodium hydroxide was used to control pH, dextrin was tested as a depressant, and copper sulfate pentahydrate as an activator. Conditioning time was 5 minutes, and the conditioning was performed in a 10 ml vessel. Afterward, this suspension was transported to a bigger vessel (50 ml) with sodium isopropyl xanthate collector (SIPX) solution circulating through a ThermoScientific GENESYS™ 180 UV-VIS spectrophotometer (Fisher Scientific Inc., ON, Canada). The solution from the 50 ml vessel was continuously pumped in a loop through a cuvette installed in the UV-VIS machine for real-time monitoring of aqueous xanthate concentrations. 301 nm wavelength has been chosen as a characteristic for the identification of the residual (non-adsorbed) concentration of the xanthate in the solution (Rao, 1971; Sheikh, 1972). To eliminate particles from the UV-VIS cuvette and record a clear adsorption signal, 0.45  $\mu\text{m}$  filter paper was installed at the pumping inlet. The five adsorption factors were investigated in the frameworks of the central composite design, namely, temperature (5-45 °C), collector concentration (1-21  $\mu\text{mol/l}$ ), activator concentration (0-120  $\mu\text{mol/l}$ ), depressant concentration (0-60  $\mu\text{mol/l}$ ), and pH level (from 8 to 12). Finally, two output adsorption parameters were extracted from the adsorption data for building response models in Minitab® Statistical Software (Minitab® LLC, State College, Pennsylvania, USA, version 21.4.2), namely: apparent adsorption rate constant ( $k_a$ ) and apparent adsorption equilibrium capacity ( $q_e$ ). Output responses were modeled using five input parameters and a second-order polynomial with 2-way interaction terms. Moreover, for maximization/minimization calculations MiniTab® optimization tool based on the desirability function has been used.

The setup arrangement consisting of a UV-VIS spectrophotometer, pump, conditioning/pre-conditioning vessels, cooling/heating system, as well as the main factors and responses is illustrated in Figure 3-9.

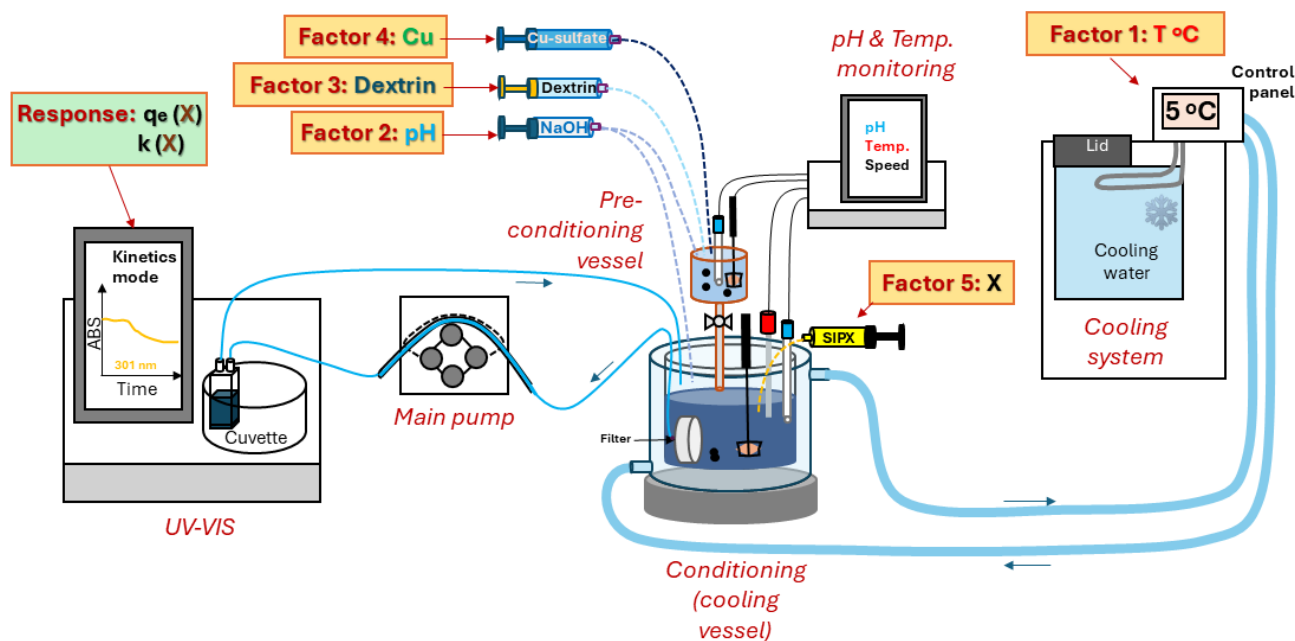


Figure 3-9. Adsorption setup: spectrophotometer (UV-VIS) connected to the double wall conditioning glass (Conditioning vessel) through peristaltic pump, with temperature being controlled with isotherm bath circulator (Cooling/Heating system). The main factors controlled: sodium isopropyl xanthate concentration (Factor 5: X), copper sulfate pentahydrate concentration (Factor 4: Cu sulfate), dextrin concentration (Factor 3: D), pH (sodium hydroxide dosage, Factor 2), and temperature (Factor 1: T °C)

Pseudo-first order adsorption model has been used to estimate the apparent adsorption rate constant ( $k_a$  in  $\text{nmol}/(\text{m}^2 \cdot \text{s})$ ) and apparent adsorption equilibrium capacity (Lagergren, 1898):

$$\frac{dq_t}{dt} = k_a(q_e - q_t)/10^3 \quad (3-3)$$

where  $q_t$  is the quantity of xanthate adsorbed on a mineral surface at time  $t$  (s),  $q_e$  is the quantity of the xanthate adsorbed at equilibrium ( $\mu\text{mol}/\text{m}^2$ ). The quantity of the xanthate adsorbed on a mineral surface at time  $t$  ( $q_t$ ) was calculated using Equation 3-4 (Ignatkina *et al.*, 2014):

$$q_t = \frac{(C_0 - C_t) \cdot V}{m \cdot A} \quad (3-4)$$

where  $C_0$  is the initial concentration of a xanthate before adsorption in  $\mu\text{mol}/\text{l}$ ,  $C_t$  is the concentration of xanthate at time  $t$  in  $\mu\text{mol}/\text{l}$ ,  $V$  is the volume of the solution in l,  $m$  is the sample mass in g,  $A$  is the specific surface area of a mineral sample in  $\text{m}^2/\text{g}$ . Activation energies were

calculated by extracting the slopes of the regression lines ( $tg \alpha$ ) for different minerals built in coordinates  $\ln(k_a) - 1/T$ , and applying the following formula (Ignatkina *et al.*, 2014):

$$E_a = -tg \alpha \cdot R \quad (3-5)$$

where  $E_a$  is the activation energy of adsorption, and  $R$  is the universal gas constant. The enthalpy and entropy of activation were also graphically extracted using the Eyler Equation (Kistemaker *et al.*, 2016):

$$\ln \frac{k_a}{T} = \frac{-\Delta H^\ddagger}{R} \cdot \frac{1}{T} + \ln \frac{k_B}{h} + \frac{-\Delta S^\ddagger}{R} \quad (3-6)$$

### 3.5. Foam/Froth Stability Measurements

In order to understand better the flotation system, first, tests in a two-phase system were performed to see the impact of common flotation reagents at different temperatures and aerations on the foam stability (to exclude the strong stabilizing effect of particles, that can potentially mask potential interaction effects). The next step consisted of investigations of different aspects of the three-phase systems (froth) in the context of mono-mineral Denver flotation systems (galena, sphalerite, pyrite), and multi-mineral Denver flotation systems (VMS and SEDEX ore).

#### 3.5.1. Foam Stability Tests

Foam stability measurements were performed in a small glass column (2 cm diameter and 20 cm height) equipped with a water cooling/heating jacket connected to the Fisher Scientific Isotemp<sup>®</sup> 4100 R20 Bath Circulator (Fisher Scientific Inc., PA, USA) (Figure 3-10). The gas bubbles were produced with ceramic frit at the bottom of the column. The camera (Canon VIXIA HF R800, Canon Canada Inc., Canada) was continuously filming the foam to extract the equilibrium foam height. A central composite design (CCD) with five factors and five levels was implemented for the experimental work. The experimental protocol consisted of water temperature adjustment, chemical conditioning, foam height testing by air injection, and foam half-life time measurements by cutting the air supply at the end of the test (recording foam height versus time). Chemical conditioning included water pH regulation with lime, dosing collector (SIPX), and frother (MIBC) at desired levels. The tested levels for indicated factors are provided in Table 3-3.

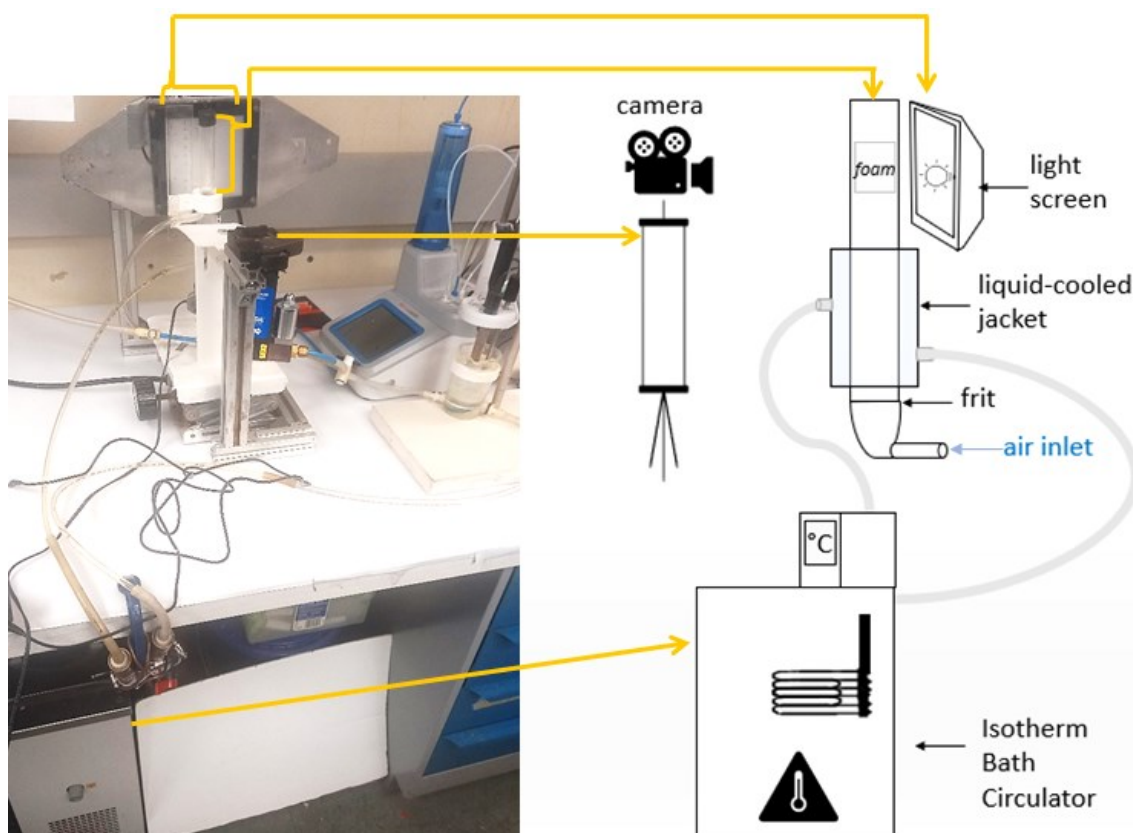


Figure 3-10. Foam stability measurement setup.

Table 3-3. Central composite design of experimental levels.

Variables	Symbol	Tested Levels	
		Lowest Level ( $-\beta$ )	Highest Level ( $+\beta$ )
Temperature, °C	$x_1$	5	45
pH	$x_2$	8	12
MIBC dosage, ppm	$x_3$	10	50
SIPX dosage, ppm	$x_4$	10	170
Superficial gas velocity ( $J_g$ ), cm/s	$x_5$	0.1	0.9

Relationships between input variables and responses were established through a second-order polynomial with 2-way interaction terms (Mathews, 2005):

$$y_k = b_0 + \sum_{i=1}^n b_i x_i + \sum_{i=1}^n b_{ii} x_i^2 + \sum_{i=1}^{n-1} \sum_{j=2}^n b_{ij} x_i x_j + \varepsilon \quad (3-7)$$

where  $y$  is the  $k^{th}$  response,  $b_0$  is an intercept,  $b_i$  is the equation linear term coefficient,  $b_{ii}$  is the equation cubic term coefficient,  $b_{ij}$  is the cross-product coefficient,  $x_i$  and  $x_j$  are the variables,  $n$  is the number of variables (5, in the current case), and  $\varepsilon$  is a residual (error). The analysis of the data was performed by using the statistical software package “Minitab® Statistical Software” (version 21.2). The confidence interval used for the analysis of statistical importance was 95%.

The video from the camera was split frame by frame and analyzed using ImageJ (version 1.53t). The processing part included contrast/brightness adjustment, 8-bit conversion of the images, setting thresholds (Otsu threshold), filling the holes, erosion, dilation, noise cleaning by setting size threshold, and size analysis of the obtained 2-bit images with foam. Foam heights were plotted against time and the equilibrium foam height was modeled by an adapted exponential Nesset et al. equation (Nesset *et al.*, 2007):

$$F_h(t) = F_{h(eq)} + m \cdot e^{-dt} \quad (3-8)$$

where  $F_h(t)$  is foam height at time  $t$  (mm),  $F_{h(eq)}$  is equilibrium foam height (mm),  $m$  is foam height reduction after reaching a peak at the beginning of the test (difference between  $F_h(t)$  and  $F_{h(eq)}$  in mm), and  $d$  is the foam height decay constant.

### 3.5.2. Froth Stability: Bubble Size in Monomineralic System

The image analysis of the top froth bubbles was performed using the Cellpose generalist algorithm for cellular segmentation. Cellpose is based on U-net neural network architecture already pre-trained on 70,000 objects (Stringer *et al.*, 2021). Cellpose was fine-tuned by manually training the algorithm on 1,000 bubbles captured by the camera on the froth surface. Such training is required for better recognition of regions of interest. Subsequently, the largest bubble size was plotted versus flotation time. A special model was developed to fit the bubble size data. As a basis of bubble size versus time model, a two-parameter Weibull distribution was used, as shown in Equation 3-9 (Heiser and Hofmeister, 2019; O'Connor and Kleyner, 2012):



$$F(t) = 1 - e^{-\frac{t^\beta}{\eta}} \quad (3-9)$$

where  $\eta$  is characteristic life (scale factor),  $\beta$  is the Weibull slope (shape parameter), and  $F(t)$  is the failure distribution function. When  $\beta < 1$ , the function decreases with time, while when  $\beta > 1$ , the function increases. It has been reported that bubble size on the froth surface rapidly decreases at the beginning of flotation, reaches the “plateau” area, and starts to slightly increase by the end of the flotation process. To produce such a “Bathtub curve”, a bi-modal distribution function (beta distribution (Walck, 2007)) was added into Equation 3-9 to allow  $\beta$  variation with time. Since beta distribution has a U-shape only at shape and scale parameters below 1, and the Weibull shape parameter needs to be below and above 1 to produce a Bathtub curve, a coefficient of 2 was added to the equation before the beta distribution term; in addition, an intercept term was added at the beginning of the equation to fit the smallest bubbles in the “plateau” area of the curve. The derived model for the description of top froth bubble size dynamics is provided in Equation 3-10:

$$D_b^{max}(t) = D_{b(eq)}^{max} + 1 - e^{-\frac{t^{2 \cdot B(a,b,t)}}{\eta}} \quad (3-10)$$

where  $D_b^{max}(t)$  is the diameter of the top bubble on the froth surface,  $D_{b(eq)}^{max}$  is an “equilibrium” top bubble size in the plateau area of the “Bathtub” curve,  $B(a, b, t)$  is beta distribution of Weibull shape parameter, and  $a$  and  $b$  are beta distribution shape parameters.

### 3.5.3. Froth Stability: Absolute Froth Height in VMS Ore System

For absolute height measurements Cole-Parmer P200-02 Benchtop pH/Conductivity Meter was used (Cole-Parmer Instrument Company, LLC., IL, USA). The conductivity probe was attached to a syringe infusion pump and used as a mechanism of smooth electrode immersion into the flotation cell (Figure 3-11).

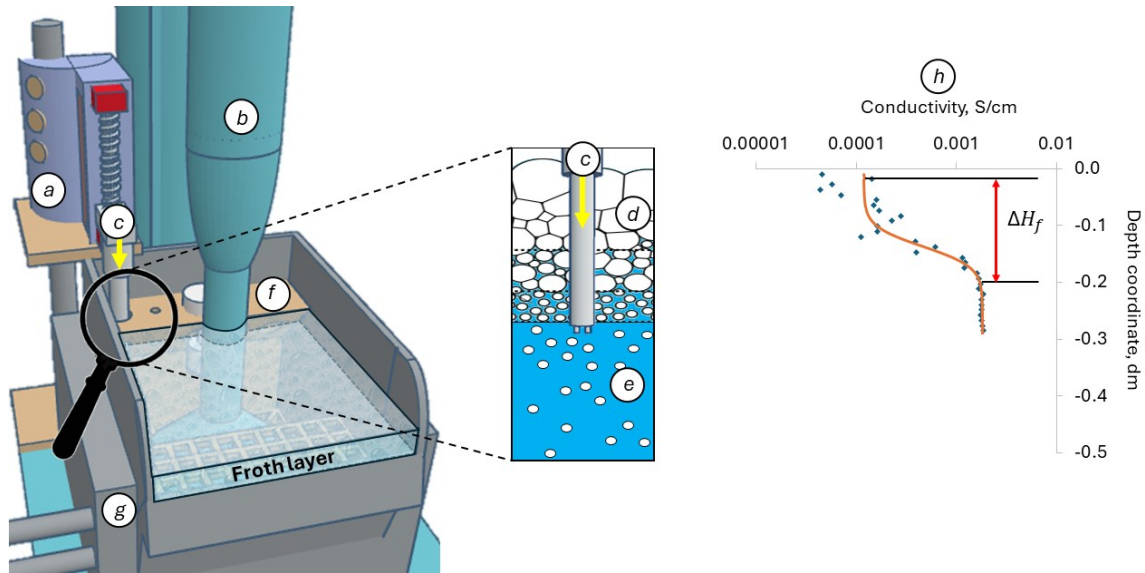


Figure 3-11. Explanation of the working principle of the set-up for absolute froth height measurements at different temperatures: immersion mechanism (screw stepper motor-based) (a), Denver impeller shaft (b), conductivity probe (c), flotation froth (d), flotation pulp zone (e), froth crowder (f), cooling/heating jacket (g), conductivity probe readings (h)

By knowing the vertical speed of the probe immersion, the recordings of conductivity were plotted versus the estimated axial position of the electrode. The froth height was assumed to be equal to a distance until conductivity measurements stabilized and did not demonstrate an increase across the conductivity profile (Figure 3-11).

### 3.5.4. Froth Stability: Stability Factor and Air recovery in SEDEX Ore System

For flotation tests a modified Denver D1 one liter flotation cell was used. On the top of the cell over the lip, an aluminum frame was installed (Figure 3-12). The frame served as a support to the Time of Flight ranging laser (VL53L0X) installed for the calculation of the froth height over the lip. A video camera was installed on the same frame to film the froth velocity and a bubble size distribution. The cell was operated in a self-overflow mode. As soon as the cell stopped overflowing, the laser sent a signal to the microcontroller (Arduino Uno R3) which turned on the relay and connected it to a water pump (a detailed scheme of the set-up is given in Appendix C).

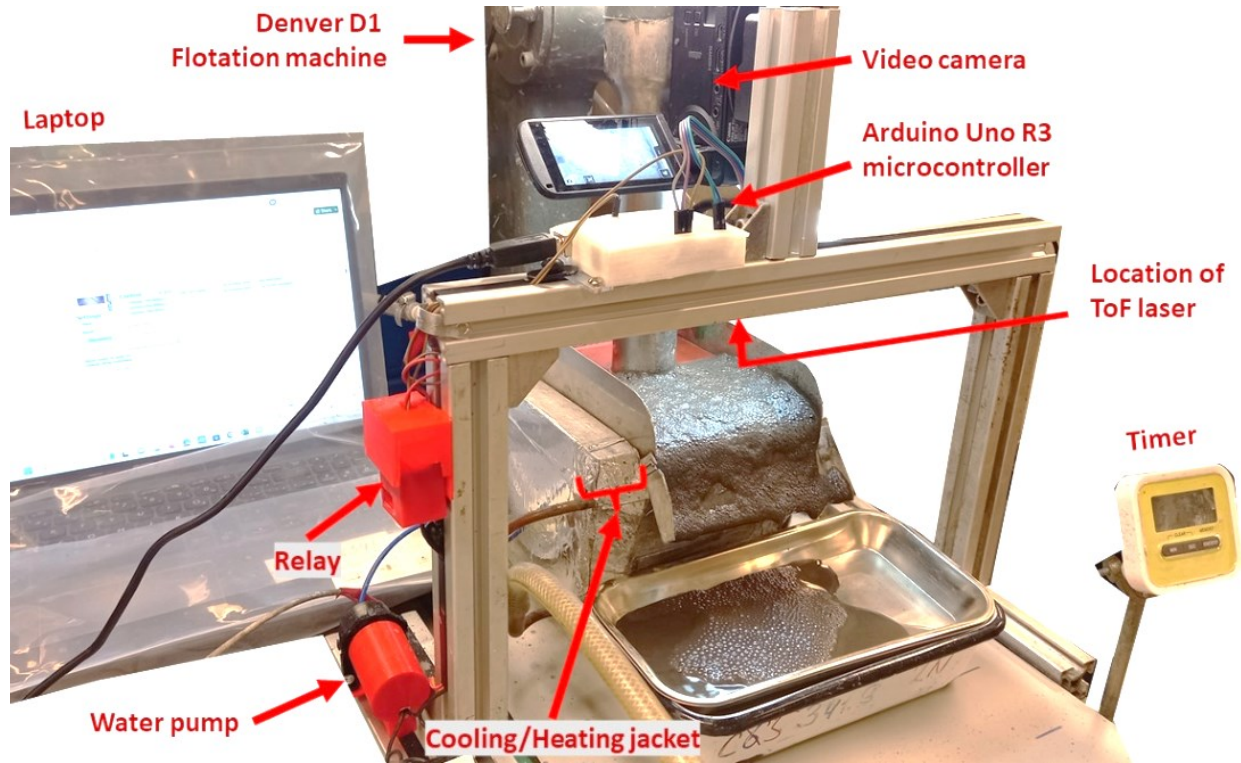


Figure 3-12. Denver flotation setup with installed froth camera and time-of-flight froth laser

Such a system ensured automatic level control in the cell. Froth height over lip, calculated from the laser readings, was used together with froth velocity readings for air recovery calculations, using the formula from Hadler and Cilliers (Hadler and Cilliers, 2009) adjusted to fit the assembled laboratory set-up and testing conditions (by taking into account the volume of water recovered):

$$\alpha = \frac{v_f(d_{l-f} - d_{l-c}) l - \gamma_w}{J_g A} \quad (3-11)$$

where  $v_f$  is the froth velocity towards flotation cell lip in cm/s,  $d_{l-f}$  is the distance from the laser to the froth surface,  $d_{l-c}$  is the distance from the laser to the cell lip (subtraction of these distances should provide froth height over the cell lip),  $l$  is a length of a cell lip in cm,  $J_g$  is a superficial gas velocity in cm/s, and  $A$  is a horizontal cross-sectional area of the cell in cm<sup>2</sup>. Air recovery can also be expressed via bubble bursting flux ( $J_b$ ) (Equation 3-12) using the following expression:

$$\alpha = 1 - \frac{J_b}{J_g} \quad (3-12)$$

where bubble bursting flux ( $J_b$ ) and superficial gas velocity  $J_g$  expressed in cm/s.

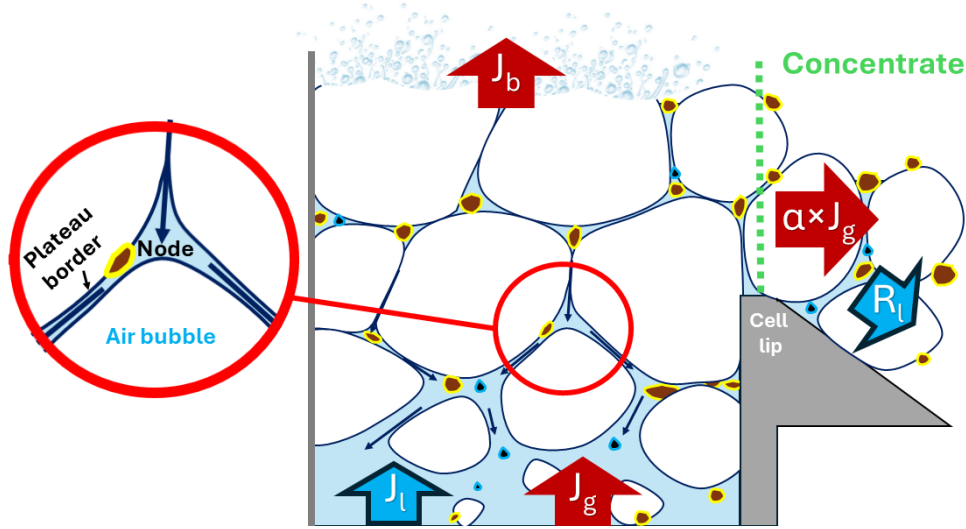


Figure 3-13. Schematic of ingoing and outgoing fluxes in a froth system

The bubble bursting flux, as can be seen from the schematic (Figure 3-13) is a fraction of  $J_g$  lost due to bursting, which is used in the frameworks of indirect measurement approach. However, in this research a simple equation based on direct measurements was derived:

$$J_b = \frac{B_r \cdot \pi \cdot d_{avg}^3 \cdot N_b}{6 \cdot A} \quad (3-13)$$

where  $B_r$  is the bubble bursting rate ( $s^{-1}$ ),  $d_{avg}$  is the average bubble diameter (cm),  $N_b$  is the number of bubbles, and  $A$  is the cross-sectional area of the cell ( $cm^2$ ). By dividing the bubble bursting flux on froth height over the lip the froth stability factor was calculated.

$$F_s = \frac{J_b}{h_{lip}} \quad (3-14)$$

where  $F_s$  is the froth stability factor in seconds, and  $h_{lip}$  is the froth height over the lip (in cm). For the investigated system the physical meaning of calculated stability factor is an indication of the amount of time that would hypothetically take froth to collapse to a level that stops concentrate recovery (overflow), assuming the immediate stop of gas flux ( $J_g$ , Figure 3-13), and an unchanged rate of froth collapse with time.

Bubble size estimations were performed using the Python library OpenCV, particularly SimpleBlobDetector Class. The class extracts blobs from an image using the following algorithm:

1. Conversion of the source image to binary with multiple thresholds from minimum to maximum with a certain step between neighboring thresholds.
2. Extraction of the connected components from binary images, calculation of their centers.
3. Grouping the blob centers from several images by their coordinates.
4. Estimation of the final blob centers from these groups, and corresponding radii of each blob.

The bubble burst rate and horizontal axial froth speed were estimated using the TrackMate FIJI plug-in (Ershov *et al.*, 2022). The algorithm for tracking consists of two main steps, namely: detection and segmentation of individual objects in each frame and linking the detected objects in a timeframe into tracks (Ershov *et al.*, 2022). The detection was based on the Differences of Gaussian (DoG) filter. The linking operator was based on Kalman filtering (linear quadratic estimation algorithm that predicts the next most likely position of an object). The lifetime of tracks contains information on bubble burst rate, while average linear track speed gives information on the froth speed.

### **3.6. Flotation Methodology**

Flotation tests were performed with increasing complexity of a system: starting with monomineralic micro-flotation (indicator of primary concentration potential), then proceeding to monomineralic Denver batch flotation at 10% solids (indicator of combined primary and secondary concentration of a potential cleaner flotation configuration) and ending with ore flotation system (indicator of combined primary and secondary concentration of a potential rougher-scavenger configuration).

#### **3.6.1. Micro-Flotation Set-Up**

As depicted in Figure 3-14, the microflotation tests were conducted in a cell designed for fine particle flotation (Espinosa-Gomez *et al.*, 1987) inspired by Siwek design (Siwek *et al.*, 1981), which was equipped with a cooling/heating jacket. First, the material was conditioned in a double-wall vessel, with dissolved oxygen, pH, and temperature probes. The flotation tests were conducted at 5, 25, and 45 °C with 3 repeats per test setting. The temperature was adjusted using the Fisher Scientific Isotherm<sup>®</sup> Bath Circulator (Fisher Scientific Inc., Pittsburgh, PA, USA). The pH was

adjusted to 9 and 11 using lime. The flotation time was 1 minute. The aeration level was set at 35 ml/min. Sodium isopropyl xanthate (SIPX) was used as a collector at a concentration of 1  $\mu\text{mol/l}$ . Methyl isobutyl carbinol (MIBC) was used as a frother in excess (30 ppm). After conditioning the monomineralic sample in the double-wall glass, the slurry was transported to the modified Hallimond tube for microflotation. The bubbles were generated by a ceramic frit at the bottom of the tube.

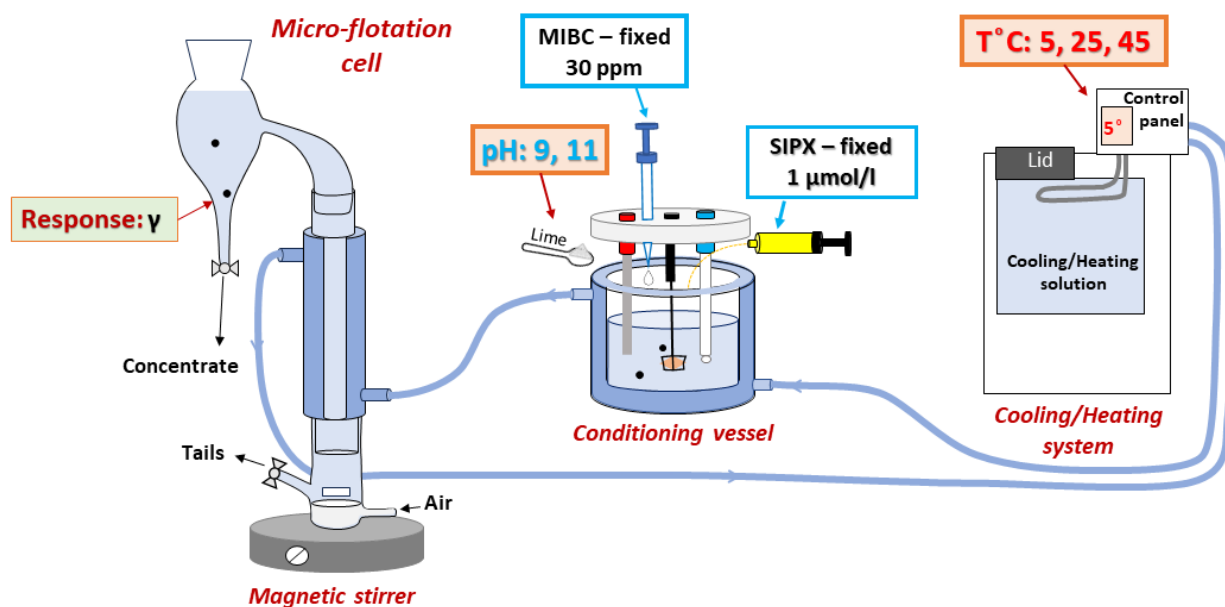


Figure 3-14. Microflotation setup with factors and a response

### 3.6.2. Denver Set-Up for Monomineralic Flotation

For flotation tests, a mechanical Denver D-1 lab flotation machine was used. A 1.3 l metal flotation cell was equipped with a water cooling/heating jacket connected to the Fisher Scientific Isotherm<sup>®</sup> Bath Circulator (Fisher Scientific Inc., Pittsburgh, PA, USA), 3D-printed froth crowder (at the back of the cell with slots for electrodes), water float with water pump (for automatic level control), froth scrapers, and endoscope camera for froth surface filming, see Figure 3-15. The pulp aeration level was set to 4 l/m, corresponding to the superficial gas velocity of approximately 0.5 cm/s. To avoid excessive turbulence in the cell, agitation was set at 800 rpm. Additionally, an under-froth grid and current stabilizers were 3D-printed and installed. The under-froth grid aimed at weakening the turbulent flows in the cell by dissipating their energy and preventing distraction of froth in the upper zone of the flotation cell (reducing mechanical disruptions of a liquid film in the froth zone



to be able to focus on temperature-originated discrepancies) (Chepurnyh *et al.*, 1980). The pulp density used in the tests was set at approximately 10 wt.% (100 g of sample per test with an effective cell volume of 1 l).

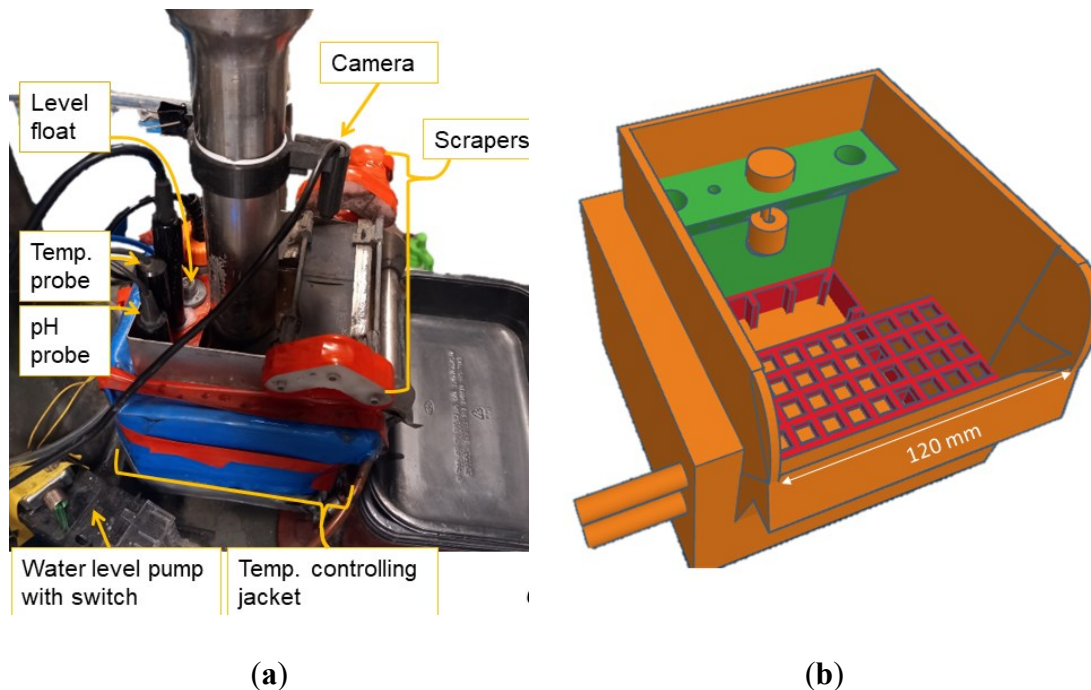


Figure 3-15. Upgraded Denver flotation setup: (a) Denver cell photo with builds on; (b) 3D model of interior current pacifiers, under-froth grid, level float, and froth crowder at the back.

Flotation tests were performed according to the general full factorial design with two repeats for each test. Since the most common Pb-Zn selective flotation method (Sheridan–Griswold method) sequentially recovers lead and zinc at alkali conditions (Glembotskij and Klassen, 1981), the monomineralic flotation tests for galena, sphalerite, and pyrite were performed at pH 9 and 11, which are commonly used pH levels in the industry (Bulatovic, 2007). Lime was used to adjust the pH, sodium isopropyl xanthate (SIPX) was used as the collector at a dosage of 90 g/t, while methyl isobutyl carbinol (MIBC) served as the frother at a concentration of 30 ppm (which is above the critical coalescence concentration (Nassif, 2013; Nasset *et al.*, 2002)). The tested temperatures were 10, 20, 30, and 40 °C. The detailed monomineralic flotation workflow is shown in Figure 3-16.

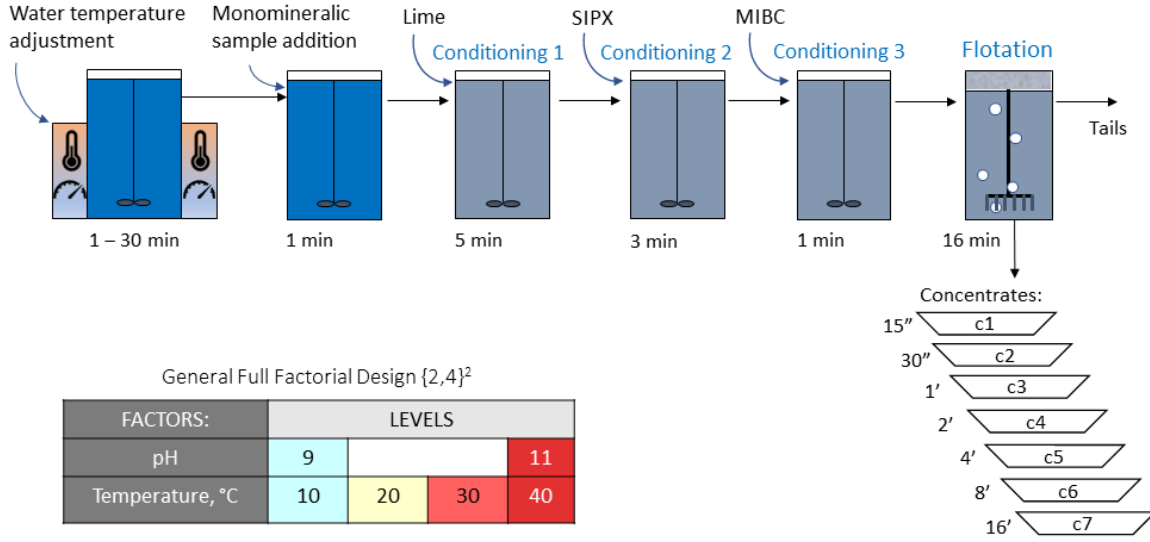


Figure 3-16. Monomineralic flotation workflow.

Kinetic flotation tests were performed by collecting seven concentrates and fitting the flotation recovery to the gamma distribution model (Equations 3-15 and 3-16) using the least squares approach (Equation 3-17) (Rubinstein and Filippov, 1980; Vinnett *et al.*, 2022):

$$\varphi(K) = \frac{e^{-K\lambda} \cdot K^{p-1} \cdot \lambda^p}{\Gamma(p)} \quad (3-15)$$

$$\hat{R}(t) = R_{\infty} \left( 1 - \left( \frac{\lambda}{\lambda + t} \right)^p \right) \quad (3-16)$$

$$\min \sum_{i=1}^n \left( \hat{R}(t_i) - R(t_i) \right)^2 \quad (3-17)$$

where  $p$  is the shape factor,  $\lambda$  is the scale factor,  $\varphi(K)$  is the probability density function of flotation rate constant distribution,  $K$  is flotation rate constant,  $\Gamma(p)$  is Euler's gamma function,  $\hat{R}(t)$  is modeled recovery at time  $t$ ,  $R(t)$  is experimental recovery value at time  $t$ , and  $R_{\infty}$  is ultimate recovery.



### 3.6.3. Denver Set-Up for Lead-Zinc Ore Flotation

The flotation was performed according to the central composite design of the experiment with 5 levels and 3 factors. The investigated parameters were temperature, copper sulfate dosage, and zinc vitriol dosage. The factors and levels investigated are illustrated in Figure 3-17.

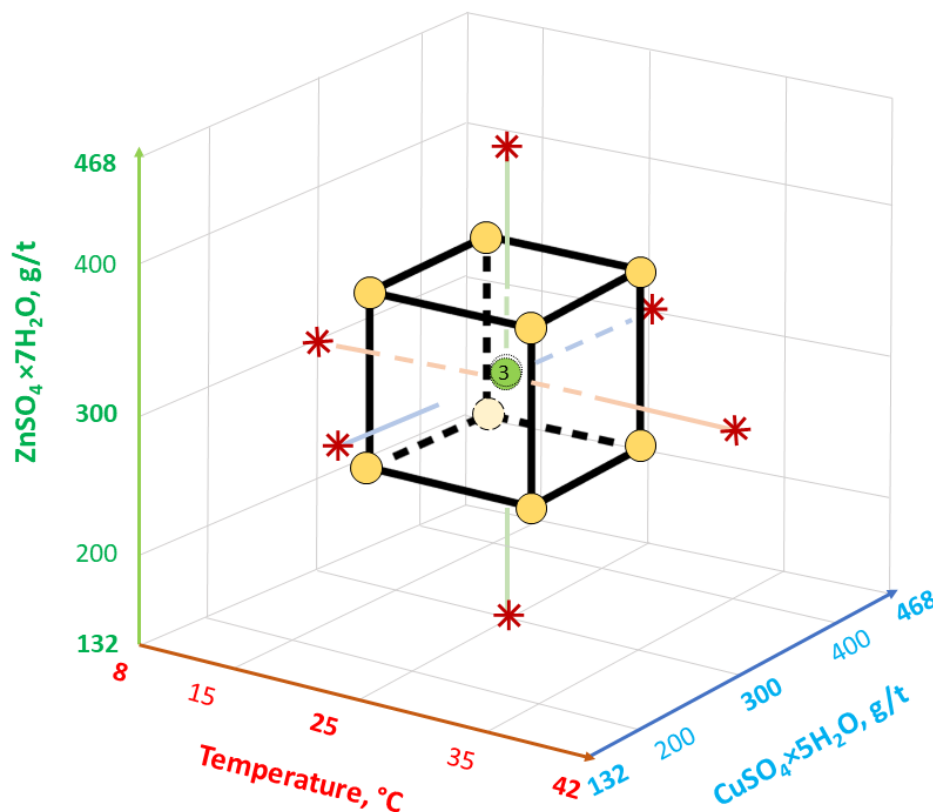


Figure 3-17. Central composite design with 5 levels and 3 factors

The flotation procedure started with the adjustment of the temperature of a flotation cell by passing preheated/precooled ethylene glycol solution through the external contour of a metal flotation cell with the Isotherm Bath Circulator. After temperature adjustment, the pH of the pulp was increased to 9 by dosing with lime. Following the pH modification, the pulp was conditioned with a depressant (varying dosages of zinc sulfate), 20 g/t SIPX collector, and 10 g/t MIBC frother. After 12 minutes of conditioning, the material was floated for 8 minutes (lead rougher flotation). Sequentially, after lead flotation, zinc was recovered in a similar manner. First, the pH was increased by adding lime until 11. Then sphalerite was activated with copper sulfate, followed by

the addition of 20 g/t SIPX and 10 g/t MIBC. Conditioning steps 5 to 8 were also followed by 8 min flotation (zinc circuit) (Figure 3-18).

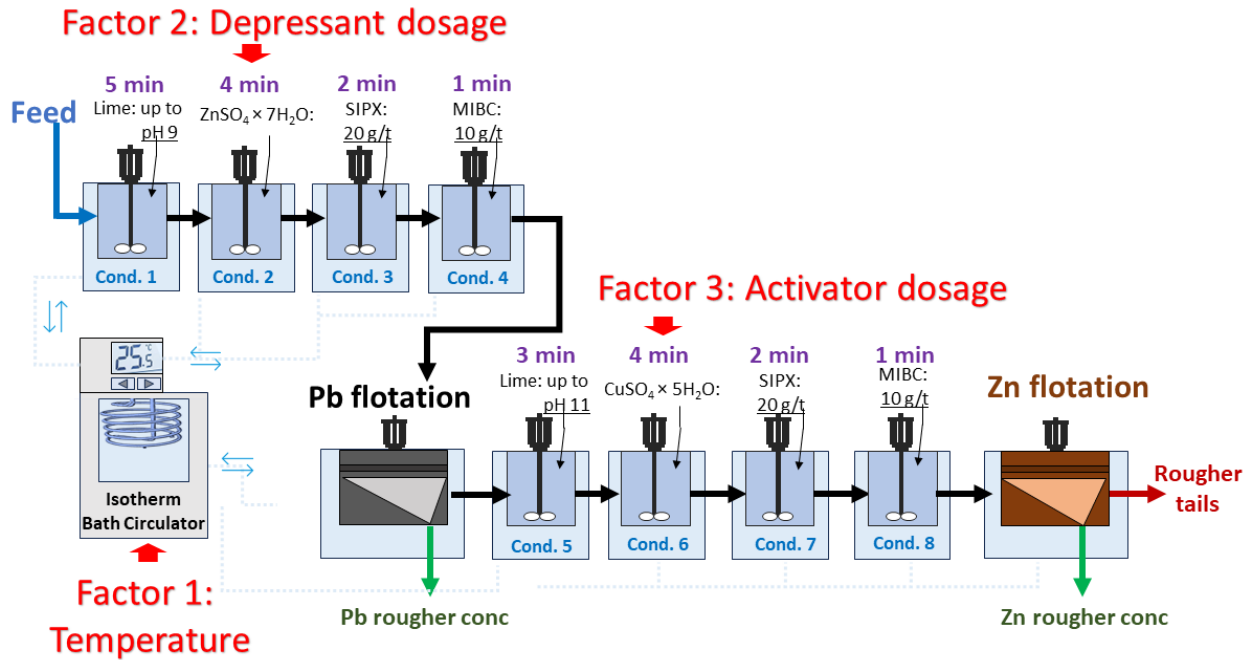


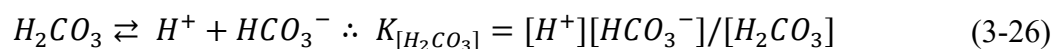
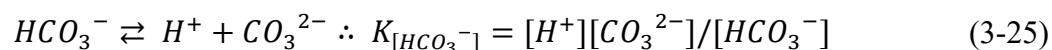
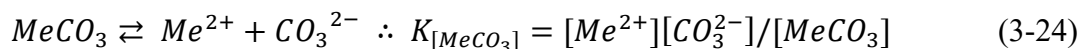
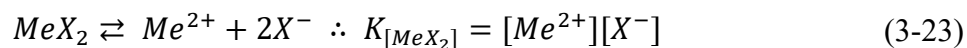
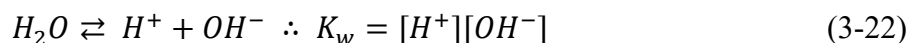
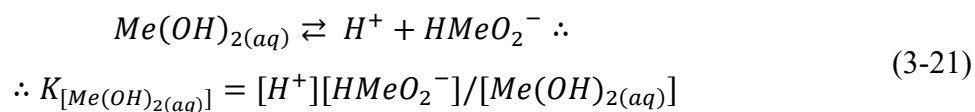
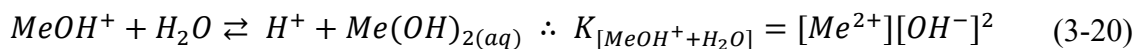
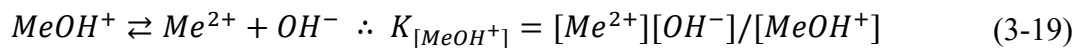
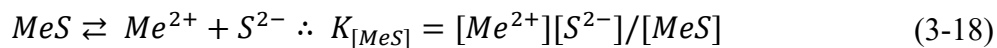
Figure 3-18. Flowsheet of laboratory trials with investigated factors

### 3.7. Methodology of Numerical Simulations and Data Processing

#### 3.7.1. Primary Concentration: Thermodynamic Calculations

In the second half of the 20<sup>th</sup> century, it was suggested that a sulfide flotation system may be described in terms of solution chemistry, particularly solubility data of metal xanthates (du Rietz, 1957, 1976; Kakovsky and Arashkevich, 1968). Xanthates forming metal precipitates with lower solubilities are expected to more rapidly adsorb on the metal sites of a sulfide mineral (Taggart *et al.*, 1930). In a metal-xanthate system, a range of other chemical reactions take place involving ion hydrolysis, hydroxide precipitation, formation of soluble metal xanthate complexes and carbonates (Zhang *et al.*, 2018). Through the lens of this chemical theory, the flotation process is driven by the fact that the oxidation/hydrolysis products at a mineral surface are more soluble than the product of collector-mineral surface interaction (Fuerstenau *et al.*, 1990).

For systems with divalent metal cations, the following reactions should be considered:



Additionally, in an open system, carbon dioxide dissolves in water. Thus, the total concentration of carbon-containing species at room temperature (25 °C) is as follows:

$$C = [H_2CO_3] + [HCO_3^-] + [CO_3^{2-}] = 1 \times 10^{-5} mol/l \quad (3-27)$$

As can be seen from Equations (3-18) – (3-21) and Equation 3-24, under conditions of mineral surface oxidation, first, the concentration of  $Me^{2+}$  ions will increase in the solution until it will be sufficient for the formation of metal compounds with  $CO_3^{2-}$  and  $OH^-$ . Then, the metal ion concentration will be determined by the solubility of formed metal-carbonates or metal-hydroxy carbonates. Therefore, assuming an equilibrium between metal oxidation/hydrolysis products and metal xanthate complexes, it is possible to estimate the concentration of xanthate ions required for the formation of metal-xanthate species. Considering  $MeCO_3 \rightleftharpoons MeX_2$  equilibrium and the dissolved carbon dioxide from the atmosphere, which impacts the pH of the equilibrium, the balancing equation of the system is expressed as follows:

$$[H_2CO_3] + [HCO_3^-] + [CO_3^{2-}] = \\ = C + [Me^{2+}] + [MeOH^+] + [Me(OH)_{2(aq)}] + [HMeO_2^-] \quad (3-28)$$

According to Abramov (Abramov, 2010), by re-expressing Equation 3-28 in terms of equilibrium constants (Equations (3-18) – (3-26)), the final balancing equation is obtained (Equation 3-29):

$$\begin{aligned}
 & K_{[MeOH^+]} \cdot K_{[MeCO_3]} \cdot [H^+]^3 \cdot [X^-]^4 ([H^+]^2 + K_{[H_2CO_3]} \cdot [H^+] + K_{[HCO_3^-]} \cdot K_{[H_2CO_3]}) = \\
 & = K_c \cdot K_{[MeOH^+]} \cdot K_{[MeX_2]} \cdot K_{[HCO_3^-]} \cdot K_{[H_2CO_3]} \cdot [H^+]^3 \cdot [X^-]^2 + K_{[MeX_2]}^2 \cdot K_{[HCO_3^-]} \\
 & \quad \cdot K_{[H_2CO_3]} \cdot (K_{[MeOH^+]} \cdot [H^+]^3 + K_w \cdot [H^+]^2 + K_w \cdot K_{[MeOH^++H_2O]} \cdot \\
 & \quad \cdot [H^+] + K_{[MeOH^++H_2O]} \cdot K_{[Me(OH)_2(aq)]} \cdot K_w)
 \end{aligned} \tag{3-29}$$

Then, by solving Equation 3-29 for  $[X^-]$  the minimum xanthate concentration required for the formation of a metal-xanthate complex on the mineral surface can be determined (a detailed numerical example of thermodynamic derivations is given in Appendix J). For galena (Pb), sphalerite (Zn) and pyrite (Fe) systems, the values of equilibrium (solubility) constants at standard conditions were found in the literature (Table 3-4). For pyrite and sphalerite systems, the xanthate dosage was assumed to be defined by  $MeOH^+$  ions in the Helmholtz layer, produced during oxidation (Abramov, 1977), with respective equilibrium constants used for the calculations.

Table 3-4. Solubility constants of reactions used for thermodynamic calculations

Reaction	$K_{T\ominus}$			Reference
	Pb	Zn	Fe	
$MeOH^+ \rightleftharpoons Me^{2+} + OH^-$	$1.5 \cdot 10^{-8}$	$1.0 \cdot 10^{-9}$	$4.5 \cdot 10^{-6}$	(Abramov, 2010; Leussing and Kolthoff, 1953; Powell <i>et al.</i> , 2013)
$MeCO_3 \rightleftharpoons Me^{2+} + CO_3^{2-}$	$1.5 \cdot 10^{-13}$	$1.5 \cdot 10^{-10}$	$2.1 \cdot 10^{-11}$	(Abramov, 2010; CHEMINFO, 2007; Flowers <i>et al.</i> , 2019)
$Me(OH)_{2(aq)} \rightleftharpoons H^+ + HMeO_2^-$	$1.2 \cdot 10^{-11}$	$2.1 \cdot 10^{-17}$	$5.0 \cdot 10^{-19}$	(Abramov, 2010; Hem and

Reaction	$K_{T\ominus}$			Reference
	Pb	Zn	Fe	
				Cropper, 1959; Talbot and Talbot, 1998)
$MeOH^+ + nH_2O \rightleftharpoons$ $\rightleftharpoons H^+ + Me(OH)_{n+1(aq)}$	$1.3 \cdot 10^{-11}$	$3.0 \cdot 10^{-17}$	$6.0 \cdot 10^{-10}$	(Abramov, 1977, 2010; CHEMINFO, 2007)
$MeX_2 \rightleftharpoons Me^{2+} + 2X^-$ (iPX)	$1.6 \cdot 10^{-18}$	$8.1 \cdot 10^{-14}$	$1.0 \cdot 10^{-11*}$	(Abramov, 1977; Kakovsky and Arashkevich, 1968; Pålsson and Forssberg, 1989) *-estimated
$H_2O \rightleftharpoons H^+ + OH^-$	$1.0 \cdot 10^{-14}$			(Abramov, 2010; CHEMINFO, 2007)
$CaCO_3 \rightleftharpoons Ca^{2+} + CO_3^{2-}$	$3.4 \cdot 10^{-9}$			
$Ca(OH)_{2(s)} \rightleftharpoons Ca^{2+} + 2OH^-$	$5.0 \cdot 10^{-6}$			(Abramov, 2010)
$H_2CO_3 \rightleftharpoons H^+ + HCO_3^-$	$4.2 \cdot 10^{-7}$			
$HCO_3^- \rightleftharpoons H^+ + CO_3^{2-}$	$4.8 \cdot 10^{-11}$			

Estimations of unknown  $K_{T\ominus}$  values for xanthate complexes of different chain length were conducted using the following relationship:

$$\log K_{T\ominus} = a - bm \quad (3-30)$$

where  $m$  is the number of  $CH_2$  groups,  $a$  and  $b$  are xanthate complex-specific coefficients (Kakovskii, 1956). Additionally, assuming the sphalerite surface being activated by copper ions,

xanthate demand was also estimated using the following equation, developed for copper sulfide flotation:

$$\log [X^-] = -5 + \log[CuOH^+][X^-] - \log K_w + \frac{1}{4}\log[O_2] + pH \quad (3-31)$$

where  $[CuOH^+][X^-]$  for isopropyl xanthate at standard conditions was estimated based on the data from literature ( $1 \cdot 10^{-25}$ ) (Abramov, 1977),  $[O_2]$  is experimentally found oxygen concentration in the pulp.

Since the considered ion system is reversible, in an endothermic environment an increase in entropy will be defined by the amount of energy absorbed by a substance from its surroundings divided by temperature (Garrels and Christ, 1990):

$$dS = \frac{\delta q}{T} \quad (3-32)$$

Using the definition of the heat capacity from Equation 3-33 a new expression of entropy (Equation 3-34) can be derived for constant pressure (Garrels and Christ, 1990):

$$C_P = \left( \frac{\delta q}{\partial T} \right)_P \quad (3-33)$$

$$dS = \left( \frac{C_P dT}{T} \right)_P \quad (3-34)$$

By partially integrating Equation 3-34, an expression of entropy change with temperature is obtained (Garrels and Christ, 1990):

$$S_T - S_{T_\ominus} = \int_{T_\ominus}^T \frac{C_P}{T} dT \quad (3-35)$$

Considering that in a reversible process at a constant pressure  $\delta q = dH$  (Tane, 2012), the change of enthalpy with respect to temperature will take the following form (Garrels and Christ, 1990):

$$\Delta H_T - \Delta H_{T_\ominus} = \int_{T_\ominus}^T \Delta C_P dT \quad (3-36)$$

by combining Equations 3-35 and 3-36, and by using the definition of Gibbs free energy for constant temperature and pressure conditions the following equations can be deduced (Puigdomènech *et al.*, 1999):

$$\Delta G_T = \Delta H_{T_\ominus} + \int_{T_\ominus}^T \Delta C_P dT - T \left( \Delta S_{T_\ominus} + \int_{T_\ominus}^T \frac{\Delta C_P}{T} dT \right) \quad (3-37)$$

$$\Delta G_T = \Delta G_{T_\ominus} - (T - T_\ominus) \Delta S_{T_\ominus} + \Delta C_P \left( T - T_\ominus - T \cdot \ln \left( \frac{T}{T_\ominus} \right) \right) \quad (3-38)$$

Since the third term of the equation with heat capacity multiplier is an order of magnitude lower than the second term of the equation with entropy multiplier, Equation 3-38 may be further simplified (Puigdomènech *et al.*, 1999):

$$\Delta G_T = \Delta G_{T_\ominus} - (T - T_\ominus) \Delta S_{T_\ominus} \quad (3-39)$$

By combining Equation 2-20 and 3-39 into Equation 3-40, temperature corrections of solubility constants were conducted for further thermodynamic calculations:

$$K_T = \exp \left( \frac{RT_\ominus \ln K_{T_\ominus} + (T - T_\ominus) \Delta S_{T_\ominus}}{RT} \right) \quad (3-40)$$

The changes in the entropies for Equation 3-40 were calculated using the data from Table 3-5. The  $K_{T_\ominus}$  were taken from Table 3-4.

Table 3-5. Entropy values for ionic species used in thermodynamic calculations

General formula	Entropy, $J/(mol \cdot K)$			Reference
	Pb	Zn	Fe	
$MeOH^+$	111.8	-23.6	-29.0	(CHEMINFO, 2007; Iorish and Jungman, 2003; Ziemniak <i>et al.</i> , 2004)
$Me(OH)_{2(aq)}$	-8.7	-132.3	-152.6	(Iorish and Jungman, 2003)

General formula	Entropy, $J/(mol \cdot K)$			Reference
	Pb	Zn	Fe	
$MeCO_3$	131.0	82.4	95.4	(CHEMINFO, 2007; Iorish and Jungman, 2003)
$HMeO_2^-$	67.1	62.8	62.7	(Amend and Shock, 2001; Jiao <i>et al.</i> , 2022; Townsend, 1970)
$Me^{2+}$	10.5	-112.1	-137.7	(CHEMINFO, 2007)
$H_2CO_3$	189.6			(Iorish and Jungman, 2003)
$OH^-$	-10.8			(CHEMINFO, 2007)
$CO_3^{2-}$	-56.9			
$HCO_3^-$	91.2			
$H_2O$	70.0			
$CaCO_3$	91.7			
$Ca(OH)_2 (s)$	83.4			
$Ca^{2+}$	-53.1			

Since no information on the entropy data for isopropyl xanthate-metal complexes was found in the literature, these values were estimated using an approach applied by Rao for lead-ethyl xanthate system (Rao, 1970) as well as the results of isopropyl xanthate molecule simulation in an open-source molecular builder and visualization tool Avogadro (Version 1.2.0) (Appendix E) (Hanwell *et al.*, 2012).

From Avogadro simulations (Appendix E), the coordinates of each atom of the metal-xanthate complex were extracted and used for entropy calculations. The total entropy of the adsorbed molecule/complex was assumed to be composed of three main components (Garza, 2019):

$$S_{AD} = S_v + S_{tr} + S_r \quad (3-41)$$

where  $S_{AD}$  is a total entropy of adsorbed species,  $S_v$  is vibrational entropy,  $S_{tr}$  is translational entropy, and  $S_r$  is rotational entropy (all in  $J/(K \cdot mol)$ ). Since vibrational entropy was found to have



a negligible effect on the total entropy for xanthate-metal systems (Rao, 1970), only the contributions from the translational and rotational entropies were calculated using the following equations:

$$S_{tr \vee r} = R \left( \ln Q + T \left( \frac{\partial \ln Q}{\partial T} \right) \right) \quad (3-42)$$

$$Q_{tr} = \left( \frac{2\pi mRT}{h^2} \right) \cdot (x \cdot y) \quad (3-43)$$

$$Q_r = \frac{8\pi^2 IRT}{h^2} \quad (3-44)$$

where  $Q$  is a partition function ( $Q_{tr}$  is a translational function,  $Q_r$  is a rotational function),  $m$  is mass of xanthate ion (kg),  $h$  is Planck's constant ( $6.626 \cdot 10^{-34}$  J·s),  $I$  is a moment of inertia of adsorbed xanthate ions around any principal axis ( $\text{kg}\cdot\text{m}^2$ ),  $(x \cdot y)$  is xanthate ion area ( $\text{m}^2$ ). The moments of inertia were calculated using atomic coordinates (Appendix D) and the following equations:

$$I_\varphi = A_r(\bar{\varphi} - \varphi)^2 \cdot 1 \text{ amu} \quad (3-45)$$

$$\bar{\varphi} = \frac{\sum_{i=1}^n A_{r_i} \cdot \varphi_i}{M_r} \quad (3-46)$$

where  $\varphi$  is a principal axis (X, Y, or Z) coordinate,  $A_r$  is the atomic mass of an element in the molecule,  $M_r$  is a molecular mass,  $1 \text{ amu}$  equals  $1.66 \times 10^{-24}$ .

In order to get the entropy of the formation of adsorbed xanthate species, the total entropy of species constituting the Me-xanthate compound (Equation 3-47) was calculated using an additive Latimer method (Latimer, 1921, 1951). This value was subsequently subtracted from the entropy of the adsorbed complex, calculated from Equation 3-48:

$$\begin{aligned} S_{\ominus}^{\circ}(\text{Me} - \text{SSCOC}_3\text{H}_7) &= S_{\ominus}^{\circ}(\text{Me}) + 4 \cdot S_{\ominus}^{\circ}(\text{C}) + 3.5 \cdot S_{\ominus}^{\circ}(\text{H}_2) + \\ &+ 0.5 \cdot S_{\ominus}^{\circ}(\text{O}_2) + 2 \cdot S_{\ominus}^{\circ}(\text{S}) \end{aligned} \quad (3-47)$$

$$\Delta S_{T_{\ominus}} = S_{AD} - S_{\ominus}^{\circ} \quad (3-48)$$

Water equilibrium constant values were also adjusted using the following empirical equation, linking temperature and pressure to  $K_w$  (Verma, 2003):

$$\log(K_w) = -10.026 + \frac{559.958}{T} - 0.01 \cdot P - \frac{518914.5}{T^2} + 0.177 \cdot \frac{P}{T} + 10^{-5} \cdot P \quad (3-49)$$

In addition to the water equilibrium constant, temperature would also impact the value of dissolved carbon dioxide, and hence, the “C-value” in Equation 3-28. According to Henry’s law, gas solubility in water is described using the following equation (Henry and Banks, 1803; Sander, 1999):

$$C^{\ominus} = k_H^{\ominus} \cdot p_g \quad (3-50)$$

where  $C^{\ominus}$  is a concentration of a component in an aqueous phase at standard conditions,  $k_H^{\ominus}$  is Henry’s constant at standard conditions,  $p_g$  is a partial pressure of a component in a gas phase above the aqueous phase. Henry’s constant is a temperature-dependent parameter, and was calculated for different temperature scenarios using the van’t Hoff equation (Sander, 1999):

$$k_H^T = k_H^{\ominus} \cdot \exp\left(\frac{-\Delta_{sol}H}{R} \cdot \left(\frac{1}{T} - \frac{1}{T_{\ominus}}\right)\right) \quad (3-51)$$

where  $k_H^T$  is Henry’s constant at a temperature of interest,  $k_H^{\ominus}$  is Henry’s constant at standard conditions,  $\Delta_{sol}H$  is solution enthalpy, and  $T_{\ominus}$  is standard conditions temperature (298.15 K).  $-\Delta_{sol}H/R$  multiplier was reported to have a value of 2,400 for the carbon dioxide system (Sander, 1999).

### 3.7.2. Secondary Concentration: Froth Drainage Simulation

For froth drainage numerical simulations at different temperatures the following formula was used (Nguyen *et al.*, 2003):

$$V_t = -\frac{\rho \cdot g \cdot A}{150\mu} \quad (3-52)$$

where  $V_t$  is theoretical froth drainage,  $\rho$  is continuous phase density (kg/m<sup>3</sup>),  $g$  is gravity acceleration (9.8 m/s<sup>2</sup>),  $A$  is froth plateau border cross-section (m<sup>2</sup>),  $\mu$  is continuous phase viscosity (Pa·s). The cross-sectional area was calculated using the following expressions linking it to bubble

radius ( $r_b$ ) and foam/froth liquid fraction ( $\varepsilon$ ) (Stevenson and Stevanov, 2004; Weaire and Hutzler, 1999):

$$A = \left( \sqrt{3} - \frac{\pi}{2} \right) r^2 \quad (3-53)$$

$$r = r_b (1.28 \varepsilon^{0.46}) \quad (3-54)$$

where  $r$  is the Plateau border radius (m). For different temperature scenarios experimental data for bubble radius and liquid fraction were used for calculations. Temperature corrections for viscosity were conducted using the following equation (Çengel and Cimbala, 2006):

$$\mu(T) = a \cdot 10^{\frac{b}{T-c}} \quad (3-55)$$

where  $a$ ,  $b$ ,  $c$  are liquid-specific constants (for water:  $a = 2.414 \cdot 10^{-5}$  Pa·s,  $b = 247.8$  K,  $c = 140$  K). After calculating the viscosity of water at different temperatures these values were adjusted for solids content using the Batchelor-Green equation (Batchelor and Green, 1972):

$$\mu(\varphi) = \mu(T) + 2.5\varphi + 7.6\varphi^2 \quad (3-56)$$

where  $\varphi$  is the volumetric fraction of solids. For the continuous phase density, the calculated solids density for the SEDEX ore (used in froth stability tests) was 3,626 kg/m<sup>3</sup> (at 32 wt. % solids) while for monomineralic samples the used values were 7,600 kg/m<sup>3</sup> for galena, 4,100 kg/m<sup>3</sup> for sphalerite, and 5,000 kg/m<sup>3</sup> for pyrite (Carmichael, 2018) (at 10 wt.% solids in the pulp). The density correction for temperature can be expressed using the following equation (Young *et al.*, 2019):

$$\rho_T = \rho_0 (1 - \gamma \Delta T) \quad (3-57)$$

where  $\rho_T$  is the density of the substance at temperature  $T$ ,  $\rho_0$  is the initial substance density, and  $\gamma$  is the thermal expansion coefficient. Since the thermal expansion coefficient is one to two orders of magnitude lower for solids compared to liquids (Urone and Hinrichs, 2022), and by considering relatively low-temperature change in flotation systems, changes in solids density were ignored for pulp density change calculations. For the changes in the density of the liquid component of the pulp density, the following empirical expression was used (Jones and Harris, 1992):

$$\begin{aligned} \rho_w(T) = & 999.853 + 6.327 \cdot 10^{-2}T - 8.524 \cdot 10^{-3}T^2 + \\ & + 6.943 \cdot 10^{-5}T^3 - 3.82110^{-7}T^4 \end{aligned} \quad (3-58)$$

where  $T$  is a temperature in °C. For calculations of the drainage change with frother type, a model developed for a mean drainage velocity of a single Plateau border was used (Nguyen, 2002):

$$V_t^P = \frac{A}{\mu} \cdot \frac{dp}{dz} \cdot \left( \frac{a \cdot \sqrt{Bo}}{c + Bo^m} + 0.02 \right) \quad (3-59)$$

$$Bo = \frac{\mu_s}{\mu \cdot r} \quad (3-60)$$

where  $dp/dz$  is a pressure gradient in the Plateau border in the axial direction,  $Bo$  is the Boussinesq number,  $\mu_s$  is a surface shear viscosity. The coefficients  $a$ ,  $c$ ,  $m$  are equal to 0.0655, 0.209, and 0.628 respectively (Nguyen, 2002). Considering that the height of the froth in the tests with mechanical flotation cells was relatively small, the calculations were additionally simplified by neglecting the pressure gradient term. For calculations of drainage with different frothers the surface shear viscosities for MIBC, polypropylene glycols, propylene glycol ethers, and sodium dodecyl sulfate were used (Table 3-6) (Harvey *et al.*, 2005; Nguyen *et al.*, 2024; Stevenson, 2005; Tan *et al.*, 2009).

Table 3-6 Surface shear viscosity of solutions with different surfactants

Frother	Surface shear viscosity, $\mu_s$ (Pa·s)	Reference
Methyl isobutyl carbinol (MIBC)	$5.0 \times 10^{-7}$ to $6.0 \times 10^{-7}$	(Nguyen <i>et al.</i> , 2024)
Polypropylene glycols: (PPG425 and PPG725)	$2.0 \times 10^{-5}$ to $5.0 \times 10^{-5}$	(Tan <i>et al.</i> , 2009)
Propylene glycol ethers: (Dowfroth 250 and Dowfroth 400)	$2.5 \times 10^{-5}$ to $5.5 \times 10^{-5}$	(Harvey <i>et al.</i> , 2005)
Sodium dodecyl sulphate (SDS)	$2.0 \times 10^{-8}$ $3.6 \times 10^{-8}$ $2.5 \times 10^{-8}$	(Pitois <i>et al.</i> , 2005) (Koehler <i>et al.</i> , 2002) (Mysels, 1959)

For the calculations of froth drainage Monte-Carlo simulations were run 1,000 times per each temperature setting per each frother type.

### 3.7.3. Analysis of Correlations between Flotation Responses and Foam Stability

To investigate the covariances between foam stability parameters, flotation responses, temperature, and pH, principal component analysis (PCA) was used as a data transformation tool, allowing data dimensionality to be reduced and allowing for the visualization of intercorrelations in the data. This data transformation permits one to describe the same amount of variability contained in the original variables but with fewer uncorrelated dimensions (principal components) (Daultrey, 1976). The covariance matrix was constructed by calculating covariance for each pair of variable/response vectors, as per Equation 3-61:

$$cov_{\vec{X},\vec{Y}} = \frac{1}{N} \sum_{i=1}^n (X_i - \mu_X) \cdot (Y_i - \mu_Y) \quad (3-61)$$

where  $\vec{X}$  and  $\vec{Y}$  is a pair of variable/response vectors compared,  $N$  is a number of points,  $\mu_X$  and  $\mu_Y$  are the mean values, and  $X_i$  and  $Y_i$  are individual points in the respective vectors. For the next step, to perform the transformation of the covariance matrix  $\mathbf{A}$  that contains covariations of the initial variables and responses, eigenvalues describing variance of principal components were found by solving Equation 3-62:

$$\det(\mathbf{A} - \lambda_i \mathbf{I}) = 0 \quad (3-62)$$

where  $\lambda_i$  are eigenvalues (scalar) and  $\mathbf{I}$  is the identity matrix. As the third step, corresponding eigenvectors to each  $\lambda_i$  were found by solving Equation 3-63:

$$\mathbf{A} \cdot \vec{v}_i = \lambda_i \vec{v}_i \quad (3-63)$$

where  $\vec{v}_i$  are eigenvectors. After normalizing eigenvectors by dividing each component by a vector length, a matrix of eigenvectors ( $\mathbf{V}$ ) was used to calculate a matrix of scores, as shown in Equation 3-64:

$$\mathbf{Z} = \mathbf{M} \cdot \mathbf{V} \quad (3-64)$$

where  $\mathbf{Z}$  is a matrix with scores and  $\mathbf{M}$  is a matrix with standardized original data (Daultrey, 1976; Hadavand-Siri and Deutsch, 2012).

### 3.7.4. Analysis of Plant Data

For the primary investigation of possible linear dependencies between fluctuations in plant metallurgical performance and potential triggers (meteorological and operational parameters) Pearson's correlation coefficient was calculated (Pearson, 1920):

$$r_{pearson} = \frac{\sum_{i=1}^n (x_i - \bar{x})(y_i - \bar{y})}{\sqrt{\sum_{i=1}^n (x_i - \bar{x})^2 \sum_{i=1}^n (y_i - \bar{y})^2}} \quad (3-65)$$

where  $x_i$  and  $y_i$  are  $i^{th}$  observations from compared arrays  $X$  and  $Y$ ,  $\bar{x}$  and  $\bar{y}$  are average values of the arrays  $X$  and  $Y$ . For the exploration of both, linear and non-linear dependencies in the datasets maximum information coefficient has been used. The maximum information coefficient is defined as normalized mutual information (Kinney and Atwal, 2014). Mutual information (MI) is a metric that aims at quantifying how much can be understood from one variable about another (de Siqueira Santos *et al.*, 2013). Mutual information is computed using the following equation:

$$MI(X, Y) = \iint f_{X,Y}(x, y) \log_2 \left( \frac{f_{X,Y}(x, y)}{f_X(x) f_Y(y)} \right) \quad (3-66)$$

---

## Chapter 4. Temperature Effect on Primary Concentration: Surface Chemistry of Galena, Sphalerite, and Pyrite

### 4.1. Introduction

Adsorption of flotation reagents is a crucial step for achieving selective flotation performance (Bulatovic, 2007). Conditioning provides time and a special environment for the reagents to attach to mineral surfaces before froth flotation (Henwood, 1994). Hydrophobization of the surfaces is achieved using collector reagents, while regulators control activation, depression, and pH among other sub-processes (Wills and Finch, 2016). Gibbs free energy changes ( $\Delta G$  in J/mol) and equilibrium conditions are the key parameters for a comprehensive understanding of flotation, related to each other through Equation 4-1:

$$\Delta G = -RT \ln K \quad (4-1)$$

where  $\Delta G$  is Gibbs free energy (J/mol),  $R$  is the gas constant (8.314 J/(mol·K)),  $T$  is the absolute temperature (K), and  $K$  is the equilibrium constant of the reaction. The adsorption reaction may be characterized by adsorption density. Collector adsorption reduces a mineral's surface energy, rendering it hydrophobic. The hydrophobic film bridges the solid surface and gas bubbles, enabling flotation (Pattanaik and Venugopal, 2019). In a simplified form, the thermodynamic possibility of the formation of this bridge could be expressed through Dupre's Equation 4-2:

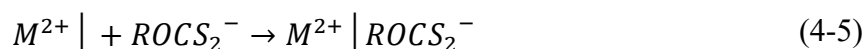
$$\Delta G = \gamma_{SG} - \gamma_{LG} - \gamma_{SL} < 0 \quad (4-2)$$

where  $\Delta G$  is the change in free energy after bubble attachment,  $\gamma_{SG}$ ,  $\gamma_{LG}$ , and  $\gamma_{SL}$  are surface tensions at the solid-gas, liquid-gas, and solid-liquid interfaces. Considering the thin liquid layer between the bubble and solid surface, Equation 4-2 may be rewritten using Laskowki's interpretation (Fuerstenau *et al.*, 2007):

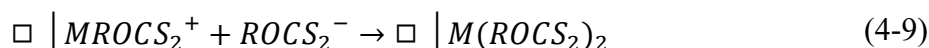
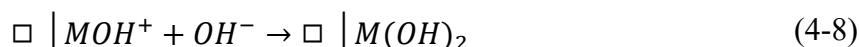
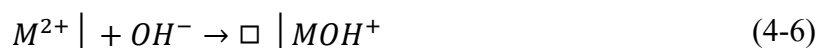
$$\Delta G(H) = \gamma_{LG}(H) - \gamma_{LG} \quad (4-3)$$

where  $\Delta G(H)$  is the energy barrier for bubble attachment (free energy of liquid layer of thickness  $H$ ),  $\gamma_{LG}(H)$  is a surface tension of liquid–gas interface depending on liquid layer thickness  $h$ ) (Fuerstenau *et al.*, 2007). When mineral surface coverage by a collector increases, the degree of

mineral surface hydrophobicity and flotation recovery also increases (Fuerstenau, 1982). Buckley and Woods demonstrated with galena that surface fractional coverage with ethyl xanthate of around 0.15 allowed 80% of the mineral to float, while the fractional coverage of 0.5 further improved the recovery to 90% (Buckley and Woods, 1991). Mitrofanov reported 50% galena recovery at a surface coverage of approximately 0.15, and 90% at a coverage of approximately 0.25 with butyl dithiophosphate (Mitrofanov, 1966). Glembotskij and Klassen summarized that for successful chalcocite flotation a surface coverage of approximately 15% from a potential monolayer is sufficient (Glembotskij and Klassen, 1981). However, based on the data from Abramov (Abramov, 2010), apart from the quantity of the adsorbed collector, the form of collector adsorption also plays a decisive role. Thus, the highest efficiency of flotation was observed when collector molecules were presented as a mix of chemisorbed and physisorbed compounds on a mineral surface (Abramov, 2010). In a general form, chemisorption may be described by the following equations:



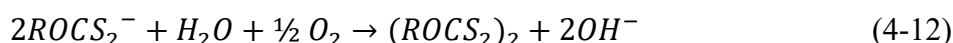
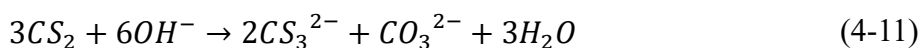
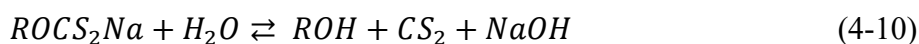
In this case, xanthate ions interact directly with a surface site. The reaction of xanthates with hydrolyzed sites and xanthate physisorption may be represented by the following equations taking place in the electrical double layer:



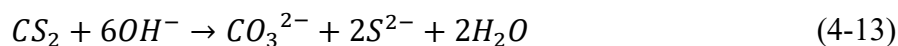
where  $|$  denotes mineral surface, and  $\square$  represents a vacant site ( $V$  was not used due to the italicization of the equations) (Fuerstenau *et al.*, 2007). For galena and pyrite, Abramov reported that minerals did not float even at a fractional surface coverage of 0.5 when butyl xanthate compounds were found to be either just chemisorbed (as metal xanthates) or only physisorbed (as dixanthogen) (Abramov, 2010). In another example, non-activated sphalerite particles with chemisorbed xanthate compounds were poorly floated. However, after activation with copper ions, the mineral was recovered almost completely, as a result of physisorption of 20 to 40% of the



xanthate species onto the mineral surface (Abramov, 2010). The copper activation mechanism was found by Albrecht *et al.* to be affected by the temperature regime of the flotation system (Albrecht *et al.*, 2016). In the adsorption tests conducted by Mustafa *et al.*, the temperature was also found to change the quantitative and qualitative characteristics of xanthate adsorption on chalcopyrite (Mustafa *et al.*, 2004). Higher temperatures generally promoted xanthate ions adsorption in the pH range of 8-10. The cuprous xanthate at a mineral surface was found to oxidize to dixanthogen with increasing temperature (Mustafa *et al.*, 2004). The increased decomposition of xanthate was also demonstrated by Shen *et al.*, which could be described by a series of reactions, involving xanthate dissociation and limited oxidation to dixanthogen (Shen *et al.*, 2016):



A further increase in the concentration of  $OH^-$  inhibits  $CS_2$  formation according to reaction (Equation 4-10), with strong alkali media (pH above 9) forcing further  $CS_2$  decomposition:



Oxidation to dixanthogen was found to be also strongly pH-dependent. Moreover, the dixanthogen formation reaction (Equation 4-12) was reported to be at an equilibrium when approximately 5 to 10% of xanthate was oxidized (Australian Government, 1995). Strong *et al.* also concluded from tests with amyl xanthate that at elevated temperatures the formation of dixanthogen accelerates (Strong *et al.*, 2005). Dixanthogen coverage of mineral surfaces was also shown to improve with temperature increase, originating from the low melting point of dixanthogen (around 30 °C) (Rao, 1971). An and Zhang subsequently demonstrated using AFM that at low temperatures dixanthogen was adsorbed on chalcopyrite as smooth round patches, while at elevated temperatures dixanthogen melted, and soft patches spread around mineral surfaces more easily (An and Zhang, 2020). Apart from the adsorption form and coverage density, the degree of uniformity of the surface coverage also plays an important role in the flotation. More uniform coverage is considered to improve mineral floatability (Glembotskij and Klassen, 1981).

The kinetics of xanthate adsorption also increased with temperature in studies with copper sulfide in the temperature range of 10 to 20 °C (Naeem *et al.*, 2008). Kinetic adsorption studies in a temperature range of 18 to 50 °C with pyrite, pyrrhotite, sphalerite, and chalcopyrite revealed low activation energy of butyl xanthate adsorption, which suggested diffusion as a limiting stage (Ignatkina *et al.*, 2013). Conversely, temperature was found to have little effect on a xanthate adsorption capacity in studies on chalcopyrite in the temperature range 15 to 30 °C (Zanin *et al.*, 2019).

Despite being an extensively investigated topic, temperature effects on the adsorption of flotation reagents in the context of flotation performance and surface energy still need to be explored for a variety of sulfide minerals, such as sphalerite, galena, and pyrite. Additionally, limited information is available on the acting mechanisms and parameters during collector adsorption. Thus, the current understanding of the driving mechanisms in sulfide flotation lacks a quantitative approach for describing reagents competition for a mineral surface under temperature constraints. The current investigation aims at a better understanding the flotation selectivity problems arising from changes in flotation pulp temperature (Marais, 1980).

#### **4.2. Thermodynamic Models of Hydrophobization at Different Temperatures**

As a result of thermodynamic calculations, entropy values for isopropyl xanthate complexes with lead, zinc, iron and copper were estimated as  $-552 \text{ J}/(\text{mol} \cdot \text{K})$ ,  $-532 \text{ J}/(\text{mol} \cdot \text{K})$ ,  $-518 \text{ J}/(\text{mol} \cdot \text{K})$  and  $-524 \text{ J}/(\text{mol} \cdot \text{K})$  respectively. Based on these values, equilibrium constants were estimated for isopropyl xanthate-metal compounds among solubility constants of other hydrophilizing species at different temperature scenarios (Figure 4-1).

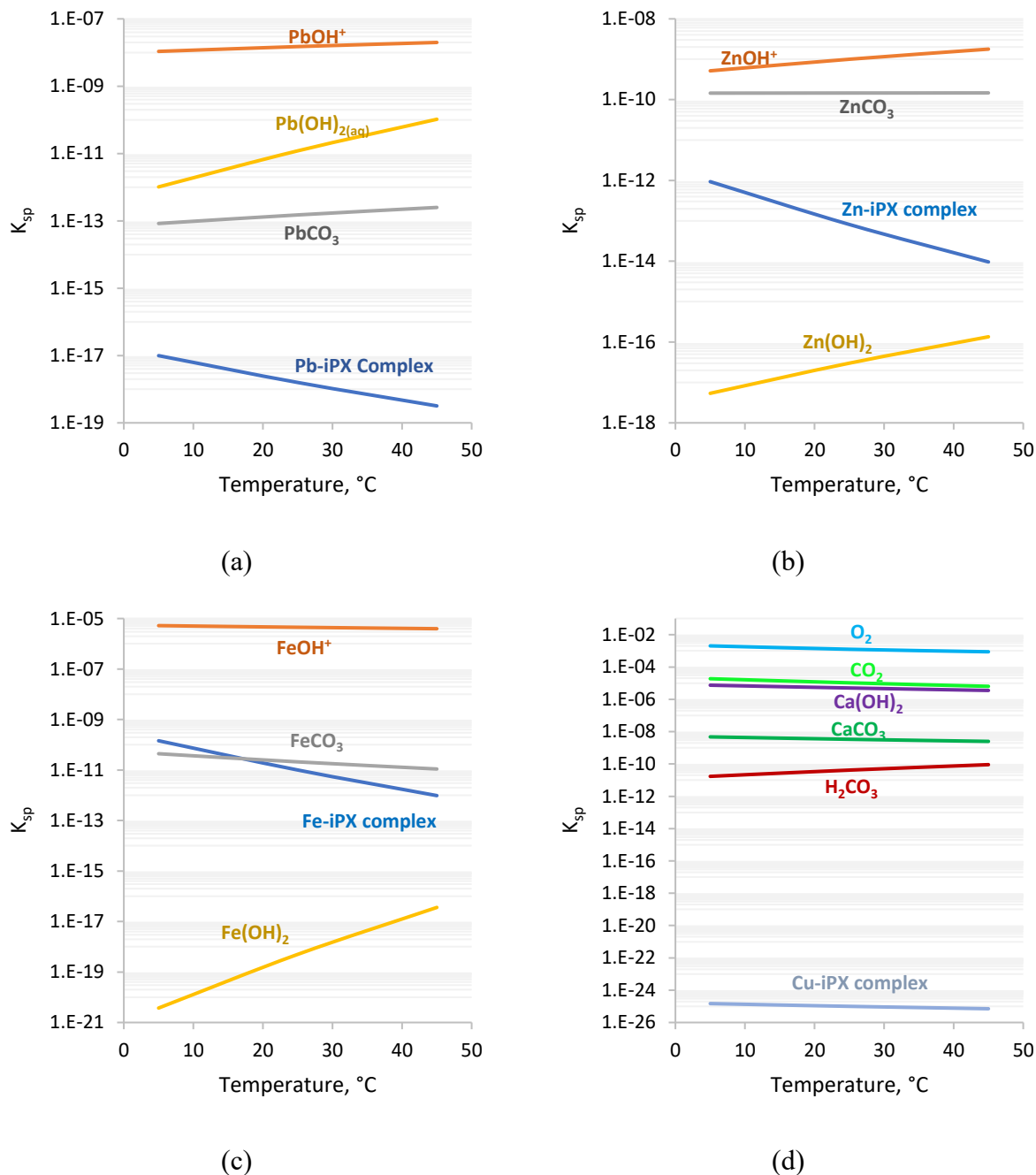


Figure 4-1. Solubility constants at different temperatures for: (a) different lead species, (b) different zinc species, (c) different iron species, (d) different calcium and carbonate species, gasses, and copper-xanthate complex

As can be seen from Figure 4-1, the solubility of metal-xanthate complexes decreases with an increase in temperature, while the solubility of metal-hydroxides and metal-carbonate complexes increases, indicating a shift in the equilibrium towards the formation of metal-xanthate complexes on a mineral surface. The solubility of gasses, as outlined by Henry's law, will also decrease with

temperature, which is illustrated by lower carbon dioxide solubility values at 45 °C. In instances where lime is used for pH control during the flotation process, the solubility of calcite and calcium hydroxide should be also considered, as calcium would bind with dissolved carbon dioxide to form precipitates (Figure 4-1b), which is consistent with literature (Belattar *et al.*, 2021; Korchef and Touaibi, 2020). This process is reflected through a decrease in the calcite solubility constants with temperature.

Additionally, as can be seen from the solubility constant curves (Figure 4-1), the lead system has several orders of magnitude lower solubility values compared to the zinc system, suggesting more efficient adsorption of isopropyl xanthates on the galena surface. From the above equilibrium constants, the minimum required concentrations of isopropyl xanthates were estimated for different pH and temperature (Figure 4-2).

From the minimum required concentration plot it can be seen that with an increase in pH, the amount of xanthate dosed to a flotation system should be exponentially increased. In contrast, an increase in temperature exponentially reduces the demand for xanthate in a system. From the slopes of exponential curves describing the change in the minimum required xanthate concentration over the temperature range, it can be assumed that xanthate adsorption on sphalerite has higher sensitivity towards temperature swings compared to galena. From Figure 4-2 it is also evident that for efficient flotation of galena, the required xanthate concentration is three orders of magnitude lower than the one for non-activated sphalerite. The highest calculated demand for xanthate was found for pyrite.

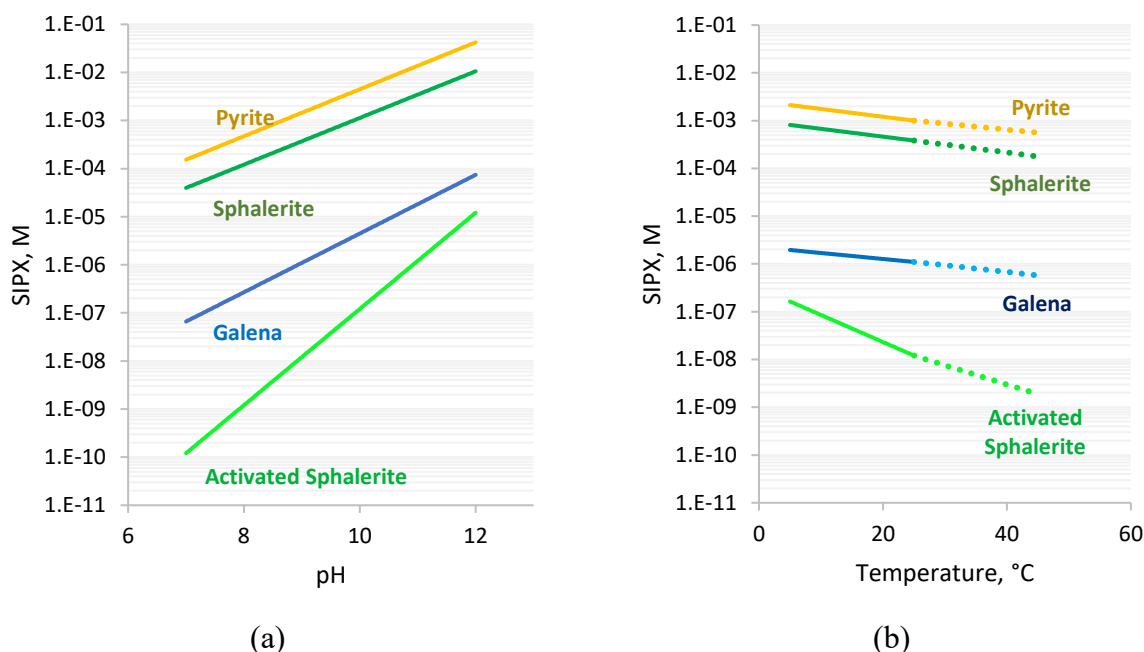


Figure 4-2. Theoretically estimated minimum isopropyl xanthate concentration required for pyrite, sphalerite, galena and activated sphalerite flotation at different pH (a); and temperature (at pH 9) (b)

Figure 4-2 also shows that variations in pH have a stronger effect on the required minimum concentration of xanthates, and hence, mineral floatability, compared to temperature fluctuations. It should also be noted that even though the calculations suggest a continuous decrease in the required concentration of xanthates over the investigated temperature range (5-45 °C), it does not consider potential changes in the mechanisms of xanthate adsorption, decomposition, mineral surface oxidation/hydration, formation of new precipitates, which may change at elevated temperatures.

### 4.3. Temperature-constrained Reagent Adsorption

The apparent adsorption rate constants for SIPX varied from around 1 nmol/(m<sup>2</sup>·s) up to around 11 nmol/(m<sup>2</sup>·s) as is seen from the adsorption experimental results (Appendix F). The highest apparent adsorption kinetics was generally associated with xanthate interaction with the galena surface. The apparent adsorption capacity ranged from below 0.1 to above 1.5 μmol/m<sup>2</sup>, with the highest values of collector adsorption per unit area observed also for the tests with galena.

The models, built for adsorption responses, passed the statistical significance test, with all obtained F-values being above the F critical value ( $>2.65$ ), as shown in Table 4-1. The p-values of the models are all below 0.05, which renders them adequate given the chosen confidence interval of 95% (alpha value = 0.05). Moreover, since all  $R^2$  values are above 0.8, good performances of all produced regression models are expected (Chicco *et al.*, 2021b).

Table 4-1. Characteristics of the models for pyrite, sphalerite, and galena adsorption tests

	<b>Pyrite responses</b>		<b>Sphalerite responses</b>		<b>Galena responses</b>	
	$k_a^{Py}$	$q_e^{Py}$	$k_a^{Sph}$	$q_e^{Sph}$	$k_a^{Gn}$	$q_e^{Gn}$
F-value	3.44	28.62	2.66	3.28	4.78	11.81
p-value	0.020	0.000	0.049	0.024	0.005	0.000
$R^2$	86.22	98.11	82.85	85.63	89.67	95.55
$R_{adj}^2$	61.17	94.69	51.65	59.49	70.90	87.46
SD	0.99	0.02	1.71	0.17	1.50	0.12

Modified Pareto charts (Figure 4-3) reveal the magnitude and importance of tested factors on adsorption responses. For adsorption kinetics for all three minerals (Figure 4-3 a, c, e) it transpires that the most important factors in descending order are: pH (negative effect), temperature (positive effect), and copper sulfate dosage (positive effect). For apparent adsorption equilibrium capacities of pyrite, sphalerite, and galena (Figure 4-3 b, d, f) the most critical parameter was the initial concentration of collector (SIPX), which had a positive standardized effect. For pyrite and galena, the second most important factor of the design of experiment was pH level (negative effects), while the second most critical factor for sphalerite was copper sulfate concentration (positive effect). From a detailed analysis, it derives that for pyrite adsorption the pH factor had a quadratic negative effect, with adsorption rapidly decreasing at higher pH values.

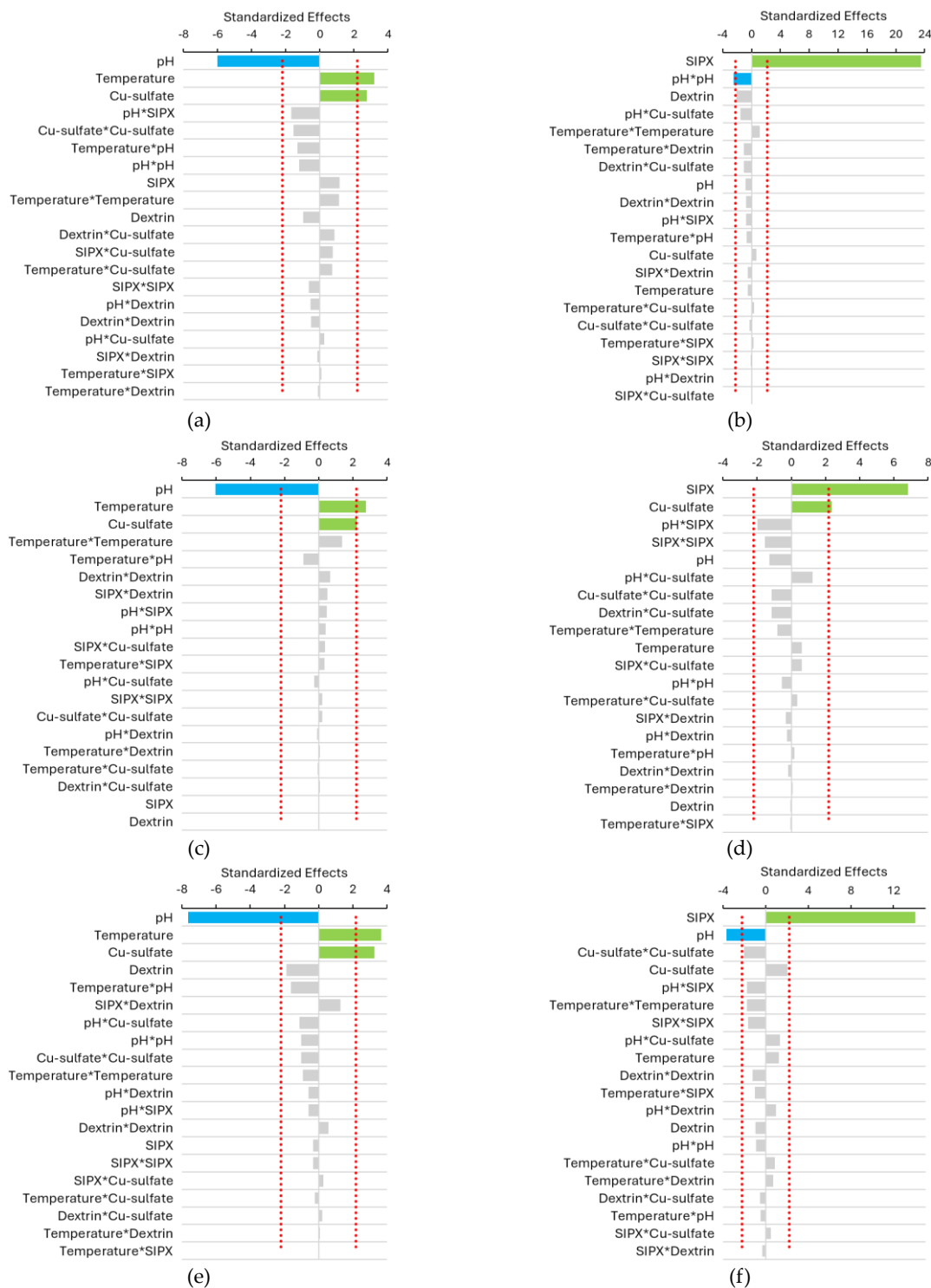


Figure 4-3. Standardized effects of model parameters: a – adsorption rate constant on pyrite, b – equilibrium adsorption capacity of pyrite surface, c - adsorption rate constant on sphalerite, d - equilibrium adsorption capacity of sphalerite surface, e - adsorption rate constant on galena, f - equilibrium adsorption capacity of galena surface. Non-significant factors are gray bars, significant factors are green (positive effect) and blue (negative effect) bars

Contour plots of the adsorption rate on three minerals show similar adsorption patterns in pH-temperature coordinates (Figure 4-4 a-c): the rate increases with a decrease in pH and an increase in temperature. Based on the areas on the contour plots representing conditions with an adsorption rate above  $10 \text{ nmol}/(\text{m}^2\cdot\text{s})$  it can be concluded that under the investigated conditions the most kinetically active surface in terms of isopropyl xanthate adsorption was galena followed by sphalerite. The slowest adsorption rates per unit area were found for pyrite. The highest adsorption rates for galena ( $>10 \text{ nmol}/(\text{m}^2\cdot\text{s})$ ) were found at temperatures above  $21^\circ\text{C}$ , while for sphalerite and pyrite at the lowest pH, these values were  $32^\circ\text{C}$  and  $42^\circ\text{C}$  respectively.

Regarding the temperature effect on apparent adsorption equilibrium capacity, as observed from contour plots in SIPX-temperature coordinates, the effect is not pronounced, which is also confirmed by Pareto charts (Figure 4-3 b, d, f) where standardized effects of temperature terms were all below the t-critical value. There is, however, a strong effect of initial collector concentration on the apparent adsorption equilibrium capacity, explaining the almost horizontal orientation of isolines on the contour plots (Figure 4-4 d-f).

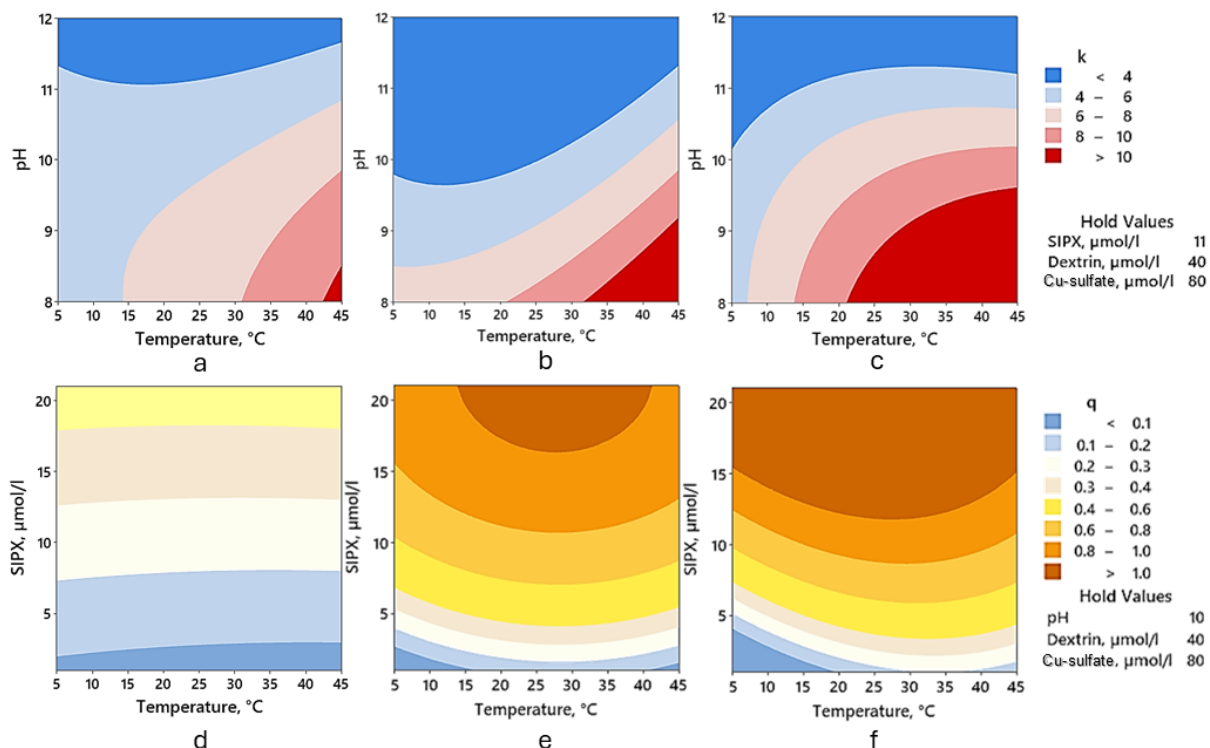


Figure 4-4. Contour plots of  $k$  (apparent adsorption rate constant in  $\text{nmol}\cdot\text{m}^{-2}\cdot\text{s}^{-1}$ ) (a-c) at different temperatures and pH: a - for pyrite, b - for sphalerite, c - for galena; contour plots of apparent equilibrium adsorption capacity in collector dosage – temperature coordinates: d – for pyrite, e – for sphalerite, f – for galena



Adsorption data at central point conditions was also fit to different adsorption isotherms. The goodness of fit for three different models is given in Table 4-2. The Langmuir model demonstrated the worst fit to the data, the Freundlich model was able to explain up to around 83 to 85% of the variability in the adsorption data, while the highest coefficients of determination were achieved using the Temkin model ( $R^2$  values for all isotherms above 0.9). The largest Freundlich adsorption capacities, as follows from higher  $K_F$  values, are observed for sphalerite and galena, while the highest heterogeneity factor ( $n$ ) is found for sphalerite.

Table 4-2. Adsorption isotherms for SIPX adsorption on pyrite, sphalerite, and galena

	Langmuir model	Freundlich model	Temkin model
General isotherm equation	$q_e = \frac{Q_o K_L C_e}{1 + K_L C_e}$	$q_e = K_F C_e^{1/n}$	$q_e = \frac{RT}{b} \ln (K_m C_e)$
<i>Pyrite data</i>			
- Isotherm equation	$q_e = \frac{22.3 \cdot 10^{-3} \cdot C_e}{1 - 10^{-3} \cdot C_e}$	$q_e = 3 \cdot 10^{-2} \cdot C_e^{1/1.1}$	$q_e = \frac{RT}{19,611} \ln (1.2 \cdot C_e)$
- $R^2$	0.39	0.84	0.96
<i>Sphalerite data</i>			
- Isotherm equation	$q_e = \frac{12 \cdot 8 \cdot 10^{-3} \cdot C_e}{1 + 8 \cdot 10^{-3} \cdot C_e}$	$q_e = 0.1 \cdot C_e^{1/1.2}$	$q_e = \frac{RT}{7,111} \ln (1.2 \cdot C_e)$
- $R^2$	0.64	0.85	0.94
<i>Galena data</i>			
- Isotherm equation	$q_e = \frac{6.4 \cdot 10^{-2} \cdot C_e}{1 - 10^{-2} \cdot C_e}$	$q_e = 0.1 \cdot C_e^{1/1.1}$	$q_e = \frac{RT}{5,608} \ln (1.1 \cdot C_e)$
- $R^2$	-0.26	0.83	0.94

From Temkin adsorption isotherms (Figure 4-5) the galena has the highest apparent adsorption capacity values per unit surface area at central point conditions of the design of the experiment (pH 10, 25 °C, 40  $\mu\text{mol/l}$  dextrin, 80  $\mu\text{mol/l}$  copper sulfate), while pyrite apparent adsorption capacity was the smallest among three tested minerals, and did not exceed 0.4  $\mu\text{mol/m}^2$ . Moreover,

since the b-coefficient from the Temkin model was the smallest for galena (Table 4-2), the slope of the isotherm was the largest for this mineral (hence more preferential adsorption for galena).

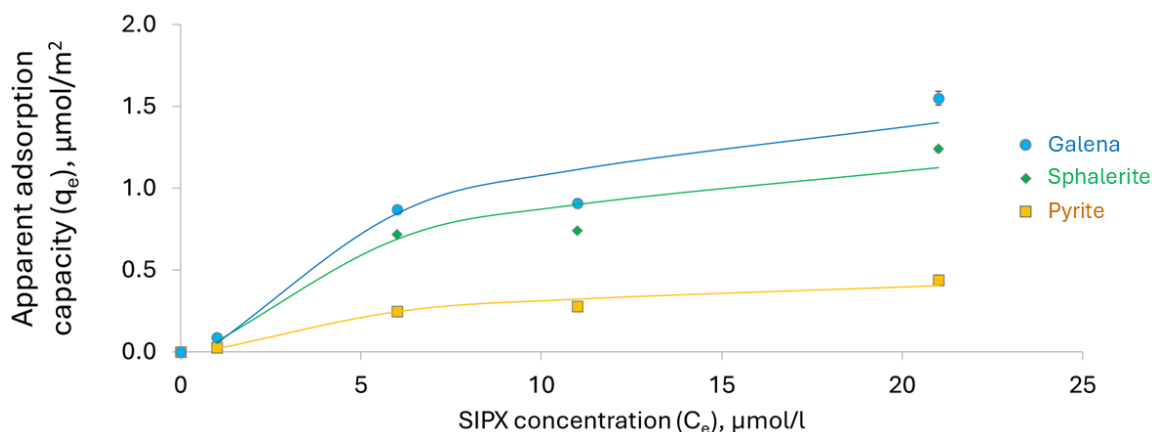


Figure 4-5. Temkin adsorption isotherms for pyrite, sphalerite, and galena (pH 10, 25 °C, 40  $\mu\text{mol/l}$  dextrin, 80  $\mu\text{mol/l}$  copper sulfate)

By applying the optimization (desirability function) and overlaid contour plot tools in Minitab® an attempt was made to check the selectivity in potential mixed systems with adsorption on galena and sphalerite in the presence of pyrite. Such analysis ignores interactions between minerals and may not be considered a robust tool. However, it may provide some additional information and indicate some possible trends. The desirability function for the adsorption rate responses was maximizing galena and sphalerite responses and minimizing pyrite responses. As it is shown in Figure 4-6a, with an increase in temperature pH must be increased to maintain the highest selectivity in adsorption rates between both pairs of minerals: galena and pyrite, and sphalerite and pyrite. The inflection points for sphalerite-pyrite and galena-pyrite selectivity curves are between 30 and 40 °C. However, by increasing the temperature (Figure 4-6b) the concentration of collector molecules should be reduced to keep the highest possible selectivity against pyrite.

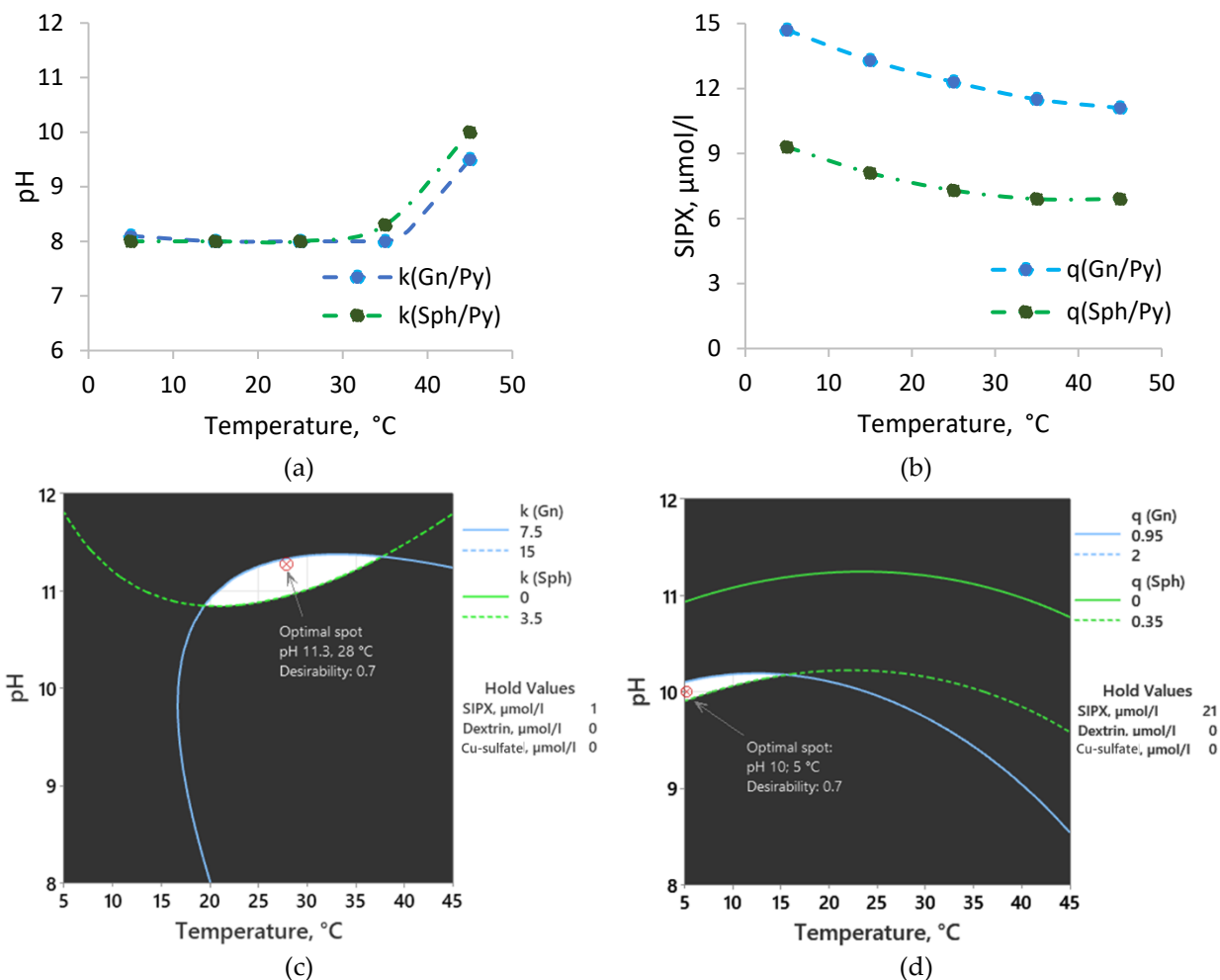


Figure 4-6. Optimal pH for largest selectivity of adsorption kinetics on galena and sphalerite compared to pyrite at different temperatures (a), optimal initial collector dosage for highest selectivity in adsorption capacity against pyrite, depending on temperature (b), overlaid contour plot showing optimal conditions for the highest selectivity in adsorption kinetics between galena and sphalerite (c), overlaid contour plot showing optimal conditions for the highest selectivity in adsorption capacity between galena and sphalerite (d)

When considering overlaid contour plots (Figure 4-6c-d) demonstrating potential selectivity in adsorption rates and capacities between galena and sphalerite, it could be seen that by setting arbitrary boundaries the desirability spots fit the feasible solution areas (illustrated as white shapes). For adsorption rate, the highest value of the desirability function was found at high pH (pH 11) and temperatures close to central point conditions (28 °C). Moreover, the feasible solution zone extends diagonally, which means that when increasing temperature, the pH should also be increased to maintain adequate selectivity levels. For the apparent adsorption capacity, the highest selectivity between sphalerite and galena was found at the coldest tested temperature (5 °C), at pH

around 10. The extension of the feasible solution zone suggests that the highest selectivity may be traced up to around 15 °C.

Another pair of investigated responses through desirability function was the sphalerite-pyrite apparent adsorption capacity. This time, responses for sphalerite were maximized, while responses for pyrite were minimized. Particularly, the effect of temperature on a potential sphalerite selectivity against pyrite was investigated. As can be seen in Figure 4-7, the highest selectivity was observed at the highest pH and the highest copper sulfate concentrations. With an increase in temperature, an increase in the feasible (white area) zone could be traced on the overlaid contour plots up to 25 °C (from Figure 4-7a to Figure 4-7c). However, a further increase in the temperature from 25 to 45 °C at a fixed collector concentration leads to a decrease in the feasible zone area, and a notable increase in the pH values required for achieving the desired selectivity level (Figure 4-7d-e).

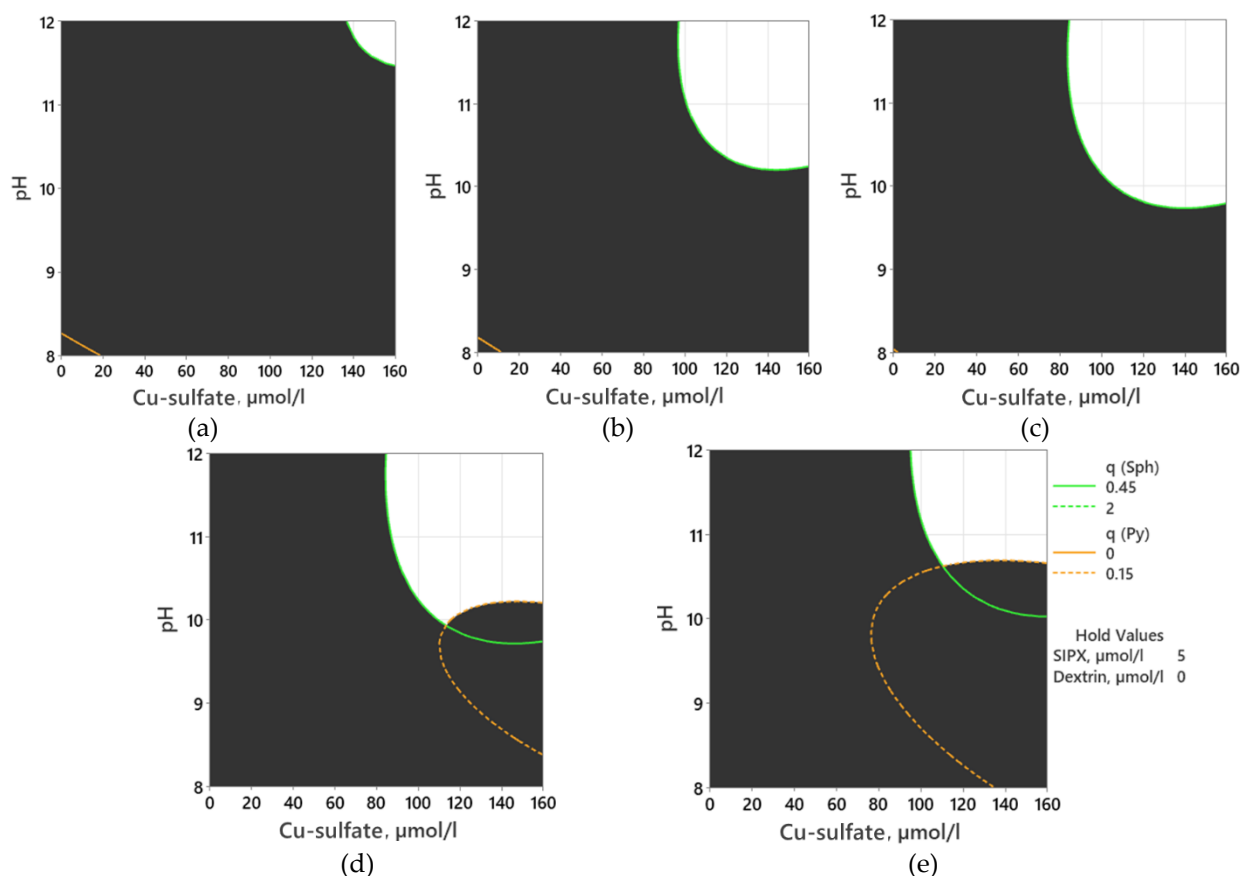


Figure 4-7. Overlaid contour plots showing the change of the feasible area in coordinates of copper sulfate concentration and pH that allows to achieve maximum adsorption selectivity between sphalerite and pyrite at different temperature scenarios:  
(a) 5 °C, (b) 15 °C, (c) 25 °C, (d) 35 °C, (e) 45 °C

In order to determine which mineral exhibited the highest adsorption sensitivity towards temperature changes, activation energies were estimated for all three minerals (Figure 4-8a and Table 4-3). The highest apparent activation energy of approximately 25 kJ was found for galena, followed by sphalerite (19 kJ) and pyrite (*ca.* 15 kJ). Galena also demonstrated the highest apparent enthalpy of activation with minerals following the same order as in the activation energy case (galena>sphalerite>pyrite).

The apparent entropy of activation showed an inverse order with galena possessing the lowest entropy values and pyrite having the highest entropy. Consequently, the resulting apparent Gibbs energy of activation was the highest for sphalerite, and the lowest for galena (Figure 4-8b, Table 4-3).

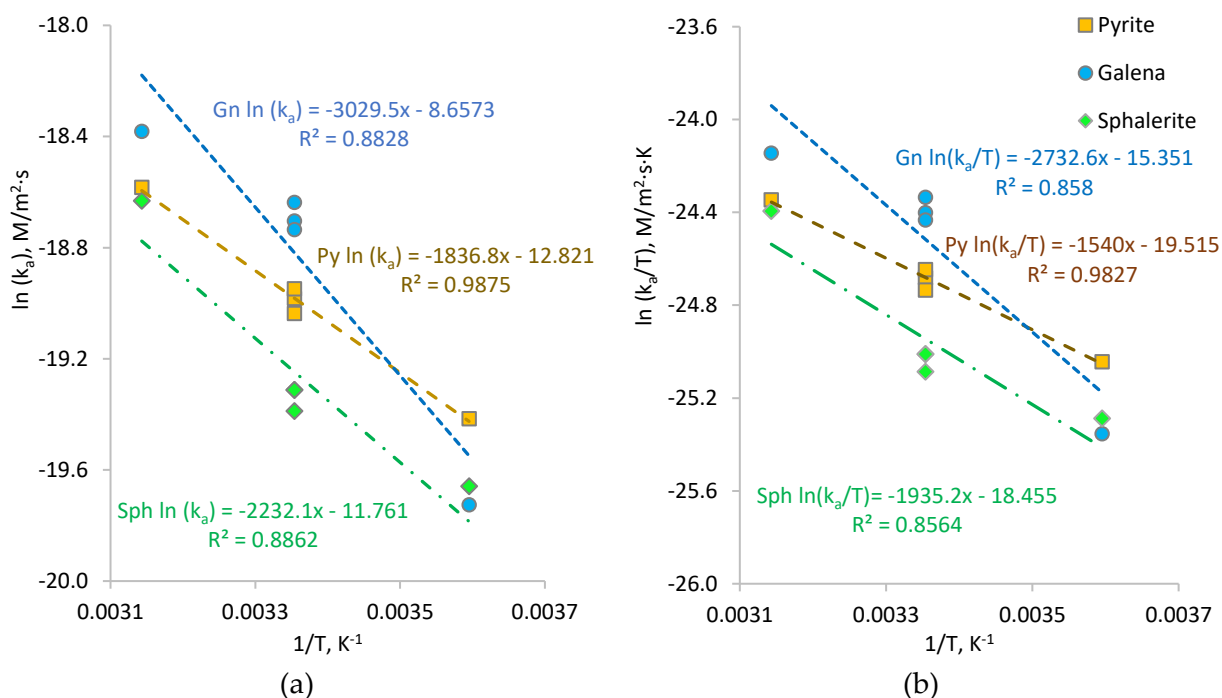


Figure 4-8. Graphical estimation of apparent activation energies for adsorption of SIPX on pyrite, galena, and sphalerite at pH 10 in the temperature range 5-45 °C (a); graphical estimation of entropy and enthalpy of activation (b)

Table 4-3. Results of calculations of apparent activation parameters for iPX adsorption

	Pyrite - iPX	Galena - iPX	Sphalerite – iPX
Arrhenius equation ( $k_a$ in mol/(m <sup>2</sup> ·s))	$k_a = 2.7 \cdot 10^{-6} e^{\frac{1837}{T}}$	$k_a = 1.7 \cdot 10^{-4} e^{\frac{3029}{T}}$	$k_a = 7.3 \cdot 10^{-6} e^{\frac{2232}{T}}$
Activation energy, kJ	15.3	25.2	18.6
Entropy of activation, J/(mol·K) ( $\Delta S^\ddagger$ )	-325	-360	-351
Enthalpy of activation, kJ/mol ( $\Delta H^\ddagger$ )	12.8	22.7	16.1
Gibbs energy of activation, kJ/mol ( $\Delta G_{298.15}^\ddagger$ )	120.1	119.7	120.7

#### 4.4. True Flotation Recovery and Surface Energy at Varying Temperatures

The microflotation recoveries are depicted in Figure 4-9. The optimum temperature for the recovery of galena and sphalerite was found to be room temperature (25 °C) with galena showing the highest flotation yield among the three minerals. Pyrite however did not present a high recovery, and temperature did not seem to have any significant effect on pyrite flotation either at pH 9 or pH 11. In fact, the flotation yields for sphalerite and galena were 3-4 times larger than that of pyrite.

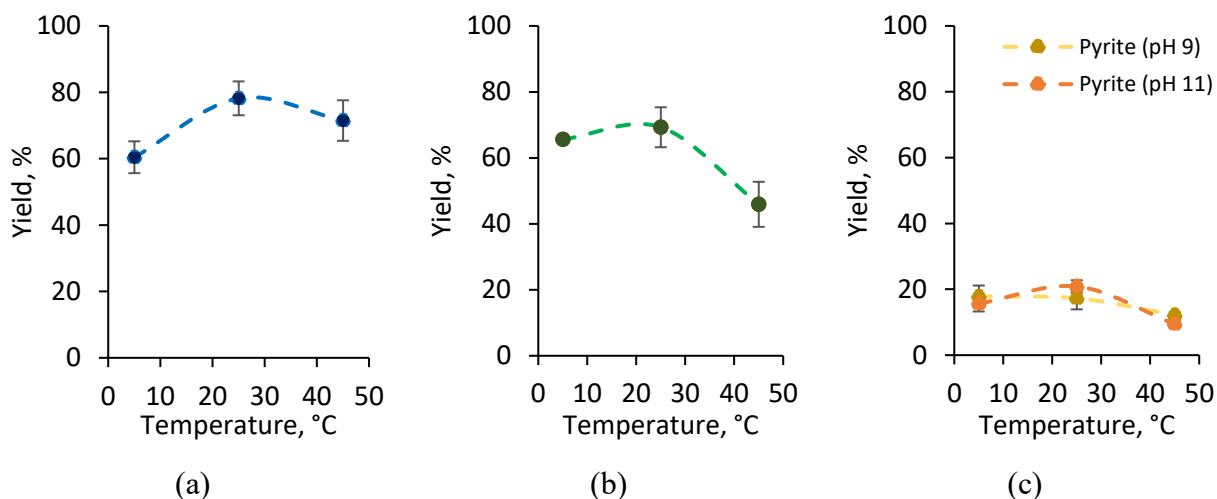


Figure 4-9. Microflotation results for galena (pH 9), sphalerite (pH 11), and pyrite (pH 9 and 11)

Investigations of surface characteristics of the investigated minerals using XPS revealed the presence of activating ions for sphalerite surface (lead and traces of copper) (Figure 4-10), which can explain the observed high sphalerite recoveries. Higher intensity of oxygen peak (O1s) for pyrite compared to galena and sphalerite may suggest a greater degree of surface oxidation and explain lower flotation recoveries for pyrite.

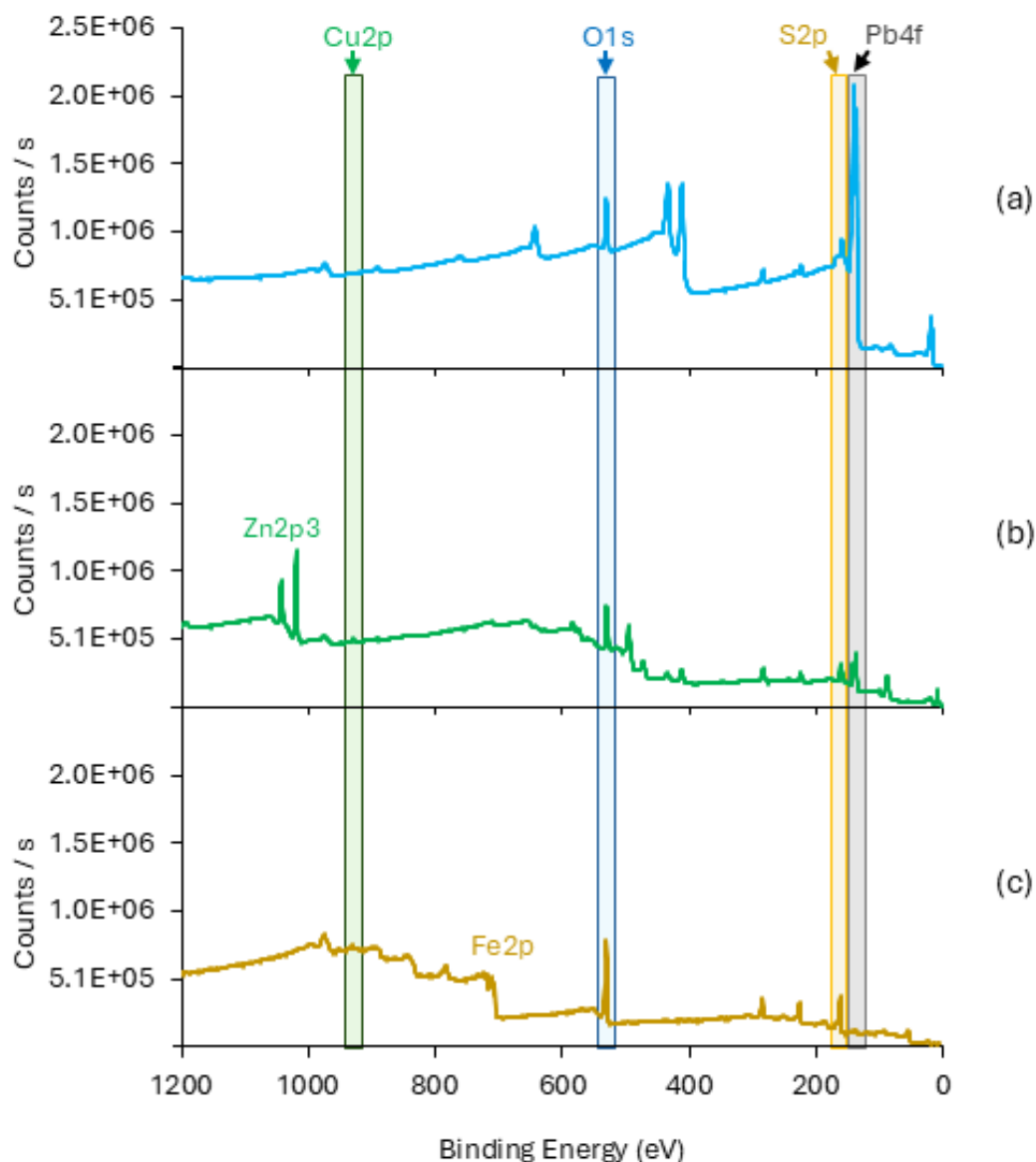


Figure 4-10. XPS results for feed samples: galena (a), sphalerite (b), pyrite (c)

Since theoretically calculated xanthate demand ( $[X_t]$ ) changes with temperature, the ratio between dosed ( $[X_d]$ ) and theoretically required xanthate dosage (from thermodynamic calculations) will

also change at different temperatures. It has been reported that by approaching a ratio of 1 the highest mineral yields may be found. The mineral yield plotted versus xanthate supply/demand ratio explains low pyrite recoveries, as at alkali pH xanthate demand is relatively high, which decreases the ratio (Figure 4-11).

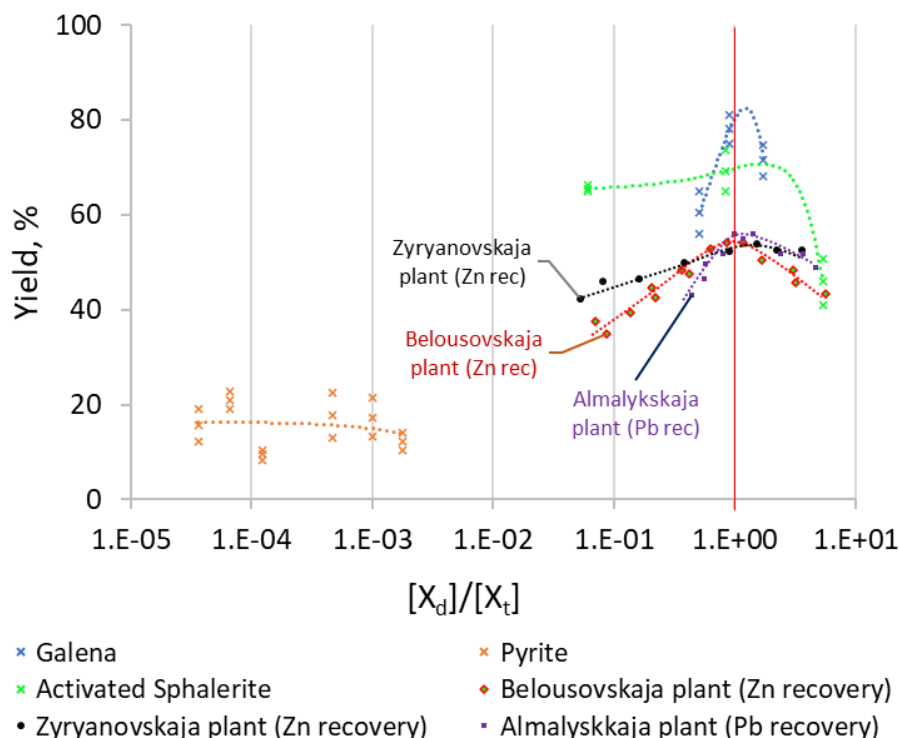


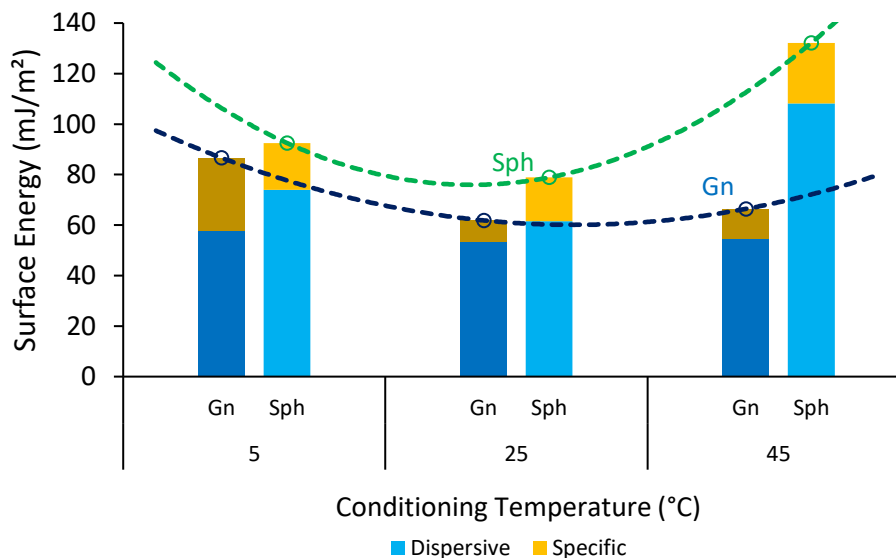
Figure 4-11. Mineral yield versus xanthate supply/demand ratio for the tested monomineralic samples (galena, sphalerite, and pyrite) and for industrial plants (data from (Abramov, 2010))

Moreover, if it is assumed that the xanthate demand continuously decreases even at temperatures above ambient, the xanthate supply/demand ratio will exceed 1 at 45 °C. It has been reported that at a ratio above 1 there may be a decrease in the sphalerite and galena recovery related to increased xanthate consumption by ions in the pulp, supported by observations from some Pb-Zn flotation plants (Abramov, 2010) (Figure 4-11).

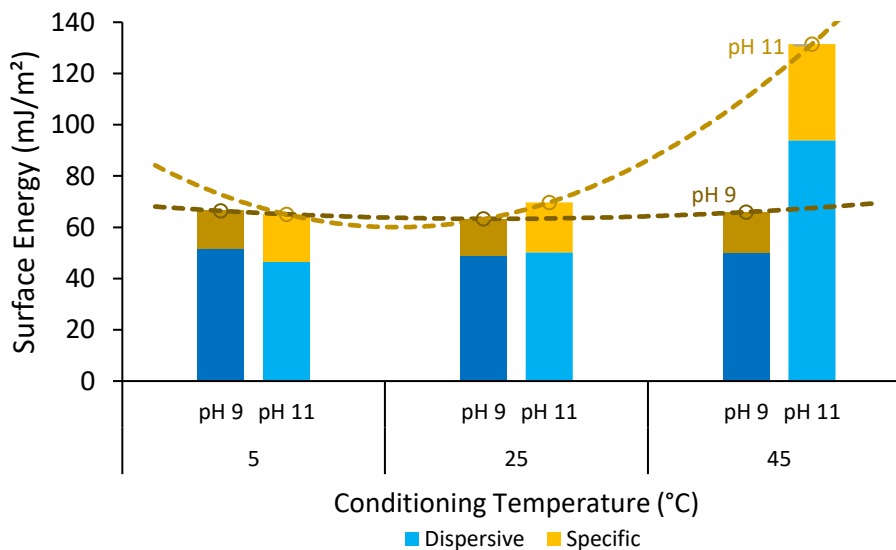
In order to investigate the correlation between surface free energy and flotation behavior of the minerals, the dispersive ( $\gamma^d$ ) and specific ( $\gamma^{ab}$ ) components of surface free energy of galena and sphalerite conditioned with SIPX at 5, 25, and 45 °C were determined (Figure 4-12). The surface energy values of each sample corresponded well to microflotation results. The galena sample, in general, had much lower surface energy than sphalerite. The lowest surface energy can be an



indication of higher hydrophobicity, meaning that conditioning at 25 °C had the highest effect on both mineral surfaces. These are the samples which showed the highest flotation recoveries. The decrease in the specific component of the surface energy can be attributed to the presence of less active polar surface sites, which could be due to the high density/stability of the adsorbed collector on the mineral surface. Additionally, the samples with higher flotation recovery had the lower specific surface component, which is a measure of surface hydrophilicity (Bai *et al.*, 2023).



(a)



(b)

Figure 4-12. Dispersive (blue bars) and specific (orange bars) components of the surface energy of the microflotation products (at 5% coverage): a – galena and sphalerite, b – pyrite

Although a single surface energy value is a useful parameter for explaining the surface behavior of the minerals at various conditions, it should be kept in mind that real mineral surfaces, similar to other solid materials, are fundamentally energetically heterogeneous and a single value as surface energy may not be the best representative of the entire surface.

The surface energy heterogeneity profiles of the galena and sphalerite are given in Figure 4-13 and Figure 4-14. For both minerals the dispersive and specific surface energies decreased after adsorption of xanthate at different temperatures (Figure 4-13 and Figure 4-14), potentially indicating lower polarizability and higher surface hydrophobicity.

The galena sample conditioned at 5 °C showed the highest total (a sum of dispersive and specific energies) surface energy heterogeneity with more energetic surface sites (Figure 4-13a). For all samples, both  $\gamma^d$  and  $\gamma^{ab}$  change as a function of surface coverage; however, there is a notable difference between the maximum and minimum surface free energies of the 5 °C sample. The dispersive and specific components of surface energy of this sample range from ~58 to ~29 and from ~29 to as low as ~3 mJ/m<sup>2</sup>, respectively, indicating that the surface is energetically highly heterogeneous, in which the specific component of surface energy plays an important role.

Conditioning of galena at 25 °C led to a less energetic and more homogeneous surface (Figure 4-13a, Figure 4-13b). This sample showed the highest flotation recovery. Compared to 25 °C, conditioning the sample at 45 °C seems to have less significant effect on the distribution of the surface energy on the galena surface (Figure 4-13c). Based on the shape of the modeled curves, the specific component of the surface energy showed the highest heterogeneity. Thus, the decay constant at 5 °C is remarkably higher (122.4) than at 25 and 45 °C (27.5 and 24.2), respectively, suggesting a higher surface heterogeneity at the lowest tested temperature (5 °C).

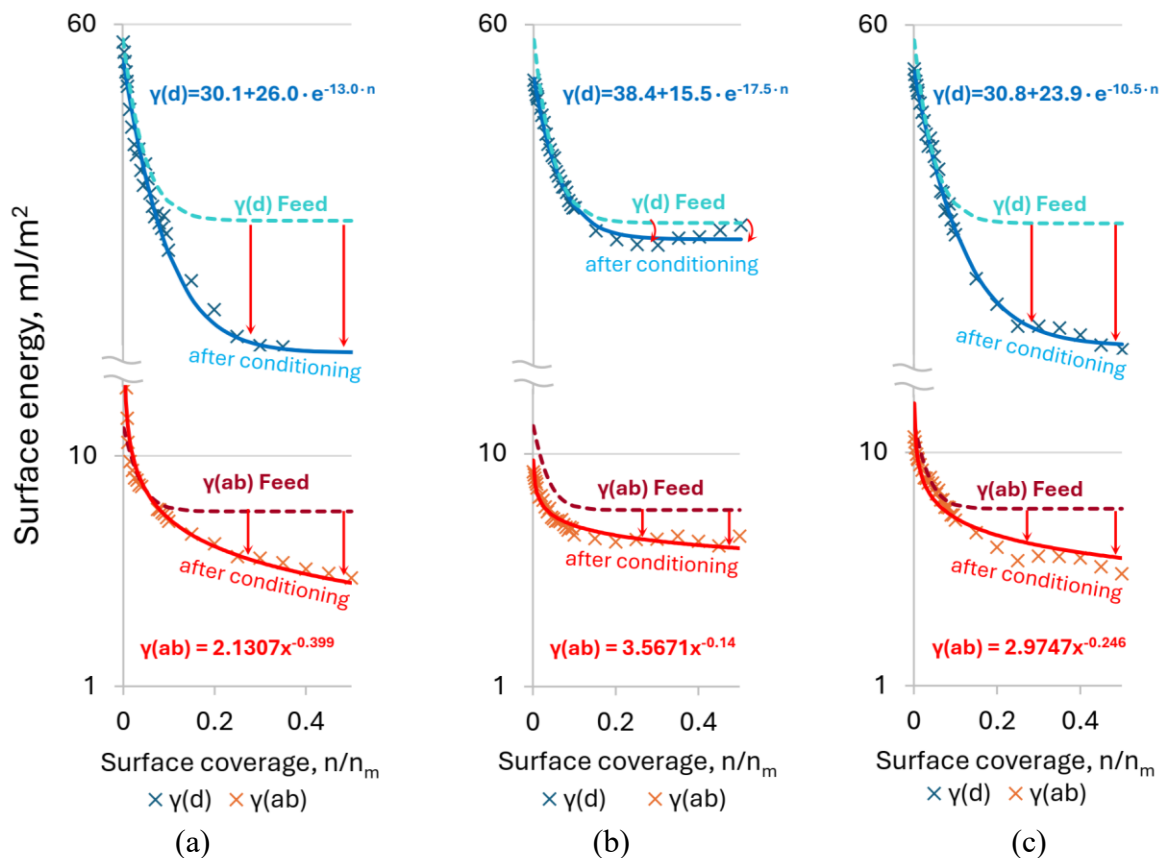


Figure 4-13. Surface energy heterogeneity profiles of galena after conditioning with SIPX at different temperatures: 5 °C (a), 25 °C (b), and 45 °C (c);  $\gamma^d$ ,  $\gamma^{ab}$  – represent dispersive and specific surface energy, respectively.

In the case of sphalerite, the impact of the surface treatment with SIPX at 5 and 25 °C were comparable while a significant difference was observed between the highest and lowest surface free energy after conditioning at 45 °C (Figure 4-14). Contrary to galena, the main component responsible for the heterogeneous distribution of sphalerite surface energy sites at 45 °C is the dispersive component (Figure 4-14c), which may be due to a phenomenon other than the collector adsorption, for example, precipitation of a hydrophilic phase on the mineral surface.

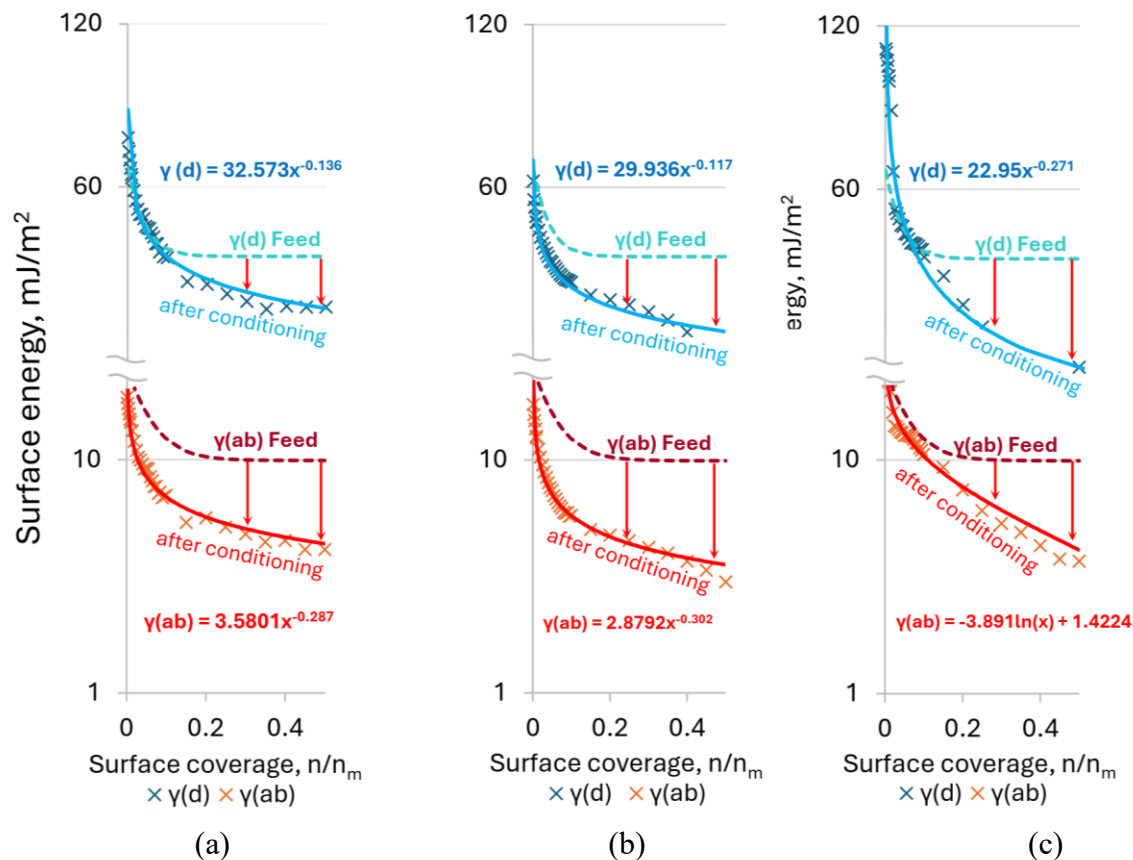


Figure 4-14. Surface energy heterogeneity profiles of sphalerite after conditioning at 5 °C (a), 25 °C (b), and 45 °C (c);  $\gamma^d$ ,  $\gamma^{ab}$  – represent dispersive and specific surface energy, respectively

Surface heterogeneity profiles can also be represented by an energy distribution function to provide more comprehensive information on the surface energy sites. The surface energy distribution is a plot of the surface energy versus area increment (percentage of surface), obtained by a point-by-point integration of the surface energy profiles. The specific surface energy distributions of galena and dispersive surface energy distribution of sphalerite samples are given in Figure 4-15a and Figure 4-15b, respectively. The plots demonstrate more uniform distribution of surface energy for galena and sphalerite conditioned at 25 °C.

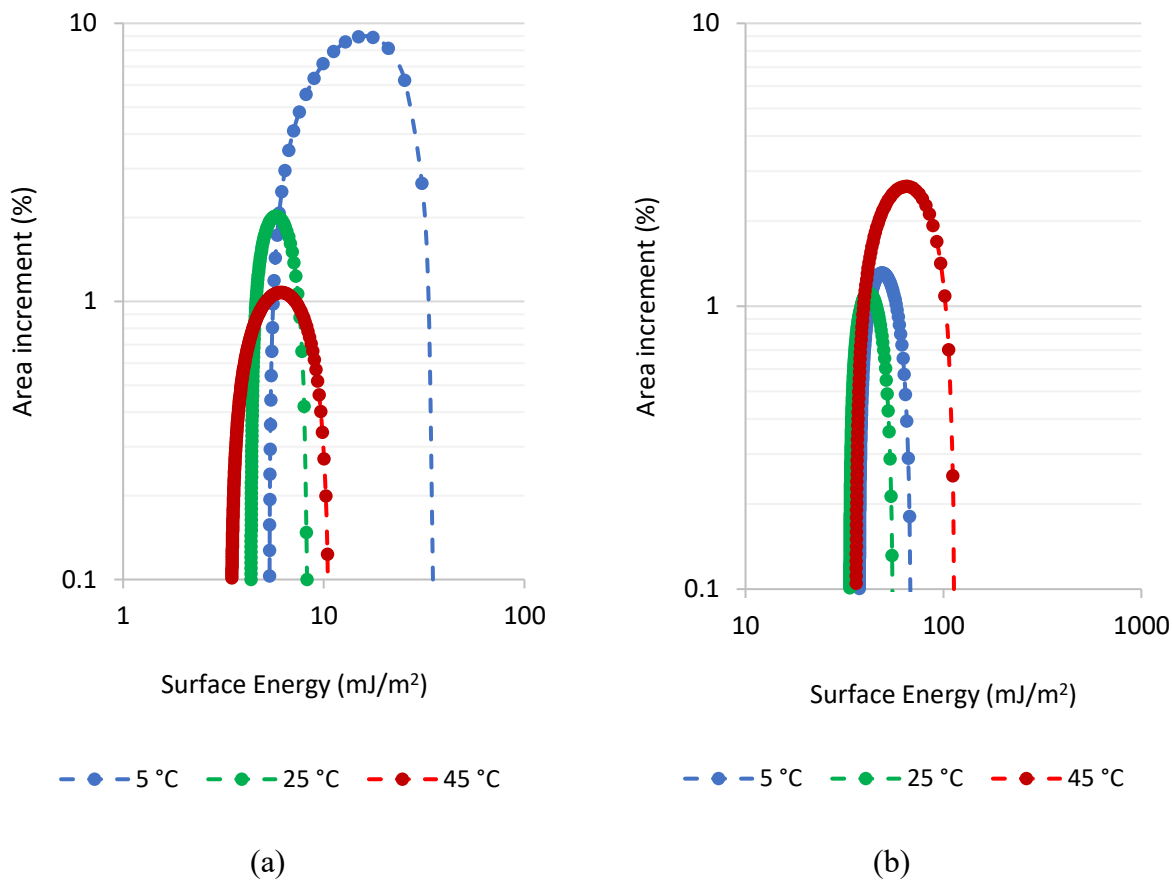


Figure 4-15. Specific surface energy distributions galena conditioned at 5, 25, and 45 °C (a) and dispersive surface energy distributions of sphalerite conditioned at 5, 25, and 45 °C (b)

Because sphalerite tests showed the largest decrease in flotation yield and an increase in total surface energy and surface heterogeneity at higher temperatures, the tailings were additionally analyzed to reveal possible reasons for such flotation behavior. As can be seen from SEM images (Figure 4-16), some calcium carbonate precipitates were found on the mineral surface. The results were confirmed by point analysis and EDS mapping.

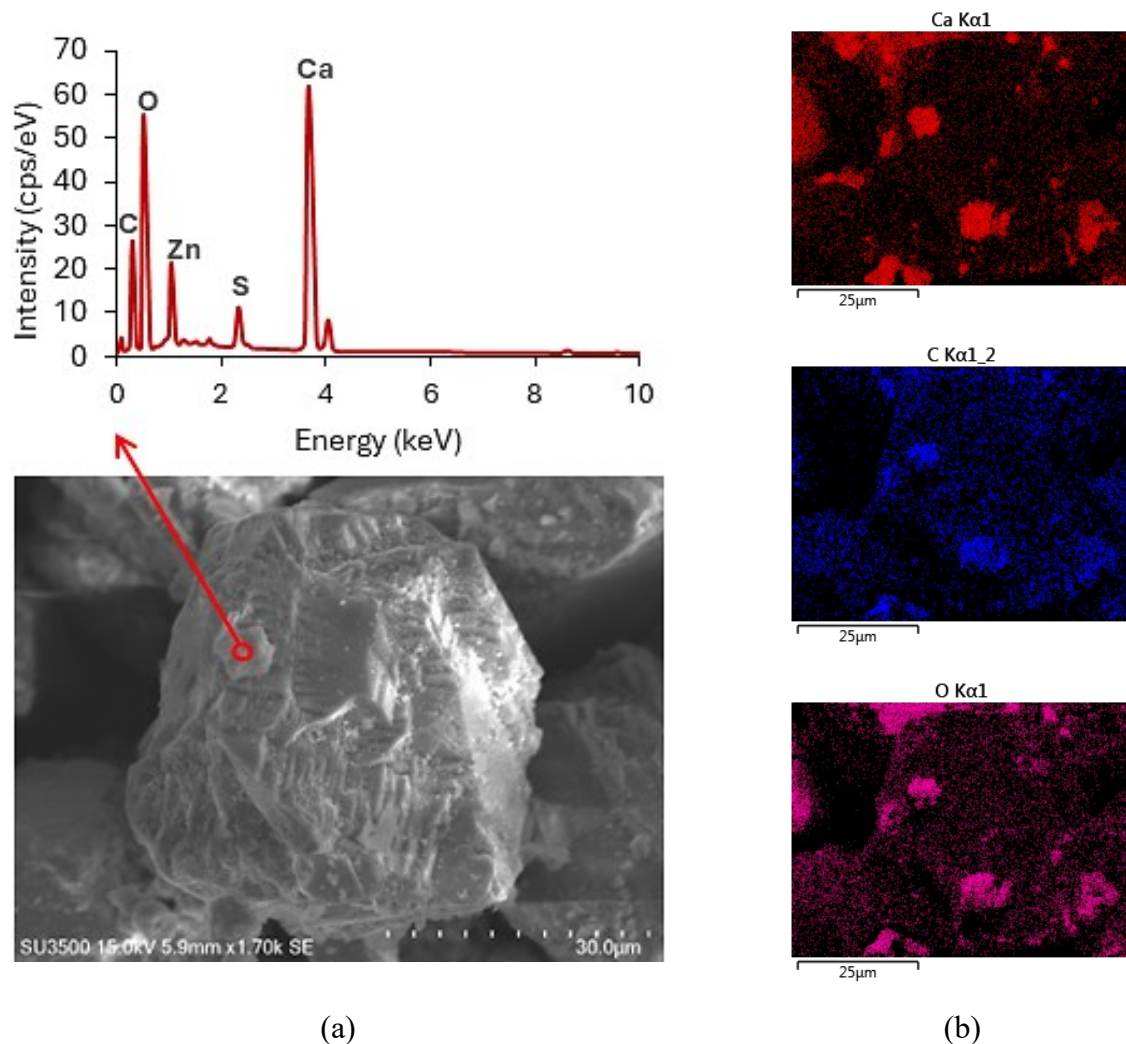


Figure 4-16. Scanning electron microscopy image of a sphalerite grain in micro-flotation tails (45 °C test): (a) sphalerite grain image and EDS point analysis of precipitate on a mineral surface, (b) EDS mapping of the grain

The appearance of calcium on sphalerite surface at 45 °C was also confirmed with XPS (Figure 4-17a). Moreover, based on XPS detailed scan of calcium 2p spectra it is likely that the observed calcium carbonate polymorph is calcite. This derives from the positions of  $\text{Ca}2p_{1/2}$  and  $\text{Ca}2p_{3/2}$  peaks (350.4 eV and 346.9 eV respectively, versus 350.5 eV and 346.9 eV reported in the literature for calcite) (Ni and Ratner, 2008).

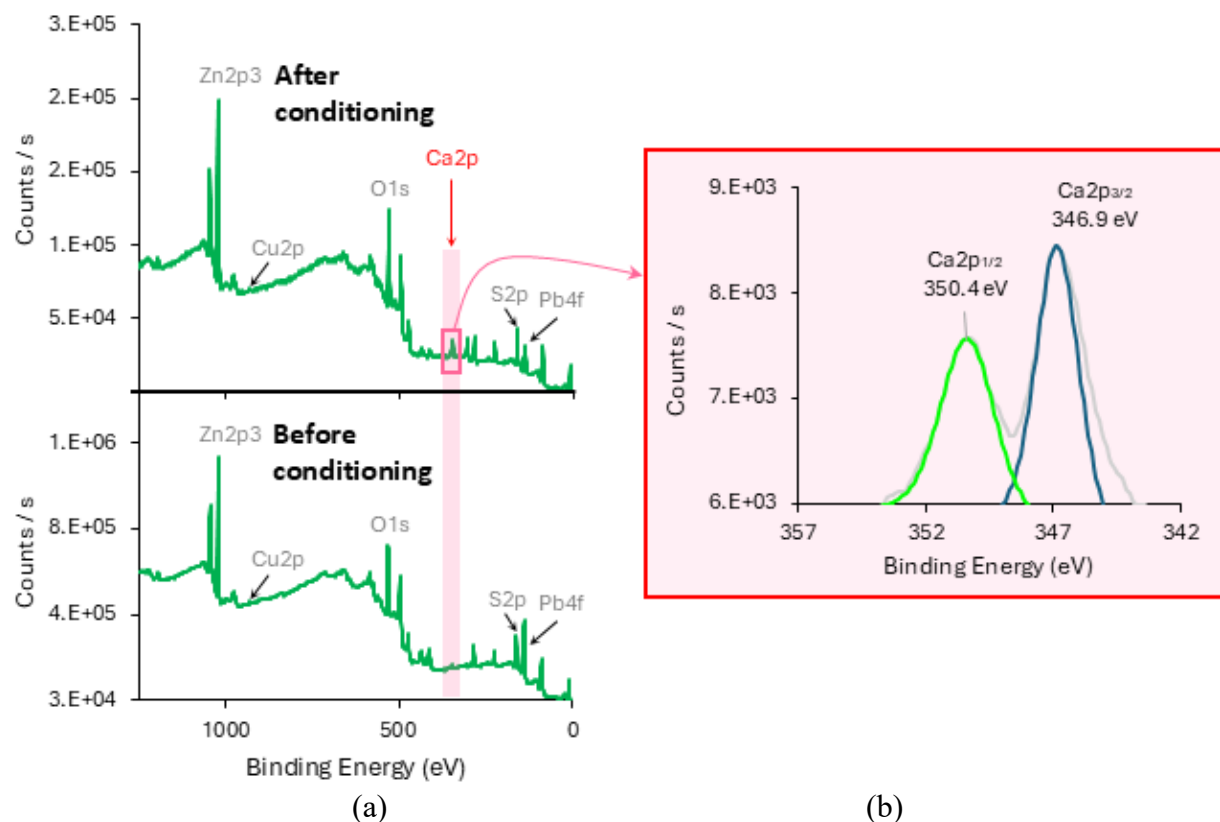


Figure 4-17. XPS results for sphalerite tailing sample (before and after conditioning and flotation at 45 °C): general spectrum (a), detailed calcium scan after conditioning (b)

Since oxygen also plays an important role in mineral surface oxidation and xanthate adsorption, it was monitored during the tests. From dissolved oxygen levels for all microflotation tests at different stages, one major and two minor trends were observed (Figure 4-18). The main trend is a decrease in dissolved oxygen concentration with an increase in pulp temperature. For example, at 5 °C it varies around 9.9 ppm; for 25 °C around 6.8 ppm; and around 4.9 ppm at 45 °C. There is also a traceable slight decrease in dissolved oxygen concentration after mineral addition to the pulp related to oxygen consumption for surface oxidation. This decrease is followed by a restoration of the oxygen levels after flotation to approximately “Test start” conditions.

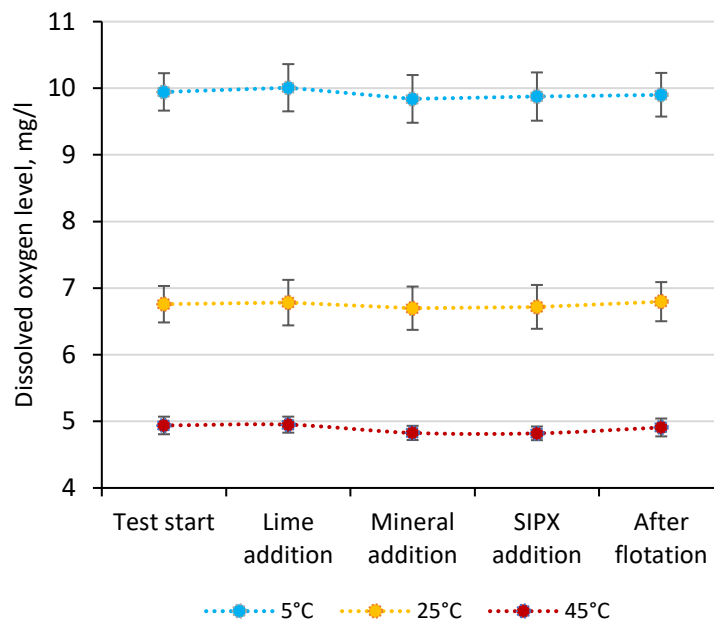


Figure 4-18. Dynamics of dissolved oxygen concentration with temperature at different microflotation stages

Regarding the lime dosage, certain trends with temperature on lime demand have also been observed (Figure 4-19). Naturally, one to two orders of magnitude more lime was needed to adjust pH at 11 compared to pH 9. Additionally, with an increase in temperature from 5 to 45 °C the demand for lime approximately doubled.

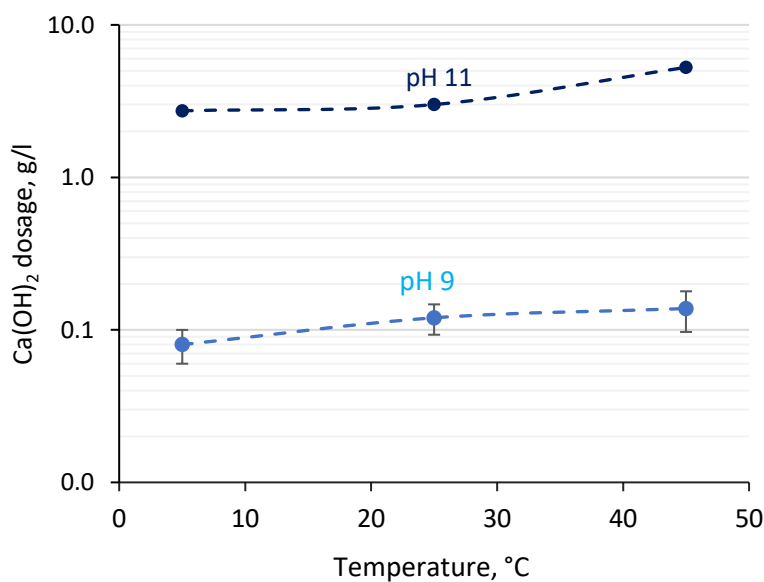


Figure 4-19. Lime consumption at different pH and temperatures



#### 4.5. Discussions

From the adsorption results, it can be seen that for the rate the most important factors were pH, temperature, and copper sulfate concentration. For a successful xanthate chemisorption, different species on the mineral surface, including hydroxyl ions, have to be replaced by the xanthate ions. Therefore, by increasing pH (essentially, the concentration of  $OH^-$  ions) the adsorption of xanthate decelerates (Fuerstenau *et al.*, 1990). Conversely, by increasing the concentration of xanthate ions, the adsorption of the collector should improve. Therefore, it could be suggested that the concentration of isopropyl xanthate is the most crucial factor for the apparent adsorption capacity. The relationship between xanthate,  $OH^-$  concentration, and adsorption density ( $\Gamma$ ) may be expressed by the following equation:

$$\Gamma = p + q \cdot \log \frac{[X^-]}{[OH^-]} \quad (4-14)$$

where  $X^-$  is a concentration of xanthate ions,  $OH^-$  is a concentration of hydroxyl ions, and  $p$  and  $q$  are empirical constants (Rau, 1961). The concentration of the  $OH^-$  ion in Equation 4-14 may be replaced by any depressant ion present in the pulp (Rau, 1961), such as  $SH^-$ ,  $S_xO_y^{n-}$ ,  $CN^-$  etc. (Poling, 1976).

Several mechanisms that may explain an improvement of xanthate adsorption with temperature have been suggested in the literature, such as through an increased collision frequency between adsorbate and adsorbent, increased diffusion rate, and increased chemical interactions (Khambhaty *et al.*, 2009; Salarirad *et al.*, 2021). From ethyl xanthate adsorption tests in the literature (Salarirad *et al.*, 2021) it follows that the highest resistance to mass transfer of xanthate molecules during adsorption occurs during the diffusion step. Since all activation energies for isopropyl adsorption on sulfides in the tests presented here were relatively low (15 to 25 kJ), it was concluded that diffusion was a limiting adsorption step for this system as well (Buxton *et al.*, 1988; Ulf, 2017). An increase in diffusion with an increase in temperature may be attributed to decreased viscosity of the solution (Chowdhury *et al.*, 2011). Positive values of the enthalpy of activation indicated the endothermic character of isopropyl xanthate adsorption on copper-activated surfaces of sulfide minerals in this study. Theoretically, that would mean an increase in the adsorption capacity of adsorbent with temperature (Åqvist *et al.*, 2017). However, similar to the conclusions reported for chalcopyrite adsorption tests in the literature (An and Zhang, 2020; Zhang *et al.*, 2019), these

temperature-driven changes were not pronounced (in this case – not statistically significant for all tested minerals). Observed negative values of the entropy of activation may be interpreted by a loss in the rotational and translational motions of adsorbate (in this case - xanthate molecules) after adsorption (Åqvist *et al.*, 2017). Negative entropies may also indicate that no major changes in the internal structure of the adsorbent (mineral surface) occur during the xanthate adsorption process (Chowdhury and Saha, 2011). Small enthalpies and negative entropy values in our tests confirm the associative character of the reactions (bond creation prevails over bond breaking, and energy distribution has lower degrees of freedom) (Bellam and Jaganyi, 2017). Large positive Gibbs activation energy values indicate that the adsorption of xanthate molecules requires energy to form adsorption products on a mineral surface (Chowdhury *et al.*, 2011). The lowest Gibbs activation energy among the three tested minerals was estimated for galena (Table 4-3), which implies higher adsorption rates for this mineral (Papamichael *et al.*, 2019; Zhu *et al.*, 2009). Thus, isopropyl xanthate apparent adsorption rate under the tested conditions varied between around 2 to 11 nmol/(m<sup>2</sup>·s) for galena, while for pyrite and sphalerite, this range was 2-9 nmol/(m<sup>2</sup>·s) and 1-10 nmol/(m<sup>2</sup>·s) respectively.

Regarding copper sulfate concentration, it has been seen to positively impact the adsorption rate of xanthates on sulfidic surfaces and improve the adsorption capacity of a sphalerite surface. Since sphalerite has a large band gap leading to a low ability to transfer electrons and interact with the xanthate collector, activation of sphalerite surfaces with copper ions through an ion-exchange mechanism lowers the band gap more than 3 times (Abramov, 2010). Therefore, copper activation facilitates electron transfer reactions with the collector, producing metal-xanthate complexes with lower solubility on mineral surfaces (Buckley *et al.*, 1989; Gerson *et al.*, 1999; Kartio *et al.*, 1998). Based on the solubility values these complexes are arranged in the literature in the following order: FeX<sub>2</sub>>ZnX<sub>2</sub>>PbX<sub>2</sub>>CuX<sub>2</sub> (Sheikh, 1972). In order to explain the effect of copper activation on the adsorption rate of xanthate the following mathematical expression was suggested in the literature (Ejtemaei, 2016):

$$\frac{dx}{dt} \propto [A]_{surf}[X] \quad (4-15)$$

where  $x$  is the amount of xanthate adsorbed on a mineral surface,  $[A]_{surf}$  is the density of available activated adsorption sites on a mineral surface,  $[X]$  is the concentration of xanthate ions in the

solution. In the current research the initial concentration was not seen to significantly impact the adsorption rate. Haung and Miller investigated an adsorption order of xanthate on pyrite and showed that, depending on pH level, it varied from around 0.2 to 0.6 (Haung and Miller, 1978). Therefore, since xanthate adsorption is best described by an equation with an adsorption order lying between zero-order kinetics (rate is independent of the initial concentration (Petrucchi *et al.*, 2007)) and the first-order kinetics (controlled by initial reagent concentration (Petrucchi *et al.*, 2007)), statistically significant effects of initial concentrations on the adsorption rate were not observed.

Apart from the copper sulfate, activation of the sites on a mineral surface for collector adsorption is achieved by dissolved oxygen presence. Dissolved oxygen adsorption on sulfidic surfaces is known to render them less predisposed to form thick hydration layers (Klymowsky, 1968). Moreover, for example, non-oxidized galena as an n-type semiconductor has an excess of free electrons at the surface layers preventing xanthate adsorption. Oxygen adsorption takes up these free electrons rendering galena a p-type semiconductor. At this point, xanthate ions may adsorb by transferring electrons to a new p-type galena surface (Plaksin, 1957, 1959). Conversely, prolonged exposure to oxygen may be detrimental and lead to the formation of thiosulfates on sulfidic surfaces (Klymowsky, 1968), which compete with xanthate for adsorption sites. Another aspect of dissolved oxygen's importance in flotation is that together with temperature, high DO concentrations were reported to increase the rate of xanthate decomposition (Grano *et al.*, 1997b). These two parameters should be monitored on a plant as factors impacting flotation sub-processes and performance by impacting pulp potential. For example, low DO levels were noted to improve copper activation of sphalerite by lowering pulp potential (as oxidizing conditions inhibit copper uptake by sphalerite surface) (Dichmann, 2000). It could potentially explain lower xanthate adsorption kinetics and capacity for sphalerite in our tests at lower temperatures (high levels of dissolved oxygen in cold pulps may potentially counteract copper activation of sphalerite, which impairs xanthate adsorption).

Dissolved oxygen levels are also important for the application of cyanide depressants in flotation. It has been suggested that the rate of metal dissolution ( $d[Me]/dt$ ) with cyanides is dependent on cyanide concentration ( $[CN^-]$ ) and dissolved oxygen concentrations ( $[O_2]$ ), Equation 4-16:

$$\frac{d[Me]}{dt} = k_s \sqrt{[CN^-][O_2]} \quad (4-16)$$

where  $k_s$  is a leaching rate constant (Crundwell and Godorr, 1997; Ellis and Senanayake, 2004). Theoretically, this would imply better cyanide action at lower temperatures because of higher dissolved oxygen levels. However, it has been demonstrated that even though oxygen levels are lower at higher temperatures, temperature has a stronger positive effect on the metal dissolution process in cyanide leaching until 85 °C (Currie, 1937; Julian *et al.*, 1921). These conclusions are supported by captive bubble tests. For example, at 35 °C two times less cyanide was needed to prevent bubble contact with a pyrite surface as compared to 10 °C tests (Wark and Cox, 1938). Therefore, there is evidence that the cyanide regime is sensitive to temperature variations and may be theoretically responsible for poor performance of flotation plants in winter.

Dextrin, however, has been considered a possible substitute for toxic inorganic pyrite depressants (*e.g.* cyanides, sulfites) in base-metal recovery systems (Koleini *et al.*, 2012; López-Valdivieso *et al.*, 2007). For all adsorption tests an absence of an effect of dextrin concentration on xanthate adsorption was noted (for both adsorption rate and adsorption capacity). This corresponds well with current perceptions on the mechanism of dextrin depression of sulfide minerals. It is believed that xanthate and this polysaccharide are co-adsorbed, and the depressing action is achieved by larger dextrin molecules enveloping smaller xanthate species on a mineral surface (López-Valdivieso *et al.*, 2004; López-Valdivieso *et al.*, 2018).

Considering that polysaccharide adsorption is enhanced by the presence of  $Ca^{2+}$  species through reduction in electrostatic repulsion (Asimi Neisiani *et al.*, 2023; Bicak *et al.*, 2007), and by taking into account that lime solubility is improved at lower temperatures (illustrated through lower lime demand at lower temperatures in our tests), it may be speculated that dextrin depression could be even improved at lower temperatures. Furthermore, it has been demonstrated in the chalcocite example that mineral coverage by dextrin is increased at lower temperatures owing to the physisorption character of the process (Nyamekye, 1993). Laboratory trials conducted by Glencore showed better selectivity in sulfide flotation with dextrin at colder pulps as opposed to sodium cyanide (Malafarina and Deredin, 2021).

When considering the adsorption selectivity calculations, the highest galena-sphalerite selectivity was estimated at colder temperatures, which is in agreement with the historical flotation data from

Base Metals Mining Corp. (USA), where an improved selectivity against zinc in lead cleaners was observed during winter at pulp temperatures around 16 °C (Taggart, 1945). Regarding sphalerite – pyrite and galena – pyrite adsorption rate selectivity, it corresponds well with pyrite flotation rate data (no froth) reported by O'Connor *et al.* (O'Connor *et al.*, 1984), where a second acceleration step in the flotation rate is observed between 30 and 50 °C. This acceleration step may also explain the shrinking of the feasible area on the sphalerite-pyrite selectivity overlaid contour plots (Figure 4-7) at 35 °C and 45 °C. Additionally, Liu *et al.* (Liu *et al.*, 2019) reported a considerable increase in xanthate adsorption on pyrite with temperature, which is in agreement with the results presented in this thesis. Because pyrite is the most electrochemically active mineral (the most cathodic) when compared to galena and sphalerite, it will oxidize faster and form oxy- and hydroxy- complexes on its surface with increasing pH, preventing xanthate adsorption (Boulton *et al.*, 2001). Therefore, to maintain an adequate level of selectivity, with an increase in temperature, the selectivity curve rises towards higher pH levels.

Modeling obtained adsorption responses with isotherms allowed the extraction of additional information regarding the mechanism of adsorption. The Freundlich model, designed for heterogeneous surfaces, gave an adequate fit to the adsorption data presented in this paper. Despite the Langmuir model being used extensively for describing xanthate adsorption (Han *et al.*, 2020; Potapova, 2009; Tajadod, 1998; Zhang *et al.*, 2021b), it has been confirmed by this experimental data and research done by Haung and Miller (Haung and Miller, 1978) that xanthate adsorption on non-synthetic sulfide minerals is not a Langmuir process. Moreover, for the current tests, the Temkin model gave the best fit for isopropyl xanthate adsorption on galena, pyrite, and sphalerite surfaces, which were pre-conditioned with dextrin and copper sulfate.

The Temkin model fit implies the multi-layer character of adsorption and the presence of heterogeneous binding sites on the solid surface (Chu, 2021). Temkin model constants (in J/mol) are related to the heat of adsorption and can describe the nature of the adsorption process (chemisorption or physisorption). The obtained values of Temkin constants (b-coefficients) in this work were between 5.6 and 19.6 kJ/mol. Since these values are between 1-20 kcal/mol (4.2 kJ/mol and 83.7 kJ/mol) it can be concluded that both, physical and chemical adsorptions, are taking place (Ettish *et al.*, 2021).

The most common process for selective Zn-Pb ore flotation is the Sheridan-Griswold regime, where lead minerals are floated first at pH 9, followed by zinc minerals' flotation at pH 11 (Abramov, 2004; Bulatovic, 2007). The microflotation results from this paper demonstrate fluctuations of galena, sphalerite, and pyrite floatabilities at the respective pH levels. The existence of an optimal flotation temperature level around standard conditions (25 °C) is explained by the lowest surface energy observed from the IGC data of the concentrates. Similar results with the maximum contact angle (hence, lowest surface energy) were found for galena and sphalerite between 25 and 35 °C in a potassium ethyl xanthate collector system (Gayle and Smelley, 1960).

The lowest total surface energy indicates surfaces with higher hydrophobicity. It is explained by electrons being strongly bound to such surfaces (Desmet *et al.*, 2017). Poor floatability of sulfides at temperatures above 40 °C was explained in the literature by increased desorption rate of collectors, increased decomposition of xanthate molecules, increased mineral dissolution, and increased formation of hydrophilic precipitates on a surface (*e.g.* sulfoxy complexes) (Bicak *et al.*, 2018; Le *et al.*, 2020). Moreover, Abramov has reported that at elevated temperatures the mechanism of sulfide oxidation changes with more thiosulfate ions produced, which should be addressed by xanthate dosage increase (Abramov, 2010).

The largest decrease in the recovery above the optimum temperature zone was observed for sphalerite. Scanning electron microscopy detected some precipitates on sphalerite particles. EDS mapping and point analysis revealed that these precipitates are composed of calcium carbonate. These results correspond well with thermodynamic calculations, where a decrease in calcium carbonate solubility with an increase in temperature was observed. Precipitation of hydrophilic calcium carbonate species on sphalerite may be the reason for an increase in the dispersive component (and ultimately the total surface energy) of sphalerite concentrate and tailings at 45 °C.

Slight improvements in adsorption capacity results at intermediate temperatures (room temperature conditions) were also noted for galena and sphalerite (Figure 4-4e-f), which is in line with IGC and microflotation results. Furthermore, the recorded increase in lime consumption with temperature (triggered by lower lime solubility at higher temperatures (Rabinovich and Havin, 1978)) could potentially further deteriorate the flotation process by increasing pulp temperature even more (through exothermic reaction). Thus, for example, an analysis of Neves-Corvo zinc flotation plant data has revealed a discrepancy between the theoretical energy model with plant

measurements, which were attributed to an additional energy input via increased lime addition at high temperatures and associated exothermic effects (Fernandes, 2016). Increased calcium ions released during lime dissolution in cold pulps retards copper activation by competing with them for the reactive surface sites (Deng *et al.*, 2013). Thus, calcium ions were recorded to adsorb at sphalerite–water interface by moving into the Stern layer. Even though this calcium adsorption layer was reported to be weak (adsorption of calcium was limited and reversible without a release of an equivalent number of protons in the diffuse layer and bulk solution), it renders sphalerite surface less negative and decreases an electrostatic attraction of copper hydrolysis species to the sphalerite surface (Deng *et al.*, 2013).

IGC results demonstrated heterogeneous distribution of energy sites. However, the specific energy components for galena and sphalerite had more narrow distribution functions at 25 °C. Moreover, for galena, the highest degree of heterogeneity was observed for samples conditioned at 5 °C. This may be explained by the presence of a wider variety of surface complexes, caused by increased interaction with oxygen (higher dissolved  $O_2$  levels recorded at lower temperatures), and higher calcium levels from increased lime solubility (revealed through lime consumption variation in this paper) preventing xanthate adsorption. These potential alterations in surface conditions lead to a higher competition of xanthate on a mineral surface, revealed by lower adsorption kinetics at lower temperatures and higher required xanthate dosages obtained from thermodynamic calculations.

Eventually, the higher heterogeneity of a mineral surface could also be attributed to the lower collector adsorption responses resulting in the lower microflotation yields. In the case of sphalerite, the largest variability was observed for dispersive energy components, which could be due to the precipitation of calcium carbonate complexes on a mineral surface at 45 °C, explaining the lowest microflotation recoveries.

#### 4.6. Conclusions

Adsorption kinetics of sodium isopropyl xanthate was heavily controlled by pH, temperature, and copper sulfate concentrations. The amount of adsorbed xanthate was seen to be strongly impacted by the initial xanthate concentration. Among the three minerals copper sulfate concentration significantly impacted kinetics and the adsorption capacity only for sphalerite. For galena and pyrite, pH was a stronger contributor to the adsorption capacity compared to sphalerite.

Microflotation results revealed optimum flotation conditions for all three tested minerals at around room temperature. The microflotation yields corresponded well with surface energy results (total surface energy results). Lower recovery of sphalerite at higher temperatures may be explained by the formation of calcium carbonate precipitates. Lower recoveries at lower temperatures may be explained by a shift in the xanthate – oxy-complexes equilibrium, described by thermodynamic calculations, measured dissolved oxygen levels, and surface heterogeneity. While mechanisms explaining true-flotation responses described in this Chapter significantly contribute to the overall flotation performance, they constitute only the primary concentration part of flotation. After being hydrophobized and collected by bubbles (primary concentration) mineral particles have to pass through secondary concentration in flotation froth, which is covered in the next Chapter.



---

## Chapter 5. Assessment of Temperature Impact on Secondary Concentration: Foam and Froth Stability Issues

### 5.1. Introduction

The stability of the froth plays a crucial role in the overall flotation performance. The froth phase provides another level for the separation of truly floated mineral particles (via attachment to a bubble), and entrained mineral particles (via mechanical mass transfer with water) (Harris, 1982). Therefore, this secondary concentration (separation) depends on the efficiency of water drainage from the flotation froth. A stable froth with high water recovery typically provides higher recovery values, whereas unstable froth can produce higher grades by increasing the selectivity between minerals (Morar *et al.*, 2006). Flotation froth should also be stable enough to transport the collected mineral particles over the lip of the cell to the concentrate. However, too-stable a froth creates problems with pumping and thickening after flotation (Wills and Finch, 2016).

Morar *et al.* outlined solution chemistry, concentration of particles in froth and their nature as dominant factors defining froth stability (Morar *et al.*, 2006). The following sub-sections investigate the effect of temperature on froth stability, starting with a simple two-phase system (foam), and then exploring actual froth (3-phase systems). For the foam tests, only bulk characteristics were studied, such as height and half-life. Froth analysis included bulk and surface stability characterization. Froth bulk features were reflected via bubble size on the froth surface (analysis of coalescence) and froth height. Froth surface characteristics were analyzed with bubble burst rate, the horizontal speed of the top froth layer, and air recovery.

### 5.2. Foam Stability at Different Temperatures

It is particularly important to understand the fundamental aspects of foam stability as it can help to better understand the behavior of the froth system, without masking the impact of individual factors by a strong stabilizing/destabilizing effect of particle presence (Klassen and Mokrousov, 1959).

The performed design of the experiment in a small flotation column has produced 32 foam stability responses, given in Appendix F. Response surface regression results and goodness of fit are

summarized in Table 5-1. The  $F$ -values observed for both models (responses) were above the  $F$ -critical value of 2.65, thus, meaning that under the considered confidence level of 95%, the model is acceptable. As can be seen from the  $p$ -values, under the assumption of a confidence interval of 95% ( $\alpha = 0.05$ ), the constructed models are also significant. High  $R^2$  values also indicate that models explain large proportion of the variability in the observed data. Therefore, the models may be considered statistically significant.

Table 5-1. Summary of CCD models' goodness of fit and ANOVA.

F-Value		$p$ -Value		$R^2$		$R^2_{adj}$		SD <sup>1</sup>	
$\gamma_s$	$\gamma_s^w$	$\gamma_s$	$\gamma_s^w$	$\gamma_s$	$\gamma_s^w$	$\gamma_s$	$\gamma_s^w$	$\gamma_s$	$\gamma_s^w$
1337.60	401.17	0.000	0.000	99.91%	99.72%	99.84%	99.47%	0.95	0.98

Notes: <sup>1</sup> SD—standard deviation.

The regression equations produced for foam half-life time and foam height in coded units are presented in Equations 5-1 and 5-2, with statistically significant equation parameters provided in bold:

$$\begin{aligned}
 y(t_{1/2}) = & \mathbf{1.546} - \mathbf{0.5768}x_1 + 0.01x_2 + 0.1166x_3 - 0.0163x_4 + \\
 & +0.1414x_5 + +0.1554x_1^2 + 0.0316x_2^2 + 0.1329x_3^2 + 0.0579x_4^2 - 0.1214x_5^2 + \\
 & +0.131x_1x_2 + +0.134x_1x_3 - 0.106x_1x_4 - 0.06x_1x_5 + 0.044x_2x_3 - \\
 & -0.031x_2x_4 + +0.001x_2x_5 - 0.059x_3x_4 + 0.027x_3x_5 + 0.077x_4x_5
 \end{aligned} \tag{5-1}$$

$$\begin{aligned}
 y(H_f) = & \mathbf{11.96} - \mathbf{4.429}x_1 + \mathbf{1.096}x_2 + \mathbf{0.621}x_3 + 0.138x_4 + \mathbf{7.463}x_5 + \\
 & +\mathbf{1.902}x_1^2 + \mathbf{0.602}x_2^2 + 0.327x_3^2 + 0.34x_4^2 + \mathbf{1.477}x_5^2 + 0.281x_1x_2 - \\
 & -\mathbf{0.856}x_1x_3 - 0.044x_1x_4 - \mathbf{3.969}x_1x_5 + 0.031x_2x_3 - 0.381x_2x_4 + \\
 & +\mathbf{1.044}x_2x_5 + 0.481x_3x_4 - 0.144x_3x_5 - 0.331x_4x_5
 \end{aligned} \tag{5-2}$$

Factor-by-factor investigations using the  $t$ -test revealed important parameters of the model; the results are displayed in Figure 5-1a. The level of aeration ( $J_g$ ), water temperature ( $T$ ), pH, and MIBC dosage had a pronounced effect on foam stability, while the SIPX dosage's  $t$ -value is below 2.2 ( $t_{critical}$ ). An increase in  $J_g$ , pH, and MIBC dosage had a positive effect on foam height, whereas temperature increase had a clear negative effect. Important two-way interaction terms of the model

are temperature×aeration, temperature×temperature, aeration×aeration, pH×aeration, temperature×MIBC dosage, and pH×pH. Regarding the foam half-life time, only one parameter was found to be statistically significant: temperature. Similar to the foam height case, temperature had a negative impact on the foam half-life time (as seen in Figure 5-1b).

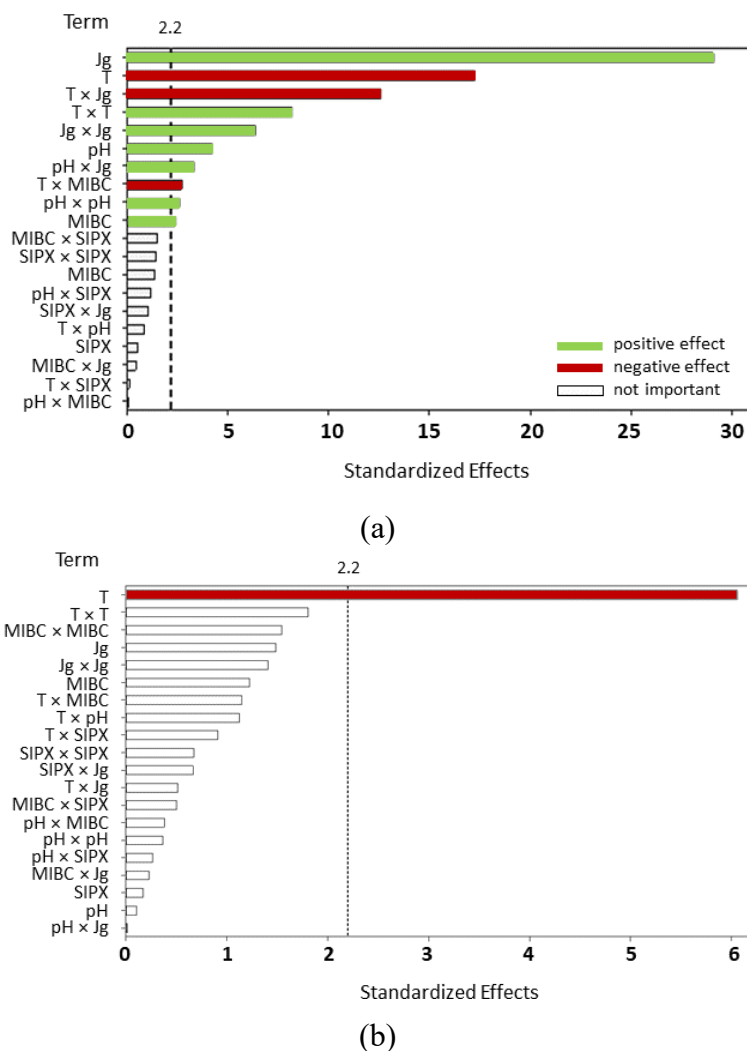


Figure 5-1. Pareto chart of standardized effects of model terms on: (a) foam height; (b) foam half-life time.

From the contour plots (Figure 5-2), Jg appears to have an impact on the foam half-life time at lower temperatures (at higher Jg, foam half-life was longer). However, this effect disappears as soon as the temperature increases above 15 °C. Conversely, pH appears to have a more pronounced effect at extreme temperatures: at higher temperatures, pH increase stabilizes foam, which is reflected by longer foam half-life. Regarding MIBC dosage, a clear effect could be observed at higher temperatures (above 25 °C).

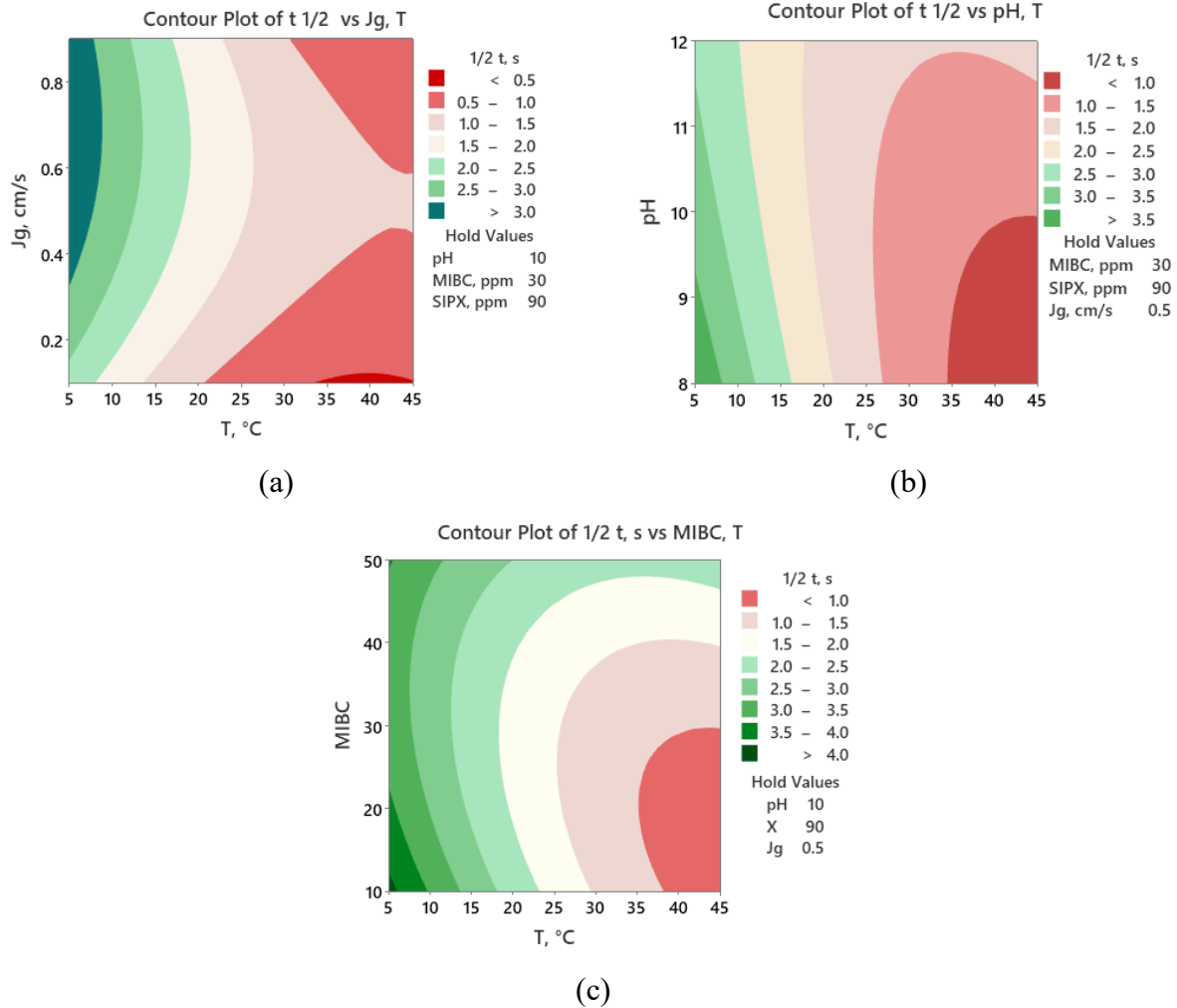


Figure 5-2. Contour plots of foam half-life time in: (a) temperature versus aeration coordinates; (b) temperature versus pH coordinates; (c) temperature versus MIBC coordinates.

From the foam height contour plots (Figure 5-3) it can be observed that pH has a similar impact on foam depth as foam half-life in pH-temperature coordinates: the pH effect is pronounced at elevated temperatures. However, the contour plot of foam height in MIBC-temperature coordinates (Figure 5-3c) shows that MIBC does not significantly affect foam height when the temperature is above 25 °C. Aeration-temperature pairing influences foam height in a different way (as seen in Figure 5-3a): temperature has a limited influence on the foamability at low  $J_g$ . The effect starts to be more pronounced only when  $J_g$  reaches 0.5 cm/s. Above this value, both factors have an approximately similar impact on foam height, as suggested by the 45° C contour line.

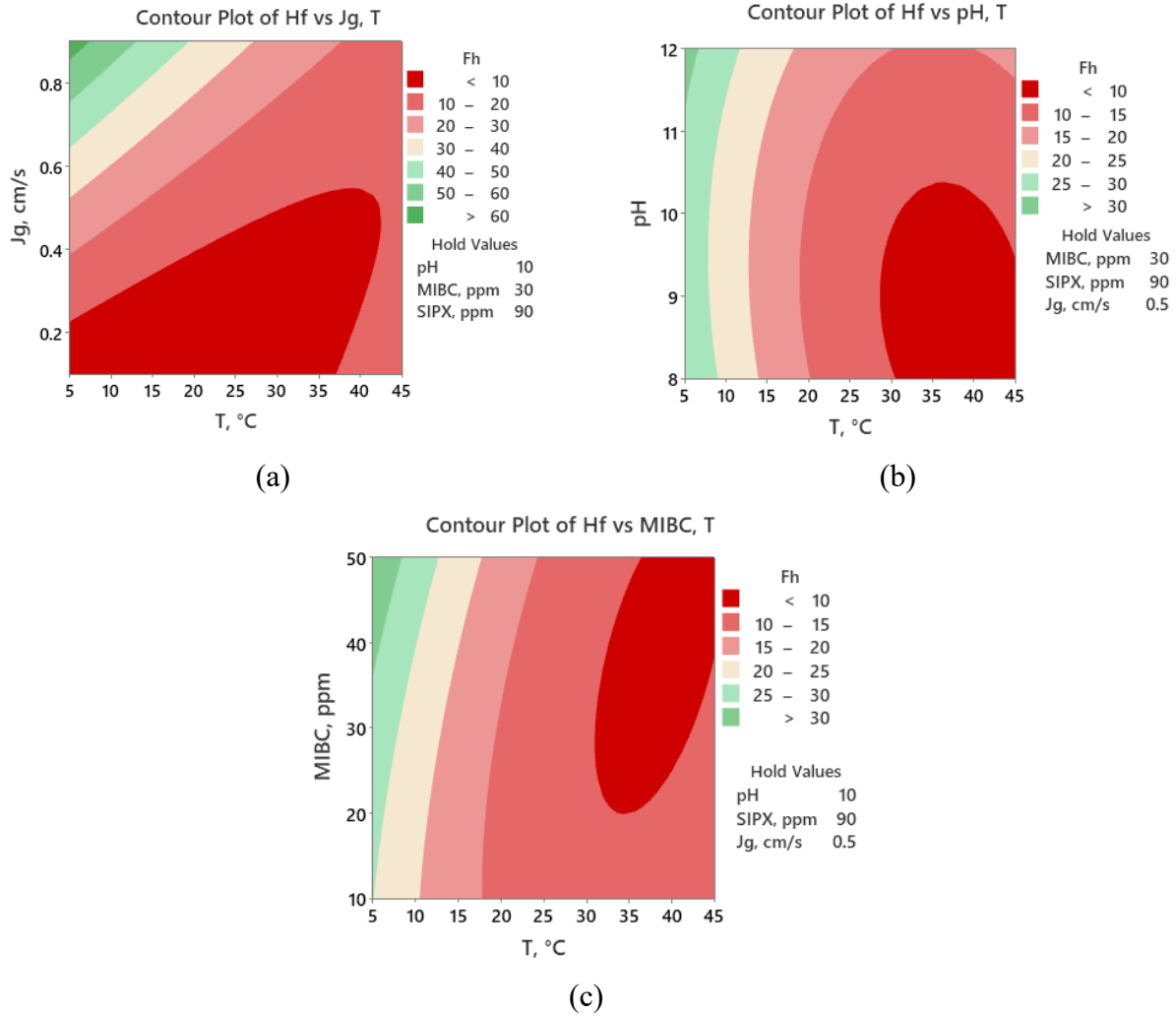


Figure 5-3. Contour plots of foam height in: (a) temperature versus aeration coordinates; (b) temperature versus pH coordinates; (c) temperature versus MIBC coordinates.

### 5.3. Temperature Effects on Froth Properties

Temperature effects on the froth properties in a Denver flotation cell are given in this chapter in the order of increasing complexity: from monomineralic systems with low solids in the pulp to poly-mineral systems with VMS and SEDEX ores. The stability parameters are also given in the increasing complexity order: from froth stability indicators (bubble size, froth height, bubble burst rate, froth height over the flotation cell lip) to calculated from the indicators stability factors (air recovery and froth stability factor).

### 5.3.1. Bubble Size in the Monomineralic Froth

The top size of bubbles on the froth surface was generally larger bubbles in cold pulps for all tested monomineralic samples at 10% solids in pulp (Figure 5-4). Additionally, it was reported that bubble sizes increase with flotation time (froth degradation). The projection area of the largest bubbles on the froth surface for the tests with all three minerals varies approximately between 0.1 and 0.4 cm<sup>2</sup>. At a temperature of 30 °C, the shapes of bubble size models represent a “bathtub” curve: rapid decrease of bubble size at the beginning of the process, reaching the curve plateau area, and a slight increase in bubble sizes by the end of the flotation test. For pulps at 10 °C for pyrite and sphalerite, the shapes of the models are different: there were no extremely large bubbles at the beginning of the flotation, as well as no extensive plateau area of the curve. The bubbles for these two minerals continuously increase during the flotation process.

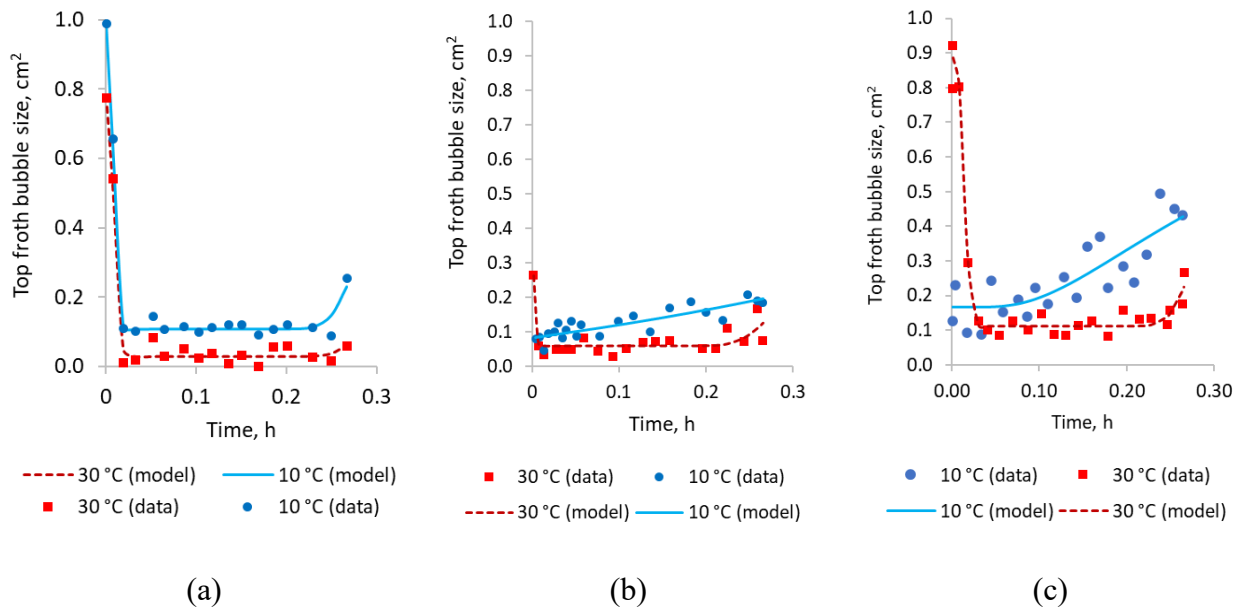


Figure 5-4. Top froth maximum bubble size versus flotation time for at 10 °C and 30 °C for: (a) galena; (b) pyrite; (c) sphalerite.

### 5.3.2. Froth Depth in Ore Flotation

Another bulk froth stability parameter, froth depth, was analyzed in tests with VMS ore. As it is seen from the plots in Figure 5-5, there is a considerable variation in froth depth with temperature. The thinnest froth was observed at above 40 °C (approximately 20 mm), while the thickest froth was recorded at below 10 °C (approximately 30 mm), indicating more stable froth at lower temperature. Thicker and more stable froth contained more water, which is reflected via positive

regression plot for froth depth versus water recovery (Figure 5-5b). Water recovery changed from slightly above 100 ml to more than 400 ml by increasing temperature to more than 30 °C. Higher froth stability and water recovery eventually resulted in generally higher mineral yields, which is reflected through another positive trend, illustrated in Figure 5-5c.

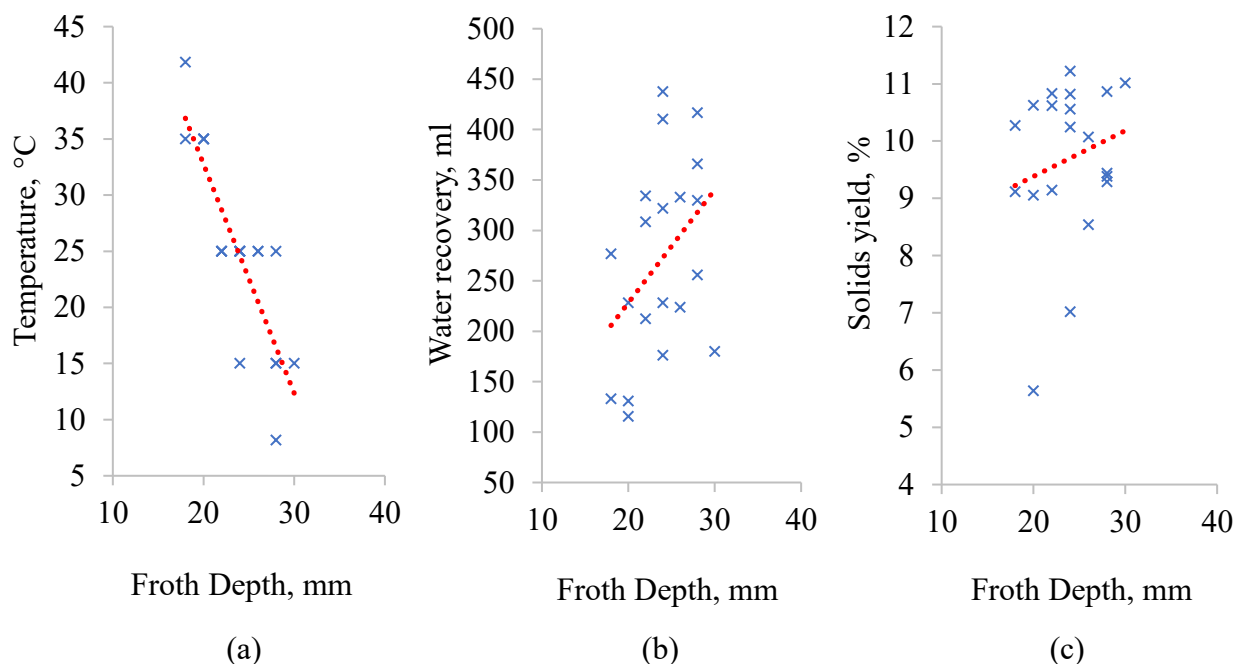


Figure 5-5. Froth depth depending versus temperature (a), water recovery (b), and solids yield (c)

### 5.3.3. Froth Stability in Ore Flotation

In SEDEX ore tests, both stability characteristics (surface and bulk) were recorded. The statistical significance of all produced models for froth stability is given in Appendix H. For all froth stability characteristics contour plots in the coordinates of Temperature and Cu-sulfate (Activator) dosage were constructed. With the decrease in temperature, a general increase in froth horizontal speed toward the concentrate zone was observed (a 15 to 20% increase across the tested temperature range). Moreover, with the decrease in temperature, laser recordings showed increased froth heights over the lip. Since both of these parameters increased at lower temperatures, the calculated air recovery also followed the same pattern (Figure 5-6). The contours of the plots were strongly controlled by the x-axis, which demonstrates high variability of investigated parameters with temperature. Copper sulfate in the applied dosages had a small positive effect on the froth height over the lip and froth speed, which may be attributed to increased stabilization through improvements in solids yield.

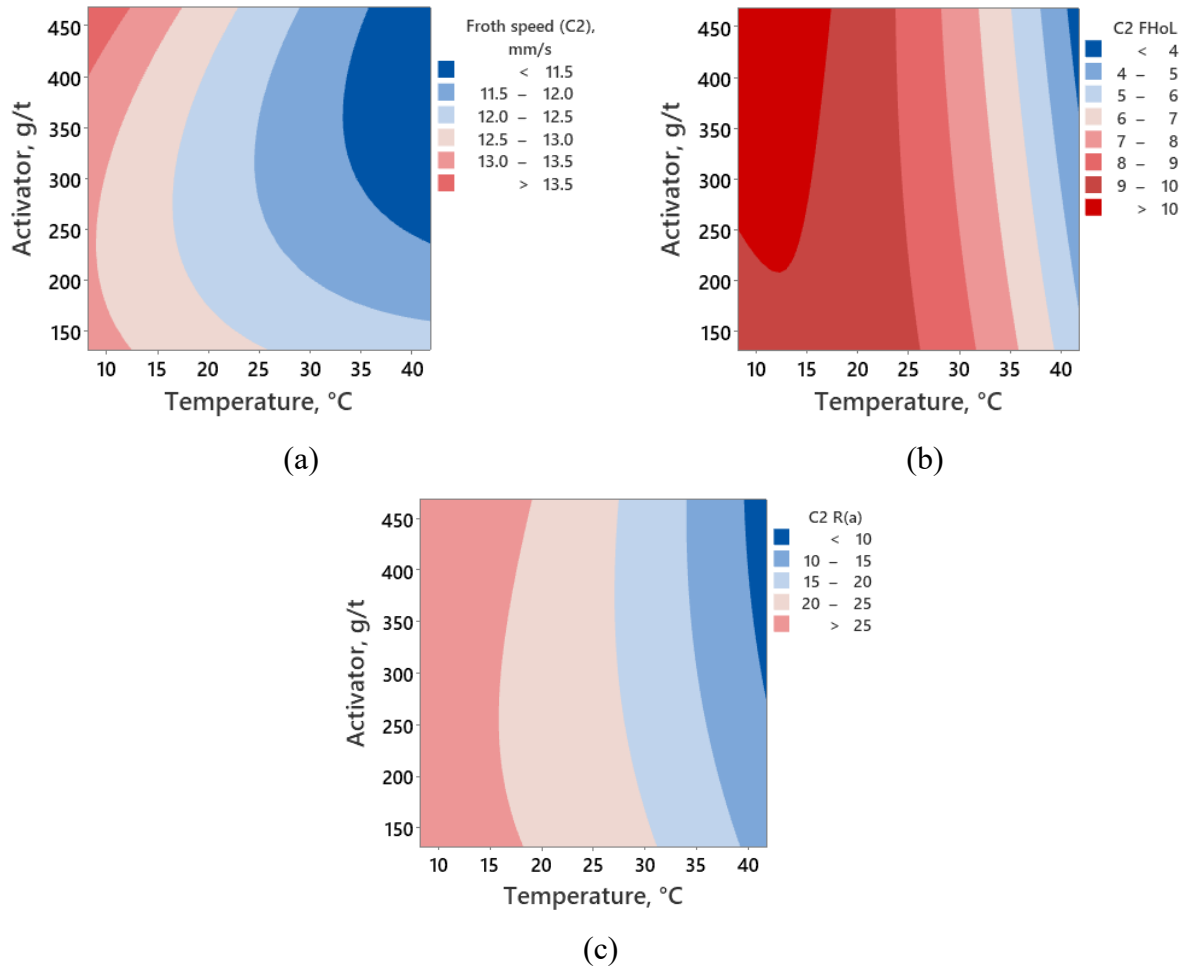


Figure 5-6. Contour plots of the horizontal froth speed (a), froth height over the lip (b) and air recovery (c) as a function of temperature and copper sulfate (activator) dosages

Bubble burst rate and bubble size, conversely, had an increasing trend with temperature (Figure 5-7). Similar to the bulk froth stability characteristics, copper sulfate dosage was seen to also have a small stabilizing effect for froth surface stability (lower burst rates and higher froth stability factor). From the froth stability factor, it can be deduced that by decreasing the temperature from above 40 °C to below 10 °C the theoretical time for the froth to collapse below the level of the cell lip increases from below 2 seconds to up to approximately 5 seconds. Detailed statistics on bubble size distribution on the forth surface at different temperatures is given in Appendix K.



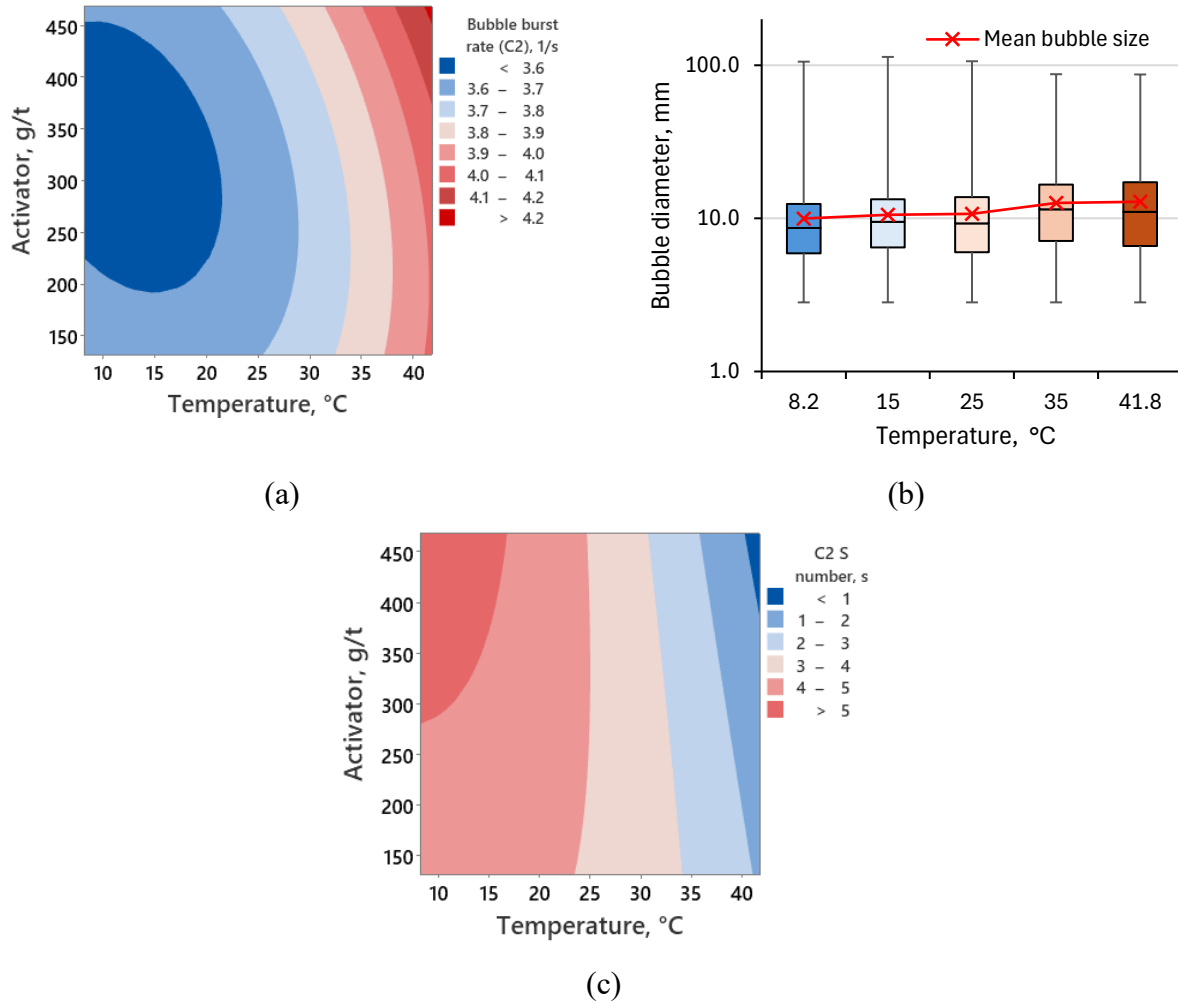


Figure 5-7. Contour plots of bubble burst rate (a) and froth stability factor (c) as a function of temperature and copper-sulfate dosage; Box and Whisker plot of bubble size with temperature (middle line represents median, the box covers upper and lower quartile, the vertical line expands until extreme values) (b)

#### 5.4. Numerical Simulation of Froth Drainage

From numerical simulations of froth drainage through a single plateau border (Figure 5-8) for SEDEX ore flotation at 32% solids in the pulp at 5 temperature scenarios (8.2, 15, 25, 35, and 42 °C), it could be seen that there is a general increasing trend for the froth drainage with temperature. In this particular simulation an effect of retardation of the froth drainage by frother molecules was not considered.

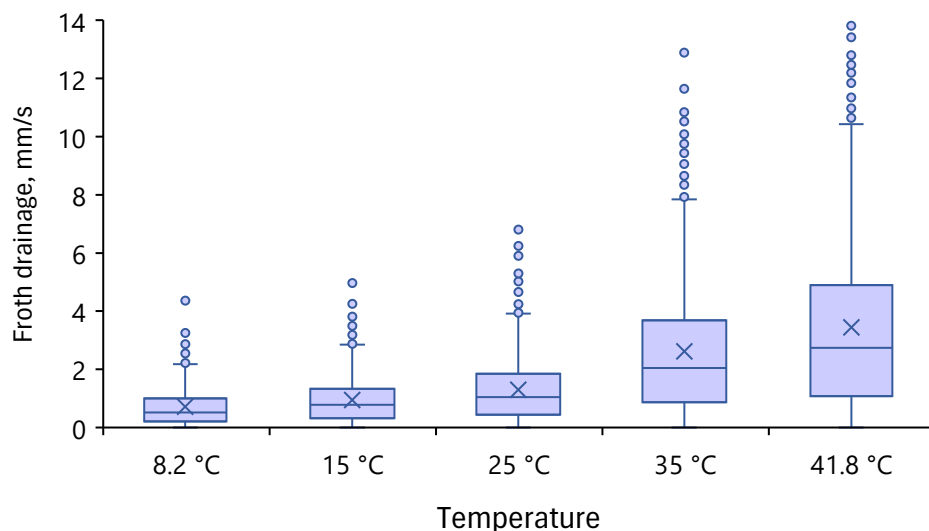


Figure 5-8. Results of Monte-Carlo simulation of a froth drainage in SEDEX ore flotation for a single plateau border

In another set of simulations Figure 5-9, models that consider drainage retardation by froth surface shear viscosity were built. These models yielded generally lower values of froth drainage but preserved similar trends with regard to a temperature effect (faster drainage at higher temperatures). From the reagent perspective, it could be seen that the fastest drainage was observed for SDS, which had the lowest surface shear viscosity. An order of magnitude lower drainage was estimated for the MIBC system and the lowest drainage for the glycol-based frother (PPG and PGE).

It should be emphasized that simulation results for SDS and PPG/PGE frothers are based on the assumption of flotation above the critical coalescence concentration (CCC). Above the CCC, bubble size depends mainly on hydrodynamic conditions in flotation and bubble generation mechanism (*e.g.* sparger geometry) (Cho, 2001). Therefore, the bubble size distribution was assumed to be the same for all three frothers for this simulation.

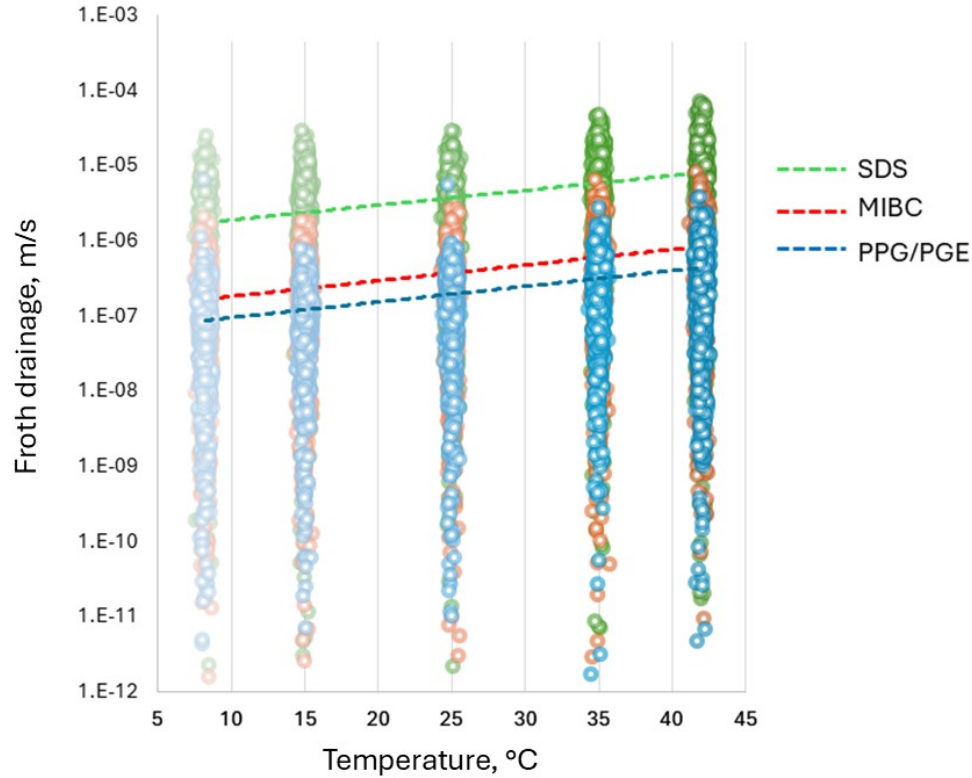


Figure 5-9. Froth drainage simulation with SDS, MIBC and PPG/PGE frothers used at concentrations in the flotation range (below 50 ppm)

## 5.5. Discussions

### 5.5.1. Foam Stability

From an analysis of the foam stability results, individual effects of temperature, aeration, pH, and MIBC dosage, as well as of a range of two-way interaction terms have statistically significant impact on foam stability. Thus, aeration is the most important factor for foam height. As the gas flow rate increases, thicker foams are produced due to more bubbles accumulating (Jiang *et al.*, 2020), which increases the volume and froth coefficient (a product of froth volume and froth stability in seconds).

Frother dosage is another important parameter for foam stability, proven by the foam height results presented. MIBC adsorption at the air/water interface increases electrostatic repulsion between bubbles, which retards the thinning of the liquid film. From the perspective of disjoining pressure, such electrostatic repulsion creates positive pressure, which stabilizes the foam (Wang and Yoon, 2006).

The aeration–pH interaction pair could be explained by aeration bubbles coming in full contact with water and helping dissolved CO<sub>2</sub> escape from the solution (outgassing). A subsequent drop in carbonate concentration induces a pH increase (Jingwei *et al.*, 2022).

The observed increase in foam height with pH (when pH is controlled by lime) correlates well with the literature (Corin *et al.*, 2011; Manono *et al.*, 2012). The suggested mechanism explaining the increased stability is the reduction of repulsive forces of bubbles and particles. This results in an increase in the ionic strength of the pulp and subsequent shrinkage of the double layer. The mechanism has previously been confirmed by zeta potential measurements (Paulson and Pugh, 1996; Yoon and Sabey, 1982). The increased foam stability eventually translates into increased water recovery and solids entrainment. Manipulation of lime dosages was also reported as a possible means of reducing frother consumption (Zanin *et al.*, 2019). In some cases, high salt concentration (such as that reported for Raglan Mine in Canada (Quinn *et al.*, 2007)) in process water allows flotation to operate without frother.

Another significant interaction between factors that control foam height was temperature and MIBC dosage. As seen from the Pareto chart (Figure 5-3a), the interaction is negative, which could be explained by the ease of MIBC evaporation, reflected by a low flash point (41 °C) (Monument Chemical, 2022). In industry, MIBC has been reported to evaporate directly from flotation cells (Poling, 1984). Thus, an increase in temperature speeds up MIBC evaporation, reducing frother concentration in the system, which produces less stable and, hence, lower height foam/froths.

The impact of aeration–temperature interaction on foamability could be explained in several ways. Foamability was reported to decrease with increasing gas solubility, which is temperature-dependent (Gevantman, 2010). Another connection between aeration, temperature, and foam height could be attributed to bubble size. An increase in aeration would increase bubble sizes (which would impact foam drainage).

For another froth stability parameter – half-life – only temperature was found to be statistically significant. Interestingly, MIBC dosage did not play a critical role in foam stability. This can be explained by the fact that the operating conditions for the tests were above or close to the critical coalescence concentration (around 10 ppm) reported for MIBC in various sources (Grau *et al.*, 2005; Gupta *et al.*, 2007; Guven *et al.*, 2020; Laskowski, 2004; Nassif, 2013). This indicates that

there was a negligible effect or no effect of the tested dosages on bubble size variation and hence, derived foam stability/instability. A stronger frother (PPG425), on the contrary, was reported to have a significant effect on foam water content/stability at values above CCC (Lepage, 2023). It can be explained by performed simulations (Figure 5-9), where a more pronounced effect of froth surface shear viscosity on the retardation of the froth drainage was observed for the PPG system, compared to the MIBC system.

### 5.5.2. Froth Stability

Tests in a three-phase system with MIBC revealed similar trends to foam stability with temperature, which is a general decrease in the stability parameters. In the bubble size results, it appears that at low solid concentrations (10 wt. %) the bubble size distribution on the froth surface in monomineralic flotation was shifting towards lower values at higher temperatures. This is counter to the results at higher solids content (32 wt. %) showing that at higher temperatures larger bubbles were observed. Additionally, Drogaris and Weiland have found in their experiments that the coalescence time exponentially decreases with an increase in temperature (Drogaris and Weiland, 1983b), and in systems with low molecular weight reagents, the coalescence time is approximately equal to the drainage time (Drogaris and Weiland, 1983a). This data from the literature explains the results with larger bubbles at higher temperatures.

For a system with low solids content, low froth stability may explain the observed bubble size trend. At low values of solids in a pulp, decreased viscosity of the system results in unstable froth (Farrokhpay and Zanin, 2011; Jeldres *et al.*, 2019). Thus, for example, in sulfide ore pulps, it was demonstrated that by increasing solids content from 5 % to 20 % almost Newtonian behavior rapidly switched to non-Newtonian, with the turning point being at 15 wt. % solids (Kilickaplan, 2009). This switch in the behavior is reflected by an increase in yield stress, which dampens the turbulence in the flotation cell (Schubert, 2008). Increased turbulence in the flotation cell coupled with detrimental temperature effects results in a shallow unstable froth, with a small bubble size as a result of increased bubble liquid film rupture, originating from increased mechanical stress. For this low solid content system a decrease in temperature, on the contrary, increases viscosity and improves froth stability, which results in thicker froth and larger bubble sizes. A schematic representation of the hypothesis is given in Figure 5-10. Concerning the origins of bubble size variations with temperature, some research claims such size variations originate from the pulp

phase (Jackman *et al.*, 2018) whereas, in other sources, it has been claimed that bubble size fluctuations are predominantly sourced from the processes occurring in the foam zone (coalescence) (Pugh, 2016). Most probably, both mechanisms play an active role in bubble size variation to a different extent and depending on the flotation conditions.

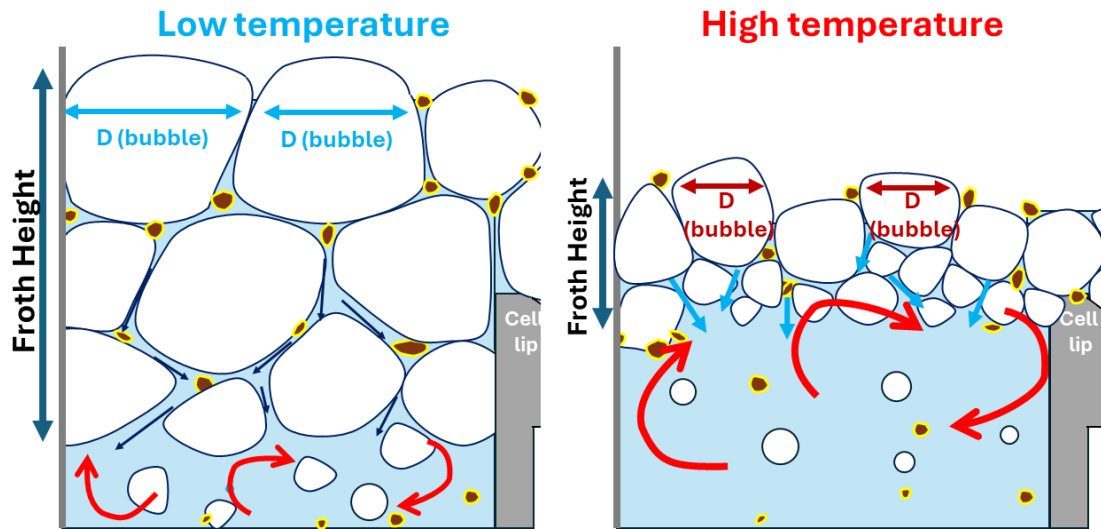


Figure 5-10. Graphical representation of the variation in bubble size at low and high temperature at low solids content (red arrows represent turbulent flows, blue arrows represent drainage, brown dots with yellow rim represent particles)

When analyzing bubble size profiles for low solid content systems, there is a trend of bubble sizes to decrease at the beginning, as a result of increasing froth drainage over time. Such increased froth drainage supposedly originates from decreasing pulp and froth viscosity, as solids in the batch system are continuously removed from the flotation chamber (recovered to the concentrate). After reaching a steady state (amounts of froth generated and collapsed become equalized), due to low MIBC concentration in the flotation cell (the frother is recovered with water to the concentrates, flotation pulp is diluted by the addition of water, a fraction of frother also evaporates), the bubble size starts to increase again, indicating froth degradation with time.

In tests with VMS ore (32 wt.% solids) froth height and water recovery increased at low temperatures, which is consistent with simulation results, that show a decrease in water drainage from the froth in cold pulps. Originating from changes in system viscosity, this decreased drainage stabilizes froth and increases solids yield. Too stable a froth is detrimental to the process as it may potentially lower the concentrate grade because of the entrainment mechanism (Schwarz and

Grano, 2005). Higher water content in the froth at lower temperatures is also reflected through increased froth mobility in the experiments with SEDEX ore flotation. Higher water content decreases froth viscosity, which means that the resistance to flow to the concentrate decreases (Sheng, 2013). Coupled with increased froth height, it results in higher air recovery at lower temperatures. Air recovery is a useful tool that can be used for the optimization of the flotation cell performance. Thus, according to the peak air recovery theory, an increase in the air rate until a certain level increases flotation recovery. By surpassing a certain peak value of aeration, froth stability starts to degrade, which causes increased losses of the valuable minerals (Shean *et al.*, 2017). It has been reported in the literature that this peak air recovery shifts to lower aeration values for shallow froths (Hadler *et al.*, 2012). Since it has been established by this research that with MIBC there is a variation in the froth thickness with temperature, it would imply that to maximize the output of a flotation operation, the aeration levels should be adjusted for each temperature season in a plant that uses MIBC as a principal frother. Air recovery, unlike bubble burst rate, was seen to decrease with temperature, which corresponds well with the inverse relationship between these parameters described by Equations 3-12.

Frother molecules and particles attached to the bubble surfaces in the froth are known to slow down the drainage process (Nguyen *et al.*, 2024; Ozan and Jakobsen, 2019). Different frothers produce different surface shear viscosities that immobilize the surface to a different degree and result in different drainage rates, which was observed in the simulations (Figure 5-9). By manipulating with frother composition, and creating blends with strong/weak frothers, desired froth drainage and froth stability for different temperature scenarios could be achieved.

## 5.6. Conclusions

For both (two-phase and three-phase) systems, temperature had a strong influence on stability parameters. In the tests with MIBC as the frother, an increase in temperature resulted in weaker, less stable, and thinner foam/froth with lower half-life, higher bubble burst rates, lower water content and lower froth mobility. The estimated air recovery and stability factor were higher at lower temperatures. Regarding bubble size at the top of the froth, solids content was a determining factor for the nature of bubble size variation. Thus, at lower solids content and higher temperatures, the froth was increasingly unstable, which resulted in lower bubble size. At higher solids content

the froth was more stable, and at higher temperatures, larger bubbles were observed as a result of increased bubble coalescence. Variations in the investigated froth stability parameters were shown to heavily impact flotation performance (solids yield). An interplay of secondary concentration factors highlighted in this Chapter and the primary concentration factors given in Chapter 4 shapes the overall metallurgical performance of froth flotation, described in the next Chapter.



## Chapter 6. Variations in the Overall Lab-Scale Flotation Performance with Temperature

### 6.1. Introduction

Overall metallurgical performance of the lab-scale batch flotation was investigated for monomineralic system (at low solids content), and poly-mineral system (SEDEX ore). The monomineralic flotation was operated at lower solids density in the pulp (10%) and higher dosage of collector and frother compared to SEDEX ore flotation, which was operated at higher pulp density and lower dosages of surfactants. Monomineralic flotation is aimed at showing a potential response of cleaner circuits, while SEDEX ore flotation aimed at simulating rougher-scavenger flotation conditions.

### 6.2. Monomineralic Flotation of Galena, Sphalerite, and Pyrite

As can be seen from Appendix I, the yield of galena ( $\gamma_g$ ), pyrite ( $\gamma_p$ ), and sphalerite ( $\gamma_s$ ) and the corresponding water recoveries ( $\gamma_g^w$ ,  $\gamma_p^w$ , and  $\gamma_s^w$ ) behave in a similar way, indicating a certain level of correlation between these parameters. For all tested minerals, it was observed that the concentrate yields increased with decreased temperature (Figure 6-1).

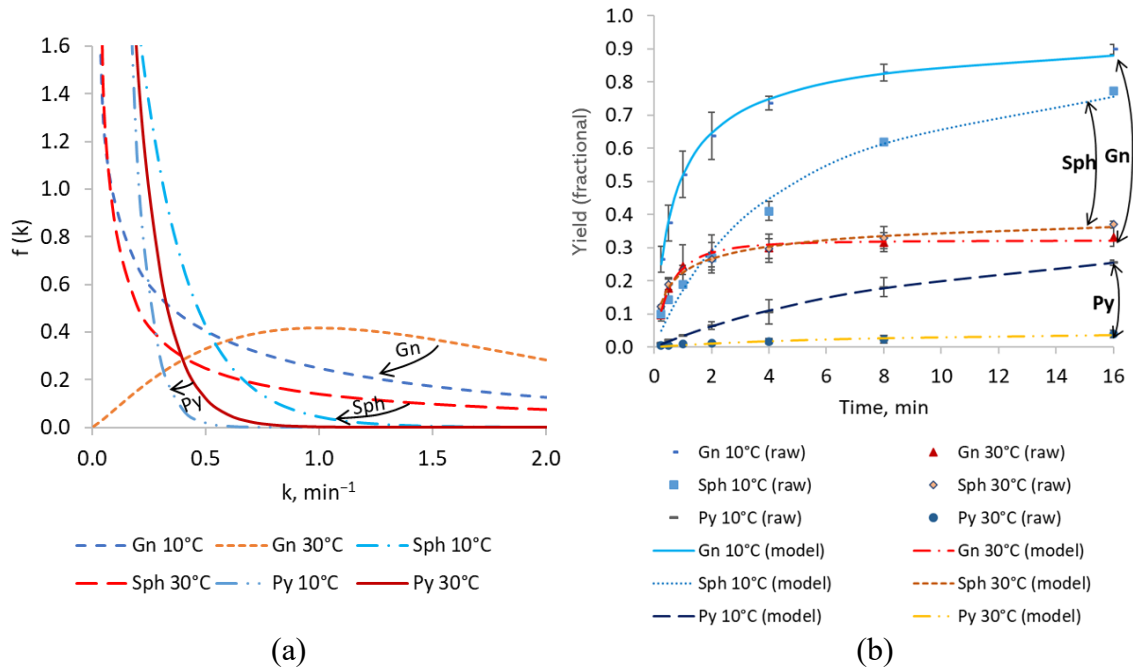


Figure 6-1. Flotation responses of galena, sphalerite, and pyrite at pH 9, 10 °C, and 30 °C: (a) kinetic yield curves; (b) distributions of flotation rate constants.

The largest observed yield variation in relative terms were observed for pyrite while, in absolute values, galena was impacted more than pyrite and sphalerite. The analysis of flotation kinetics can be adequately performed by Gamma  $f(k)$  (Vinnett, 2021). Thus, based on the distributions of flotation rate constants for galena and pyrite, there is a distinct shift of the  $f(k)$  curves towards lower values at lower temperature. Thus, at cold pulps, higher yields at a lower flotation rate may be expected for these two minerals. Regarding sphalerite, the shift in the flotation rate distribution with temperature was less evident. Changes in the flotation pH, similar to temperature variations, led to shifts in flotation rate distributions. For all tested minerals, the flotation rate was higher at pH 9 than at pH 11, as seen in Figure 6-2.

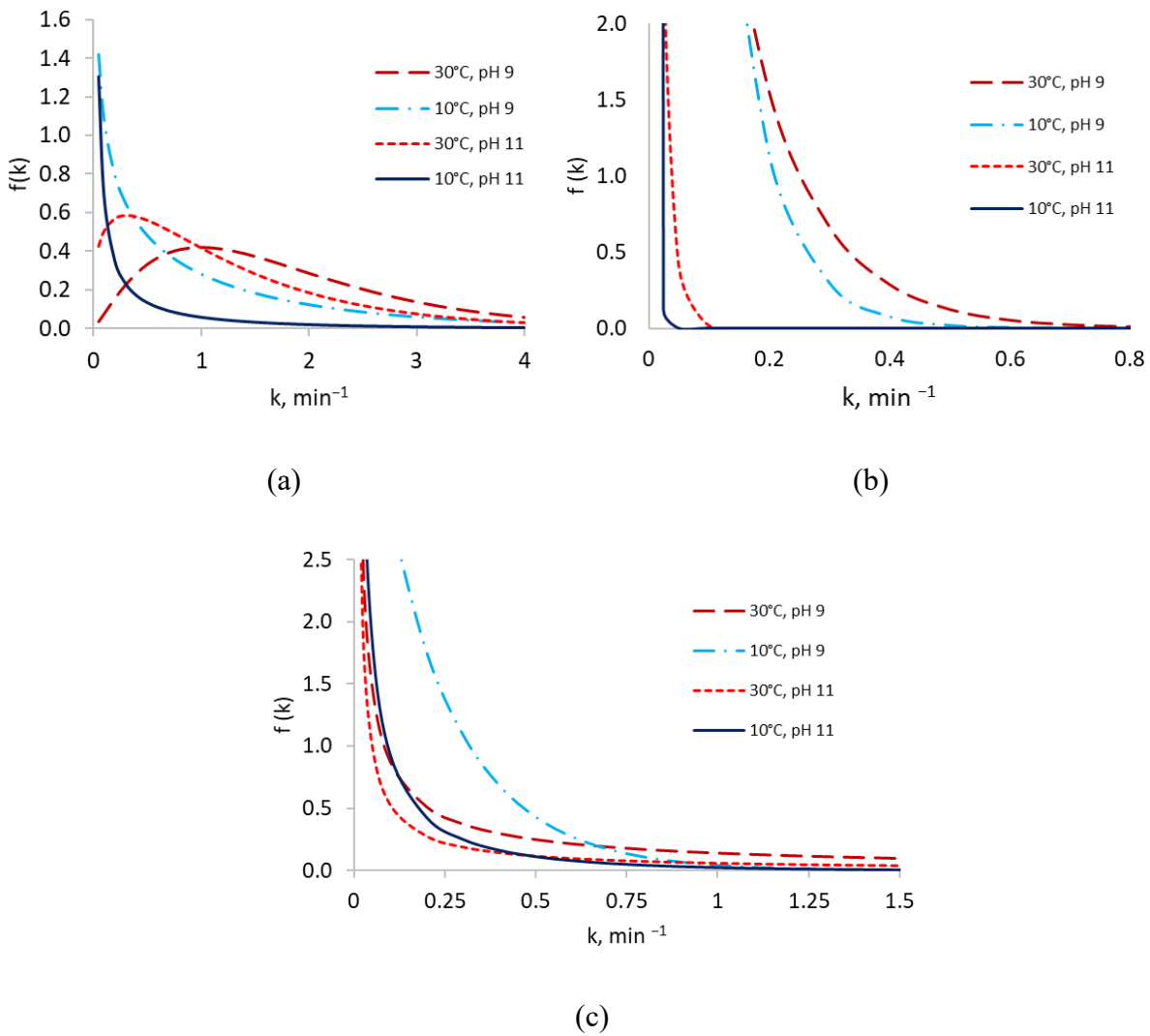


Figure 6-2. Distributions of flotation rate constants at 10 °C and 30 °C for pH 9 and 11: (a) galena; (b) pyrite; (c) sphalerite.

### 6.2.1. Galena Responses

Results of galena flotation served as a basis for the constructed MiniTab model, which was found acceptable based on high  $F$ -values and low  $p$ -values:  $F$ -value  $\gg F_{critical}$  (the critical value for the model in question is 3.5), whereas  $p$ -values are significantly below the considered  $\alpha$  of 0.05 (Table 6-1).

Table 6-1. General full factorial model summary for galena flotation responses (summary of ANOVA for regression galena flotation model).

F-value		p-value		$R^2$		$R^2_{adj}$		SD <sup>1</sup>	
$\gamma_g$	$\gamma_g^w$	$\gamma_g$	$\gamma_g^w$	$\gamma_g$	$\gamma_g^w$	$\gamma_g$	$\gamma_g^w$	$\gamma_g$	$\gamma_g^w$
764.89	764.89	0.000	0.000	99.85%	99.52%	99.72%	99.10%	1.39	1.32

Notes: <sup>1</sup> SD—standard deviation.

High  $R^2$  and  $R^2_{adj}$  values, and relatively low standard deviation indicate good fit of the models (Faraway, 2002).

Equations 6-1 and 6-2 demonstrate regressions fitting mineral and water yields, respectively, in galena sample flotation:

$$\begin{aligned}
 y_{min}^{Gn} = & 36.844 + 16.881 \cdot b(pH_9) - 16.881 \cdot b(pH_{11}) + 22.431 \cdot b(T_{10}) + \\
 & + 9.031 \cdot b(T_{20}) - 12.744 \cdot b(T_{30}) - 18.719 \cdot b(T_{40}) + 13.544 \cdot b(pH_9 T_{10}) + \\
 & + 3.844 \cdot b(pH_9 T_{20}) - 7.581 \cdot b(pH_9 T_{30}) - 9.806 \cdot b(pH_9 T_{40}) - 13.544 \cdot \\
 & \cdot b(pH_{11} T_{10}) - 3.844 \cdot b(pH_{11} T_{20}) + 7.581 \cdot b(pH_{11} T_{30}) + 9.806 \cdot \\
 & \cdot b(pH_{11} T_{40})
 \end{aligned} \quad (6-1)$$

$$\begin{aligned}
 y_w^{Gn} = & 21.394 + 1.731 \cdot b(pH_9) - 1.731 \cdot b(pH_{11}) + 20.981 \cdot b(T_{10}) + 1.006 \cdot \\
 & \cdot b(T_{20}) - 7.869 \cdot b(T_{30}) - 14.119 \cdot b(T_{40}) + 3.094 \cdot b(pH_9 T_{10}) - 0.231 \cdot \\
 & \cdot b(pH_9 T_{20}) - 1.606 \cdot b(pH_9 T_{30}) - 1.256 \cdot b(pH_9 T_{40}) - 3.094 \cdot \\
 & \cdot b(pH_{11} T_{10}) + 0.231 \cdot b(pH_{11} T_{20}) + 1.606 \cdot b(pH_{11} T_{30}) + 1.256 \cdot \\
 & \cdot b(pH_{11} T_{40})
 \end{aligned} \quad (6-2)$$

where  $b$  is a binary equation coefficient ( $b \in \{0, 1\}$ ).

As can be seen from Equations 6-1 and 6-2, the coefficients in front of  $pH_{11}$ , and  $T_{30}$  and  $T_{40}$  terms are negative, suggesting that increased pH and temperature have a negative impact on mineral and water yields. These trends could also be seen from the main effects and interaction plots (Figure 6-3).

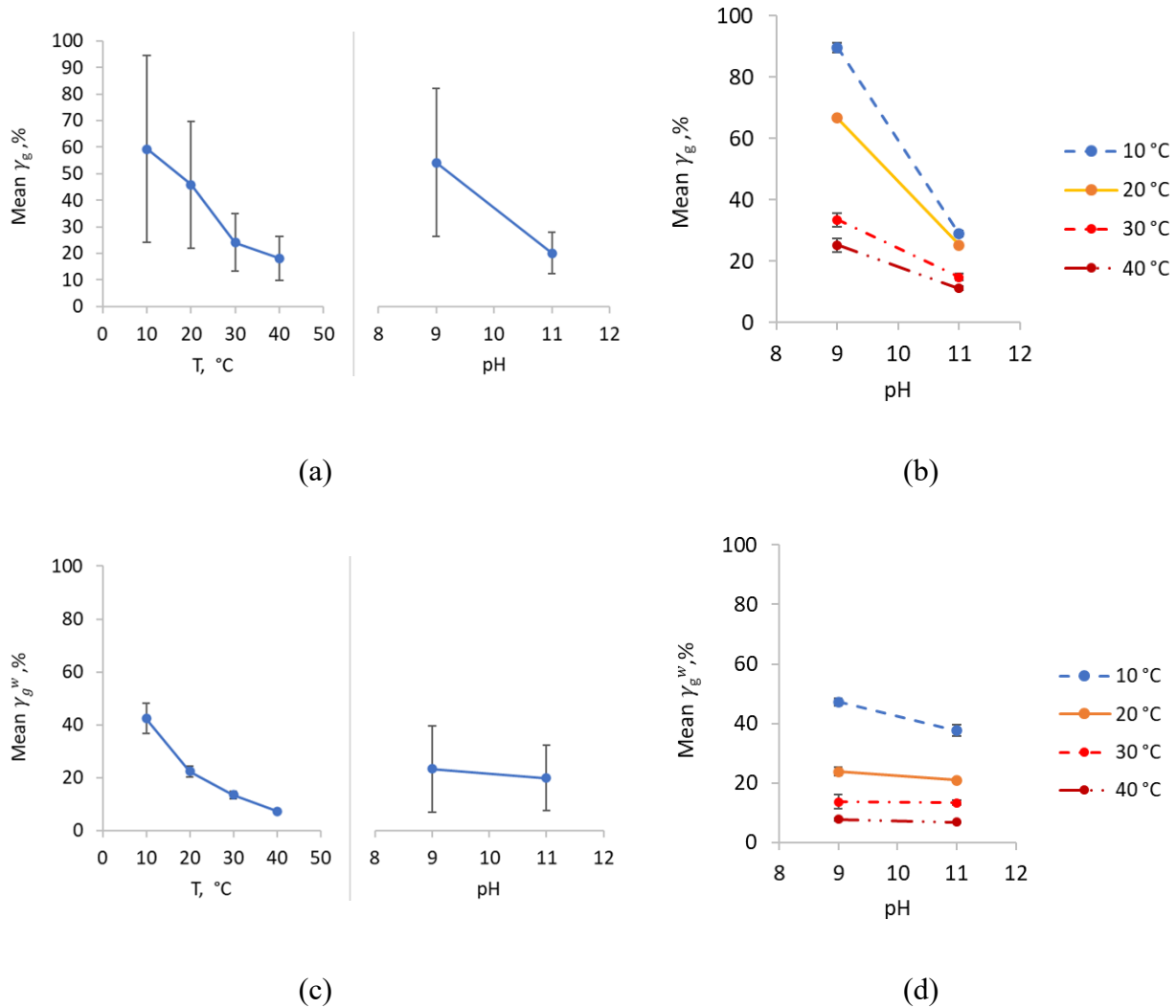


Figure 6-3. Galena flotation main effects and interaction plots: (a) main effects plot for galena recovery; (b) interaction plot for galena recovery; (c) main effects plot for water recovery; (d) interaction plot for water recovery (error bars represent  $\pm 1$  standard deviation).

By consulting the Pareto chart for standardized effects with respect to water and mineral yields, as well as water versus mineral yield plot (Figure 6-4), it could be concluded that pH is the most important parameter for mineral recovery, while temperature is the most significant factor for water recovery.

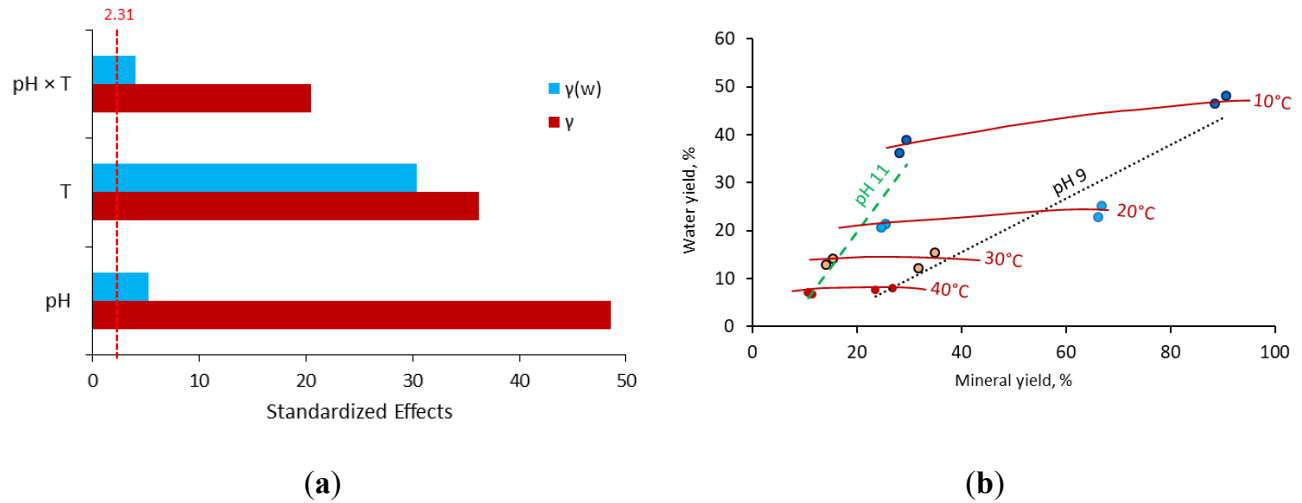


Figure 6-4. (a) Pareto chart for galena ( $\gamma_g$ ) and water yields ( $\gamma_g^w$ ); (b) water recovery versus galena yield at different pH and temperatures.

### 6.2.2. Pyrite Responses

Similar to galena flotation results, a model for pyrite flotation is significant, with  $p$ -values approaching 0 and  $F$ -values considerably greater than  $F$ -critical (Table 6-2).

Table 6-2. General full factorial model summary for pyrite flotation responses (summary of ANOVA for regression pyrite flotation model).

F-Value		p-Value		$R^2$		$R_{adj}^2$		SD <sup>1</sup>	
$\gamma_p$	$\gamma_p^w$	$\gamma_p$	$\gamma_p^w$	$\gamma_p$	$\gamma_p^w$	$\gamma_p$	$\gamma_p^w$	$\gamma_p$	$\gamma_p^w$
77.59	61.03	0.000	0.000	98.55%	98.16%	97.28%	96.55%	1.38	2.66

Notes: <sup>1</sup> SD—standard deviation.

Good regression model performance was confirmed as all  $R^2$  values were above 0.8 (Chicco *et al.*, 2021a). The standard deviations are also in the acceptable range, considering the objectives of the test work.

From the equations of pyrite and water yields (Equations 6-4 and 6-5), it could be concluded that the mineral yield increases at low pH and temperature, whereas the water recovery generally increases at higher pH and lower temperature, which is also confirmed in Figure 6-5:

$$\begin{aligned}
 y_{min}^{Py} = & 10.538 + 0.138 \cdot b(pH_9) - 0.138 \cdot b(pH_{11}) + 12.463 \cdot b(T_{10}) + \\
 & + 0.913 \cdot b(T_{20}) - 5.863 \cdot b(T_{30}) - 7.513 \cdot b(T_{40}) + 2.813 \cdot \\
 & \cdot b(pH_9 T_{10}) - 0.537 \cdot b(pH_9 T_{20}) - 1.213 \cdot b(pH_9 T_{30}) - 1.062 \cdot \\
 & \cdot b(pH_9 T_{40}) - 2.813 \cdot b(pH_{11} T_{10}) + 0.537 \cdot b(pH_{11} T_{20}) + \\
 & + 1.213 \cdot b(pH_{11} T_{30}) + 1.062 \cdot b(pH_{11} T_{40})
 \end{aligned} \quad (6-3)$$

$$\begin{aligned}
 y_w^{Py} = & 25.444 - 1.781 \cdot b(pH_9) + 1.781 \cdot b(pH_{11}) + 16.660 \cdot b(T_{10}) + 8.830 \cdot \\
 & \cdot b(T_{20}) - 7.620 \cdot b(T_{30}) - 17.870 \cdot b(T_{40}) + 1.230 \cdot b(pH_9 T_{10}) - 2.340 \cdot \\
 & \cdot b(pH_9 T_{20}) - 0.790 \cdot b(pH_9 T_{30}) + 1.910 \cdot b(pH_9 T_{40}) - 1.230 \cdot \\
 & \cdot b(pH_{11} T_{10}) + 2.340 \cdot b(pH_{11} T_{20}) + 0.790 \cdot b(pH_{11} T_{30}) - 1.910 \cdot \\
 & \cdot b(pH_{11} T_{40})
 \end{aligned} \quad (6-4)$$

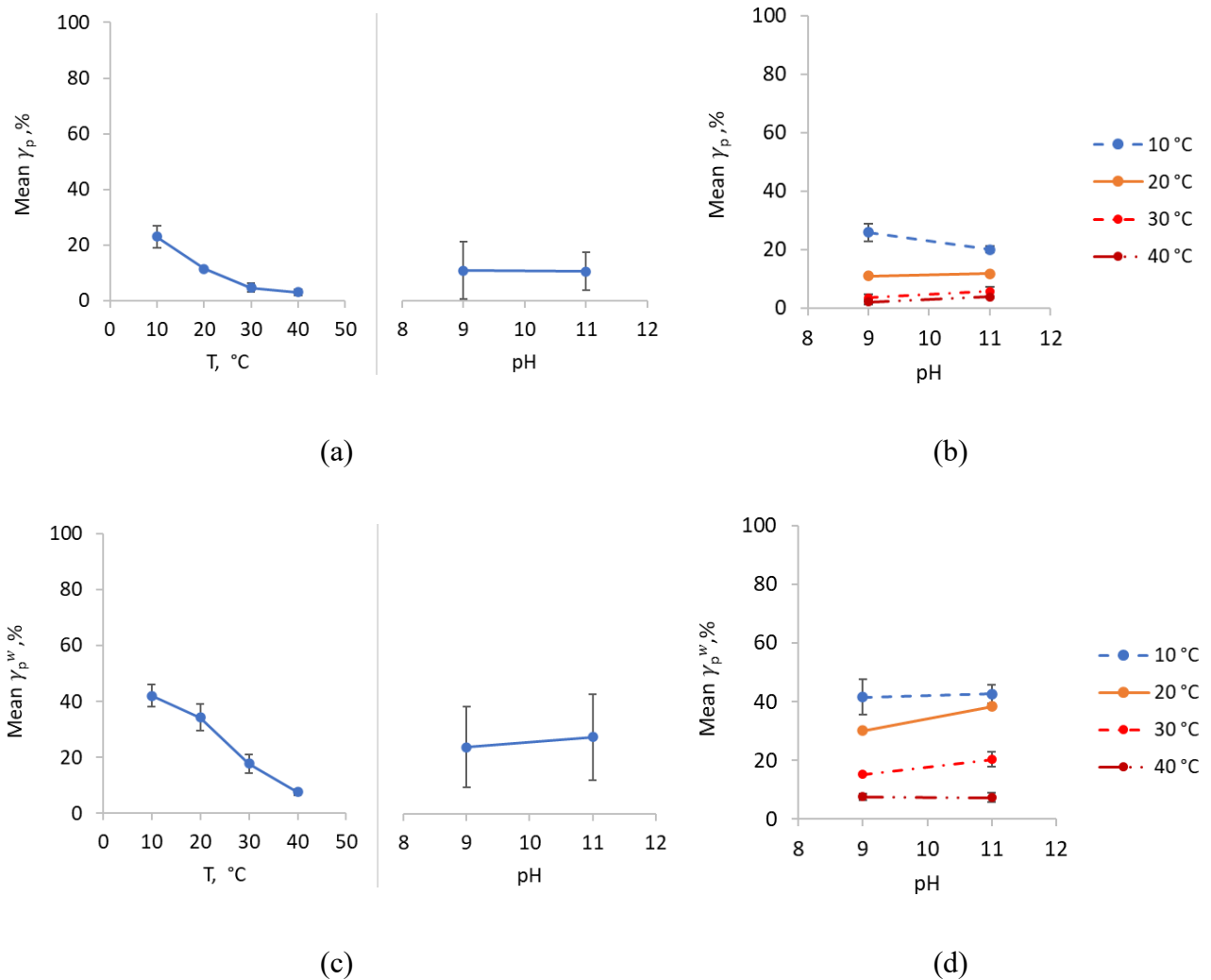


Figure 6-5. Pyrite flotation main effects and interaction plots: (a) main effects plot for pyrite recovery; (b) interaction plot for pyrite recovery; (c) main effects plot for water recovery; (d) interaction plot for water recovery (error bars represent  $\pm 1$  standard deviation).

From the Pareto chart (Figure 6-6a), it can be seen that for pyrite and water recoveries, the most important factor is temperature. For pyrite yield, the second most important factor is the interaction between temperature and pH. For water recovery, the second most important term is pH (Figure 6-6a). There is a relatively small impact of pH on water recovery as well as an insignificant pH effect on mineral recovery for the pyritic pulp system, which can be seen on the plot with mineral yields versus water recovery (Figure 6-6b). In contrast to galena flotation, for pyrite tests it is more difficult to distinguish pH lines on the scatterplot (Figure 6-6b).

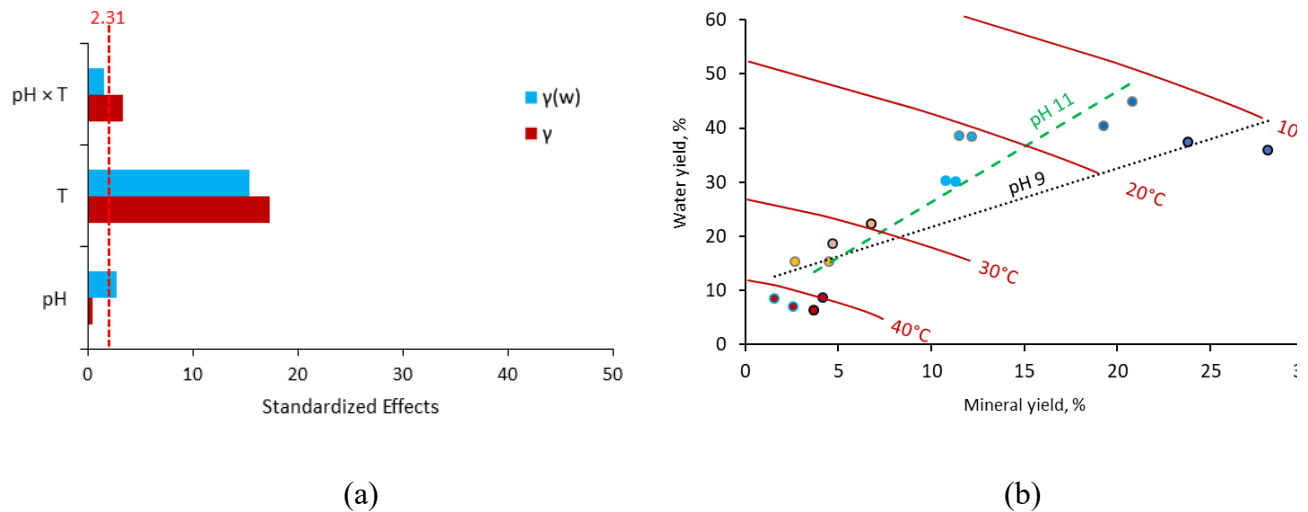


Figure 6-6. (a) Pareto chart for pyrite ( $\gamma_p$ ) and water yields ( $\gamma_p^w$ ); (b) water recovery versus pyrite yield at different pH and temperatures.

### 6.2.3. Sphalerite Responses

Sphalerite models also passed statistical significance and goodness of fit evaluation, demonstrating high  $R^2$  values,  $F$ -values above critical, and  $p$ -values below the set threshold (Table 6-3).

Table 6-3. General full factorial model summary for pyrite flotation responses (summary of ANOVA for regression pyrite flotation model).

F-Value		p-Value		$R^2$		$R^2_{adj}$		SD <sup>1</sup>	
$\gamma_s$	$\gamma_s^w$	$\gamma_s$	$\gamma_s^w$	$\gamma_s$	$\gamma_s^w$	$\gamma_s$	$\gamma_s^w$	$\gamma_s$	$\gamma_s^w$
1337.60	401.17	0.000	0.000	99.91%	99.72%	99.84%	99.47%	0.95	0.98

Notes: <sup>1</sup> SD—standard deviation.

The regression models obtained for sphalerite yield (Equation 6-5) followed a similar trend to those of the regression equations for pyrite and galena: higher yields at lower pH and temperatures.

Water recovery (Equation 6-6) in sphalerite flotation, like for galena, followed a trend like that of mineral recovery, in terms of temperature effects (Figure 6-7):

$$\begin{aligned}
 y_{min}^{sph} = & 30.294 + 13.844 \cdot b(pH_9) - 13.844 \cdot b(pH_{11}) + 20.956 \cdot b(T_{10}) + \\
 & + 6.731 \cdot b(T_{20}) - 4.294 \cdot b(T_{30}) - 23.394 \cdot b(T_{40}) + 12.206 \cdot b(pH_9 T_{10}) + \\
 & + 1.981 \cdot b(pH_9 T_{20}) - 2.744 \cdot b(pH_9 T_{30}) - 11.444 \cdot b(pH_9 T_{40}) - \\
 & - 12.206 \cdot b(pH_{11} T_{10}) - 1.981 \cdot b(pH_{11} T_{20}) + 2.744 \cdot b(pH_{11} T_{30}) + \\
 & + 11.444 \cdot b(pH_{11} T_{40})
 \end{aligned} \quad (6-5)$$

$$\begin{aligned}
 y_w^{sph} = & 25.944 + 0.531 \cdot b(pH_9) - 0.531 \cdot b(pH_{11}) + 19.681 \cdot b(T_{10}) + \\
 & + 1.831 \cdot b(T_{20}) - 5.944 \cdot b(T_{30}) - 15.569 \cdot b(T_{40}) - 1.906 \cdot b(pH_9 T_{10}) + \\
 & + 1.694 \cdot b(pH_9 T_{20}) + 0.319 \cdot b(pH_9 T_{30}) - 0.106 \cdot b(pH_9 T_{40}) + 1.906 \cdot \\
 & \cdot b(pH_{11} T_{10}) - 1.694 \cdot b(pH_{11} T_{20}) - 0.319 \cdot b(pH_{11} T_{30}) + 0.106 \cdot \\
 & \cdot b(pH_{11} T_{40})
 \end{aligned} \quad (6-6)$$

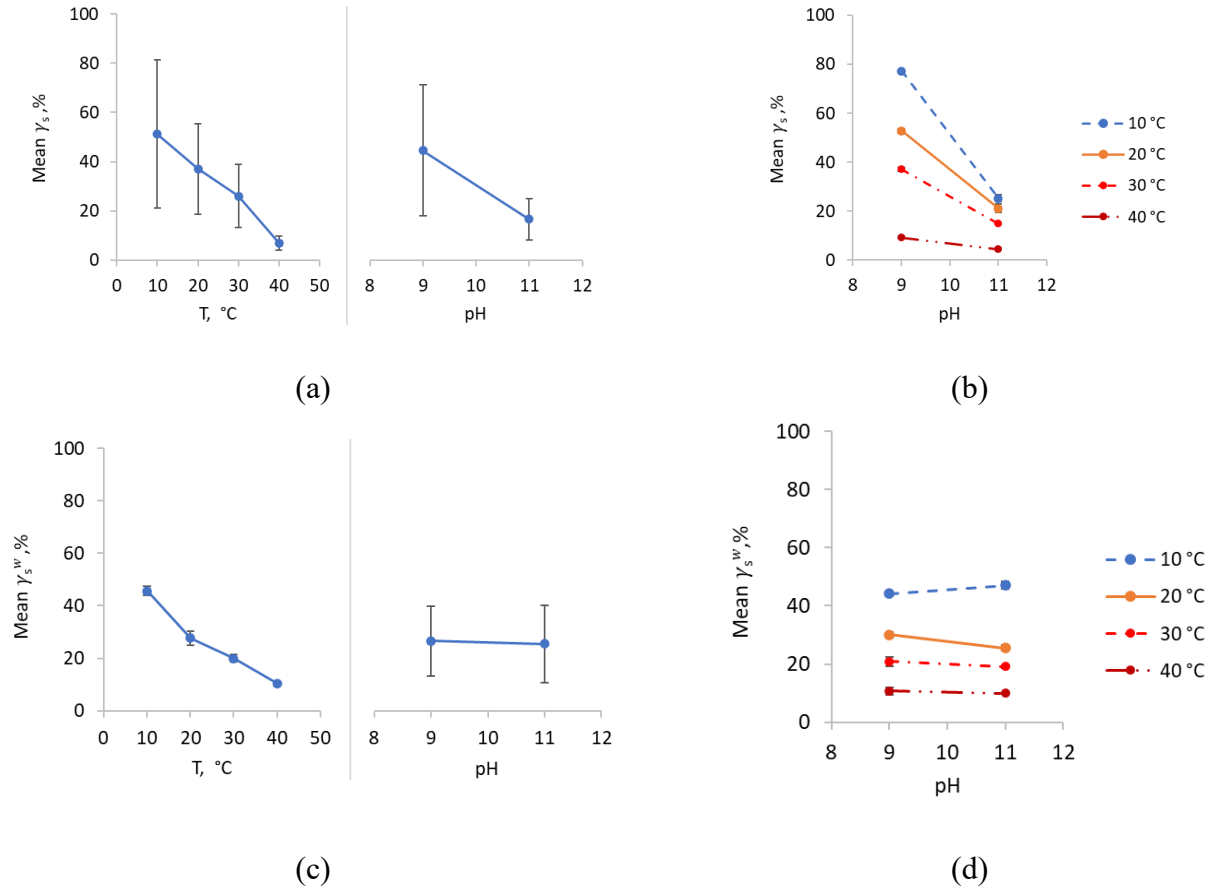


Figure 6-7. Sphalerite flotation main effects and interaction plots: (a) main effects plot for sphalerite recovery; (b) interaction plot for sphalerite recovery; (c) main effects plot for water recovery; (d) interaction plot for water recovery (error bars represent  $\pm 1$  standard deviation).



For sphalerite flotation, the most important factor, based on the absolute  $t$ -values provided on the Pareto chart, was pH. The contribution of temperature was also significant, but slightly less than pH (Figure 6-8a). The mineral yield–water recovery plot looks similar to that of galena: the lower the temperature, the larger deviation of mineral yields at different pH (as observed from Figure 6-8b).

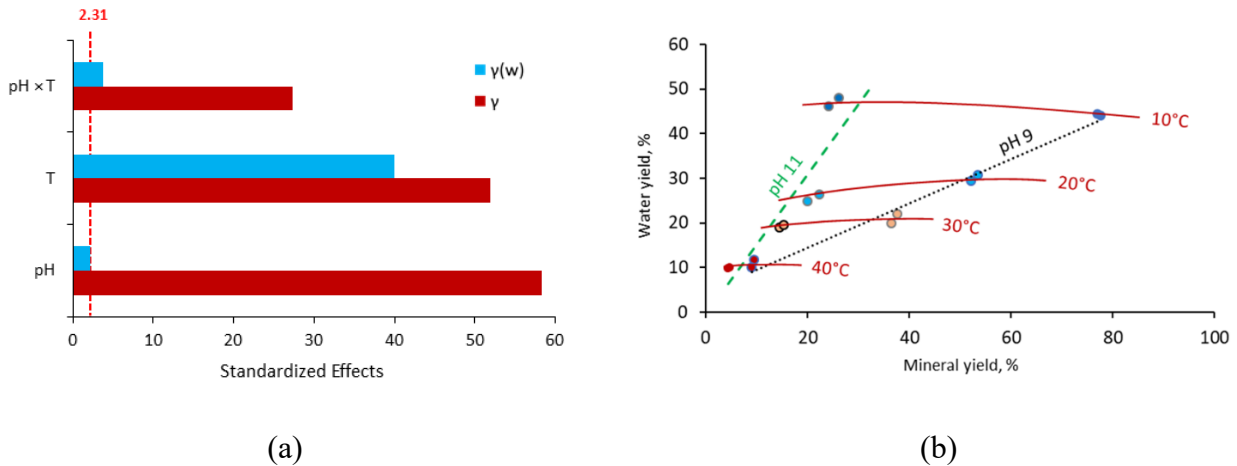


Figure 6-8. (a) The Pareto chart for sphalerite ( $\gamma_s$ ) and water yields ( $\gamma_s^w$ ); (b) water recovery versus sphalerite yield at different pH and temperatures.

#### 6.2.4. Correlation of Monomineralic Flotation Performance to Foam Stability

As indicated from the loading plots (Figure 6-9), the PCA allowed more than 85% of the total variability to be captured for all datasets by two principal components. There is a common correlation pattern between temperature and foam stability parameters (negative correlation with foam height and foam half-life) expressed by vectors facing in the opposite directions. Flotation kinetics parameters (scale and shape of gamma model) for all three minerals also exhibit negative correlation, but with pH. The positions of water recovery vectors are close to the vectors explaining foam stability, indicating high correlation. Regarding mineral yields, pyrite recovery is in good correlation with foam stability parameters, while sphalerite recovery is closely related to flotation kinetics parameter.

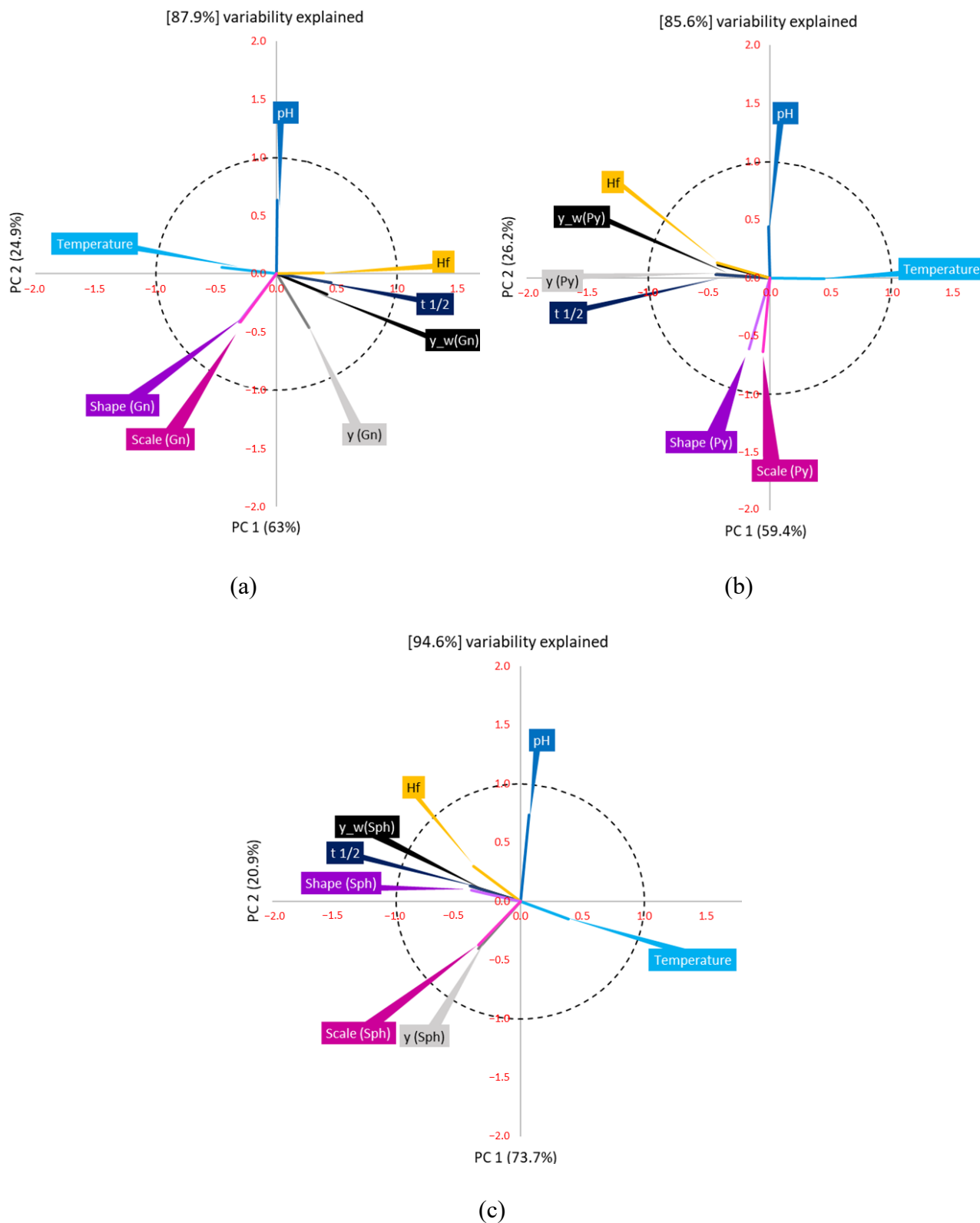


Figure 6-9. Loading plots for foam stability responses, temperature, and pH, and flotation responses of: (a) galena; (b) pyrite; (c) sphalerite.

### 6.3. Lead-Zinc Ore Flotation

For the first stage of the experiment (galena flotation from SEDEX ore), based on the F-values, it is apparent that only some models of sphalerite, quartz and baryte metallurgical performance were statistically significant (above 3.68) (Table 6-4). The factors tested throughout the experiments were temperature, copper sulfate dosage (sphalerite activator) and zinc sulfate dosage (sphalerite depressant). Since galena models were statistically significant only under the assumption of a confidence interval of 80% (corresponding F critical value is 1.92), it means that under the investigated conditions, the effect of temperature was not pronounced for galena flotation. Additionally, t-statistics indicated an absence of statistically significant factors for galena flotation in the frameworks of this DoE.

Table 6-4. Characteristics of the models for galena, sphalerite, quartz and baryte flotation to the first (Pb) concentrate

	<b>Galena</b>		<b>Sphalerite</b>		<b>Quartz</b>		<b>Baryte</b>	
	Grade	Recovery	Grade	Recovery	Grade	Recovery	Grade	Recovery
F-value	2.09	2.16	2.09	3.88	2.47	8.91	2.05	4.96
p-value	0.172	0.161	0.172	0.044	0.123	0.004	0.178	0.023
$R^2$ (%)	72.89	73.55	72.86	83.31	76.08	91.97	72.47	86.45
$R^2_{adj}$ (%)	38.03	39.54	37.96	61.86	45.33	81.66	37.08	69.03
SD	0.51	2.11	0.99	0.80	1.58	0.60	1.89	1.08

From t-statistics for sphalerite, quartz, and baryte, it could be seen (Figure 6-10) that temperature had a negative impact on the recovery of all three minerals, indicating the entrainment character of the process. For sphalerite grade in galena concentrate, also depressant dosage (zinc sulfate) had a pronounced negative impact. The contents of quartz and baryte, like in the case of recovery values, were also negatively impacted by temperature.

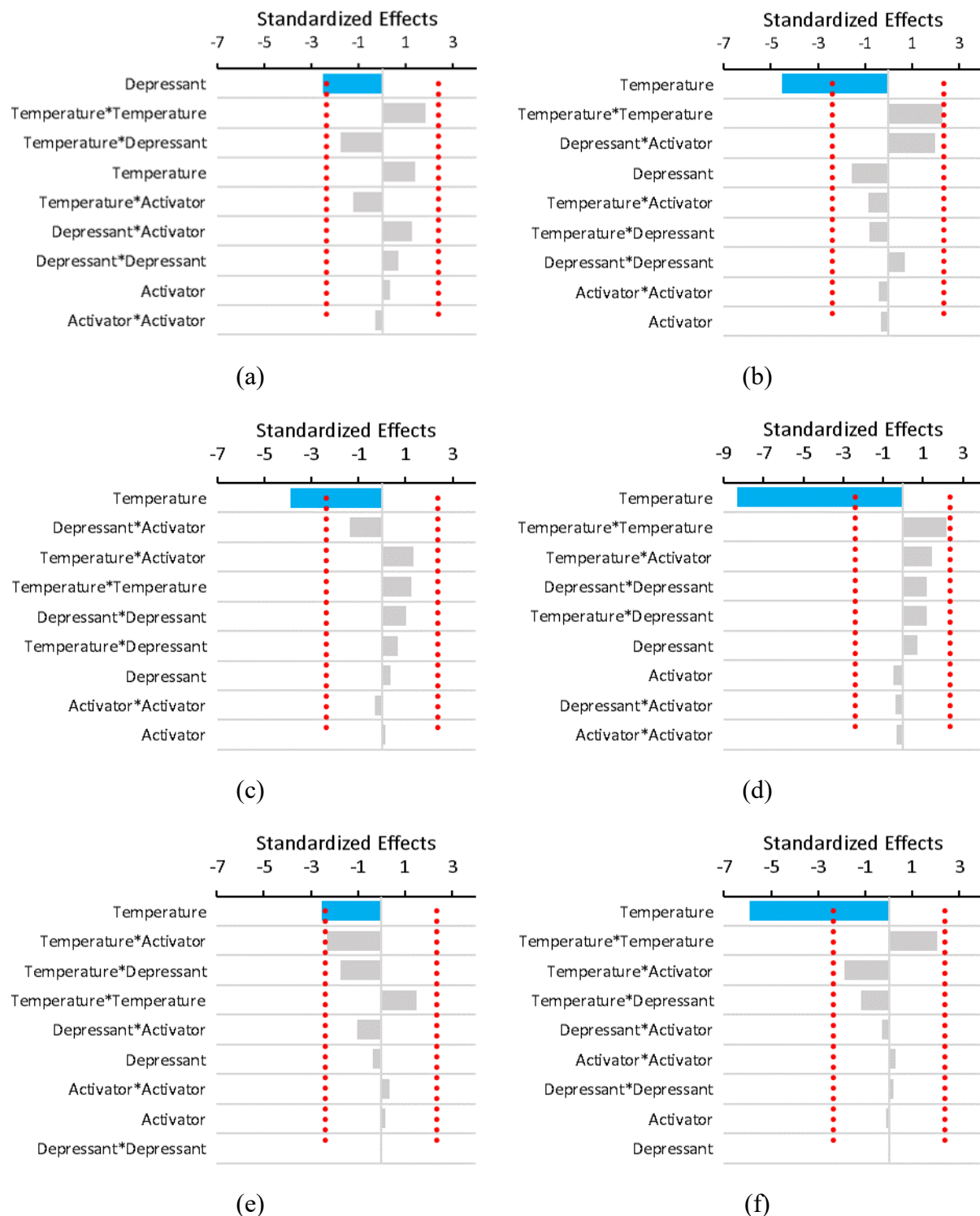


Figure 6-10. Modified Pareto charts, showing statistical significance of the factors (combinations of factors) on metallurgical performance of sphalerite (a – grade, b – recovery), quartz (c – grade, d – recovery), and baryte (e – grade, f – recovery).

From the contour plot of the recovery of sphalerite it could be seen that with an increase in temperature and depressant dosage, the amount of mineral floating to the lead concentrate decreases (Figure 6-11a). The entrainment of quartz and baryte has also increased with a decrease in temperature. Additionally, there was a slight increase in baryte and quartz recovery to the concentrate at higher dosages of zinc sulfate (Figure 6-11b and c).

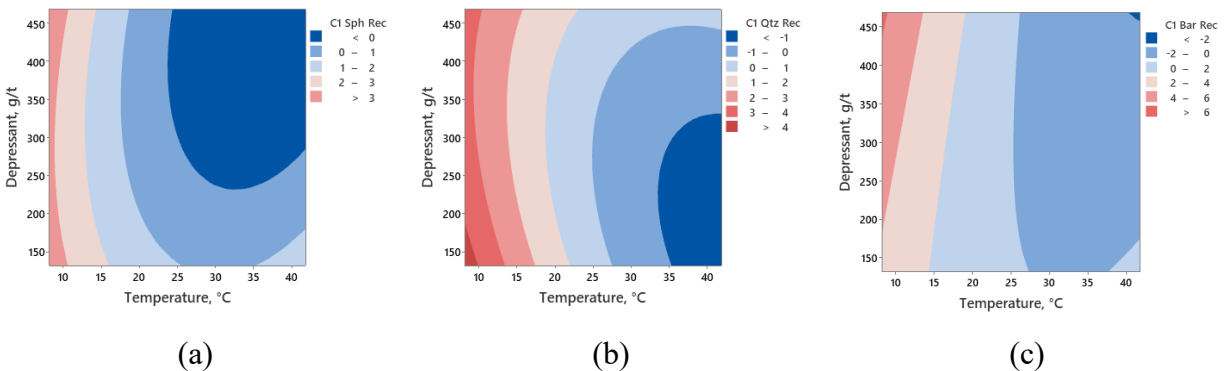


Figure 6-11. Contour plots of statistically significant models for the first flotation stage (Pb stage) of SEDEX ore in the coordinates of temperature-depressant dosage for sphalerite recovery (a), quartz recovery (b), and baryte recovery (c) (all values are given as relative numbers to a central point)

On the second flotation stage (zinc stage) only a model for sphalerite grade was considered significant based on F-statistics (Table 6-5). Similar to the first flotation stage, based on T-statistics, sphalerite, quartz, and baryte had some factors, significantly impacting the metallurgical responses (Figure 6-12).

Table 6-5. Characteristics of the models for galena, sphalerite, quartz and baryte flotation to the second (Zn) concentrate

	Galena		Sphalerite		Quartz		Baryte	
	Grade	Recovery	Grade	Recovery	Grade	Recovery	Grade	Recovery
F-value	1.90	2.11	8.20	1.41	1.66	2.54	0.51	2.49
p-value	0.204	0.169	0.006	0.355	0.259	0.116	0.826	0.121
$R^2$	70.98	73.07	91.34	64.47	68.08	76.55	39.83	76.18
$R^2_{adj}$	33.66	38.45	80.20	18.78	27.04	46.40	0.00	45.54
SD	0.39	1.60	1.91	0.93	1.75	0.74	4.07	0.92

For zinc concentrate grade, activator dosage (copper sulfate) and temperature were 2 significant factors positively impacting the flotation performance (Figure 6-12). The temperature was also found to increase sphalerite recovery to the concentrate. For quartz and baryte temperature was

generally seen to decrease their metallurgical parameters, likely through a lower degree of entrainment, similar to the lead flotation stage.

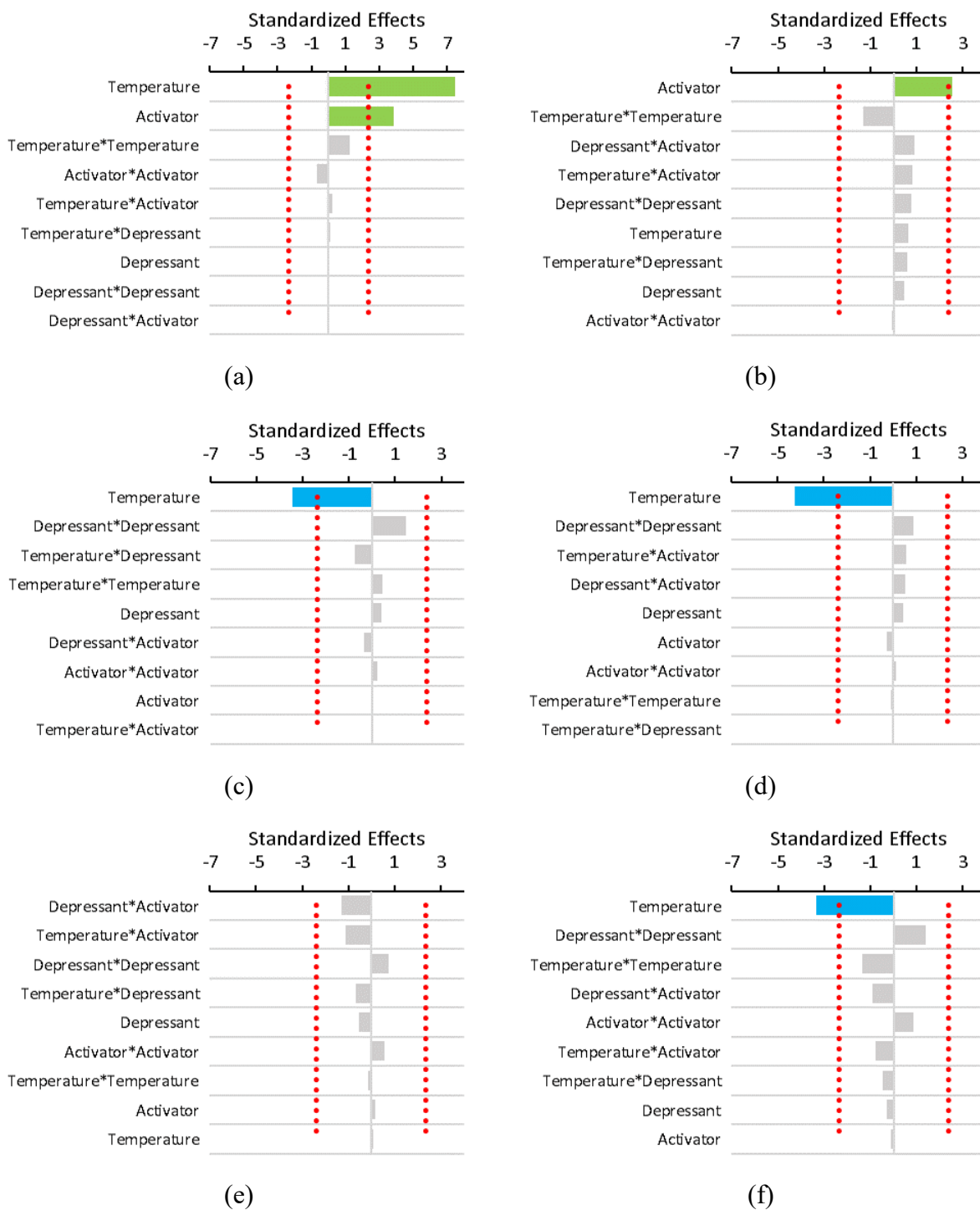


Figure 6-12. Modified Pareto charts showing an importance of factors for flotation of sphalerite (a – grade, b – recovery), quartz (c – grade, d – recovery), and baryte (e – grade, f – recovery).

From the contour plot of sphalerite grade in zinc concentrate it derives that temperature and copper sulfate dosages significantly contributed to the increase in the flotation performance. According to the model, a 15% grade swing occurred in the investigated dosage and temperature range (Figure 6-13).

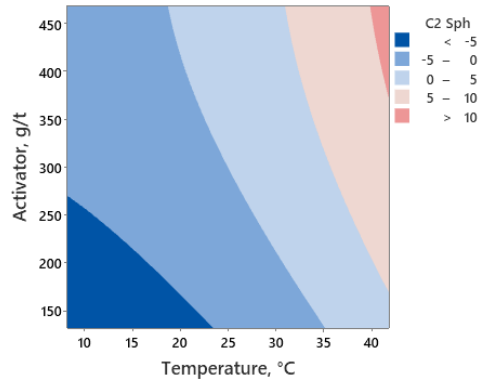


Figure 6-13. Changes in sphalerite concentrate zinc grade with temperature and activator dosage. With respect to flotation kinetics, a marginal increase in the flotation rates of sphalerite and galena was observed in the respective concentrates with an increase in temperature (Figure 6-14a and b). For quartz and baryte a small increase in flotation kinetics is observed at lower temperatures (Figure 6-14c and d), since the recovery of these minerals is controlled by entrainment, which increases at lower temperatures.

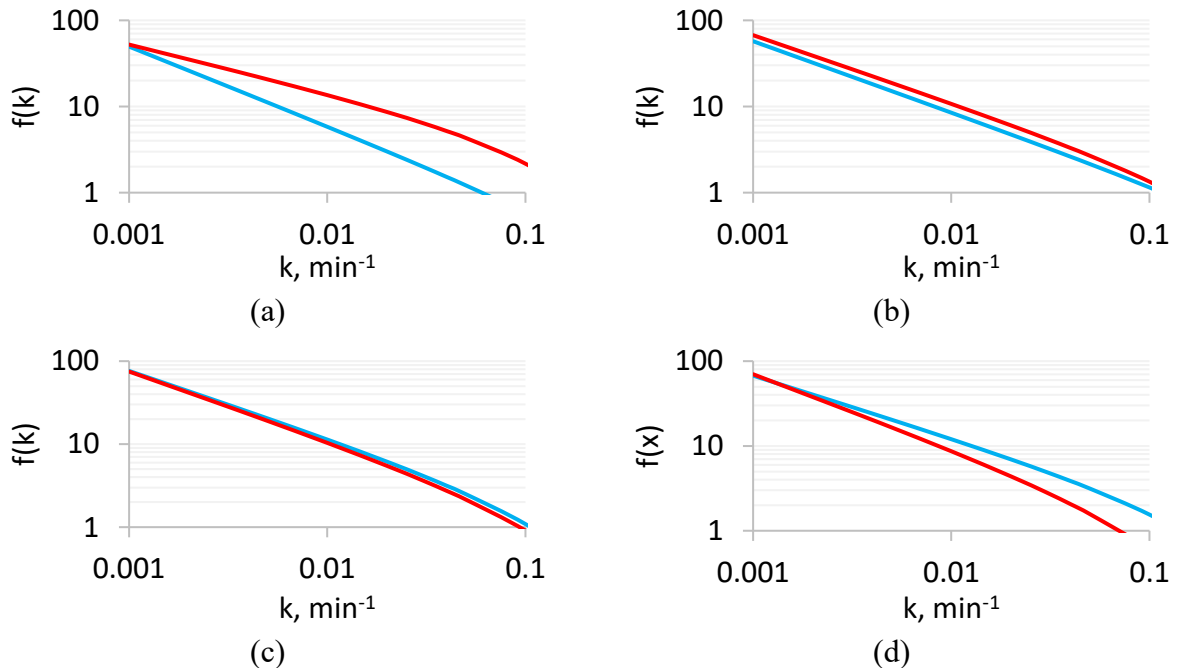


Figure 6-14. Flotation rate constant distributions at 15 °C (blue lines) and 35 °C (red lines) for: sphalerite (a), galena (b), quartz (c), and baryte (d)

Since it is clear from the results that variations of froth stability (presumably drainage) with temperature have a strong impact on the flotation results, air recovery, and froth stability factor (calculated in Section 5.3.3) were compared to sphalerite grade to see if there is any correlation between them (Figure 6-15).

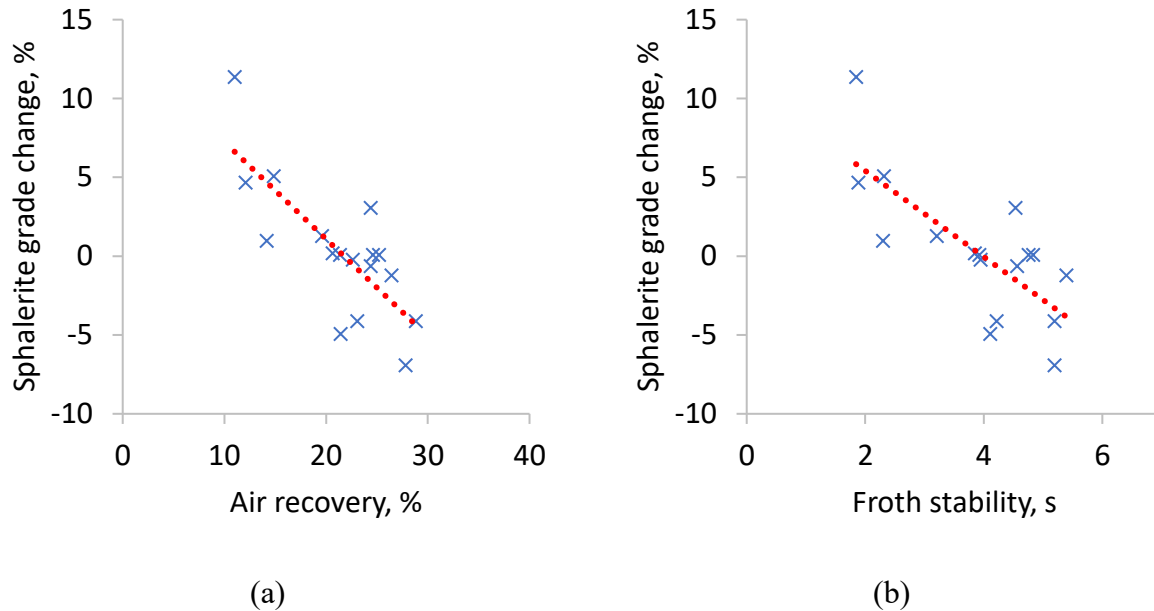


Figure 6-15. Linear regression between sphalerite grade change and air recovery (a), and froth stability factor (b)

The calculated Pearson's coefficients of -0.77 and -0.74 for air recovery and froth stability factor respectively indicate a strong negative dependence between froth stability characteristics and sphalerite grade quality.

## 6.4. Discussions

### 6.4.1. Monomineralic Flotation Performance

From the monomineralic flotation tests, it could be seen that the largest yields and fastest flotation kinetics were observed for galena, followed by sphalerite and pyrite. This could be attributed to galena being more electrochemically active than pyrite and adsorbing more collector (Piantadosi and Smart, 2002). Moreover, simulations of water molecule adsorption on pyrite and galena surfaces revealed that pyrite is generally more hydrophilic, which has been confirmed by contact angle measurements (approximately 50° for galena compared to 20° for pyrite) (Monte *et al.*, 1997; Prestidge and Ralston, 1995). Sphalerite normally has an inert surface due to a broad band gap which prevents oxygen and xanthate adsorption and renders it poorly floatable in the inactivated



state (Abramov, 2013; Yu *et al.*, 2019). Activated sphalerite, conversely, has contact angles closer to the ones observed for galena (Gayle and Smelley, 1960). In this work, based on the flotation results and mineralogical composition of the sphalerite sample, it may be suggested that sphalerite is activated by lead and copper on the surface (as shown in Figure 4-10).

Regarding the impact of temperature on water recovery and mineral yields, from Figure 6-4, Figure 6-6, and Figure 6-8 it can be concluded that only the galena plot clearly exhibited  $R_{ind}$  fraction of the feed, the flotation of which is independent from water recovery. Higher correlations of mineral yields and water recoveries observed for pyrite and sphalerite compared to galena could be attributed to lower mineral densities for the first two minerals (5 and 4.1 g/cm<sup>3</sup>, respectively, versus 7.6 g/cm<sup>3</sup>) (Carmichael, 2018), which makes their drainage from the froth less efficient.

#### **6.4.2. Lead-Zinc Ore Flotation Performance**

In the ore flotation, it was found that entrainment was one of the most important factors, since the recovery of sphalerite, quartz, and baryte to the lead concentrate, and quartz and baryte to zinc concentrates was inversely proportional to the temperature. Galena did not show any statistically significant variations in the responses, which could be explained by the added reagents (copper sulfate and zinc sulfate are modifiers of sphalerite flotation, and should not impact galena floatability), and also by high mineral density (7.6 g/cm<sup>3</sup>). Because of the high mineral density, drainage and entrainment (and, hence, the mechanical effect of temperature) had a smaller impact on galena flotation in the ore system, which is in agreement with monomineralic tests (in Section 6.2) and lower galena entrainment reported in the literature (Wang, 2016b).

Sphalerite grade and recovery to the respective concentrate, as well as flotation kinetics, were seen to improve with temperature, which could be attributed to more efficient copper activation (Albrecht *et al.*, 2016) and decreased entrainment of the main gangue (baryte and quartz). The observed increase in sphalerite grade corresponds well with the data in the literature, where a 20 % increase in zinc concentrate grade was obtained by increasing the pulp temperature from 10 to 60 °C (Bicak *et al.*, 2023). A slight increase in the recovery of baryte and quartz, traced to the addition of zinc sulfate can be explained by increased froth stability at higher ionic concentrations of flotation pulps (Bıçak *et al.*, 2012).

Exploration of the correlations between froth stability characteristics and grade/recovery revealed an opportunity in their application as a potential process performance forecasting tool (high negative correlations observed). Air recovery was a more robust metric, which is reflected in a more negative correlation coefficient, compared to the froth stability factor, which was directly calculated through the bubble burst rate. Such differences could be explained by more uncertainty and higher errors associated with precise estimation of bubble burst rate.

### **6.5. Conclusions**

Mono-mineral flotation tests revealed higher yields at colder temperatures. The flotation rate, however, was greater at elevated temperatures, which could be explained by smaller bubbles and chemical aspects of flotation. Foam height and half-life were found to be inversely correlated to temperature. Foam height was also found to be positively correlated to lime dosage, frother dosages, as well as aeration level. The principal component analysis helped to determine that, for all tested minerals, flotation rate model parameters are inversely related to pH, while water recovery was found to be strongly correlated with foam height and half-life. In multi-mineral flotation systems metallurgical performance was also seen to be strongly controlled by secondary concentration. The entrainment mechanism was used to explain the increased recovery of gangue to flotation concentrates, whereas temperature-dependent copper activation was used to explain improvements in sphalerite grade at higher temperatures. Thus, it may be concluded that froth varies with temperature, which potentially impacts the concentrate grade and mineral yield in flotation plants. The relevance of laboratory scale findings for industrial-scale production can be assessed only after a thorough study of an industrial flotation performance, which is the focus of the next Chapter.

---

## Chapter 7. Temperature Contribution to Plant-Scale Variations in Sulfide Flotation

The poor flotation performance of sphalerite from polymetallic deposits in winter is explained in the literature by the reduced efficiency of depressant and activators (Albrecht *et al.*, 2016; Umipig *et al.*, 2012). Summer sphalerite losses in some cases are attributed to decreased collector performance and mineral surface alterations at high temperatures (Abramov, 2005). A brief overview of several zinc mines located in different climate zones (Figure 7-1) may be a useful tool for a better understanding of the temperature impact on flotation in various technological contexts and weather environments.

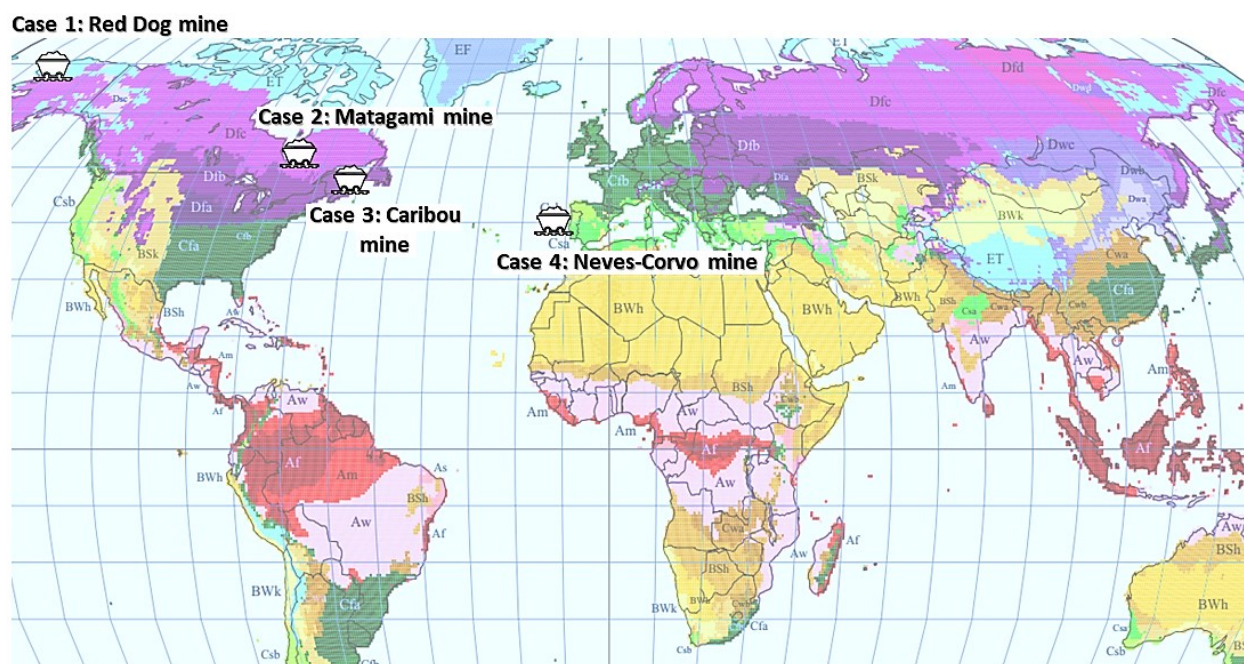


Figure 7-1. Selected zinc mines on a world climate map. Main climates: A – equatorial, B – arid, C – warm, D – snow, E – polar. Precipitation: W – desert, S – steppe, f – fully humid, s – summer dry, w – winter dry, m – monsoonal. Temperature: h – hot arid, k – cold arid, a – hot summer, b – warm winter, c – cool summer, d – extremely continental, F – polar frost, T – polar tundra (adapted from (Kottek *et al.*, 2006))

For this assessment, four different mines located in Subarctic, Temperate, and Subtropical climatic zones were considered.

### 7.1. Description of Ores and Flowsheets

*Case 1: Red Dog mine.* Red Dog mine is located in Alaska (USA) above the Arctic Circle in a polar tundra. The area experiences seasonal temperature fluctuations from -41 °C in winter to 16 °C in summer (Krolak *et al.*, 2017). The mined sedimentary exhalative ores are rich in zinc, lead, and silver. The ore is finely disseminated (Bulatovic, 2007) with the most abundant sulfide minerals being sphalerite, pyrite, and galena (Smith *et al.*, 2008). The host mineralogy is carbonaceous shale with a large amount of soluble salts and a variable content of pyrite (Bulatovic, 2007).

Red Dog mineral processing flowsheet consists of 3 stages of flotation: pre-flotation circuit, lead circuit, and zinc circuit (Figure 7-2) (Krolak *et al.*, 2017). The pre-flotation circuit removes elemental sulfur and organic carbon using rougher cells and a Jameson cleaner cell. Whenever the total organic carbon content exceeds 0.7% a frother is added to the Jameson cell to improve the organics recovery (Smith *et al.*, 2008). Pre-flotation units are followed by sequential lead – zinc flotation (Krolak *et al.*, 2017).

Bulatovic reported a limited application of lime and cyanide in the plant. The reagent scheme for the lead circuit included sphalerite depression by 300 g/t zinc sulfate, pyrite/marcasite depression by 50 g/t cyanide, galena hydrophobization by 40 g/t potassium amyl xanthate, and pH adjustment using 300 g/t CaO. Additionally, by dosing 20 g/t dithiophosphate (R208) silver recovery to a lead concentrate was facilitated. Following lead flotation, the zinc surface was activated by 2-4 kg/t copper sulfate and hydrophobized using 150 g/t potassium amyl xanthate. Gangue minerals were also depressed using 300 g/t water glass, while pH was maintained using 450 g/t CaO (Bulatovic, 2007). Despite flotation being outlined as one of the most challenging parts of the mine operations, and despite numerous optimization and expansion projects reported (Ciccione and Hope, 2003), no publicly available sources were found to claim seasonally driven changes in the flotation performance at the plant.

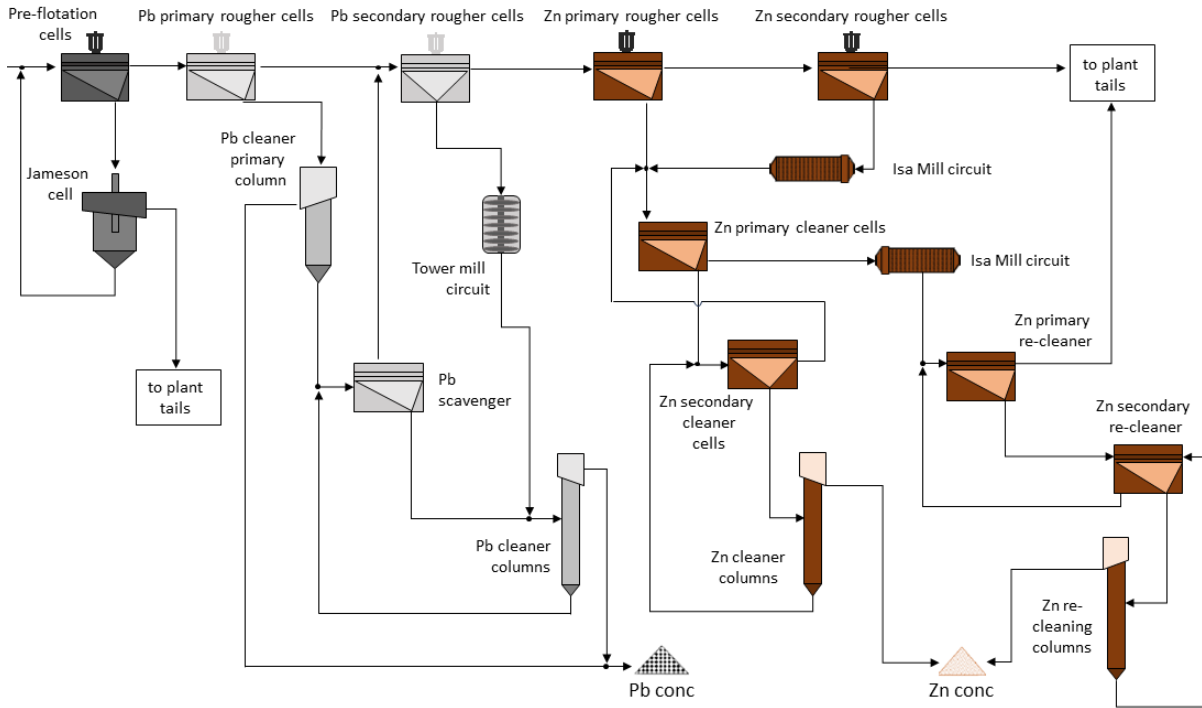


Figure 7-2. Simplified flotation flowsheet of Red Dog Concentrator (based on (Krolak *et al.*, 2017))

*Case 2. Matagami mine.* Unlike the Red Dog concentrator, the Matagami plant in the Northern part of Quebec (Canada) was designed to treat volcanogenic massive sulfides to recover copper and zinc (Fuerstenau *et al.*, 2007; Nessel *et al.*, 2002). It is located in a sub-arctic climate zone characterized by cool summers. Typical reported pulp temperatures at the plant vary from 5 °C in winter to around 30 °C in summer. These temperatures had increased up to 15 °C and 35 °C after introducing recycling water to the plant water system (Nessel *et al.*, 2002). The treated ore had a complex composition with significant variations in mineralogy. Chalcopyrite and sphalerite are the main ore minerals, while the main gangue is pyrite in sedimentary rock (Bulatovic, 2007).

The flotation circuit starts with aeration cells to improve pyrite depression (Figure 7-3). The reagent scheme in a copper circuit included pH adjustment to 9.5 with 300-600 g/t  $\text{Ca}(\text{OH})_2$ , cyanide depression of pyrite (50 g/t), sphalerite depression with  $\text{ZnSO}_4$  (450 g/t), and the depression of other hydrophobic gangue by carboxymethylcellulose (120 g/t). A mixture of collectors was used in the copper circuit, namely 20 g/t of sodium isopropyl xanthate, and 10 g/t of dithiophosphate (R3477). For the zinc circuit, 800 g/t  $\text{CaO}$  raised the pH level up to 11, followed by sphalerite activation with 350 g/t  $\text{CuSO}_4$ . Sodium isopropyl xanthate (30g/t) was used as the

only collector (Bulatovic, 2007). The plant is reported to experience up to 4% variations in zinc concentrate grade between seasons. It was speculated that the possible reasons are the efficiency of copper activation, changes in ore oxidation, and miscellaneous effects arising from air and pulp temperature, such as gas dispersion parameters (Nesset *et al.*, 2002).

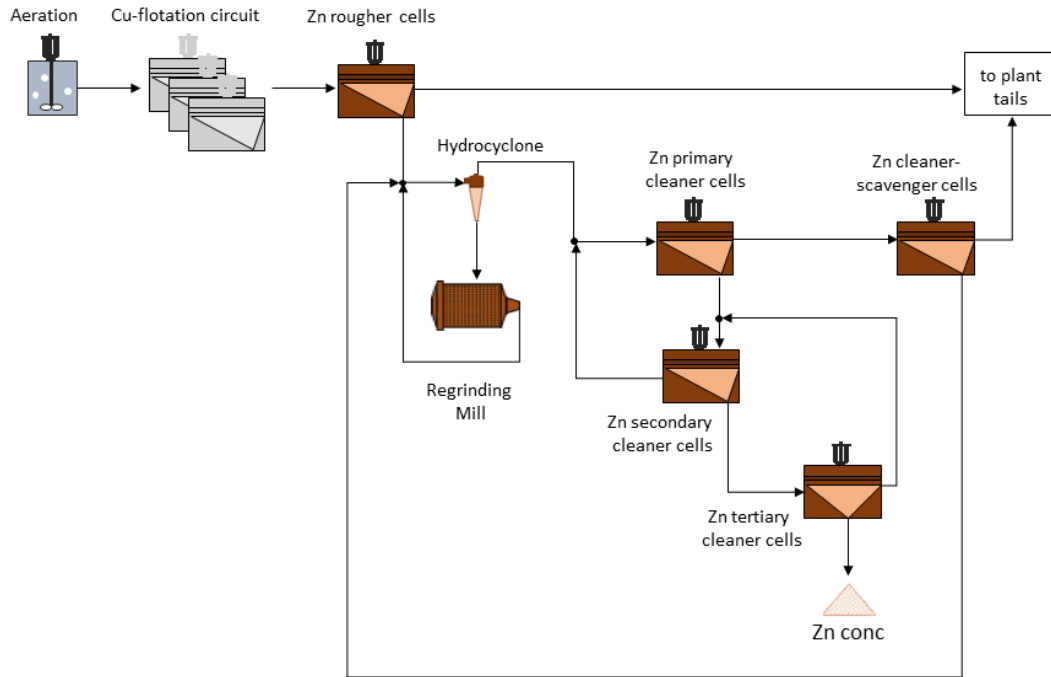


Figure 7-3. Simplified flowsheet of zinc flotation section of Matagami Concentrator (adapted from (Hamel *et al.*, 2001))

*Case 3. Caribou mine.* The mine is located in New Brunswick (Canada) in the temperate climatic zone of North America. Temperature fluctuations in the area are between  $-30\text{ }^{\circ}\text{C}$  (winter minimum), and  $30\text{ }^{\circ}\text{C}$  (summer maximum) (Jensen *et al.*, 2018). The mine extracted refractory lead-zinc ores (finely disseminated) with fine and ultrafine liberation size and high content of iron sulfides (Bulatovic, 2007). Massive sulfide zones in the deposit are made up of 90% sulfides. The main sulfide minerals are pyrite, sphalerite, galena, and chalcopyrite. The main non-sulfide gangue minerals are magnetite, siderite, stilpnomelane, quartz, and chlorite (Jensen *et al.*, 2018).

Ore conditioning starts already on the milling stage: soda ash (2-3 kg/t) and cyanide (50 g/t) are added to the grinding circuit to depress pyrite and sphalerite (Côté and Adante, 2009). The flotation section consists of 2 circuits: for lead and for zinc (Figure 7-4). In the lead circuit, the first cells work for pre-aeration to further depress pyrite. Sodium isobutyl dithiophosphine (Aerophine 3418A) is then used as the main galena collector (Jensen *et al.*, 2018), while the pH level is

maintained around 8. The zinc circuit starts with pH adjustment to above 10 with lime (1.7 kg/t). Subsequently, at the zinc cleaning stage, the pH is adjusted above 11. Copper sulfate is used as an activator (around 1.4 kg/t) (Jensen *et al.*, 2018), while sodium isopropyl xanthate is used as a collector (150 g/t) (Côté and Adante, 2009). Historically, recovery of sphalerite in New Brunswick was reported to be affected by temperature fluctuations, which was also confirmed by laboratory trials (Roberts *et al.*, 2008).

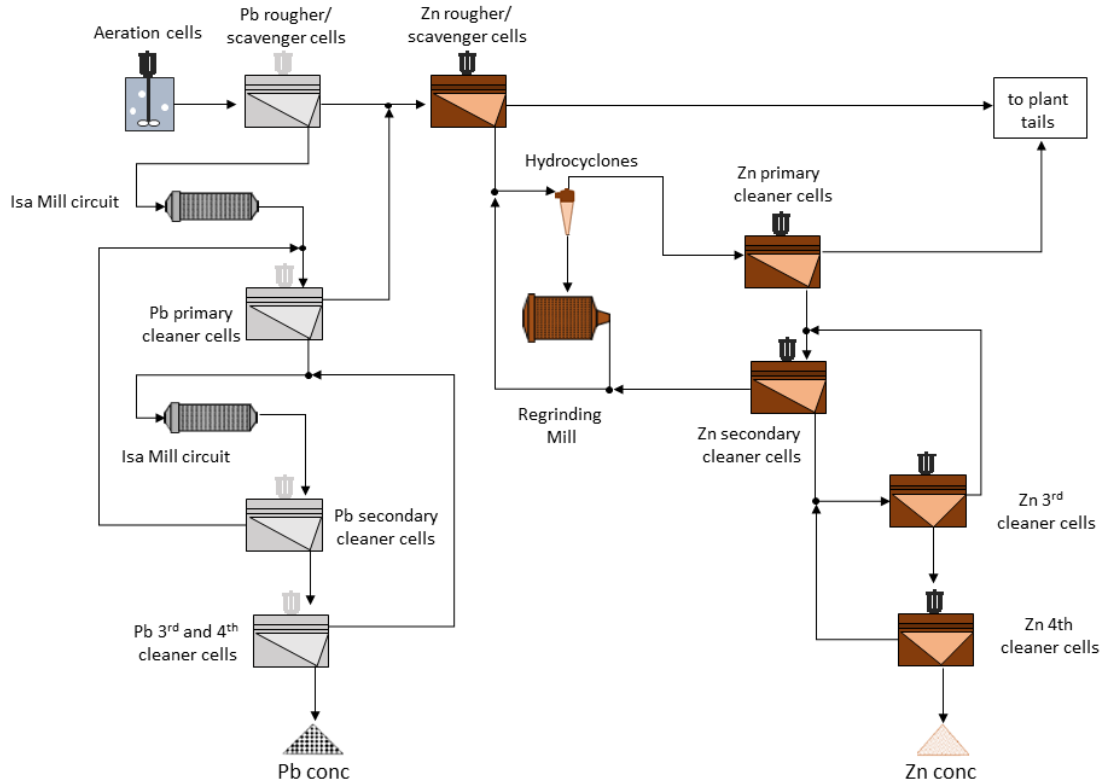


Figure 7-4. Simplified flotation flowsheet for Caribou Concentrator (adapted from (Côté and Adante, 2009))

*Case 4. Neves-Corvo mine.* Located in Southern Portugal, the Neves-Corvo mine operates in subtropical (Mediterranean) semi-arid conditions. The maximum temperature in summer reaches 40 °C, while the lowest observed winter temperature is around 4 °C (Wardell Armstrong International Limited, 2007). The ore is represented by massive sulfides high in copper and zinc (Ellis *et al.*, 2022). The mineralogy of this volcanic-hosted massive sulfide deposit consists of sphalerite, chalcopyrite, galena, pyrite, quartz, chlorite, and some minor sericite and siderite (Relvas *et al.*, 2006).

The flotation of copper and lead minerals at the plant starts by adjusting pH to 9 with lime. Bulk chalcopyrite-galena flotation is performed with a di-isobutyl dithiophosphinate collector (3418A), dosed at 40 g/t (Figure 7-5). Sphalerite depression in the copper-lead circuit is achieved using 0.5 kg/t metabisulfite. Zinc is recovered from copper-lead tails by adjusting pH to 11.5, reactivating the sphalerite surface with copper sulfate (the applied rule is 100 g/t per 1% of zinc in the feed), and hydrophobising it with 140 g/t of potassium amyl xanthate (He *et al.*, 2008). The plant has reported seasonal variations in zinc recovery related to high pulp temperatures after milling in summer. The recoveries drop at pulp temperatures above 60 °C as a result of collector desorption, and excessive formation of insoluble lead and zinc hydroxides on mineral surfaces (He *et al.*, 2008). The issue was addressed by reducing the pH from 11.5 to 10.8 and by doubling the copper sulfate dosage from 400 g/t to 800 g/t. The reduction in pH imposed a risk of increased pyrite recovery, which was suggested to be handled by an extra aeration stage after regrinding before copper activation (Fernandes, 2016).

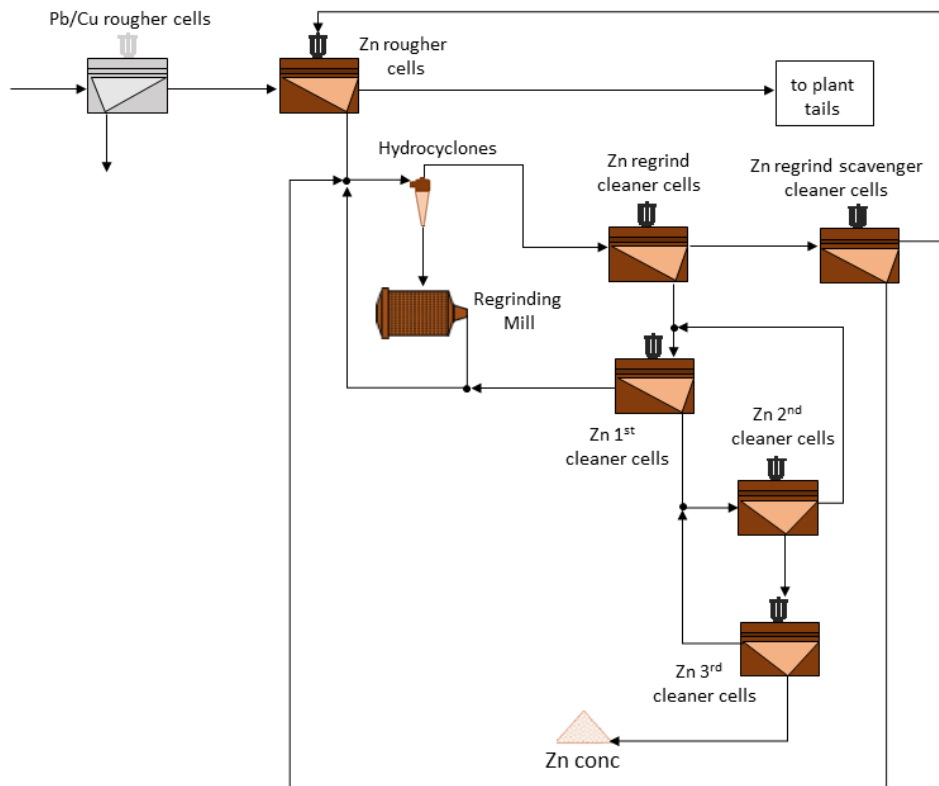


Figure 7-5. Simplified flowsheet of Neves Corvo zinc circuit of a plant (based on (He *et al.*, 2008))



The goal of this Chapter is to perform an investigation of the historical data from all four cases described in the introduction and to explore the impact of meteorological conditions on the efficiency of flotation operations.

## 7.2. Correlations Between Metallurgical Performance and Meteorological Data

Caribou Mine re-started its processing plant in August 2015 (Jensen *et al.*, 2018). The historical performance of the plant between 2015 and 2018 has been reported in a technical report by Roscoe Postle Associates Inc. (Jensen *et al.*, 2018) (Figure 7-6).

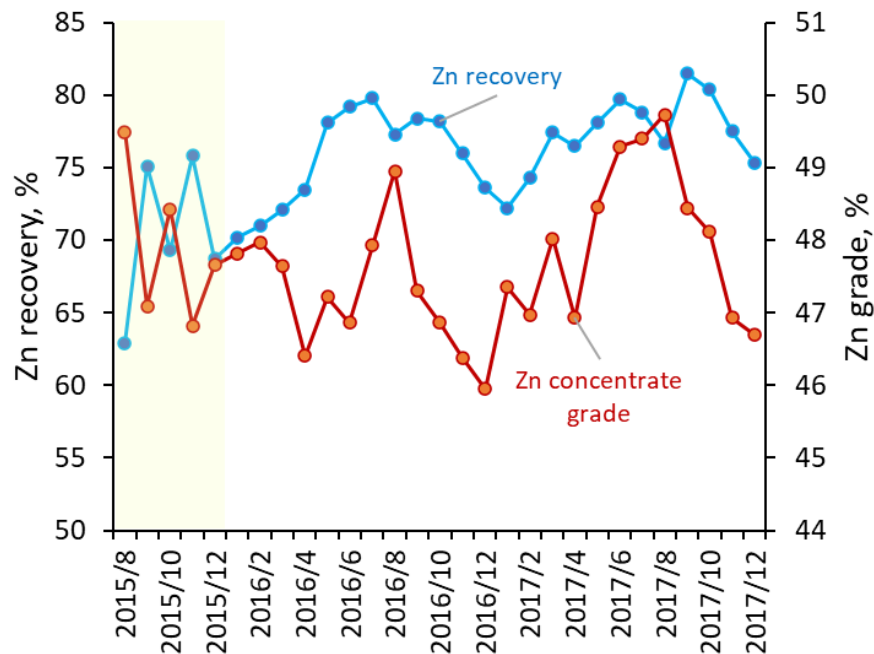


Figure 7-6. Historical performance of Caribou processing plant for zinc recovery and grade

As can be seen from the zinc grade-recovery performance (Figure 7-6), in 2015 the plant was executing major adjustments in its operation, presumably trying to achieve a sustainable spot on the grade-recovery profile with reasonable metallurgical parameters. It is reflected through synchronized fluctuations of grade and recovery curves in opposite directions (Figure 7-6). In 2016 and 2017, it could be noticed that plant performance starts to fluctuate with seasons (higher zinc grades and recoveries in summer, and lower values in winter) Figure 7-6. These observations are more evident when analyzing regression models of zinc metallurgical performance versus historical temperature recordings (Figure 7-7).

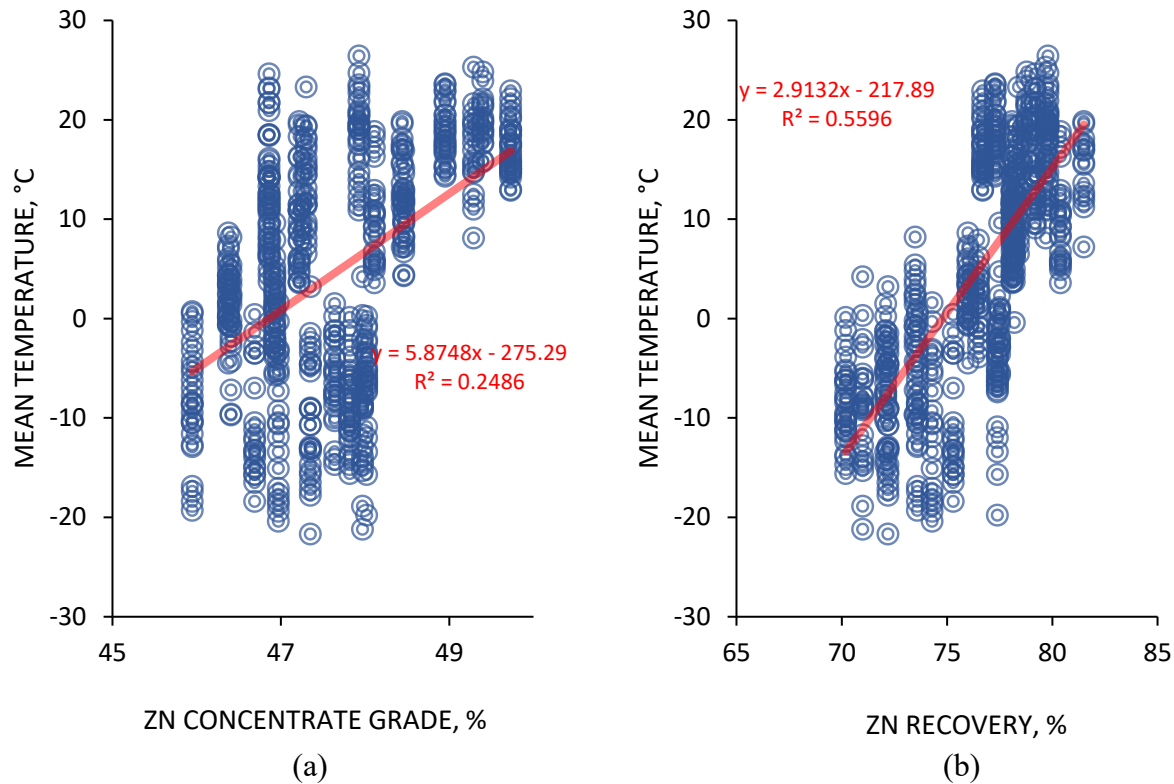


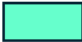
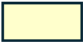
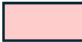

Figure 7-7. Regression analysis of zinc concentrate grade and recovery in relation to temperature (built using the data from (Jensen *et al.*, 2018)).

From the coefficients of determination given in Figure 7-7, it could be concluded that under the context of a linear model, a greater proportion of the variations in zinc recovery, compared to zinc concentrate grade, can be explained by fluctuations in temperature (0.56 versus 0.25 respectively).

This finding is also supported by a higher Pearson correlation coefficient for zinc recovery (Table 7-1). Moreover, as can be seen in Table 7-1, temperature was a stronger contributor to metallurgical variations compared to throughput and precipitations: strong positive correlations (0.79-0.6) (Dancey and Reidy, 2007) were found between temperature and zinc recovery, and moderate positive correlations (0.59-0.4) between zinc concentrate grade and temperature. Weak correlations (0.39-0.2) were also found between temperature and lead flotation performance: positive for concentrate grade, and negative for recovery. Additionally, weak positive correlations were observed between throughput and the recoveries of zinc and lead.

Table 7-1. Pearson's correlation coefficients for the metallurgical plant performance and meteorological data (calculated based on data from (Jensen *et al.*, 2018))


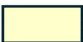


Factor	Zn concentrate grade	Zn recovery	Pb concentrate grade	Pb recovery	Ag recovery
Minimum temperature	0.463	0.7443	0.291	-0.247	-0.153
Mean temperature	0.499	0.7480	0.295	-0.252	0.033
Maximum temperature	0.512	0.7443	0.284	-0.244	0.045
Atmospheric precipitation	-0.017	0.005	0.106	-0.004	0.025
Throughput	-0.098	0.245	-0.186	0.390	0.195

 - strong correlation
  - moderate correlation
  - weak correlation
  - very weak correlation

By excluding the strong effect of temperature, the partial correlation coefficient has also shown strong correlations between throughput and zinc recovery, weak correlations between silver/lead recoveries and throughput, and precipitation and zinc recovery.

Table 7-2. Partial correlation coefficients for precipitation and throughput (built using the data from (Jensen *et al.*, 2018))





	Zn grade	Zn recovery	Pb grade	Pb recovery	Ag recovery
Atmospheric precipitation	0.107	0.257	0.097	0.009	0.017
Throughput	0.008	0.620	-0.132	0.356	0.206

 - strong correlation
  - moderate correlation
  - weak correlation
  - very weak correlation

For comprehensive data investigation, the external factors were also analyzed and ranked using the maximum information coefficient (MIC). MIC investigates linear and non-linear dependencies in the data. When considering both dependencies, it appears that throughput has the strongest association with metallurgical performance across the flotation circuit (high MIC values for zinc, lead, and silver metallurgical indicators) (Table 7-3). The mean temperature is ranked in second place, making it the most reliable forecasting tool among different temperatures reported by meteorological stations. Similar to the Pearson coefficient, atmospheric precipitation had the smallest MIC values. It means that the performance of the particular flotation plant is the least dependent on variations in the amount of rainfall.

Table 7-3. Ranking of external factors based on maximum information coefficient (built using the data from (Jensen *et al.*, 2018))

	Zn concentrate grade	Zn recovery	Pb concentrate grade	Pb recovery	Ag recovery
1. Throughput	0.999	0.999	0.999	0.999	0.999
2. Mean temperature	0.816	0.824	0.771	0.739	0.806
3. Minimum temperature	0.780	0.795	0.766	0.721	0.793
4. Maximum temperature	0.765	0.776	0.731	0.694	0.768
5. Atmospheric precipitation	0.147	0.127	0.111	0.157	0.147

 - high coefficient  
  - moderate coefficient  
  - low coefficient  
  - very low coefficient

Analysis of the historical data of another Canadian concentrator (Matagami Mine), has also revealed a certain degree of correlation between zinc metallurgical performance and climatic conditions. Thus, similar to the Caribou Mine, zinc concentrate grade increases with temperature Figure 7-8.

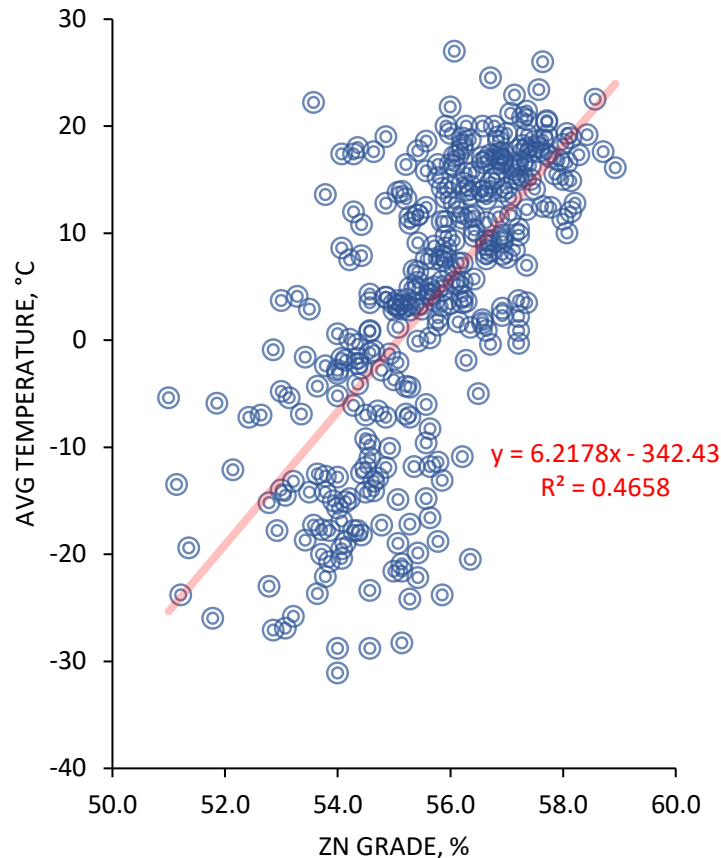


Figure 7-8. Regression analysis of zinc concentrate grade at Matagami Mine (data for analysis retrieved from (Nesset *et al.*, 2002))

As shown in Table 7-4, according to MIC and Pearson's coefficients, mean temperature has the strongest connections to zinc concentrate grade among analyzed factors. Atmospheric precipitation, similar to the Caribou case, had the smallest correlation among investigated meteorological indicators.

Table 7-4. Correlation coefficients for zinc concentrate grade and some external factors at Matagami Mine (calculated based on the data in (Nesset *et al.*, 2002))

External triggers	Pearson's correlation coefficient	Pearson's rank	MIC	MIC rank
Mean temperature	0.686	1	0.625	1
Minimum temperature	0.662	3	0.576	2
Maximum temperature	0.685	2	0.576	3
Atmospheric precipitation	0.035 -0.101* (*partial correlation)	4	0.185	4

- high coefficient
  - moderate coefficient
  - low coefficient
  - very low coefficient

Another investigated plant in the group of VMS deposits was Neves-Corvo (Portugal). For this plant, no evident correlations were observed for the entire period from 2012 to 2015 (Figure 7-9).

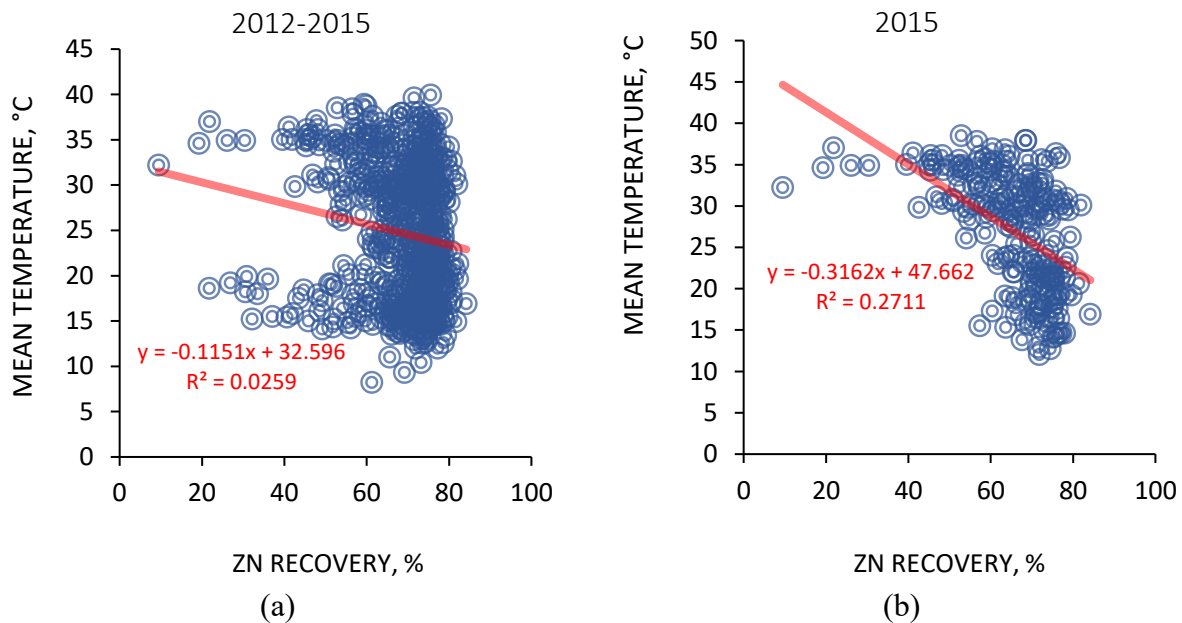






Figure 7-9. Regression models for zinc recovery with temperature at Neves-Corvo plant: (a) 2012 to 2015 data, (b) data from 2015 only (the data for the plots was taken from (Fernandes, 2016))

Further investigations of Pearson's correlation coefficient confirmed a shift in the flotation process towards a temperature-sensitive regime in 2015 (Table 7-5). Moreover, unlike for Matagami and Caribou plants, the observed correlation with temperature was moderately negative.

Table 7-5. Pearson's correlation coefficients of zinc recovery and different meteorological and process parameters (calculated based on (Fernandes, 2016))

	2012-2015	2012	2013	2014	2015
Minimum temperature	-0.122	0.206	-0.067	-0.064	-0.455
Mean temperature	-0.126	0.228	-0.076	-0.039	-0.460
Maximum temperature	-0.161	0.284	-0.108	-0.048	-0.521
Atmospheric precipitation	0.004	-0.362	0.215	-0.095	0.304
Xanthate dosage	No Data	No Data	No Data	0.034	-0.143
Lime dosage	No Data	No Data	No Data	-0.108	-0.179
Cu-sulfate dosage	No Data	No Data	No Data	-0.029	0.043

 - strong correlation
  - moderate correlation
  - weak correlation
  - very weak correlation

Moreover, from the dynamics of Pearson's correlation coefficient for atmospheric precipitation over the years, a major increase in Pearson's coefficient in 2015 could be observed. The recovery-precipitation relation appears to have an exponential trend Figure 7-10.

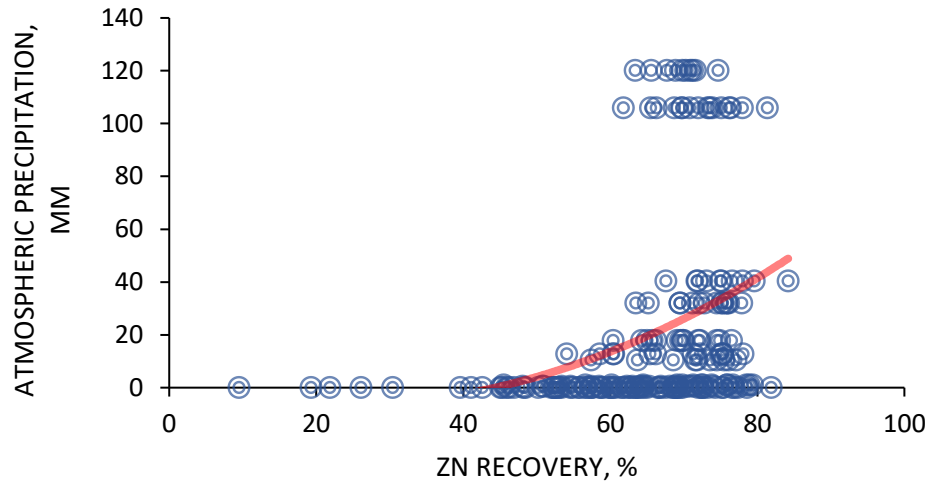


Figure 7-10. Relation between zinc recovery and atmospheric precipitation in Neves-Corvo Mine in 2015 (plotted using data published in (Fernandes, 2016))

Furthermore, the maximum information coefficient ranks atmospheric precipitation as the factor with the highest correlation among all parameters considered in this analysis, which implies the existence of some non-linear correlation between metallurgical performance and atmospheric precipitation.

Table 7-6. Maximum information coefficient of natural and process factors affecting zinc recovery in Neves-Corvo plant in 2015 (calculated based on data in (Fernandes, 2016))

Factor	MIC
Atmospheric precipitation	0.491
Maximum temperature	0.483
Mean temperature	0.439
Minimum temperature	0.435
Copper sulfate dosage	0.323
KAX dosage	0.304
Lime dosage	0.299

- high coefficient
  - moderate coefficient
  - low coefficient
  - very low coefficient



Another pair of factors with moderate correlation is the lime dosage and maximum temperature (Pearson's coefficient of 0.54), which implies generally increased lime dosage at the plant with temperature increase. Dosages of the collector (KAX) and activator (copper sulfate) compared to variations in temperature (Figure 7-11), gives an indication of the strategy applied at the plant for handling discrepancies in flotation at higher temperatures, which seems to be decreasing copper sulfate dosage and increasing xanthate dosage.

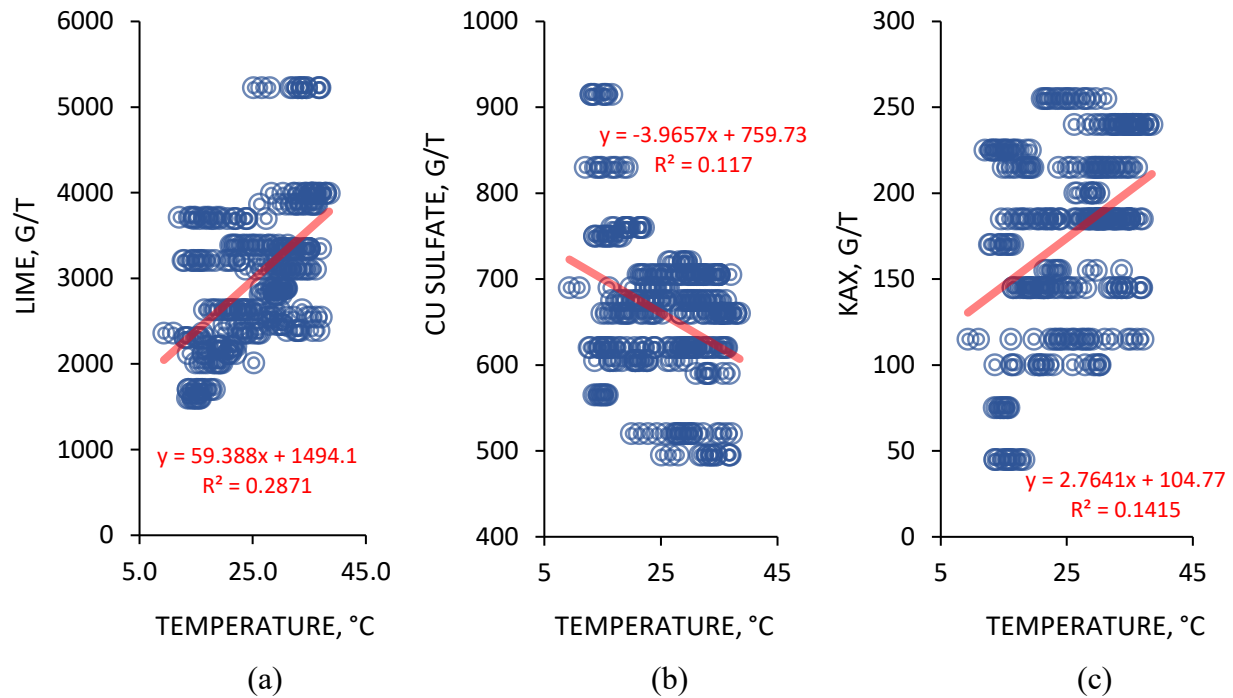


Figure 7-11. Dosages of flotation reagents compared to maximum temperature in Neves-Corvo mine: (a) lime dosage, (b) copper sulfate dosage, (c) potassium amyl xanthate dosage (constructed using the data reported in (Fernandes, 2016))

The last mine analyzed in this Chapter is Red Dog in Alaska. In 2006 the plant installed Jameson cells to pre-float organic carbon material before lead and zinc flotation circuits (Figure 7-2) (Smith *et al.*, 2008). This resulted in an improvement of zinc and lead recovery (rejection to Jameson tails for further flotation of sphalerite and galena into the respective concentrates). The improvement in the process has been reported by the mine and presented at the CMP Conference (Smith *et al.*, 2008). As can be seen from Figure 7-12, the recovery of sphalerite and galena was improved by approximately 3-4%.

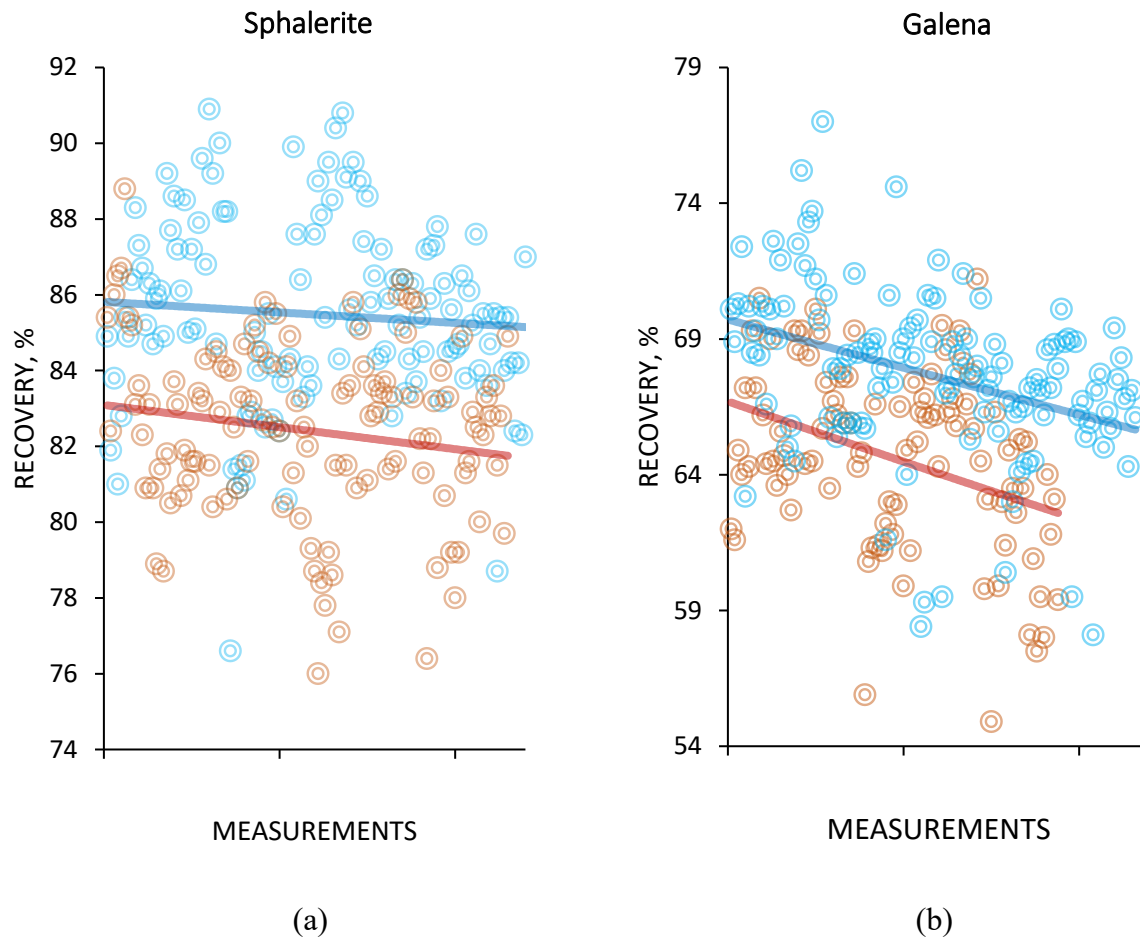


Figure 7-12. Improvement in sphalerite and galena recovery after introduction of Jameson cells on the plant (red dots and red trend line represent plant performance before installation of Jameson cells, the blue dots and blue trend line shows plant performance after installation of the cells) (adapted from (Smith *et al.*, 2008))

Assessment of the dependencies of this galena and sphalerite rejections on the temperature reveals that before this switch to Jameson cells, using conventional flotation machines there was generally a positive trend between temperature and valuable minerals' recovery to the next flotation step (Figure 7-13a and b). This trend, however, was lost after installing Jameson cells (Figure 7-13c and d).

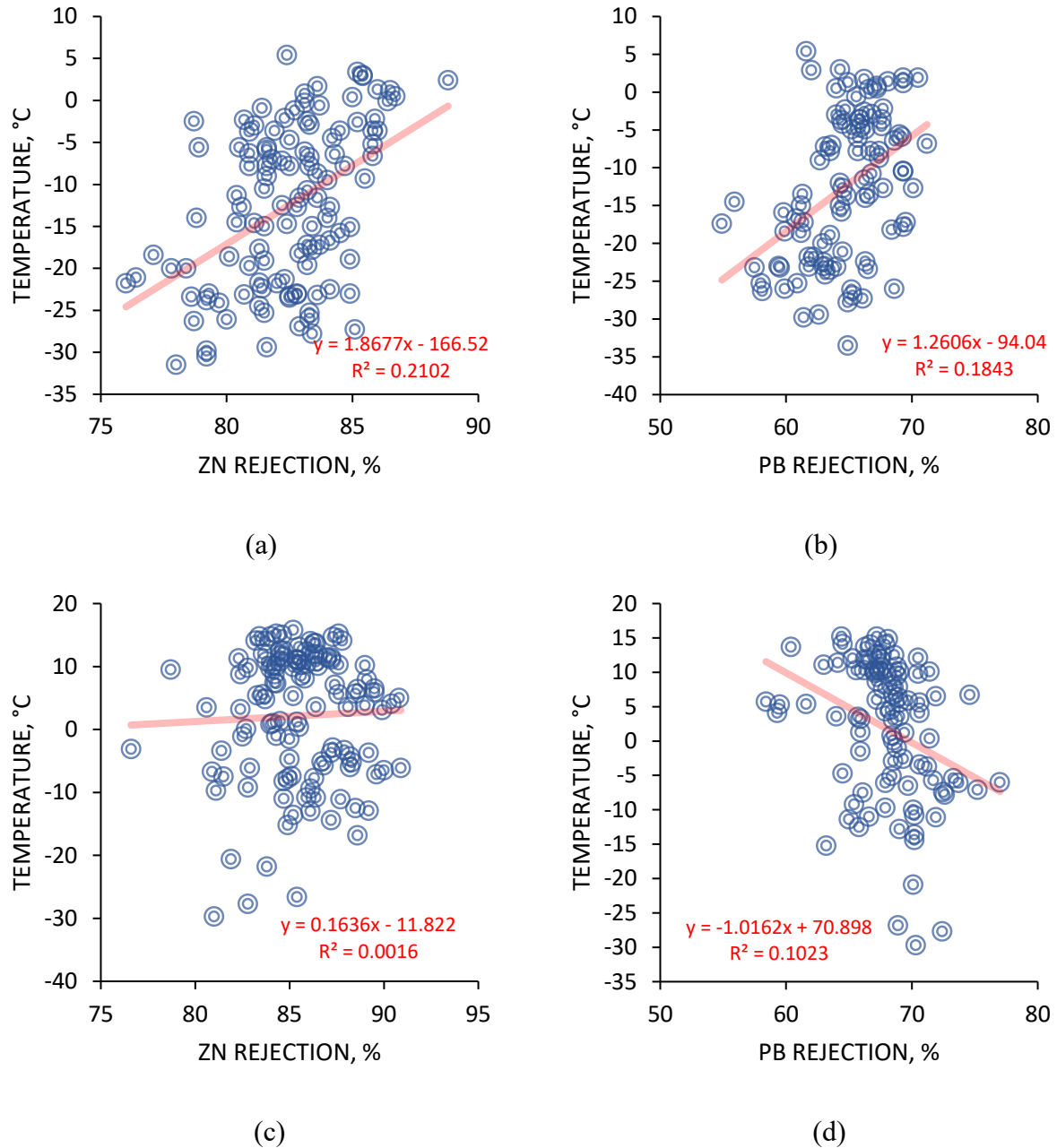


Figure 7-13. Rejection of sphalerite and galena before installation of Jameson cells (a and b), and after installation of Jameson cells (c and d), plotted based on the data published in (Smith *et al.*, 2008)

Further calculations of Pearson's coefficients confirmed a moderate positive correlation between zinc and lead recovery and temperature in conventional flotation cells, and the absence of visible impact of atmospheric precipitation on metallurgical performance. These correlations disappear after the introduction of Jameson cells (Table 7-7).

Table 7-7. Pearson's coefficients for Red Dog mine pre-flotation circuit performance versus meteorological data before and after reconstruction (based on data in (Smith *et al.*, 2008))

	Conventional flotation cell performance (operation in 2006)		Jameson flotation cell performance (operation in 2007)	
	Zn recovery	Pb recovery	Zn recovery	Pb recovery
Mean temperature	0.459	0.429	0.040	-0.342
Atmospheric precipitation	-0.142	-0.063	-0.136	-0.263

- strong correlation  
  - moderate correlation  
  - weak correlation  
  - very weak correlation

When comparing the linear sensitivity to temperature changes of laboratory and plant flotation performances, it appears that Neves-Corvo mine recovery behaves in a similar way to the microflotation of sphalerite presented in Chapter 4, and declines with an increase in temperature (Figure 7-14). Caribou mine zinc recovery, on the contrary, increases with temperature. However, the sensitivity of the Caribou mine performance to temperature is significantly lower than the one observed for the Neves-Corvo mine. On a laboratory scale, in batch flotation of SEDEX ore sphalerite recovery was also slightly increased with temperature, however, to a smaller extent compared to Caribou mine fluctuation. Regarding flotation concentrate grade, for Caribou mine, Matagami mine, and SEDEX ore an increase in temperature resulted in increased zinc concentrate grade.

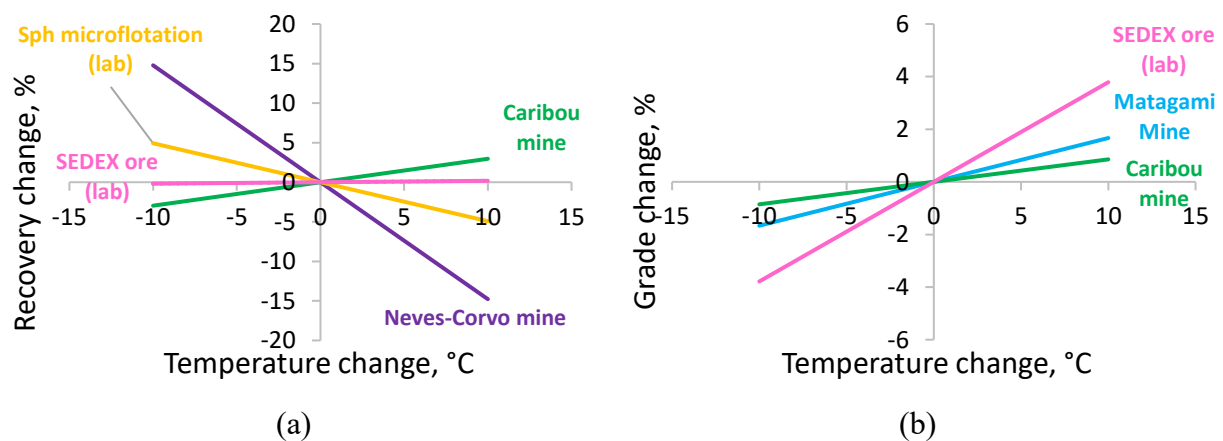


Figure 7-14. Sensitivity of laboratory investigations and plant performances in terms of sphalerite recovery (a) and sphalerite concentrate grade (b)

### 7.3. Discussions

As indicated from the analysis of the metallurgical performance of Caribou, Matagami, Neves-Corvo, and Red Dog processing plants, the temperature was a significant contributor to the process variations. Lamberg and Rosenkranz (Lamberg and Rosenkranz, 2014) have outlined 5 main problem types at the mineral processing plants:

Case I. Pure recovery issue

Case II. Combined problem of grade and recovery

Case III. Pure concentrate grade issue

Case IV. Process performance issues

Case V. Recovery issues related to quality giveaway

A common approach to address the above-mentioned issues is to adjust the aeration of the flotation cells, froth depth, reagent dosage, or throughput (Maldonado *et al.*, 2012; Remes, 2012). In the Caribou mine case, a Case II problem is observed: low temperatures had a negative impact on grade and recovery in the zinc flotation circuit of the plant. Considering the plant flowsheet which is a classical Sheridan-Grizwold regime, it means the flowsheet is vulnerable to temperature variations potentially impacting cyanide depression, copper activation, and pyrite depression with lime. There was a stronger correlation of recovery to temperature compared to grade. In some tests with lead-zinc ores from Sweden, similar effects (stronger impact on zinc recovery) were observed in the frameworks of the investigations of temperature impact on copper activation of sphalerite (Manouchehri *et al.*, 2012).

For the Matagami mine, only concentrate quality changes with temperature were reported as a production issue (Nesset *et al.*, 2002), which leads it to be classified as a Case III problem. One of the hypotheses suggested in the literature to explain these variations in production is changes in froth drainage (Nesset *et al.*, 2002). Since the plant flowsheet has MIBC as the main frother, some of the froth stability results presented in this thesis are very relevant to this operation. The laboratory data has indeed confirmed a possibility of flotation operation being impacted by lower water drainage rates in winter as a result of increased pulp viscosity in cold pulps. As the plant has experienced temperature variations from 15 to 35 °C between seasons, based on the performed simulation, it would theoretically correspond to approximately 2 times faster water drainage from

the froth. Based on this hypothesis, more efficient drainage could improve zinc concentrate grade by up to 4%.

The Neves-Corvo mine operation was historically experiencing problems in the flotation plant performance with temperature, particularly in cleaner flotation after regrinding the rougher concentrate (Figure 7-5), where the temperature of the pulp was increased above 60 °C (He *et al.*, 2008). The reported issues were with mineral recovery (Case I problem) (He *et al.*, 2008). Some of the suggested reasons in the literature were desorption/decomposition of the collector, precipitation of calcium sulfate at higher temperatures, surface oxidation of sphalerite and grinding media, oxidation of galena, and detrimental impact of lead hydroxides on sphalerite floatability (He *et al.*, 2008). Additionally, water quality has been outlined as one of the challenges in the plant, since its water supply relies on recycled water (Chadwick, 2017). In 2015 it was reported that the plant decreased lime addition to reduce the operating pH and improve the chemistry in the zinc flotation circuit (Newall *et al.*, 2017). Chronologically it also coincides with the discontinuation of direct lime addition to the water ponds at the mine site, and rearrangements of the water supply system in early 2015, which led to a 60% increase in sulfate concentration in the water ponds (Verburg and Oliveira, 2016).

Therefore, water quality variations may also exacerbate the impact of temperature variations, as has been shown in other investigations with zinc ores (Ikumapayi and Rao, 2015). Based on the data analysis presented in this research, temperature negatively impacted zinc recovery starting in 2015, while atmospheric precipitation was shown to positively impact plant performance in a non-linear way. It suggests water quality issues at the mine site (decreased lime addition supposedly increases dissolved metal concentration) have further accelerated the detrimental temperature effects on flotation through possible hydrophilization of the mineral surface by increased precipitation of iron hydroxides on sphalerite grains. This precipitation has the potential to reduce the efficiency of copper activation, and subsequently reduce mineral recovery (He *et al.*, 2008).

In the Red Dog pre-flotation circuit, similar to the Neves-Corvo operation, a Case I problem is detected (recovery issue). Since the purpose of this circuit is to float already highly hydrophobic material from the ore (*e.g.* sulfur and organic carbon), there is very little reagent application in the circuit, which narrows the choice of the possible causes of process discrepancies to froth drainage issues, similar to the explanation given to Matagami plant case. As can be seen from Figure 7-13,

with a decrease in temperature the rejection of galena and sphalerite decreases, meaning that these minerals were non-selectively dragged into the concentrate. To ensure that natural hydrophobicity does not lead to galena recovery to the pre-flotation concentrate the plant also reported the addition of dextrin as a depressant (Smith *et al.*, 2008). After the installation of the Jameson cell, the entrainment rates of galena and sphalerite decreased, which is explained by the design features of the machine. First of all, diffuser plates (with optimized shape and porosity) in Jameson cells facilitate even dispersion of bubbles, which further reduces entrainment in the froth (Cowburn *et al.*, 2005). Secondly, Jameson cells are typically equipped with a wash water system above the froth to facilitate the drainage of entrained material (Ding, 2016).

A comparison of laboratory and plant sensitivities toward temperature revealed similar trends. Thus, similarities in Neves-Corvo mine flotation trends and microflotation results from Chapter 4 suggest primary concentration (surface chemistry) origins of the issue (possibly related to the hydrophilization of mineral surface at higher temperatures by the formation of some precipitates). Lower magnitude increases in recovery at the Caribou mine and in SEDEX ore laboratory tests could be attributed to increased copper activation efficiency at higher temperatures. Matagami and Caribou mine concentrate grades, similar to SEDEX ore flotation tests, also demonstrated higher values at higher temperatures. Considering an established highly negative correlation between zinc concentrate grade in SEDEX ore flotation and froth stability parameters (air recovery and froth stability factor), it could be suggested that one of the possible driving mechanisms is related to decreased froth stability accompanied by increased drainage and lower entrainment.

## **7.4. Conclusions**

It has been demonstrated that meteorological data can be used to explain the variations observed on flotation plants. Temperature was generally a more important parameter as opposed to atmospheric precipitation. The maximum information coefficient is a useful tool that allows tracing just not only linear dependencies but also non-linear correlations between environmental factors and metallurgical performance. A range of hypotheses was derived based on correlations in the datasets, starting with froth drainage effects, and ending with water quality issues. The application of more efficient flotation machinery can improve the metallurgical performance and reduce temperature effects on flotation responses.

---

## Chapter 8. Global Discussions and Conclusions

### 8.1. Global Discussions

Based on the results presented in this thesis (experimental, theoretical computations, and plant data analysis), it is concluded that the broad variety of operational conditions does not allow for formulating a uniform recipe that would encompass all temperature-related issues observed at different processing plants. Each processing plant must be individually investigated as many temperature-induced effects of a completely different nature may have a similar impact on grade and recovery. It has been demonstrated with four mine cases located in different climatic zones that the same degree of variation in temperature may have the opposite effect on the flotation of ores that belong to the same geological classification.

From the conducted laboratory investigations, it can be concluded that the main lead-zinc ore minerals, such as galena and sphalerite, as well as the main gangue mineralogy (such as pyrite, quartz, and baryte) are all, to a different degree, subjected to temperature-driven variations. The largest and the most consistent variations across different flotation test settings (in monomineralic form and as a part of the multi-mineral suspension of different pulp density, in tests with and without secondary concentration in flotation froth) were generally observed for sphalerite (Sections 4.4, 6.2.3, and 6.3).

From the broad investigation of the problem at different levels the majority of temperature-induced issues in sphalerite froth flotation can be grouped into surface chemistry-based (*e.g.* copper activation (Section 6.3), collector adsorption (Section 4.3), formation of hydrophilic precipitates at the mineral surface (Section 4.4), or flotation depressant effect (Section 6.3), *etc.*), and issues related to froth stability (gangue drainage from flotation froth (Sections 5.4, 6.3), decreased froth carrying capacity (Section 6.2.3), *etc.*

Before addressing temperature-induced issues a baseline for the flotation operation has to be established, data analysis of the metallurgical performance has to be performed (Chapter 7), and mineralogical investigations have to be conducted (Sections 3.1, 3.2) to ensure the variations are not caused by fluctuations in the properties/composition of the feed material. For that, the mineralogical diagnostic approach must be run first, consisting of analysis of particle size



distribution (Section 3.2), modal mineralogy analysis (using different techniques: surface-based (Section 3.2.1) and bulk-based (Section 3.2.2)) for flotation feed and flotation products. Since in the experiments detailed in this thesis, all samples were prepared in a batch manner (all at once), they were properly blended, and representatively partitioned using a rotary splitter / sampled using the best laboratory practices, the effect of ore (experimental feed) variation was minimized. To ensure quality control, feed samples were analyzed before running the experiments. Flotation is a dynamic system responsive to environmental changes, just like a living organism. Therefore, diagnostic/treatment approaches from medicine can be applied to it.

Thus, in the framework of a seasonal metallurgy diagnostic/treatment campaign, the main steps would be to collect the baseline information (mineralogical, process, and environmental), followed by performing laboratory testing and sample analysis. Once the problem is understood, the next steps would be to suggest possible treatments (creating initial hypotheses), and testing them on a laboratory scale, followed by potential implementation at pilot scale before being introduced into industry. Monitoring the outcome, by performing sampling, and making modifications to the recipe if needed is crucial and should not be ignored as some issues may change over time, or some solutions may seem beneficial in the short term but have a negative long-term impact. Throughout the process of diagnostics and testing of potential treatments it is extremely important to remove bias, which was addressed in this research by the application of multiple designs of experiments with test randomization.

After establishing the temperature-driven nature of observed variations in the operation, the cause of the process discrepancy must be further narrowed down. It should be identified whether the observed issues are surface chemistry-based or froth stability-based (or both). Surface chemistry-based issues may be identified by checking the surface energy of the valuable minerals (as described in Section 4.4). Hydrophobic minerals would show low surface energy, while sufficiently hydrophobized material would demonstrate higher values of surface energy. For example, the correlation between surface energy and microflotation response in this research assisted in establishing that the cause of the problem was surface chemistry-based and not related to the transport of flotulas (bubble-particle aggregates) to the concentrate. Additionally, by performing microflotation tests the effect of foam/froth is excluded; thus, primary concentration may be investigated separately. In order to address the surface chemistry-based issues it should be

established which conditioning step is a bottleneck in the process (efficiency of which flotation reagent compromises the flotation process), and/or which hydrophilic species appear on the valuable mineral surface (or hydrophobic species on gangue surface). After establishing the presence of hydrophilizing species on the mineral surface (*e.g.* by using SEM-EDS and XPS, Section 4.4) it must be determined where they originate from.

The next step in the diagnostic/treatment algorithm is to attempt to address temperature-related metallurgical issues on the laboratory scale. On the lowest level of decision-making (the simplest solution) it would encompass an increase/decrease in the reagent dosage (depending on the calculated/experimentally established demand of the reagent (*e.g.* methodology described in Section 3.7.1.)) to tilt the equilibrium back towards hydrophobization of the target mineral surface.

It is also known that pH has a crucial role in this equilibrium (Section 4.2) as it facilitates/prevents reagent adsorption, and acts as an activator/depressant for different minerals and reagents at different levels. “Tuning” pH may be considered as a possible option to restore flotation performance. For example, the most efficient activation of sphalerite by copper is achieved at pH values around 6. The second maximum is observed at pH 11 (Mitrofanov, 1966). Additionally, pH above 11 renders pyrite hardly floatable (Bai *et al.*, 2019). The importance of pH and its variations with temperature were also highlighted in reports from industry (Weise *et al.*, 1978).

Lime is often used as a pH modifier; however, its solubility changes with temperature (Section 4.4). Calcium from lime addition may also precipitate in different forms in flotation pulps which was found to have a seasonal detrimental effect on sphalerite flotation in this research (Section 4.4), in laboratory flotation experiments from the literature (Shumskaya *et al.*, 2016) and at plant scale (*e.g.* Neves-Corvo mine (Chadwick, 2017)). In another laboratory investigation, it was found that zinc recovery did not change significantly at higher pulp temperatures (like in SEDEX ore flotation tests in Section 6.3), except when high concentrations of calcium, sulfate, and thiosulfate were added to the flotation pulp, which likely led to gypsum/aragonite precipitation and decreased sphalerite recovery (Bicak *et al.*, 2023). In order to decrease calcium content in a system and prevent undesirable precipitation of calcium complexes (such as, *e.g.* calcite or gypsum) on sphalerite, utilization of lime alternatives should be considered (*e.g.* soda ash).

From the perspective of reagent adsorption kinetics, when it has been confirmed at the laboratory scale that reagent adsorption is reduced at lower temperatures (as demonstrated in Section 4.3), reconfiguration of the reagent addition point in a flowsheet can be considered in order to increase the conditioning time (*e.g.* addition of a reagent already on a milling stage). In the case of some flotation reagents, considerable time should be allocated for successful adsorption. For example, copper activation of sphalerite is known to be efficient at weakly acidic conditions. However, in an alkali environment for complete surface activation, an increase in the conditioning time of up to 20 min may be required (Mitrofanov, 1966).

From the perspective of cell hydrodynamics and gas dispersion, aeration levels may also be adjusted, as according to some investigations in peak air recovery theory (Hadler *et al.*, 2012), different froth heights (which can be observed at different temperatures, Section 5.3) have different optimal conditions maximizing the production outcome. These four approaches normally comprise the most widely applied, simple, and low-cost process adjustments. However, they may not always help to solve the problem.

In cases when the desired flotation properties are not restored by simple low-cost optimizations at the plant, some additives may be added to increase the efficiency of temperature sensitive flotation reagents. For example, it has been broadly demonstrated (Albrecht *et al.*, 2016; Siva Reddy and Konda Reddy, 1988) that copper activation efficiency decreases at low temperatures. This issue can be, for example, addressed by introducing ammonium sulfate in the flotation pulp together with copper sulfate. That would facilitate the formation of a soluble copper-ammonium complex, serving as a reserve of copper cations for sphalerite activation. Depending on the season (pulp temperature) ammonium sulfate dosage can be decreased (*e.g.* in summer) given conditions accelerating copper sulfate solubility (Mitrofanov, 1966) and efficiency are in place.

Whenever the introduction of the additives does not fully restore flotation performance to a baseline state, a switch between reagents in different seasons may be considered. For example, as has been described in Section 2.5.3, in the potash industry longer chain amines are used in winter, while shorter chain amines are applied in summer. By using a similar approach, it may be suggested to introduce in zinc flotation longer chain xanthates at temperature conditions corresponding to lower sphalerite recovery (for example at lower temperatures, where xanthate demand increases, as demonstrated in Section 4.2). Longer chain xanthates form less soluble compounds on mineral

surfaces and, therefore, have higher collecting power (Özün and Ergen, 2019). It has been reported that even insufficiently activated by copper sulfate, sphalerite may still be floated using a longer chain xanthate (Pålsson and Forssberg, 1989). Additionally, increased oxidation of mineral surfaces is handled easier with stronger long-chain xanthate. The choice of xanthate chain length is, however, limited (between C2 to C5), as xanthates with longer chains have solubility problems in aqueous systems (Özün and Ergen, 2019). Alternatively, the synergistic effects of collector blends may be exploited. By mixing collectors from the same or different reagent families (*e.g.* thiol-thiol, thiol-anionic, thiol-cationic, or thiol-polymer) flotation performance can be also improved (Bradshaw *et al.*, 1998)

As for the depressant regime, another potential reagent substitution may be considered, such as the replacement of cyanides in pyrite depression, since cyanide efficiency is also known to fluctuate with temperature (a decrease in depressing power at lower temperatures has been reported (Wark and Cox, 1938)). Possible eco-friendly alternatives to cyanide for pyrite depression in zinc circuits include biodegradable reagents, such as dextrin (whose adsorption mechanism was studied in Section 4.3), lactic acid, humic acid, *etc.* (Asimi Neisiani and Chehreh Chelgani, 2023). Some of these reagents, like humic acid, have inverse-temperature solubility (Shaffer and von Wandruszka, 2015), which can be particularly useful for improving mineral depression at lower temperatures.

From the perspective of froth stability issues, as demonstrated in Chapter 5, for MIBC systems there is a general decrease in frothing properties with an increase in temperature. This has three main implications. First, too low a pulp density (10%) coupled with the weak nature of MIBC frother, high water drainage in the froth, and increasingly turbulent conditions create an extremely unstable froth, which can result in low recoveries of valuable minerals, as described in Section 6.2. Secondly, at low temperatures, increased froth stability and low drainage can deteriorate concentrate quality through increased entrainment of the gangue (demonstrated in the example of SEDEX ore in Section 6.3). Thirdly, higher drainage rates at higher temperatures and pulp solid density values above 30% may help to produce higher-grade concentrates (Section 6.3 and Section 7.2).

Therefore, froth stability is a delicate flotation parameter, since too stable and too weak froth are both detrimental to the process. Since an optimal grade-recovery balance is at the core of a successful processing plant operation, froth properties should correspond to the required levels of

stability and flexibility. Froth stability and associated process discrepancies can be targeted by numerous means, such as improved flotation machines (described in Chapter 7), variation in frother dosage (highlighted in Section 5.2), changes in aeration levels (Section 5.2), application of frothers of different strength at different seasons (Section 5.4), application of drainage-facilitating rheology modifiers (such as *e.g.* sodium silicate (Molifie *et al.*, 2023), or application of different polymers (Farrokhpay *et al.*, 2013; Wang and Li, 2020)).

In terms of flotation machinery, the application of flotation columns or Jameson cells with installed wash water systems above the froth is seen as a potential way of mitigating entrainment issues caused by temperature variations (as demonstrated in Section 7.2). For example, flotation columns normally operate at higher froth depth, which leads to more efficient gangue drainage. Thus, for example, O'Connor and Mills demonstrated in the example of a column that gangue entrainment across different temperatures may be reduced by increasing the operating froth height (O'Connor and Mills, 1990).

In view of froth-related issues, frothless flotation may also be considered as an option for the reduction of temperate impact on the process. Such machines as the Reflux<sup>TM</sup> Flotation Cell or HydroFloat<sup>TM</sup> may be used (with certain limitations) depending on the ore characteristics. Generally, all high-intensity flotation machines (Jameson<sup>TM</sup>, Imhoflot<sup>TM</sup>, Reflux<sup>TM</sup>, Concorde Cell<sup>TM</sup>, StackCell<sup>®</sup>, *etc.*) (Hassanzadeh *et al.*, 2022; Yáñez *et al.*, 2024), would improve flotation kinetics, which is especially beneficial in view of decreased flotation rates at lower temperatures, which was observed in this research using conventional mechanical flotation cell (Section 6.2 and Section 6.3).

Apart from flotation kinetics, froth mobility was also found to change with temperature (Section 5.3.3). Potential issues with froth transport can be addressed by physical flow modifiers, that facilitate froth flow. Some examples of such physical flow modifiers include froth crowders (applied in the flotation experiments and detailed in Chapter 3) or froth launders, *etc.* Froth drainage, bubble bursting rate, and froth stability were generally found to fluctuate with temperature (Section 5.3). They may be also impacted by using froth baffles and scrapers, which have previously been found to have a profound effect on the froth characteristics (Jera and Bhondayi, 2021). Installation of these additional accessory parts provides another degree of freedom in controlling the flotation performance. Moreover, the application of vertical froth baffles

is known to change the pattern of the flow of froth, which could potentially address high turbulence issues in the froth zone manifested through low bubble size, shallow froth, and low mineral yields demonstrated in Section 5.3. A horizontal under-froth grid for froth stabilization was also installed in the laboratory experiments conducted in this research (Section 3.2.1), however this had limited impact.

Another way for exerting impact on the flotation froth is by manipulating ionic composition, which was seen to increase froth stability, level of entrainment, and gangue recovery in Section 6.3. In view of water scarcity in some areas of the world, as well as considering the United Nations sustainable development goals on responsible water use, such froth stabilization methods should be investigated further in the frameworks of seawater use in froth flotation (Gutierrez *et al.*, 2020).

From the perspective of frother chemistry, stronger frothers may be applied during the summer season (*e.g.* PPG, or PEG) whenever degraded froth stability decreases the recovery of valuable minerals. Lower water drainage will facilitate the building of a stronger froth under higher temperature conditions (as demonstrated in Section 5.4). Similar to the suggestions for flotation collectors, frother blends may be also investigated (Bradshaw *et al.*, 1998), and potentially applied at different blend ratios for different temperature scenarios to maintain the same froth-carrying capacity throughout the seasons.

Another promising field in increasing froth stability at higher temperatures is the application of Gemini surfactants. Gemini surfactants are dimers that consist of two surfactants linked by a spacer. These surfactants are gaining attention because of their low critical micelle concentration, high solubility, and remarkable foaming properties (Guerrero-Hernández *et al.*, 2022). For example, Gemini (GACB) was demonstrated to have smart foam drainage properties: higher drainage at lower temperatures and lower drainage at higher temperatures (Jia *et al.*, 2022), which is inverse to what was observed for the MIBC system in this research. Gemini surfactants were also demonstrated to be efficient collectors at extremely cold temperatures, which was demonstrated in the example of Gemini BBDB at 0 °C in kaolinite flotation (Zhang *et al.*, 2021a), and may be considered as an option for reverse flotation for cleaning lead-zinc concentrates in the context of ores with high clay content.

Apart from developing solutions to temperature-driven variations in flotation, performance tracking and forecasting tools are also important, as they could potentially inform in real time on possible shifts in the flotation equilibrium, caused by intrinsic and extrinsic factors, including ore quality or variations in meteorological conditions. Thus, froth property monitoring with the help of different sensors (*e.g.* conductivity, ultrasonic, optical, piezoelectric, torque, *etc.*) can help to obtain comprehensive information on froth stability parameters, quantity of water, froth height, bubble burst rate, froth loading, *etc.* All this information can be used to create more robust flotation performance predictors and appropriately react to the changes in the process. Thus, *e.g.* air recovery and froth stability were shown to be correlated to froth flotation grade (Section 6.3).

## **8.2. Contributions to the Original Knowledge**

Overall, through laboratory experiments, theoretical calculations/simulations, and data analysis this thesis has made a number of important contributions to the field of seasonal flotation metallurgy, which can be summarized in the following twelve points:

1. This research is the first comprehensive investigation of primary and secondary concentration aspects of lead-zinc flotation at different temperatures.
2. Several mechanisms were discovered, potentially explaining seasonal variations observed at different flotation plants, such as, for example, calcite precipitation on the sphalerite surface at higher temperatures.
3. This research for the first time shows the application of inverse gas chromatography for surface energy measurements of minerals conditioned and floated at different temperatures. The validity of the iGC methodology for investigations in lead-zinc flotation seasonal metallurgy was proven. This research additionally demonstrated how this data could be efficiently used to better understand the underlying process problem and screen out possible reasons for the discrepancies in flotation.
4. This research also extended the thermodynamic approach for flotation optimization (developed by Abramov) by introducing a temperature-correction procedure, which allowed the development of models for multiple temperature scenarios.

5. From a foam/froth stability perspective, this research for the first time comprehensively investigated these 2 and 3-phase systems at different temperature conditions and flotation scenarios (mimicking cleaner and rougher-scavenger conditions). Froth characteristics were linked to an actual metallurgical performance.
6. For the calculations of air recovery, the classical simplified approach was amended by considering the effects of water volume, which produced more precise results.
7. In this research for the first time the froth stability factor was directly calculated in the context of temperature-induced variations in the froth. A simplified equation was derived for the direct calculation of the froth stability parameter based on laboratory experimental data.
8. The physical meaning of the froth stability factor was changed to encompass not the total froth height but only the froth height over the lip part, linking it this way more tightly to the continuous flotation process. The new definition of froth stability factor used in this thesis is: under the condition of immediate stop of air influx, the stability factor represents the time that froth would take to collapse until the level when cell self-overflowing stops (by assuming the recorded burst rate and bubble size captured from the top of the surface are unchanged). By narrowing the definition of the froth stability factor to a portion of a froth height over the lip, the produced values of potential froth collapse time are more accurate, since in real flotation tests froth bubble size and bubble burst rate would change over the froth profile.
9. An equation for bubble size change on the top of the froth over time was developed
10. In this research for the first time industrial-scale seasonal metallurgy data from different mines was compared to laboratory flotation performance
11. At the end of the thesis an algorithm for addressing complex seasonal metallurgy flotation production issues was described, which is not comprehensive and can be amended. However, it covers most of the seasonal metallurgy issues reported in the literature, as well as discovered through theoretical calculations, experimental laboratory work, and plant data analysis in this thesis.
12. Additionally, this research explored the applicability of a novel laboratory semi-continuous flotation approach, developed on a base on a mechanical flotation cell (fully automatized standard



Denver flotation cell equipped with temperature jacket, a laser for automatic level control, camera for bubble size and froth speed measurements, and connected to a laptop for continuous recording). This scraper-free flotation approach allows investigations of the froth phase concurrently to running flotation tests, which allows linking metallurgical performance to froth properties.

### **8.3. Global Conclusions**

The main conclusions covering primary, secondary concentration, and based on experimental and computational results are the following:

1. As a result of this research all main flotation components were successfully investigated under different temperature conditions.
2. Temperature has been demonstrated to have a pronounced effect on reagent adsorption (sodium isopropyl xanthate) and froth/foam stability. Nevertheless, based on microflotation results bubble-particle transport mechanism did not have a pronounced effect on the floatability changes of investigated minerals (galena, sphalerite and pyrite) with temperature (in the range 5-45 °C).
3. From a surface-chemistry perspective, theoretical calculations and experimental data suggest temperature-driven variations originating from the formation of hydrophilic carbo-hydroxy complexes on the mineral surface, and the formation of different hydrophilic precipitates. The kinetics of reagent adsorption (sodium isopropyl xanthate) was also demonstrated to be impacted by temperature.
4. From the froth stability perspective froth drainage is shown as the principal driving mechanism of secondary concentration changes with temperature. Froth stability change with temperature was demonstrated to have a negative and positive impact on flotation performance.
5. For more efficient utilization of froth stability information, all recorded indicators were used to calculate air recovery and a froth stability factor. Further, these 2 parameters were demonstrated to be strong predictors of flotation performance on the laboratory scale.
6. The research has demonstrated a link between observed at the plants variations in metallurgical performance and flotation results obtained on the lab scale.

7. Mitigation of temperature-induced variations can be potentially tackled by improvements in pulp chemistry, manipulation in operating conditions, or utilization of more efficient flotation machinery.

#### **8.4. Recommendations for Future Work**

The following are suggestions for the next stages of seasonal flotation metallurgy research, which can expand the findings of this thesis:

1. Recovery and grade -maximizing optimal aeration conditions should be discovered for each temperature scenario
2. Since for this research Denver cell was primarily used, the sensitivity of flotation performance to temperature variations in conventional flotation cells of different designs (*e.g.* OK type, Wemco, Sala, Wedag, etc) should be considered, and an impact of temperature on cell hydrodynamic conditions should be investigated
3. The sensitivity of high-intensity and pneumatic flotation cells to temperature variations should be investigated, and optimal conditions found
4. Testing of different collectors (of different families and different hydrocarbon chain length) and frothers (alcohol and glycol-based) to develop seasonally tailored recipes is also an emerging direction of flotation seasonal metallurgy
5. As it has been briefly discussed in this research, water quality has also a significant impact on the flotation performance, and it was found to impact different flotation aspects. Investigations of an interplay between temperature and water quality will allow an even better understanding of the variations at the plant level
6. Temperature-sensitive (or temperature-robust) reagents should be explored to find a way to exploit their changing characteristic with temperature to improve the flotation process (*e.g.* Gemini reagents).

---

## References

- Abdel Khalek, M., 2011, Performance of different surfactants in deinking flotation process: The Journal of Ore Dressing, v. 13, p. 15-21.
- Abere, D. V., Ayodele, T. J., Emmanuel-Alonge, T., Adejo, O. H., Filusi, G. F., John, M. J., and Otebe, S. I., 2018, Enrichment of zinc concentration of Ishagu lead-zinc ore deposit through beneficiation techniques: Open Science Journal of Analytical Chemistry, v. 3, no. 4, p. 33-38.
- Abkhoshk, E., Jorjani, E., Al-Harashsheh, M. S., Rashchi, F., and Naazeri, M., 2014, Review of the hydrometallurgical processing of non-sulfide zinc ores: Hydrometallurgy, v. 149, p. 153-167.
- Abramov, A., 1977, Физико-химическое моделирование флотационных систем. Раздел: Физико-химическое моделирование взаимодействия реагентов с минералами при флотации / Physical-chemical modeling of flotation systems. Section: physical-chemical modeling of interaction between reagents and minerals during flotation (Textbook) [in Russian], Moscow, Moscow Steel and Alloy Institute, p. 100
- Abramov, A., 2004, Fundamentals for optimization of cyanide processes in flotation: The European Journal of Mineral Processing and Environmental Protection, v. 4, no. 1, p. 15-29.
- Abramov, A., 2005, Технология переработки и обогащения руд цветных металлов / Technology for processing and concentration of non-ferrous metal ores (Textbook) (in Russian), Moscow State Mining University, v. 2, p. 575
- Abramov, A., 2010, Флотация, физико-химическое моделирование процессов/ Flotation, physical-chemical modelling of processes [in Russian], Moscow, Izd. Gornaja Kniga, v. 6, p. 607
- Abramov, A., 2012, Флотация: реагенты собиратели / Flotation: collector reagents (in Russian), Moscow, Izd. Gornaja kniga, v. 7, p. 41
- Abramov, A., 2013, Флотация: сульфидные минералы / Flotation: sulfide minerals (in Russian), Moscow, Gornaja Kniga, v. 8, p. 33-301

- Abramov, A., and Forssberg, K. S. E., 2005, Chemistry and optimal conditions for copper minerals flotation: theory and practice: *Mineral Processing and Extractive Metallurgy Review*, v. 26, no. 2, p. 77-143.
- Abu-Hamatteh, Z. S. H., and Al-Amr, A. M., 2008, Carnallite froth flotation optimization and cell efficiency in the arab potash company, Dead Sea, Jordan: *Mineral Processing and Extractive Metallurgy Review*, v. 29, no. 3, p. 232-257.
- Albrecht, T., Fornasiero, D., and Addai-Mensah, J., Effect of water temperature on sphalerite flotation, 2010, *in Chemeca Proceedings: Engineering at the Edge*, pp. 1–10.
- Albrecht, T. W. J., Addai-Mensah, J., and Fornasiero, D., 2016, Critical copper concentration in sphalerite flotation: Effect of temperature and collector: *International Journal of Mineral Processing*, v. 146, p. 15-22.
- Aliferova, S., 2007, Активация процессов флотации шламов и сильвина при обогащении калийных руд / Activation of flotation processes for slimes and sylvite during potassium salt processing (in Russian) PhD Thesis: Ural State University, Mineral Processing, p. 194
- Amend, J. P., and Shock, E. L., 2001, Energetics of overall metabolic reactions of thermophilic and hyperthermophilic Archaea and Bacteria: *FEMS Microbiology Reviews*, v. 25, p. 175-243.
- An, D., and Zhang, J., 2020, A study of temperature effect on the xanthate's performance during chalcopyrite flotation: *Minerals*, v. 10, no. 5, 426.
- Anderson, A. E., and Hedley, N., 1939, Differential flotation of lead-zinc ores, US Patent Office, Patent No.: US2150114A, p. 3.
- Anderson, C. D., 2015, Improved understanding of rare earth surface chemistry and its application to froth flotation PhD Thesis: Colorado School of Mines Metallurgical and Materials Engineering, p. 242
- Åqvist, J., Kazemi, M., Isaksen, G. V., and Brandsdal, B. O., 2017, Entropy and enzyme catalysis: *Accounts of Chemical Research*, v. 50, no. 2, p. 199-207.
- Arrhenius, S., 1889, Über die Dissociationswärme und den Einfluss der Temperatur auf den Dissociationsgrad der Elektrolyte / About the heat of dissociation and the influence of temperature on the degree of dissociation of the electrolytes (in German): *Zeitschrift für Physikalische Chemie / Journal of Physical Chemistry*, no. 1, p. 96-116.

- Arustamjan, A., 2004, Влияние температуры пульпы на показатели цинковой флотации / Pulp Temperature influence on zinc flotation performance (in Russian): Zapiski Gornogo Instituta / Journal of Mining Institute, v. 159, no. 1, p. 140-141.
- Asimi Neisiani, A., and Chehreh Chelgani, S., 2023, Biodegradable acids for pyrite depression and green flotation separation – an overview: Critical Reviews in Biotechnology, v. 46, no. 6, p. 12.
- Asimi Neisiani, A., Saneie, R., Mohammadzadeh, A., Wonyen, D. G., and Chehreh Chelgani, S., 2023, Polysaccharides-based pyrite depressants for green flotation separation: An overview: International Journal of Mining Science and Technology, v. 33, no. 10, p. 1229-1241.
- Ata, S., Ahmed, N., and Jameson, G. J., 2003, A study of bubble coalescence in flotation froths: International Journal of Mineral Processing, v. 72, no. 1, p. 255-266.
- Australian Government, 1995, Sodium ethyl xanthate. Full public report: Australian Government Publishing Service, Canberra. <https://www.industrialchemicals.gov.au/sites/default/files/PEC5-Sodium-ethyl-xanthate.pdf.pdf>
- Australian Government: Australian Trade and Investment Commission, 2023, Opportunities in Korea for Australian critical minerals: Australian Trade and Investment Commission. <https://www.austrade.gov.au/content/dam/austrade-assets/global/wip/austrade/documents/Opportunities-in-Korea-for-Australian-critical-minerals.pdf>
- Avdohin, V., Физико-химические основы оптимизации флотации сульфидов / Physicochemical foundations of sulfide flotation optimization (in Russian), in Proceedings Symposium Modern Mining: Education, Science, Industry, Moscow, 1996, Sholokhov Moscow State University, p. 3-8.
- Bai, S., Yu, P., Li, C., Wen, S., and Ding, Z., 2019, Depression of pyrite in a low-alkaline medium with added calcium hypochlorite: Experiment, visual MINTEQ models, XPS, and ToF–SIMS studies: Minerals Engineering, v. 141, p. 105853.
- Bai, X., Yan, G., Kong, S., Yang, T., Yao, J., Wen, P., and Li, G., 2023, Study on the mechanism of the influence of surfactant alkyl chain length on the wettability of anthracite dust based on EDLVO theory and inverse gas chromatography: Fuel, v. 353, 129187.
- Bailey, D., 2015, Relative stability of precipitates and complex ions of  $\text{Cu}^{2+}$ , Chemistry 1B. General Chemistry Laboratory Manual: Sacramento, California State University, p. 57-61.

- Bailey, R., and Whelan, P. F., 1953, The influence of pulp temperature on the froth flotation of four British fine coals: *Journal of the Institute of Fuel*, v. 25, p. 304-307.
- Balarini, J. C., Polli, L. d. O., Miranda, T. L. S., Castro, R. M. Z. d., and Salum, A., 2008, Importance of roasted sulphide concentrates characterization in the hydrometallurgical extraction of zinc: *Minerals Engineering*, v. 21, no. 1, p. 100-110.
- Baranovskii, N., 1968, Flotation beneficiation of Semibratsk magnesite: *Refractories*, v. 8, no. 12, p. 740-741.
- Baranovskii, N., 1980, Flotation beneficiation of Savinsk magnesites: *Refractories*, v. 21, no. 7, p. 349-352.
- Barbian, N., Hadler, K., Ventura-Medina, E., and Cilliers, J. J., 2005, The froth stability column: linking froth stability and flotation performance: *Minerals Engineering*, v. 18, no. 3, p. 317-324.
- Barbian, N., Ventura-Medina, E., and Cilliers, J. J., 2003, Dynamic froth stability in froth flotation: *Minerals Engineering*, v. 16, no. 11, p. 1111-1116.
- Barton, M., 1988, Quartz Hill molybdenum project mine development: final environmental impact statement, U.S. Dept. of Agriculture, Forest Service, Tongass National Forest, Ketchikan, AK, USA, p. 23.
- Barton, P. B., and Bethke, P. M., 1987, Chalcopyrite disease in sphalerite; pathology and epidemiology: *American Mineralogist*, v. 72, no. 5-6, p. 451-467.
- Batchelor, G. K., and Green, J. T., 1972, The determination of the bulk stress in a suspension of spherical particles to order  $c^2$ : *Journal of Fluid Mechanics*, v. 56, no. 3, p. 401-427.
- Batelaan, J. G., Van Ginkel, C. G., and Balk, F., 1992, Carboxymethylcellulose (CMC): *Handbook of Environmental Chemistry*, v. 3, p. 329-336.
- BCS Inc., 2002, Energy and environmental profile of the U.S. Mining Industry, Washington, DC. p. 26. <https://www.energy.gov/sites/prod/files/2013/11/f4/overview.pdf>.
- Belattar, M. B., Hadfi, A., Ben-Aazza, S., Karmal, I., Mohareb, S., El Housse, M., Hafid, N., and Driouiche, A., 2021, Efficiency of one scale inhibitor on calcium carbonate precipitation from hot water sanitary: effect of temperature and concentration: *Heliyon*, v. 7, no. 2, p. e06152.
- Bellam, R., and Jaganyi, D., 2017, Substitution kinetics of  $[\text{Fe}(\text{PDT}/\text{PPDT})\text{n}(\text{phen})\text{m}]^{2+}$  ( $\text{n} \neq \text{m}$ ;  $\text{n}, \text{m} = 1, 2$ ) with 2,2'-Bipyridine, 1,10-Phenanthroline,

- and 2,2',6,2"-Terpyridine: International Journal of Chemical Kinetics, v. 49, no. 3, p. 182-196.
- Bhattacharya, S., and Pascoe, R. D., 2005, Effect of temperature on coal flotation performance - A review: Mineral Processing and Extractive Metallurgy Review, v. 26, no. 1, p. 31-61.
- Bhatti, M. A., Kazmi, K. R., Ahad, A., Tabassum, A., Mehmood, R., and Akram, A., 2016, Beneficiation studies on low-grade complex polymetallic lead-zinc ore of Duddar (Lasbela) Balochistan, Pakistan: Pakistan Journal of Scientific and Industrial Research Series A: Physical Sciences, v. 59, p. 130.
- Bhondayi, C., 2014, A study of flotation froth phase behaviour, Master Thesis: University of Witwatersrand, Faculty of Engineering and the Built Environment, p. 287
- Bicak, O., Cakir, E., Ozcelik, S., and Ekmekci, Z., 2023, The impact of pulp temperature on the flotation performance of copper-lead-zinc sulphide ore: Minerals, v. 13, no. 9, p. 1181.
- Bicak, O., Ekmekci, Z., Bradshaw, D. J., and Harris, P. J., 2007, Adsorption of guar gum and CMC on pyrite: Minerals Engineering, v. 20, no. 10, p. 996-1002.
- Bıçak, Ö., Ekmekçi, Z., Can, M., and Öztürk, Y., 2012, The effect of water chemistry on froth stability and surface chemistry of the flotation of a Cu–Zn sulfide ore: International Journal of Mineral Processing, v. 102-103, p. 32-37.
- Bicak, O., Ozturk, Y., Ozdemir, E., and Ekmekci, Z., Effects of pulp temperature on flotation of a complex sulphide ore, *in* Proceedings Proceedings of the 16th International Mineral Processing Symposium, Antalya, Türkiye, 2018, p. 23-25.
- Binks, S., 2023, It's not critical: but it is essential: London, UK, International Lead Association. <https://ila-lead.org/its-not-critical-but-it-is-essential/>
- Bocharov, V., Интенсивные методы рудо- и пульпоподготовки при комплексной переработке сульфидных руд цветных металлов / Intensive methods of ore and pulp conditioning during complex processing of base metal sulphidic ores (in Russian), *in* Proceedings Симпозиум Современное горное дело: образование, наука, промышленность / Symposium: Modern Mining Education, Science, Industry, Moscow, Russia, 1996, p. 40-45.
- Bodnar, R., Vityk, M., Hryn, J., and Mavrogenes, J., Phase Equilibria in the system H<sub>2</sub>O-NaCl-KCl-MgCl<sub>2</sub> relevant to salt cake processing, *in* Proceedings The 126th Annual Meeting of the Minerals, Metals, and Materials Society, Orlando, USA, 1997, p. 1-7.

- Boeke, C. L., and Gunther, G. G., 1952, Deleading zinc concentrate at the Parral and Santa Barbara mines, *in* Transactions of the AIME, May, p. 495-498.
- Boulton, A., Fornasiero, D., and Ralston, J., 2001, Depression of iron sulphide flotation in zinc roughers: Minerals Engineering, v. 14, no. 9, p. 1067-1079.
- Boyd, R., Bjerkgård, T., Nordahl, B., and Schiellerup, H., 2016, Mineral resources in the Arctic, Geological Survey of Norway, [https://www.ngu.no/upload/Aktuelt/CircumArctic/Mineral\\_Resource\\_Arctic\\_Shortver\\_Eng.pdf](https://www.ngu.no/upload/Aktuelt/CircumArctic/Mineral_Resource_Arctic_Shortver_Eng.pdf)
- Bradshaw, C. T., Harris, and O'connor, P. J., 1998, Synergistic interactions between reagents in sulphide flotation: Journal of The South African Institute of Mining and Metallurgy, v. 98, p. 187-192.
- Brito-Parada, P. R., Neethling, S. J., and Cilliers, J. J., 2012, CFD study of liquid drainage in flotation foams, 22nd European Symposium on Computer Aided Process Engineering: London, p. 1143-1147.
- Buckley, A. N., and Woods, R., 1991, Adsorption of ethyl xanthate on freshly exposed galena surfaces: Colloids and Surfaces, v. 53, no. 1, p. 33-45.
- Buckley, A. N., Woods, R., and Wouterlood, H. J., 1989, An XPS investigation of the surface of natural sphalerites under flotation-related conditions: International Journal of Mineral Processing, v. 26, no. 1, p. 29-49.
- Bulatovic, S. M., 2007, Chemistry, theory and practice: flotation of sulfide ores, Elsevier Science, Handbook of Flotation Reagents, p. 458
- Buxton, G. V., Greenstock, C. L., Helman, W. P., and Ross, A. B., 1988, Critical review of rate constants for reactions of hydrated electrons, hydrogen atoms and hydroxyl radicals ( $\cdot\text{OH}/\cdot\text{O}-$  in aqueous solution: Journal of Physical and Chemical Reference Data, v. 17, no. 2, p. 513-886.
- Cai, J., Liu, D., Shen, P., Zhang, X., Song, K., Jia, X., and Su, C., 2021, Effects of heating-sulfidation on the formation of zinc sulfide species on smithsonite surfaces and its response to flotation: Minerals Engineering, v. 169, no. 5, 106956.
- Calvo, G., Mudd, G., Valero, A., and Valero, A., 2016, Decreasing ore grades in global metallic mining: A theoretical issue or a global reality?: Resources, v. 5, no. 4, p. 1-14.



- Carlos Silva, A., Maria Schons Silva, E., Emérito, P., and Nascimento Sousa, D., 2017, Temperature influence in cornstarch gelatinization for froth flotation: REM: International Engineering Journal, v. 70, no. 2, p. 231-235.
- Carmichael, R. S., 1989, Practical handbook of physical properties of rocks and minerals (1988) (1<sup>st</sup> ed.), Boca Raton, CRC Press, p. 756.
- Çengel, Y. A., and Cimbala, J. M., 2006, Fluid mechanics: fundamentals and applications, Boston, McGraw-Hill Higher Education, McGraw-Hill series in mechanical engineering (4<sup>th</sup> ed.), p. 1024
- Chadwick, J., 2017, Water, water everywhere, International Mining Magazine, v. 3: Berkhamsted, International Mining Team Publishing Ltd, p. 28-41. <http://www.senvc.com/wp-content/uploads/2017/03/International-Mining-Magazine-Article.pdf>
- Chang, G., Xing, Y., Zhang, F., Yang, Z., Liu, X., and Gui, X., 2020, Effect of nanobubbles on the flotation performance of oxidized coal: ACS Omega, v. 5, no. 32, p. 20283-20290.
- CHEMINFO, 2007, CHEMINFO: Chemical information sources : Tables relocated or removed from CRC Handbook of chemistry and physics, 71st through 87th editions, Gary Wiggins.
- Chen, C., Zhu, H., Sun, W., Hu, Y., Qin, W., and Liu, R., 2017, Synergetic effect of the mixed anionic/non-ionic collectors in low temperature flotation of scheelite: Minerals, v. 7, no. 6., p. 87.
- Chen, C., Zhu, H. l., Qin, W. q., Chai, L. y., and Jia, W. h., 2018, Improving collecting performance of sodium oleate using a polyoxyethylene ether in scheelite flotation: Journal of Central South University, v. 25, no. 12, p. 2971-2978.
- Chen, H., Ren, Z., Gao, H., Xie, Y., Xing, B., and Wang, Z., 2020, 石油磺酸钠低温浮选石英型萤石的试验研究 / Experimental study on low-temperature flotation of quartz-type fluorite with petroleum sodium sulfonate (in Chinese): Conservation and Utilization of Mineral Resources, v. 40, no. 3, p. 135-139.
- Cheng, F. Q., Xue, N., Cao, B., Cao, Q., and Jiao, Y., Experimental study on mixed amine collector for KCl flotation at low temperature, in Proceedings XXVI IMPC, New Dehli, India, 24 - 28 September 2012, p. 888-898.
- Chepurnyh, S. F., Stepanov, J. V., Kuznetsov, V. D., Karpenko, T. G., and Plastovets, I. H., 1980, Флотационная машина/Flotation machine [in Russian], Государственный комитет

- СССР по делам изобретений и открытий/USSR State Committee on Inventions and Discoveries, Patent No. 751436: USSR, p. 3.
- Chicco, D., Warrens, M. J., and Jurman, G., 2021a, The coefficient of determination R-squared is more informative than SMAPE, MAE, MAPE, MSE and RMSE in regression analysis evaluation: *PeerJ Comput Sci*, v. 7, p. 623.
- Chicco, D., Warrens, M. J., and Jurman, G., 2021b, The coefficient of determination R-squared is more informative than SMAPE, MAE, MAPE, MSE and RMSE in regression analysis evaluation: *PeerJ Computer Science*, v. 7, e623.
- Cho, Y.-s., 2001, Effect of flotation frothers on bubble size and foam stability, Master's Thesis: The University of British Columbia, Department of Mining and Mineral Processing Engineering, p. 83
- Choung, J., Walker, J., Xu, Z., and Masliyah, J., 2008, Effect of temperature on the stability of froth formed in the recycle process water of oil sands extraction: *The Canadian Journal of Chemical Engineering*, v. 82, no. 4, p. 801-806.
- Chowdhury, S., Mishra, R., Saha, P., and Kushwaha, P., 2011, Adsorption thermodynamics, kinetics and isosteric heat of adsorption of malachite green onto chemically modified rice husk: *Desalination*, v. 265, no. 1, p. 159-168.
- Chowdhury, S., and Saha, P., 2011, Insight into adsorption thermodynamics, *in* Tadashi, M., ed., *Thermodynamics*: Rijeka, InTechOpen, p. 450.
- Christie, T., and Brathwaite, B., 1995, Mineral commodity report 6 — lead and zinc: Institute of Geological and Nuclear Sciences Ltd., Lower Hutt, p. 9.
- Chu, K. H., 2021, Revisiting the Temkin isotherm: dimensional inconsistency and approximate forms: *Industrial & Engineering Chemistry Research*, v. 60, no. 35, p. 13140-13147.
- Cicccone, S., and Hope, G. H., The Red Dog VIP mill optimization project, *in* Proceedings 35th Annual Meeting of the Canadian Mineral Processors, Ottawa, 2003, CIM, p. 1-12.
- Cook, M., and Last, A., 1950, Fluorite flotation II: *Bulletin of the University of Utah (Bulletin No. 47)*, v. 40, no. 14.
- Cooke, S., Iwasaki, I., and Choi, H. S., 1960, Effect of temperature on soap flotation of iron ore: *Trans. AIME*, v. 217, p. 76-83.

- Corin, K. C., Reddy, A., Miya, L., Wiese, J. G., and Harris, P. J., 2011, The effect of ionic strength of plant water on valuable mineral and gangue recovery in a platinum bearing ore from the Merensky reef: *Minerals Engineering*, v. 24, no. 2, p. 131-137.
- Corpas-Martínez, J. R., Pérez, A., Navarro-Domínguez, R., Amor-Castillo, C., Martín-Lara, M. A., and Calero, M., 2020, Testing of new collectors for concentration of fluorite by flotation in pneumatic (modified hallimond tube) and mechanical cells: *Minerals*, v. 10, no. 5, 482
- Côté, L., and Adante, J., Design, start-up and optimization of Pb & Zn flotation circuits utilizing ultra-fine grinding technology, *in* Proceedings 41st Annual Meeting of the Canadian Mineral Processors, Ottawa, 2009, CIM, p. 3-27.
- Cowburn, J., Stone, R., Bourke, S., and Hill, B., Design developments of the Jameson cell, *in* Proceedings Centenary of Flotation 2005 Symposium, Brisbane, Australia, 2005, p. 24.
- Crundwell, F. K., 2021, The impact of light on understanding the mechanism of dissolution and leaching of sphalerite (ZnS), pyrite (FeS<sub>2</sub>) and chalcopyrite (CuFeS<sub>2</sub>): *Minerals Engineering*, v. 161, 106728.
- Crundwell, F. K., and Godorr, S. A., 1997, A mathematical model of the leaching of gold in cyanide solutions: *Hydrometallurgy*, v. 44, no. 1, p. 147-162.
- Currie, R., 1937, The effect of temperature on the rate of dissolution of gold in cyanide solutions which have a constant oxygen content, *Bachelors Theses and Reports*, 1928 - 1970. Paper 75.
- Cytec Industries Inc., 2010, Mining Chemicals Handbook, Meriden, CT, USA, Mining Chemicals Handbook (2<sup>nd</sup> ed.), p. 506
- Damodaran, S., 2006, Protein stabilization of emulsions and foams: *Journal of Food Science*, v. 70, no. 3, p. R54-R66.
- Dancey, C. P., and Reidy, J., 2007, Statistics without maths for psychology (4<sup>th</sup> ed.), Pearson education, p. 619
- Das, A., and Sarkar, B., 2018, Advanced gravity concentration of fine particles: a review: *Mineral Processing and Extractive Metallurgy Review*, v. 39, no. 6, p. 359-394.
- Dassey, A., and Theegala, C., 2012, Optimizing the air dissolution parameters in an unpacked dissolved air flotation system: *Water*, v. 4, no. 1, p. 1-11.
- Daultrey, S., 1976, Principal components analysis, Norwich, Geo Abstracts Ltd., University of East Anglia, p. 51

- Davidson, A., Ryman, J., Sutherland, C. A., Milner, E. F., Kerby, R. C., Teindl, H., Melin, A., and Bolt, H. M., 2014, Lead, Ullmann's Encyclopedia of Industrial Chemistry, p. 1-55.
- Dávila-Pulido, G. I., and Uribe-Salas, A., 2014, Effect of calcium, sulphate and gypsum on copper-activated and non-activated sphalerite surface properties: *Minerals Engineering*, v. 55, p. 147-153.
- Dawson, K. M., 1995, Skarn deposits, *in* Eckstrand, O. R., Sinclair, W. D., and Thorpe, R. I., eds., *Geology of Canadian Mineral Deposit Types*, Volume 8, Geological Society of America, p. 447-501.
- De Castro, F. H. B., and Borrego, A. G., 1996, The influence of temperature during flotation of celestite and calcite with sodium oleate and quebracho: *International Journal of Mineral Processing*, v. 46, no. 1-2, p. 35-52.
- De Oliveira Balduino, R., Martins, M., Rodrigues, M. V. T., and De Salles Leal Filho, L., Influence of temperature, water quality and collector type on flotation performance of a peruvian phosphate ore, *in* Proceedings XXVI IMPC, New Dehli, India, 24 - 28 September 2012, p. 327-335.
- de Siqueira Santos, S., Takahashi, D. Y., Nakata, A., and Fujita, A., 2013, A comparative study of statistical methods used to identify dependencies between gene expression signals: *Briefings in Bioinformatics*, v. 15, no. 6, p. 906-918.
- Delahaije, R. J. B. M., Lech, F. J., and Wierenga, P. A., 2019, Investigating the effect of temperature on the formation and stabilization of ovalbumin foams: *Food Hydrocolloids*, v. 91, p. 263-274.
- Delevingne, L., Glazener, W., Grégoir, L., and Henderson, K., 2020, Climate risk and decarbonization: What every mining CEO needs to know, Volume 2022, McKinsey.
- Deng, J., Zhu, Y., Hu, F., and Cheng, Q., 1993, 油酸低温下浮选萤石的研究 / Study on fluorite flotation with oleic acid at low temperature (in Chinese): *化工矿山技术 / Chemical Mining Technology*, v. 22, no. 5, p. 24-26.
- Deng, M., Liu, Q., and Xu, Z., 2013, Impact of gypsum supersaturated water on the uptake of copper and xanthate on sphalerite: *Minerals Engineering*, v. 49, p. 165-171.
- Department of Mineral Resources and Energy of the Republic of South Africa, 2022, The exploration strategy for the mining industry of South Africa: South African Government,

- Department of Mineral Resources and Energy, Pretoria.  
[https://www.gov.za/sites/default/files/gcis\\_document/202204/46246gon2026.pdf](https://www.gov.za/sites/default/files/gcis_document/202204/46246gon2026.pdf)
- Desmet, C., Valsesia, A., Oddo, A., Ceccone, G., Spampinato, V., Rossi, F., and Colpo, P., 2017, Characterisation of nanomaterial hydrophobicity using engineered surfaces: *Journal of Nanoparticle Research*, v. 19, no. 3, p. 117.
- Dichmann, T. K., 2000, The role of copper ions in sphalerite and pyrite flotation selectivity, Master's Thesis: McGill University, Department of Mining and Metallurgical Engineering, 70 p.
- Dinçer, İ., and Zamfirescu, C., 2015, Appendix B: Thermophysical properties of water, *Drying phenomena: theory and applications*, John Wiley & Sons, Ltd., p. 457-459.
- Ding, X. Z., 2016, The effect of cell geometrical design and hydrodynamic conditions on the gas dispersion of Jameson cell, Master's Thesis: McGill University Libraries, Mining and Materials Engineering, 80 p.
- Downing, J. A., 1984, The effects of temperature and pH in flotation deinking of ultraviolet-cured inks: *Paper Engineering Senior Theses*, v. 124.
- Drogaris, G., and Weiland, P., 1983a, Coalescence behaviour of gas bubbles in aqueous solutions of n-alcohols and fatty acids: *Chemical Engineering Science*, v. 38, no. 9, p. 1501-1506.
- Drogaris, G., and Weiland, P., 1983b, Studies of coalescence of bubble pairs: *Chemical Engineering Communications*, v. 23, no. 1-3, p. 11-26.
- Drzymala, J., 2018, Arrheniusan activation energy of separation for different parameters regulating the process: *Physicochemical Problems of Mineral Processing*, v. 54, no. 4, p. 1152-1158.
- Drzymala, J., Kliszowska, K., and Ratajczak, T., 2021, Theoretical and experimental aspects of influence of temperature on kinetics of carbonaceous materials froth flotation: *Mineral Processing and Extractive Metallurgy Review*, v. 43, no. 4, p. 422-426.
- Du, B., Zhang, Z., Grubner, S., Yurkovich, J. T., Palsson, B. O., and Zielinski, D. C., 2018, Temperature-dependent estimation of Gibbs energies using an updated group-contribution method: *Biophysical Journal*, v. 114, no. 11, p. 2691-2702.
- du Rietz, C., 1957, Xanthate analysis by means of potentiometric titration: *Svensk kemisk tidskrift*, v. 69, p. 310-327.

- du Rietz, C., Chemisorption of collectors in flotation, *in* Proceedings 11th International Mineral Processing Congress, Cagliari, 1976, Institute di Arte Mineraria, Università di Cagliari, p. 375-403.
- Dudnikov, S. V., Shubov, L. Y., Glazunov, L. A., Scherbakov, V. A., Mitrofanov, S. I., Sokolova, G. E., Kuz'kin, A. S., Gurvich, S. M., Gabrielova, L. I., Slavina, V. N., Sergeeva, R. G., Tsvetkov, I. T., Kuchnikova, V. G., and Moiseeva, R. I., 1969, Основы теории и практика применения флотационных реагентов / Theoretical fundamentals and application practice of flotation reagents, Moscow, Nedra, p. 390
- Dunne, R. C., Kawatra, K. S., and Young, C. A., 2019, SME mineral processing and extractive metallurgy handbook, Englewood, Society for Mining, Metallurgy, and Exploration, Mining Engineering, p. 2197-2197
- Einaudi, M. T., and Burt, D. M., 1982, Introduction; terminology, classification, and composition of skarn deposits: Economic Geology and the Bulletin of the Society of Economic Geologists, v. 77, no. 4, p. 745-754.
- Ejtemaei, M., 2016, Bubble attachment and amyl xanthate adsorption to copper-activated sphalerite PhD Thesis: The University of Queensland, School of Chemical Engineering, 143 p.
- Ejtemaei, M., Irannajad, M., and Gharabaghi, M., 2011, Influence of important factors on flotation of zinc oxide mineral using cationic, anionic and mixed (cationic/anionic) collectors: Minerals Engineering, v. 24, no. 13, p. 1402-1408.
- Ellis, R., King, P., Richardson, S., and Allen, A., 2022, NI 43-101 Technical report on the Neves-Corvo mine, Portugal: Wardell Armstrong International Limited, Cornwall, p. 226.
- Ellis, S., and Senanayake, G., 2004, The effects of dissolved oxygen and cyanide dosage on gold extraction from a pyrrhotite-rich ore: Hydrometallurgy, v. 73, no. 1-2, p. 39-50.
- Erkan, E., Ekmekçi, Z., and Altun, E., 2022, Comparison of flash flotation and gravity separation performance in a greenfield gold project: Physicochemical Problems of Mineral Processing, v. 58, no. 3, 146979.
- Ershov, D., Phan, M.-S., Pylvänäinen, J. W., Rigaud, S. U., Le Blanc, L., Charles-Orszag, A., Conway, J. R. W., Laine, R. F., Roy, N. H., Bonazzi, D., Duménil, G., Jacquemet, G., and Tinevez, J.-Y., 2022, TrackMate 7: integrating state-of-the-art segmentation algorithms into tracking pipelines: Nature Methods, v. 19, no. 7, p. 829-832.

- Espinosa-Gomez, R., Finch, J. A., and Laplante, A. R., 1987, Effects of the type of water on the selective flotation of pyrochlore from Niobec: *Colloids and Surfaces*, v. 26, p. 333-350.
- Essilfie, E., 2014, Modification of amine collectors for low temperature flotation of potash, Master's Thesis: University of Saskatchewan, Department of mechanical engineering, p. 78.
- Ettish, M. N., El-Sayyad, G. S., Elsayed, M. A., and Abuzalat, O., 2021, Preparation and characterization of new adsorbent from cinnamon waste by physical activation for removal of Chlorpyrifos: *Environmental Challenges*, v. 5, 100208.
- European Commission, 2020, Study on the EU's list of critical raw materials - final report: European Commission, Brussels.  
[https://rmis.jrc.ec.europa.eu/uploads/CRM\\_2020\\_Report\\_Final.pdf](https://rmis.jrc.ec.europa.eu/uploads/CRM_2020_Report_Final.pdf)
- Fa, K. Q., Miller, J., Jiang, T., and Li, G. H., 2005, Sulphidization flotation for recovery of lead and zinc from oxide-sulfide ores: *Transactions of Nonferrous Metals Society of China (English Edition)*, v. 15, p. 1138-1144.
- Faraway, J. J., 2002, *Practical regression and ANOVA using R*, The University of Michigan, p. 212.
- Farrokhpay, S., Bradshaw, D., and Dunne, R., Rheological investigation of the flotation performance of a high clay containing gold ore from Carlin trend, *in Proceedings Proceedings of the World Gold Conference*, Brisbane, Australia, 2013.
- Farrokhpay, S., and Zanin, M., 2011, Effect of water quality on froth stability in flotation, *Chemeca 2011 (39th: 2011: Sydney, NSW)*, Engineers Australia Barton, ACT, p. 31-38.
- Faust, S. D., and Aly, O. M., 1998, *Chemistry of water treatment (2nd Edition)*, Boca Raton, Taylor & Francis, p. 600.
- Feng, B., Zhong, C.-h., Zhang, L.-z., Peng, J.-x., Guo, Y.-t., Wang, T., Ning, X.-h., and Wang, H.-h., 2021, Effect and mechanism of potassium-permanganate strengthening and sodium-alginate depression of sphalerite flotation: *Chinese Journal of Engineering*, v. 43, no. 5, p. 612-618.
- Fernandes, I., 2016, *Influência da temperatura na flutuação por espumas de sulfuretos/ Influence of temperature on the fluctuation of sulfide froth [in Portuguese]*, Master's Thesis: Technical University of Lisbon, Department of Civil Engineering and Georesources, p. 102

- Feteris, S. M., Frew, J. A., and Jowett, A., 1987, Modelling the effect of froth depth in flotation: International Journal of Mineral Processing, v. 20, no. 1, p. 121-135.
- Flowers, P., Theopold, K., Langley, R., and Robinson, W. R., 2019, Chemistry 2e: Houston, Texas, OpenStax.
- Fox, H. W., and Zisman, W. A., 1950, The spreading of liquids on low energy surfaces. I. Polytetrafluoroethylene: Journal of Colloid Science, v. 5, no. 6.
- Franklin, J., Gibson, H., Jonasson, I., and Galley, A., 2005, Volcanogenic massive sulfide deposits: Economic Geology 100th Anniversary Volume, p. 523-560.
- Fuerstenau, D. W., 1962, Froth flotation 50th anniversary volume, New York, American Institute of Mining, Metallurgical, and Petroleum Engineers, Rocky Mountain Fund series, p. 677.
- Fuerstenau, M., Jameson, G., and Yoon, R., 2007, Froth flotation: a century of innovation, Littleton, Society for Mining, Metallurgy, and Exploration, p. 891.
- Fuerstenau, M. C., 1982, Sulphide mineral flotation, *in* King, R. P., ed., Principles of flotation: Johannesburg, South African Institute of Mining and Metallurgy, p. 159-182.
- Fuerstenau, M. C., Natalie, C. A., and Rowe, R. M., 1990, Xanthate adsorption on selected sulfides in the virtual absence and presence of oxygen, Part 1: International Journal of Mineral Processing, v. 29, no. 1, p. 89-98.
- Galley, A., and Koski, R., 1999, Setting and characteristics of ophiolite-hosted volcanogenic massive sulfide deposits: Reviews in Economic Geology, v. 8, p. 221-246.
- Gao, M., Metallurgist, Young, M. F., Superintendent, M., and Allum, P., IsaMill fine grinding technology and its industrial applications at Mount Isa mines, *in* Proceedings 34th Canadian Mineral Processors Meeting, Ottawa, 2002, CIM.
- Garrels, R. M., and Christ, C. L., 1990, Solutions, minerals, and equilibria, Boston, MA, USA, Jones And Bartlett Publishers, Inc., v. 1, p. 450.
- Garza, A. J., 2019, Solvation entropy made simple: Journal of Chemical Theory and Computation, v. 15, no. 5, p. 3204-3214.
- Gayle, J., and Eddy, W., 1961, Laboratory investigation of the effect of temperature on coal flotation (bureau of mines report of investigations), Washington, p. 1-11.
- Gayle, J., Eddy, W., and Shotts, R., 1965, Laboratory investigation of the effect of oxidation on coal flotation (bureau of mines report of investigations), Washington, p. 1-22.



- Gayle, J., and Smelley, A., 1960, Effects of temperature variations on contact angles for coal and related substances, U.S. Bureau of Mines, Washington, p. 7-8.
- Gerson, A. R., Lange, A. G., Prince, K. E., and Smart, R. S. C., 1999, The mechanism of copper activation of sphalerite: *Applied Surface Science*, v. 137, no. 1, p. 207-223.
- Gevantman, L. H., 2010, Solubility of selected gasses in water, *in* Haynes, W. M., ed., *CRC Handbook of Chemistry and Physics*, Taylor and Francis Group.
- Ghazi, A. M., and Millette, J. R., 1964, 4 - Lead, *in* Morrison, R. D., and Murphy, B. L., eds., *Environmental Forensics*: Burlington, Academic Press, p. 55-79.
- Gilg, H. A., Boni, M., and Cook, N. J., 2008, A special issue devoted to nonsulfide Zn–Pb deposits: *Ore Geology Reviews*, v. 33, no. 2, p. 115-116.
- Glembotskij, V. A., and Klassen, V. I., 1981, Флотационные методы обогащения/Flotation methods of mineral processing [in Russian], Moscow, Nedra, p. 304.
- Glembotsky, V., Dmitrieva, G., and Sorokin, M., 1968, Аполярные реагенты и их действие при флотации / Non-polar reagents and their application in flotation (in Russian), Moscow, Nayka, p. 1-144.
- Glembotsky, V., and Klassen, V., 1981, Флотационные методы обогащения / Flotation methods of mineral processing (in Russian), Moscow, Izd. Nedra, p. 28-28.
- Göktepe, F., 2005, Treatment of lead mine waste by a Mozley multi-gravity separator (MGS): *Journal of Environmental Management*, v. 76, no. 4, p. 277-281.
- Gorain, B. K., Developing solutions to complex flotation problems, *in* Proceedings 45th Annual Canadian Mineral Processors Operators Conference, Ottawa, January 22-24 2013, CIM.
- Gorain, B. K., Napier-Munn, T. J., Franzidis, J. P., and Manlapig, E. V., 1998, Studies on impeller type, impeller speed and air flow rate in an industrial scale flotation cell. Part 5: validation of k-Sb relationship and effect of froth depth: *Minerals Engineering*, v. 11, no. 7, p. 615-626.
- Gouvernement du Quebec, 2011, Plan Nord. Building Northern Quebec together. The project of a generation, Québec, Ministère des ressources naturelles et de la faune, p. 172.
- Grano, S. R., Treatment of naturally hydrophobic gangue minerals at the copper concentrator of Mt. Isa Mines Limited, 1991, *in* Proc. of the Fourth Mill Operators Conference, North West Tasmania and Westcoast Tasmania Branches, (Aust. Inst. Min. Metall. Publ.), p. 121-128

- Grano, S. R., Lauder, D. W., Johnson, N. W., and Ralston, J., 1997a, An investigation of galena recovery problems in the Hilton concentrator of Mount Isa mines limited, Australia: *Minerals Engineering*, v. 10, no. 10, p. 1139-1163.
- Grano, S. R., Prestidge, C. A., and Ralston, J., 1997b, Solution interaction of ethyl xanthate and sulphite and its effect on galena flotation and xanthate adsorption: *International Journal of Mineral Processing*, v. 52, no. 2, p. 161-186.
- Grau, R. A., Laskowski, J. S., and Heiskanen, K., 2005, Effect of frothers on bubble size: *International Journal of Mineral Processing*, v. 76, no. 4, p. 225-233.
- Gray, P., Bowyer, G., Castle, J., Vaughan, D., and Warner, N., 1990, *Sulphide deposits - their origin and processing* (1<sup>st</sup> ed.), London, The Institution of Mining and Metallurgy, p. 310.
- Gredelj, S., Zanin, M., and Grano, S. R., 2009, Selective flotation of carbon in the Pb–Zn carbonaceous sulphide ores of Century mine, Zinifex: *Minerals Engineering*, v. 22, no. 3, p. 279-288.
- Greet, C. J., 2023, *Regrinding: its impact on pulp chemistry and flotation behaviour*, MEI: Comminution 23: Cape Town, MEI.
- Guerrero-Hernández, L., Meléndez-Ortiz, H. I., Cortez-Mazatan, G. Y., Vaillant-Sánchez, S., and Peralta-Rodríguez, R. D., 2022, Gemini and Bicephalous Surfactants: A Review on Their Synthesis, Micelle Formation, and Uses: *Int J Mol Sci*, v. 23, no. 3.
- Guilbert, J. M., and Park, C. F., Jr., 1986, *The geology of ore deposits*, New York, W.H. Freeman, p. 985.
- Gunther, C. G., 1909, *Electro-magnetic ore separation*, Hill publishing Company, p. 193.
- Guo, B., Peng, Y., and Espinosa-Gomez, R., 2014, Cyanide chemistry and its effect on mineral flotation: *Minerals Engineering*, v. 66, p. 25-32.
- Guo, W., Han, Y., Zhu, Y., Li, Y., and Tang, Z., 2020, Effect of amide group on the flotation performance of lauric acid: *Applied Surface Science*, v. 505, no. November 2019, 144627.
- Gupta, A., and Yan, D., 2016, Chapter 16 - Gravity Separation, *in* Gupta, A., and Yan, D., eds., *Mineral processing design and operations* (Second edition): Amsterdam, Elsevier, p. 563-628.
- Gupta, A. K., Banerjee, P. K., Mishra, A., Satish, P., and Pradip, 2007, Effect of alcohol and polyglycol ether frothers on foam stability, bubble size and coal flotation: *International Journal of Mineral Processing*, v. 82, no. 3, p. 126-137.

- Gutierrez, L., Betancourt, F., Uribe, L., and Maldonado, M., 2020, Influence of seawater on the degree of entrainment in the flotation of a synthetic copper ore: *Minerals*, v. 10, no. 7, p. 615.
- Güven, O., Batjargal, K., Özdemir, O., Karakashev, S. I., Grozev, N. A., Boylu, F., and Çelik, M. S., 2020, Experimental procedure for the determination of the critical coalescence concentration (CCC) of simple frothers: *Minerals*, v. 10, no. 7, 617.
- Hacıfazlıoğlu, H., and Gerdan, G. H., 2016, Taşkömürü Tozları Flotasyonunda Sıcaklığın Etkisi / Effect of temperature on fine hard coal flotation (in Turkish): *Adıyaman Üniversitesi Mühendislik Bilimleri Dergisi*, v. 5, p. 1-8.
- Hadavand-Siri, M., and Deutsch, C. V., 2012, Some thoughts on understanding correlation matrices. CCG Annual Report 14, University of Alberta, Edmonton, paper 408.
- Hadler, K., and Cilliers, J. J., 2009, The relationship between the peak in air recovery and flotation bank performance: *Minerals Engineering*, v. 22, no. 5, p. 451-455.
- Hadler, K., Greyling, M., Plint, N., and Cilliers, J. J., 2012, The effect of froth depth on air recovery and flotation performance: *Minerals Engineering*, v. 36-38, p. 248-253.
- Hamel, D., McLaughlin, J., Plante, M., and Bedard, M.-P., Improved concentrate grade and recovery through the application of the 6 Sigma methodology at Noranda Matagami mill, *in Proceedings 33rd CMP*, Ottawa, 2001, CIM, p. 553-577.
- Hamilton, I. C., and Woods, R., 1986, Surfactant properties of alkyl xanthates: *International Journal of Mineral Processing*, v. 17, no. 1-2, p. 113-120.
- Han, C., Wei, D., Gao, S., Zai, Q., Shen, Y., and Liu, W., 2020, Adsorption and desorption of butyl xanthate on chalcopyrite: *Journal of Materials Research and Technology*, v. 9, no. 6, p. 12654-12660.
- Hanwell, M. D., Curtis, D. E., Lonie, D. C., Vandermeersch, T., Zurek, E., and Hutchison, G. R., 2012, Avogadro: an advanced semantic chemical editor, visualization, and analysis platform: *Journal of Cheminformatics*, v. 4, no. 17, p. 1-17.
- Harris, P. J., 1982, Frothing phenomena and frothers, *in King, R. P., ed., Principles of flotation: Johannesburg*, South African Institute of Mining and Metallurgy, p. 237-250.
- Harvey, P. A., Nguyen, A. V., Jameson, G. J., and Evans, G. M., 2005, Influence of sodium dodecyl sulphate and Dowfroth frothers on froth stability: *Minerals Engineering*, v. 18, no. 3, p. 311-315.

- Hassanzadeh, A., Safari, M., Khoshdast, H., Güner, M. K., Hoang, D. H., Sambrook, T., and Kowalczyk, P. B., 2022, Introducing key advantages of intensified flotation cells over conventionally used mechanical and column cells: *Physicochemical Problems of Mineral Processing*, v. 58, no. 5, p. 155101.
- Huang, H. H., and Miller, J. D., 1978, Kinetics and thermochemistry of amyl xanthate adsorption by pyrite and marcasite: *International Journal of Mineral Processing*, v. 5, no. 3, p. 241-266.
- He, H., He, T., Wang, X., and Yu, B., 2020, 矿浆温度对方铅矿浮选效果的影响及机理研究 / Study on the effect and mechanism of pulp temperature on galena flotation (in Chinese): *Conservation and Utilization of Mineral Resources/矿产保护与利用*, v. 40, no. 6, p. 88.
- He, S., Grano, S., Manouchehri, H., Fordham, M., and Curral, J., The detrimental impact of high pulp temperature on sphalerite flotation after zinc regrinding in the zinc plant of Somincor, Lundin Mining Corporation, Neves Corvo, Portugal, *in Proceedings Metallurgical Plant Design and Operating Strategies (MetPlant 2008)*, Perth, Australia, 18-19 August 2008, p. 306-324.
- Heiser, T., and Hofmeister, P., 2019, Bathtub, failure distribution, MTBF, MTTF, and more: they are related, MFPT: King of Prussia, Society for Machinery Failure Prevention Technology. <https://www.mfpt.org/wp-content/uploads/2019/10/Heiser-Thomas-Bathtub-Failure-Distribution-MTBF-Paper.pdf>
- Hellstrand, G. A., 1923, Differential flotation of ores, US Patent Office, US1469042A, p. 7.
- Hem, J. D., and Cropper, W. H., 1959, Survey of ferrous-ferric chemical equilibria and redox potentials: USGS, Washington, Paper 1459, p. 268.
- Henry, W., and Banks, J., 1803, III. Experiments on the quantity of gases absorbed by water, at different temperatures, and under different pressures: *Philosophical Transactions of the Royal Society of London*, no. 93, p. 29-274.
- Henwood, D., 1994, The effect of conditioning on froth flotation, Master's Thesis: University of Cape Town, Department of Chemical Engineering, p. 159.
- Hidmi, L., and Edwards, M., 1999, Role of temperature and pH in  $\text{Cu}(\text{OH})_2$  solubility: *Environmental Science and Technology*, v. 33, no. 15, p. 2607-2610.
- Hoff, J. H. v. t., 1887, Die Rolle des osmotischen Druckes in der Analogie zwischen Lösungen und Gasen / The role of osmotic pressure in the analogy between solutions and gases (in

- German): Zeitschrift für Physikalische Chemie / Journal of Physical Chemistry, no. 1, p. 481-508.
- Honaker, R. Q., 1992, A fundamental study of the selective hydrophobic coagulation process, PhD Thesis: Virginia Polytechnic Institute and State University Mining and Materials Engineering Department, p. 289.
- Honaker, R. Q., and Reed, S., 1995, A fine coal circuitry study using column flotation and gravity separation. Quarterly report, 1 December 1994-28 February 1995, Champaign, p. 24.
- Hu, X., Zhu, Y., Song, Z., and Chen, K., 2024, Beneficiation process reengineering under the background of green development - take the full utilization of a low-grade lead-zinc ore as an example: Journal of Physics: Conference Series, v. 2738, no. 1, 012006.
- Hughes, J., Cowper-Heays, K., Oleson, E., Bell, R., and Stroombergen, A., 2021, Impacts and implications of climate change on wastewater systems: a New Zealand perspective: Climate Risk Management, v. 31, 100262.
- Iglesias, E., Anderes, J., Forgiarini, A., and Salager, J.-L., 1995, A new method to estimate the stability of short-life foams: Colloids and Surfaces A: Physicochemical and Engineering Aspects, v. 98, no. 1, p. 167-174.
- Ignatkina, V. A., Bocharov, V. A., and D'jachkov, F. G., 2013, Исследование собирательных свойств диизобутилового дитиофосфината при флотации сульфидных минералов из колчеданных руд/Investigation of the collecting properties of diisobutyl dithiophosphate during the flotation of sulphide minerals from the pyritic ores [in Russian]: Физико-технические проблемы разработки полезных ископаемых, v. 5, p. 138-146.
- Ignatkina, V. A., Bocharov, V. A., Puntsukova, B. T., and Alekseichuk, D. A., 2014, Термодинамические и кинетические параметры адсорбции композиций и сульфгидрильных собирателей на сульфидных минералах /Thermodynamic and kinetic parameters of adsorption of sulfhydryl collector composition on sulfide minerals [in Russian]: Горный информационно-аналитический бюллетень (Mining informational and analytical bulletin), no. 2, p. 49-62.
- Ignatova, T., and Shelepov, E., 2011, Влияние температуры жидкой фазы пульпы на катионную доводку магнетитовых концентратов ОАО "Михайловский ГОК" / An influence of temperature of liquid phase of the pulp on cationic cleaner flotation of

- magnetite concentrates (in Russian): Mining informational and analytical bulletin, v. 4, p. 237-240.
- Ikumapayi, F., Makitalo, M., Johansson, B., and Rao, K. H., 2012, Recycling process water in sulfide flotation, Part A: Effect of calcium and sulfate on sphalerite recovery: Minerals and Metallurgical Processing, v. 29, no. 4, p. 183-191.
- Ikumapayi, F., and Rao, K., 2015, Recycling process water in complex sulfide ore flotation: Effect of calcium and sulfate on sulfide minerals recovery: Mineral Processing and Extractive Metallurgy Review, v. 36, no. 1, p. 45-64.
- Ikumapayi, F. K., 2010, Flotation chemistry of complex sulphide ores, Licentiate Thesis: Luleå University of Technology, Department of Chemical Engineering and Geosciences, p. 182.
- Indian Bureau of Mines, 2020, Indian minerals yearbook 2019. Part-II: Metals and alloys: Ministry of Mines, Indian Bureau of Mines, Nagpur, p. 27.
- International Zinc Association, 2017, Zinc: a sustainable material essential for modern life, International Zinc Association. <http://www.zinc.org/sustainability>
- International Zinc Association, 2019, Zinc essential for modern life, Volume 2024, International Zinc Association.  
<https://www.zinc.org/#:~:text=Zinc%2C%20an%20Essential%20Element%20with,consumer%20products%2C%20and%20food%20security>.
- Iorish, V. S., and Jungman, V. S., 2003, База данных: Термические константы веществ / Database: Thermal constants of substances [in Russian]: Moscow, Moscow State University. <https://www.chem.msu.ru/cgi-bin/tkv.pl>
- Isshiki, J., 1961, 余市選鉱場におけるパルプ温度の浮選成績におよぼす影響 / Pulp temperature produce effects on flotation at Yoichi mill (in Japanese): 日本鉱業会誌 / Journal of the Japan Mining Association, v. 77, no. 879, p. 724-728.
- Ivanova, V., and Mitrofanova, G., 2009, О роли смоляных кислот при флотации апатита талловыми маслами в условиях водооборота / About the role of resin acids during apatite flotation with tall oils and recycled water (in Russian): Вестник МГТУ, v. 12, no. 4, p. 583-587.
- Ivanova, V., Mitrofanova, G., and Perunkova, T., Флотация апатито-нефелиновой руды жирокислотным собирателем на оборотной воде в условиях холодной пульпы / Flotation of apatite-nefeline ore with fatty acid collector and recycled waters under the

- conditions of cold pulp (in Russian), *in* Proceedings Gornoje delo v Arktike, Apatity, 2005, Tipografia Ivan Fedorov, p. 294-299.
- Jackman, M., Bussonnière, A., Leung, H. L., Xu, Z., Tsai, P. A., and Liu, Q., 2018, Effect of temperature on foamability using a thermoresponsive polymer: AIP Advances, v. 86, 075320.
- Jeldres, R. I., Uribe, L., Cisternas, L. A., Gutierrez, L., Leiva, W. H., and Valenzuela, J., 2019, The effect of clay minerals on the process of flotation of copper ores - a critical review: Applied Clay Science, v. 170, p. 57-69.
- Jensen, T., Blakley, I. T., Jacquemin, T., and Woods, S., 2018, Technical report on the Caribou mine, Bathurst, New Brunswick, Canada, Toronto, p. 238.  
[https://minedocs.com/11/TrevaliMining\\_Caribou\\_TR\\_2018.pdf](https://minedocs.com/11/TrevaliMining_Caribou_TR_2018.pdf)
- Jeong, S., and Kim, K., 2018, Pre-concentration of iron-rich sphalerite by magnetic separation, Minerals, v. 8, no. 7, 272.
- Jera, T. M., and Bhondayi, C., 2021, A review of flotation physical froth flow modifiers: Minerals, v. 11, no. 8, p. 864.
- Jia, W., Xian, C., and Wu, J., 2022, Temperature-sensitive foaming agent developed for smart foam drainage technology: RSC Advances, v. 12, no. 36, p. 23447-23453.
- Jiang, J., Zu, Y., Li, X., Meng, Q., and Long, X., 2020, Recent progress towards industrial rhamnolipids fermentation: Process optimization and foam control: Bioresource Technology, v. 298, p. 122394.
- Jiao, Y., Zhang, S., and Tan, Y., 2022, Thermodynamic analysis and crystallographic properties of  $\text{MFe(2)O(4)}$ ,  $\text{MCr(2)O(4)}$  and  $\text{MAl(2)O(4)}$  ( $\text{M} = \text{Fe, Ni, Zn}$ ) formed on structural materials in pressurized water reactor primary circuit under zinc and zinc-aluminum water chemistry: Entropy (Basel), v. 24, no. 2, 245.
- Jingwei, W., Qisen, Z., Chenyao, G., Qiangkun, L., Yawei, H., Xinman, J., Yanchao, Z., Jing, W., and Qiang, Z., 2022, Effects of aeration on pollution load and greenhouse gas emissions from agricultural drainage ditches, Water, v. 14, no. 22, 3783.
- Johnson, C. A., Piatak, N. M., and Miller, M. M., 2017, Barite (Barium), 1802D, Reston, VA, USA, p. 30.

- Jones, F. E., and Harris, G. L., 1992, ITS-90 Density of water formulation for volumetric standards calibration: The Journal of Research of the National Institute of Standards and Technology, v. 97, no. 3, p. 335-340.
- Jong, K., Paek, I., Kim, Y., Li, I., and Jang, D., 2020, Flotation mechanism of a novel synthesized collector from Evodiaefructus onto fluorite surfaces: Minerals Engineering, v. 146, 106017.
- Julian, H. F., Smart, E., and Allen, A., 1921, Cyaniding gold and silver ores: A practical treatise; embracing technical and commercial investigations, the chemistry and physics of theory and practice, the design and construction of equipment and the operation of the process. 3d ed., revised throughout, re-set, and greatly enlarged, by A. W. Allen, C. Griffin and company Ltd., London, p. 417.
- Kakovskii, I. A., 1956, Изучение физико-химических свойств некоторых органических флотационных реагентов и их солей с ионами тяжелых цветных металлов / Investigations of physical-chemical properties of some organic flotation reagents and their complexes with heavy metal ions [in Russian], Труды Института Горного Дела Академии Наук СССР, v. 3: Moscow, Publishing House of the USSR Academy of Sciences, p. 255-289.
- Kakovsky, L. A., and Arashkevich, V. M., 1968, The study of the properties of organic disulfides, 8th IMPC: Leningrad, USSR, p. 10.
- Kang, J., Chen, C., Sun, W., Tang, H., Yin, Z., Liu, R., Hu, Y., and Nguyen, A. V., 2017, A significant improvement of scheelite recovery using recycled flotation wastewater treated by hydrometallurgical waste acid: Journal of Cleaner Production, v. 151, p. 419-426.
- Kang, J., Hu, Y., Sun, W., Liu, R., Gao, Z., Guan, Q., Tang, H., and Yin, Z., 2018, Utilisation of FGD gypsum for silicate removal from scheelite flotation wastewater: Chemical Engineering Journal, v. 341, p. 272-279.
- Kania, H., and Saturnus, M., 2023, Evaluation and current state of primary and secondary zinc production - a review: Applied Sciences, v. 13, no. 3, 2003.
- Kartio, I. J., Basilio, C. I., and Yoon, R. H., 1998, An XPS Study of sphalerite activation by copper: Langmuir, v. 14, no. 18, p. 5274-5278.
- Kawatra, S., Eisele, T., Zhang, D., and Rusesky, M., 1988, Effects of temperature on hydrocyclone efficiency: International Journal of Mineral Processing, v. 23, p. 205-210.



- Kawatra, S. K., 2009, Froth flotation - fundamental principles, Mining Engineering Handbook: Houghton, Michigan Technological University, p. 30.
- Kaye, G. W. C., and Laby, T. H., 1962, Tables of physical and chemical constants, London, New York, Toronto, Longmans, v., p. 41-46.
- Keating, J., 2015, Lead, The Canadian Encyclopedia.  
<https://www.thecanadianencyclopedia.ca/en/article/lead>
- Kesler, S., and Simon, A., 1994, Mineral resources, economics and the environment, Cambridge University Press, p. 419.
- Khambhaty, Y., Mody, K., Basha, S., and Jha, B., 2009, Kinetics, equilibrium and thermodynamic studies on biosorption of hexavalent chromium by dead fungal biomass of marine *Aspergillus niger*: Chemical Engineering Journal, v. 145, no. 3, p. 489-495.
- Kienko, L., 2008, Разработка эффективной технологии обогащения карбонатно-флюоритовых руд Вознесенского рудного района /Development of an efficient processing technology for carbonate-fluorite ores of the Voznesensky ore field (in Russian), PhD Thesis, Russian Academy of Science: Far East Mining Institute, p. 182.
- Kienko, L., Samatova, L., Voronova, O., and Kondratyev, S., 2010, К проблеме снижения температуры флотации при обогащении карбонатно-флюоритовых руд / Addressing a problem of lowering a temperature of flotation during processing of carbonate-fluorite ores (in Russian): Fiziko-tehnicheskie problemy razrabotki poleznyh iskopаемых, v. 3, p. 97-104.
- Kilickaplan, I., 2009, Effect of pulp rheology on flotation: the nickel sulfide ore with asbestos gangue system, Master's Thesis: University of British Columbia, Mining Engineering, p. 83.
- Kinney, J. B., and Atwal, G. S., 2014, Equitability, mutual information, and the maximal information coefficient: Proceedings of the National Academy of Sciences of the United States of America, v. 111, no. 9, p. 3354-3359.
- Kistemaker, J. C. M., Lubbe, A. S., Bloemsma, E. A., and Feringa, B. L., 2016, On the role of viscosity in the Eyring equation: Chemphyschem, v. 17, no. 12, p. 1819-1822.
- Klassen, V., and Plaksin, I., 1954, О механизме действия некоторых реагентов и аэрации пульпы при флотации каменных углей / About mechanism of action of some reagents

- during aeration in hard coal flotation (in Russian): *Izv. Akademii Nauk SSSR. Otdelenie Tehnicheskikh nauk*, v. 3, p. 65.
- Klassen, V. I., and Mokrousov, V. A., 1959, Введение в теорию флотации / An introduction to the theory of flotation [in Russian], Moscow, Metallurgizdat, v. 2, p. 636.
- Klevens, H. B., 1953, Structure and aggregation in dilute solution of surface active agents: *Journal of the American Oil Chemists Society*, v. 30, no. 2, p. 74-80.
- Klochko, K., 2018, 2018 Minerals yearbook - lead, U.S.G.S., Washington, p. 17.  
<https://pubs.usgs.gov/myb/vol11/2018/myb1-2018-lead.pdf>
- Klymowsky, I. B., 1968, The role of oxygen in xanthate flotation of galena, pyrite, and chalcopyrite, Master's Thesis: McGill University Metallurgical Engineering, p. 152.
- Knockhardy, P., 2015, Reactions of some transition metal ions, p. 1-8.  
[https://www.knockhardy.org.uk/sci\\_htm\\_files/15tmet2.pdf](https://www.knockhardy.org.uk/sci_htm_files/15tmet2.pdf)
- Koehler, S. A., Hilgenfeldt, S., Weeks, E. R., and Stone, H. A., 2002, Drainage of single Plateau borders: direct observation of rigid and mobile interfaces: *Physical Review E*, v. 66, no. 4, p. 040601.
- Kohad, V. P., Flotation of sulphide ores - HZL experience, *in* Proceedings Workshop on Froth Flotation: Recent Trends, Bhubaneswar, 1998, Regional Research Laboratory, p. 18-41.
- Kökkılıç, O., Mohammadi-Jam, S., Chu, P., Marion, C., Yang, Y., and Waters, K. E., 2022, Separation of plastic wastes using froth flotation – an overview: *Advances in Colloid and Interface Science*, v. 308, 102769.
- Koleini, S. M. J., Abdollahy, M., and Soltani, F., 2012, The comparison between sodium cyanide and white dextrin as pyrite depressants in the sequential flotation Cu-Zn massive sulphide ore Irantaknar, *in* Proceedings XXVI IMPC, New Delhi, 24 - 28 September 2012, p. 5120-5128.
- Konev, V. A., 1985, Флотация сульфидов / Sulfide flotation, Moscow, Nedra, p. 262.
- Korchef, A., and Touaibi, M., 2020, Effect of pH and temperature on calcium carbonate precipitation by CO<sub>2</sub> removal from iron-rich water: *Water and Environment Journal*, v. 34, no. 3, p. 331-341.
- Kottek, M., Grieser, J., Christoph, B., and Bruno, R., 2006, World map of the Köppen-Geiger climate classification updated: *Meteorologische Zeitschrift*, v. 15, no. 3, p. 259-263.

- Krolak, T., Palmer, K., Lacouture, B., and Paley, N., 2017, NI 43-101 Technical report. Red Dog mine. Alaska, USA, Anchorage, AK, USA, p. 143. Miningdataonline.com. [https://www.miningdataonline.com/reports/Red%20Dog%20Mine\\_TR12312016.pdf](https://www.miningdataonline.com/reports/Red%20Dog%20Mine_TR12312016.pdf).
- Kubota, T., Yoshida, M., Hashimoto, S., and Shimoizaka, J., 1974, 黄銅鉱および方鉛鉱の浮選分離における温度の影響に関する基礎研究 / Fundamental study on the effect of pulp temperature in copper-lead bulk differential flotation (in Japanese): 日本鉱業会誌 / Journal of the Japan Mining Association, v. 90, no. 1040, p. 641-641.
- Kulkarni, R. D., and Somasundaran, P., 1980, Flotation chemistry of hematite/oleate system: Colloids and Surfaces, v. 1, no. 3-4, p. 387-405.
- Kupka, N., and Rudolph, M., 2018, Froth flotation of scheelite – a review: International Journal of Mining Science and Technology, v. 28, no. 3, p. 373-384.
- Kyzas, G., and Matis, K., 2018, Flotation in water and wastewater treatment: Processes, v. 6, no. 8, 116.
- Lagergren, S., About the theory of so-called adsorption of soluble substances, *in* Proceedings Kungliga Svenska Vetenskapsakademiens Handlingar [Proceedings of the Royal Swedish Academy of Sciences], Stockholm, 1898, Volume 24, Royal Swedish Academy of Sciences, p. 1-39.
- Lamberg, P., Pertti, H., Pentti, S., and Sari, S., 1997, Mineralogical balances by dissolution methodology, Short course on ore and environmental mineralogy: Mamede de Infesta, Portugal, IMA Commission on Ore Mineralogy, p. 1-29.
- Lamberg, P., and Rosenkranz, J., Systematic diagnosis of flotation circuit performance based on process mineralogical methods, *in* Proceedings 14th International Mineral Processing Symposium, Kuşadası, Turkey, 2014, p. 417-423.
- Laskowski, J. S., 1989, Thermodynamic and kinetic flotation criteria: Mineral Processing and Extractive Metallurgy Review, v. 5, no. 1-4, p. 25-41.
- Laskowski, J. S., 2004, Testing flotation frothers: Physicochemical Problems of Mineral Processing v. 38, p. 13-22.
- Latimer, W. M., 1921, The mass effect in the entropy of solids and gases: Journal of the American Chemical Society, v. 43, no. 4, p. 818-826.
- Latimer, W. M., 1951, Methods of estimating the entropies of solid compounds: Journal of the American Chemical Society, v. 73, no. 4, p. 1480-1482.

- Le, T. M. K., Schreithofer, N., and Dahl, O., 2020, Dissolution test protocol for estimating water quality changes in minerals processing plants operating with closed water circulation: *Minerals*, v. 10, no. 8, p. 653.
- Leach, D., Sangster, D., Kelley, K., Large, R., Garven, G., Allen, C., Gutzmer, J., and Walters, S., 2005, Sediment-hosted lead-zinc deposits. A global perspective, *in* Hedenquist, J. W., Thompson, J. F. H. G., Richard J. , and Richards, J. P., eds., *Economic geology: one hundredth anniversary volume*, Society of Economic Geologists, p. 561-608.
- Leite, M., 1992, Liberation by size reduction, consequences and improvements on flotation kinetics, *in* Mavros, P., and Matis, K., eds., *Innovations in Flotation Technology: Thessaloniki*, Springer-Science + Business Media B.V., p. 149-170.
- Lepage, M. R., 2023, Conductivity measurements of the froth zone in flotation, PhD Thesis: McGill University, Department of Mining and Materials Engineering, p. 440.
- Leussing, D. L., and Kolthoff, I. M., 1953, The solubility product of ferrous hydroxide and the ionization of the aquo-ferrous ion: *Journal of the American Chemical Society*, v. 75, no. 10, p. 2476-2479.
- Levanaho, J., Hoover, K., Spence, C., and Bachewich, B., 2005, Effect of pulp temperature on copper and gold collectors at Hudson Bay mining and smelting: 37th Annual Meeting of the Canadian Mineral Processors, p. 481-496.
- Li, C., and Hui, Y., 2013, 安徽李楼铁矿强磁选尾矿反浮选温度试验 / Temperature test of reverse flotation for high intensity magnetic separation tailings of Anhui Lilou iron ore (in Chinese): *现代矿业 / Modern Mining*, v. 534, p. 112-113.
- Li, C., Runge, K., Shi, F., and Farrokhpay, S., 2016, Effect of flotation froth properties on froth rheology: *Powder Technology*, v. 294, p. 55-65.
- Li, C., Xu, M., Xing, Y., Zhang, H., and Peuker, U. A., 2020, Efficient separation of fine coal assisted by surface nanobubbles: *Separation and Purification Technology*, v. 249, no. 5, 117163.
- Li, D., Leng, X., and Qin, F., 2010, 宜昌磷矿低温捕收剂研究 / Low temperature collector for Yichang phosphate rock (in Chinese): *化工矿物与加工 / IM & P*, v. 10, p. 1-4.

- Li, F., and Zeng, X.-l., 1999, 攀西地区氟碳 矿速矿工艺研究/ Beneficiation technology for bastnaesite in Panxi area (in Chinese): Journal of Shanghai Second Polytechnic University, v. 1, p. 1-7.
- Li, J., Sun, X., Zhang, D., and Zhu, Y., 2014, 某铜钨矿中白钨矿的低温浮选效果优化 / Optimization on low temperature floatation of scheelite from copper-tungsten ore (in Chinese): Metal Mine, v. 9, p. 56-59.
- Li, M., Gao, K., Zhang, D., Duan, H., Ma, L., and Huang, L., 2018, The influence of temperature on rare earth flotation with naphthyl hydroxamic acid: Journal of Rare Earths, v. 36, no. 1, p. 99-107.
- Li, Q., Yin, W. Z., Ma, Y. Q., and Liu, M. B., 2011, 含镁碳酸盐矿物溶解度 模拟计算及对浮选过程的影响/ Simulation and effects on flotation of solubility of magnesium carbonate minerals (in Chinese): Journal of Northeastern University (Natural Science), v. 32, no. 9, p. 1348-1351.
- Li, S., Gong, D., Zhang, W., Li, G., and Jue, K., 2020, Improving fluorite flotation under low temperature and neutral pH conditions: Surface Review and Letters, v. 27, no. 8, 1950187.
- Liesbet, G., Acker, K. v., Beretta, S., and Heron, C., 2022, Metals for clean energy: pathways to solving Europe's raw materials challenge: KU Leuven, Leuven, p. 117. <https://eurometaux.eu/media/rqocjybv/metals-for-clean-energy-final.pdf>
- Lin, I. J., 1989, The effect of seasonal variations in temperature on the performance of mineral processing plants: Minerals Engineering, v. 2, no. 1, p. 47-54.
- Liu, G., Liu, Z., Liu, Y., and Yu, J., 2011, 一种钽铌尾矿浮选分离锂云母精矿的方法 / A method for concentrating lepidolite from tantalum-niobium tailings through flotation (in Chinese), State Intellectual Property Office of the People's Republic of China, Patent No. CN 102151616 B, p. 4.
- Liu, X., Li, Z., Li, Z., Wang, Y., Deng, Z., and Xie, X., 2019, 黄铁矿低温浮选试验及机理分析/ Study and mechanism analysis on the flotation of pyrite in low temperature (in Chinese): Conservation and utilization of mineral resources, v. 39, no. 4, p. 115-120.
- Long, T., Chen, Y., Shi, J., Chen, W., Zhu, Y., Zhang, C., and Bu, X., 2020, Effect of grinding media on the flotation of copper-activated marmatite: Physicochemical Problems of Mineral Processing, v. 56, no. 2, p. 229-237.

- López-Valdivieso, A., Celedón Cervantes, T., Song, S., Robledo Cabrera, A., and Laskowski, J. S., 2004, Dextrin as a non-toxic depressant for pyrite in flotation with xanthates as collector: *Minerals Engineering*, v. 17, no. 9-10, p. 1001-1006.
- López-Valdivieso, A., Sanchez-Lopez, A. A., Padilla-Ortega, E., Robledo-Cabrera, A., Galvez, E., and Cisternas, L., 2018, Pyrite depression by dextrin in flotation with xanthates. Adsorption and floatability studies, *Physicochemical Problems of Mineral Processing*, v. 54, no. 4, p. 1159-1171.
- López-Valdivieso, A., Sánchez López, A. A., Song, S., García Martínez, H. A., and Licón Almada, S., 2007, Dextrin as a regulator for the selective flotation of chalcopyrite, galena and pyrite: *Canadian Metallurgical Quarterly*, v. 46, no. 3, p. 301-309.
- Lukio Co. Ltd., 2005, Mineral processing of complex sulfide ore (Kuroko), Tokyo, p. 4. [https://mric.jogmec.go.jp/public/report/1988-04/No2\\_eng.pdf](https://mric.jogmec.go.jp/public/report/1988-04/No2_eng.pdf)
- Lutterotti, L., Matthies, S., and Wenk, H. R., 1999, MAUD: a friendly Java program for material analysis using diffraction: *CPD Newsletter*, v. 21, p. 14-15.
- Luttrell, G. H., Phillips, D. I., and Honaker, R. Q., Enhanced gravity separators: new alternatives for fine coal cleaning, *in* COAL PREP '95: international coal preparation exhibition and conference, Lexington, KY, USA, 2-4 May 1995, p. 322.
- Lydon, J. W., 1995, Exhalative base metal sulphides, *in* Eckstrand, O. R., Sinclair, W. D., and Thorpe, R. I., eds., *Geology of Canadian mineral deposit types*, Geological Survey of Canada, no. 8, p. 130-152.
- Malafarina, L., and Deredin, C., 2021, Sudbury integrated nickel operations Strathcona mill [PowerPoint slides], 53rd Annual Canadian Mineral Processors' Conference: online, CIM.
- Maldonado, M., Araya, R., and Finch, J., 2012, An overview of optimizing strategies for flotation banks: *Minerals*, v. 2, no. 4, p. 258-271.
- Manono, M. S., Corin, K. C., and Wiese, J. G., 2012, An investigation into the effect of various ions and their ionic strength on the flotation performance of a platinum bearing ore from the Merensky reef: *Minerals Engineering*, v. 36-38, p. 231-236.
- Manouchehri, H. R., Johansson, B., and Ikumapayi, F., 2012, Effect of temperature in flotation of Zn from massive sulfide ores, *in* Proceedings XXVI IMPC, New Delhi, India, 24-28 September 2012, p. 3227-3238.

- Marais, P., 1980, Some practical considerations in the design and operation of a plant for the differential flotation of mixed sulphides, especially copper and zinc: *Journal of The South African Institute of Mining and Metallurgy*, v. 80, no. 11, p. 385-394.
- Marois, J. S., Downey, D., Matton, G., Dodier, Y., and Cappucitti, F., 2018, Resolving detrimental seasonal effect on the flotation processes at Niobec: 50th Annual Canadian Mineral Processors' Conference, p. 106-118.
- Mathews, P. G., 2005, *Design of experiments with MINITAB*, Milwaukee, Wis., ASQ Quality Press, Milwaukee, WI, USA, p. 490.
- McCreedy, H. H., and Honeywell, W. R., 1966, Effect of xanthate in cyanidation: Paper presented at the Annual Meeting of the Canadian Gold Metallurgists, held in Ottawa, Canada, January, 1966, p. 66-69.
- McNeill, L. S., 2000, Water quality factors influencing iron and lead corrosion in drinking water PhD Thesis: Virginia Polytechnic Institute and State University, Civil and Environmental Engineering, 104 p.
- Mehri, A., Haghani, M., and Mozaffari, E., 2019, Flotation of potash for carnallite resources in Khur Playa of Iran using Jameson flotation cell: *Journal of Environmental Analytical Chemistry*, v. 6, no. 1, p. 2-9.
- Mekis, É., Vincent, L. A., Shephard, M. W., and Zhang, X., 2015, Observed trends in severe weather conditions based on humidex, wind chill, and heavy rainfall events in Canada for 1953-2012: *Atmosphere - Ocean*, v. 53, no. 4, p. 383-397.
- Menéndez, M., Vidal, A., Toraño, J., and Gent, M., 2004, Optimisation of spodumene flotation: *The European Journal of Mineral Processing and Environmental Protection*, v. 4, no. 2, p. 130-135.
- Meng, Q.-y., Feng, Q.-m., and Ou, L.-m., 2018, Effect of temperature on floatability and adsorption behavior of fine wolframite with sodium oleate: *Journal of Central South University*, v. 25, no. 7, p. 1582-1589.
- Mhonde, N., Schreithofer, N., Corin, K., and Mäkelä, M., 2020, Assessing the combined effect of water temperature and complex water matrices on xanthate adsorption using multiple linear regression: *Minerals*, v. 10, no. 9, 733.
- Mikhlin, Y., Karacharov, A., Vorobyev, S., Romanchenko, A., Likhatski, M., Antsiferova, S., and Markosyan, S., 2020, Towards understanding the role of surface gas nanostructures: effect

- of temperature difference pretreatment on wetting and flotation of sulfide minerals and Pb-Zn ore: *Nanomaterials*, v. 10, no. 7, p. 1-12.
- Miller, J., and Ackerman, J., Bench scale flotation of alunite ore with oleic acid, *in* Proceedings Fine Particle Symposium, New York, 1980, AIME, p. 832-852.
- Mills, R., 2022, Tight lead-zinc market keeping a floor under prices, 11/22/22, Streetwise Reports. <https://www.streetwisereports.com/article/2022/11/22/tight-lead-zinc-market-keeping-a-floor-under-prices.html>
- Mindat.org, The mineralogy of lead, *in* Ralph, J., ed., Volume 2024, Hudson Institute of Mineralogy. <https://www.mindat.org/element/Lead>
- Mindat.org, The mineralogy of zinc, *in* Ralph, J., ed., Volume 2024, Hudson Institute of Mineralogy. <https://www.mindat.org/element/Zinc>
- Mingulina, E., Maslennikova, G., Korovin, N., and Filippov, E., 1990, Курс общей химии/General chemistry course (in Russian), Vysshaya Shkola, p. 115-119.
- Mitrofanov, S., 1966, Селективная флотация/Selective flotation [in Russian], Moscow, Nedra, p. 584.
- Mohammadi-Jam, S., 2017, An investigation into the applicability of inverse gas chromatography to mineral flotation, PhD Thesis: McGill University, Department of Mining and Materials Engineering, p. 184.
- Mohammadi-Jam, S., and Waters, K. E., 2014, Inverse gas chromatography applications: a review: *Advances in Colloid and Interface Science*, v. 212, p. 21-44.
- Mohr, S., Giurco, D., Retamal, M., Mason, L., and Mudd, G., 2018, Global projection of lead-zinc supply from known resources: *Resources*, v. 7, no. 1, 17.
- Molifie, A., Becker, M., Geldenhuys, S., and McFadzean, B., 2023, Investigating the reasons for the improvement in flotation grade and recovery of an altered PGE ore when using sodium silicate: *Minerals Engineering*, v. 195, p. 108024.
- Monsalve, A., and Schechter, R., 1984, The stability of foams: dependence of observation on the bubble size distribution: *Journal of Colloid and Interface Science*, v. 97, no. 2, p. 327-335.
- Monte, M. B. M., Lins, F. F., and Oliveira, J. F., 1997, Selective flotation of gold from pyrite under oxidizing conditions: *International Journal of Mineral Processing*, v. 51, no. 1, p. 255-267.



- Monument Chemical, 2022, Methyl isobutyl carbinol safety data sheet, Monument Chemical.  
[https://monumentchemical.com/uploads/files/SDS/MIBC\\_-\\_SDS\\_\(US\).pdf?v=1661804588840](https://monumentchemical.com/uploads/files/SDS/MIBC_-_SDS_(US).pdf?v=1661804588840)
- Morar, S., Hatfield, D., Barbian, N., Bradshaw, D., Cilliers, J., and Triffett, B., 2006, A comparison of flotation froth stability measurements and their use in the prediction of concentrate grade, *in* Proceedings XXIII IMPC, Istanbul, Turkey, 1 January 2006, p. 739-744.
- Mudd, G. M., Jowitt, S. M., and Werner, T. T., 2017, The world's lead-zinc mineral resources: scarcity, data, issues and opportunities: *Ore Geology Reviews*, v. 80, p. 1160-1190.
- Mustafa, S., Hamid, A., and Naeem, A., 2004, Temperature effect on xanthate sorption by chalcopyrite: *J Colloid Interface Sci*, v. 275, no. 2, p. 368-375.
- Mysels, K. J., 1959, *Soap films: studies of their thinning and a bibliography*, Pergamon Press, New York, London, Paris, Los Angeles, p. 116.
- Naeem, A., Ali, H., Mustafa, S., Qamar, S., Tasleem, S., and Begum, D., 2008, Kinetics of xanthate sorption by copper sulphide: *Journal of the Chemical Society of Pakistan*, v. 30, no. 4, p. 517-520.
- Nassar, N. T., and Fortier, S. M., 2021, Methodology and technical input for the 2021 review and revision of the U.S. critical minerals list, 2021-1045, Reston, VA, USA, p. 31.  
<https://pubs.usgs.gov/publication/ofr20211045>
- Nassif, M., 2013, Developing critical coalescence concentration curves using dilution and determining frother-like properties of oil sands process, Master's Thesis: McGill University, Department of Mining and Materials Engineering, p. 103.
- Natural Resources Canada, 2019, The Canadian minerals and metals plan, Ottawa, p. 52.  
[https://natural-resources.canada.ca/sites/nrcan/files/CMMP/CMMP\\_The\\_Plan-EN.pdf](https://natural-resources.canada.ca/sites/nrcan/files/CMMP/CMMP_The_Plan-EN.pdf)
- Natural Resources Canada, 2022, The Canadian critical minerals strategy from exploration to recycling: powering the green and digital economy for Canada and the world: Natural Resources Canada, Ottawa, p. 52. <https://www.canada.ca/content/dam/nrcan-nrcan/site/critical-minerals/Critical-minerals-strategyDec09.pdf>
- Nayak, A., Jena, M. S., and Mandre, N. R., 2021, Beneficiation of lead-zinc ores – a review: *Mineral Processing and Extractive Metallurgy Review*, v. 43, no. 5, p. 564-583.

- Nesset, J. E., Finch, J. A., and Gomez, C. O., 2007, Operating variables affecting bubble size in force-air mechanical flotation machines, The 9th Mill Operators Conference: Fremantle, Australia, AusIMM, p. 55–65.
- Nesset, J. E., Gomez, C. O., Finch, J. A., Hernandez-Aguilar, J., and DiFeo, A., The use of gas dispersion measurements to improve flotation performance, *in* Proceedings 34th Annual Meeting of the Canadian Mineral Processors, Ottawa, 2002, CIM, p. 361-383.
- Newall, P., Hill, A., Ellis, R., King, P., Holley, S., Richardson, S., Tarrant, S., Luneva, V., and Glücksman, E., 2017, NI 43-101 Technical report for the Neves-Corvo mine, Portugal, Wardell Armstrong, p. 236. [https://minedocs.com/12/Neves-Corvo\\_2017\\_TR.pdf](https://minedocs.com/12/Neves-Corvo_2017_TR.pdf)
- Ng, W. S., Sonsie, R., Forbes, E., and Franks, G. V., 2015, Flocculation/flotation of hematite fines with anionic temperature-responsive polymer acting as a selective flocculant and collector: *Minerals Engineering*, v. 77, p. 64-71.
- Nguyen, A. V., 2002, Liquid drainage in single Plateau borders of foam: *Journal of Colloid and Interface Science*, v. 249, no. 1, p. 194-199.
- Nguyen, A. V., Harvey, P. A., and Jameson, G. J., 2003, Influence of gas flow rate and frothers on water recovery in a froth column: *Minerals Engineering*, v. 16, no. 11, p. 1143-1147.
- Nguyen, T. T. P., Nguyen, N. N., and Nguyen, A. V., 2024, Investigating the effect of interfacial hydrogen bonding on the surface mobility and foam drainage kinetics: *Journal of Molecular Liquids*, v. 401, p. 124656.
- Ni, M., and Ratner, B. D., 2008, Differentiation of calcium carbonate polymorphs by surface analysis techniques - an XPS and TOF-SIMS study: *Surf Interface Anal*, v. 40, no. 10, p. 1356-1361.
- Noirant, G., Benzaazoua, M., Kongolo, M., Bussière, B., and Frenette, K., 2019, Alternatives to xanthate collectors for the desulphurization of ores and tailings: Pyrite surface chemistry: *Colloids and Surfaces A: Physicochemical and Engineering Aspects*, v. 577, p. 333-346.
- Nyamekye, G. A., 1993, Adsorption of dextrin onto sulphide minerals and its effect on the differential flotation of the Inco matte PhD Thesis: The University of British Columbia, Department of Mining and Mineral Process Engineering, p. 215.
- O'Connor, C. T., Dunne, R. C., and de Sousa, A. M. R. B., 1984, Effect of temperature on the flotation of pyrite: *Journal of The South African Institute of Mining and Metallurgy*, v. 84, no. 12, p. 389-394.

- O'Connor, C. T., and Mills, P. J. T., 1990, The effect of temperature on the pulp and froth phases in the flotation of pyrite: *Minerals Engineering*, v. 3, no. 6, p. 615-624.
- O'Connor, P. D. T., and Kleyner, A., 2012, *Practical reliability engineering*, Hoboken, NJ, USA, John Wiley & Sons, p. 512.
- Oetjen, K., Bilke-Krause, C., Madani, M., and Willers, T., 2014, Temperature effect on foamability, foam stability, and foam structure of milk: *Colloids and Surfaces A: Physicochemical and Engineering Aspects*, v. 460, p. 280-285.
- Ofor, O., and Nwoko, C., 1997, Oleate flotation of a nigerian baryte: The relation between flotation recovery and adsorption density at varying oleate concentrations, pH, and temperatures: *Journal of Colloid and Interface Science*, v. 186, no. 2, p. 225-233.
- Oladunni Oyelola, A., Babatunde Oyeboode, A., Meshack Basan, B., Magnus, T. I., Dare Victor, A., and Aboki Abdul, D., 2016, Comparative test for the upgrading of lead in Sabon Layi lead-zinc ore (Alkaleri local government area, Bauchi State), using gravity and froth flotation beneficiation methods: *International Journal of Advanced Engineering, Management and Science*, v. 2, no. 6, p. 780-786.
- Oliazadeh, M., Aghamirian, M., Grammatikopoulos, T., and Imeson, D., An overview of potash flotation, *in Proceedings 44th Annual Meeting of the Canadian Mineral Processors*, Ottawa, 2012, CIM, p. 431-442.
- Önal, G., Bulut, G., Gül, A., Kangal, O., Perek, K., and Arslan, F., 2005, Flotation of Aladag oxide lead-zinc ores: *Minerals Engineering*, v. 18, p. 279-282.
- Orii, M., 1961, 温水浮選について / On warm pulp flotation (in Japanese): *The Resources Processing Society of Japan*, v. 15, p. 6-17.
- Ozan, S. C., and Jakobsen, H. A., 2019, On the role of the surface rheology in film drainage between fluid particles: *International Journal of Multiphase Flow*, v. 120, p. 103103.
- Özün, S., and Ergen, G., 2019, Determination of optimum parameters for flotation of galena: effect of chain length and chain structure of xanthates on flotation recovery: *ACS Omega*, v. 4, no. 1, p. 1516-1524.
- Palace, W., 2014, Gabriel Lafitte. *Spoiling Tibet: China and Resource Nationalism on the Roof of the World*, Routledge, Asian Affairs, v. 3, 516-518 p.
- Pallanch, R., A., 1936, Factors governing the separation of lead and zinc in ore by flotation, *The American Institute of Mining, Metallurgical, and Petroleum Engineers*.

- Pallanch, R. A., 1928, The role of sulfites in the differential flotation plants of the U. S. Smelting, Refining & Mining Co, Annual Meeting of the American Institute of Mining, Metallurgical, and Petroleum Engineers: Salt Lake City, The American Institute of Mining, Metallurgical, and Petroleum Engineers.
- Pålsson, B., and Forssberg, K. S. E., 1989, Computer-assisted calculations of thermodynamic equilibria in sphalerite xanthate systems: *International Journal of Mineral Processing*, v. 26, p. 223-258.
- Papamichael, E. M., Stamatidis, H., Stergiou, P.-Y., Foukis, A., and Gkini, O. A., 2019, Enzyme kinetics and modeling of enzymatic systems, in Singh R. S., Singhanian R. R., Pandey A., Larroche C. eds. *Advances in Enzyme Technology*, Amsterdam: Elsevier, p. 71-104.
- Parkins, E., 1975, Effect of temperature on the conditioning and flotation of an ilmenite ore, PhD Thesis: Imperial College London (University of London), 174 p.
- Parrent, M. D., 2012, Separation of pyrolusite and hematite by froth flotation, Master's Thesis: University of Alberta, Department of Chemical and Materials Engineering, p. 179.
- Pattanaik, A., and Venugopal, R., 2019, Role of surfactants in mineral processing: an overview, in Dutta, A. K., ed., *Surfactants and Detergents*, IntechOpen, p. 102.
- Pattison, I. G., 1981, The action of sodium sulphite as a depressant in sulphide mineral flotation systems containing chalcopyrite, galena, pyrite and sphalerite, Melbourne, University of Melbourne, p. 674.
- Paulson, O., and Pugh, R. J., 1996, Flotation of inherently hydrophobic particles in aqueous solutions of inorganic electrolytes: *Langmuir*, v. 12, no. 20, p. 4808-4813.
- Pavez, O., and Peres, A. E. C., 1993, Effect of sodium metasilicate and sodium sulphide on the floatability of monazite-zircon-rutile with oleate and hydroxamates: *Minerals Engineering*, v. 6, no. 1, p. 69-78.
- Pearson, K., 1920, Notes on the history of correlation: *Biometrika*, v. 13, no. 1, p. 25-45.
- Pease, J. D., Young, M. F., Curry, D., and Johnson, N. W., 2010, Improving fines recovery by grinding finer: *Mineral Processing and Extractive Metallurgy*, v. 119, no. 4, p. 216-222.
- Peng, Y., and Grano, S., 2010, Effect of iron contamination from grinding media on the flotation of sulphide minerals of different particle size: *International Journal of Mineral Processing*, v. 97, no. 1-4, p. 1-6.

- Perucca, C. F., 2000, Testing and evaluation of modifying reagents in potash flotation, Master's Thesis: The University of British Columbia, Department of Mining and Mineral Processing Engineering, p. 123.
- Petrucchi, R. H., Harwood, W. S., Herring, F. G., and Madura, J. D., 2007, General chemistry: principles and modern applications, Upper Saddle River, NJ, USA, Pearson Education, p. 1172.
- Piantadosi, C., and Smart, R. S. C., 2002, Statistical comparison of hydrophobic and hydrophilic species on galena and pyrite particles in flotation concentrates and tails from TOF-SIMS evidence: International Journal of Mineral Processing, v. 64, no. 1, p. 43-54.
- Pitois, O., Fritz, C., and Vignes-Adler, M., 2005, Liquid drainage through aqueous foam: study of the flow on the bubble scale: Journal of Colloid and Interface Science, v. 282, no. 2, p. 458-465.
- Plaksa, N., 1970, Совмещение пропарки и селективной флотации медно-молибденовых концентратов/Combination of low-temperature steaming and selective flotation of copper-molybdenum concentrates (in Russian): Tsvetnye Metally, v. 43, no. 1, p. 79-82.
- Plaksin, I. N., Microautoradiography for the study of flotation, *in* Proceedings of the Second International Congress of Surface Activity, London, 1957, v. 3, p. 355.
- Plaksin, I. N., 1959, Interaction of minerals with gases and reagents in flotation: Mining Engineering, The American Institute of Mining, Metallurgical, and Petroleum Engineers, v. 11, p. 319.
- Plotnikova, A. A., and Bragin, V. I., 2018, Повышение сортности свинцовых концентратов магнитными методами / The use of magnetic techniques for lead concentrate upgrading [in Russian]: Tsvetnye Metally, v. 12, no. 912, p. 21-26.
- Plotnikova, A. A., Bragin, V. I., and Knyazev, J. V., 2019, Минералого-технологические особенности сфалерита в свинцово-цинковых рудах Горевского месторождения / Mineralogical and technological features of sphalerite in lead-zinc ores of Gorevsky deposit [in Russian]: Физико-технические проблемы разработки полезных ископаемых / Physical and Technical Problems of Mineral Development, v. 4, p. 1-16.
- Pol'kin, S. I., and Adamov, E. V., 1975, Обогащение руд цветных и редких металлов / Processing of ores of non-ferrous and rare metals [in Russian], Moscow, Nedra, p. 461.

- Poling, G. W., 1976, Reactions between thiol reagents and sulphide minerals, *in* Fuerstenau, M. C., ed., Flotation - A. M. Gaudin Memorial: New York, NY, American Institute of Mining, Metallurgical, and Petroleum Engineers, p. 334-363.
- Poling, G. W., 1984, Comments on ODCE report regarding milling chemicals for proposed U.S. Borax Quartz Hill molybdenite concentrator.: U.S. Borax Corp., Los Angeles, CA, USA, p. 13.
- Pomianowski, A., and Leja, J., 1963, Spectrophotometric study of xanthate and dixanthogen solutions: Canadian Journal of Chemistry, v. 41, no. 9, p. 2219-2230.
- Potapova, E., 2009, Studies on the adsorption of flotation collectors on iron oxides Licentiate Thesis Licentiate Thesis: Luleå University of Technology Department of Chemical Engineering and Geosciences, p. 94.
- Powell, K. J., Brown, P. L., Byrne, R. H., Gajda, T., Hefter, G., Leuz, A.-K., Sjöberg, S., and Wanner, H., 2013, Chemical speciation of environmentally significant metals with inorganic ligands. Part 5: The  $\text{Zn}^{2+} + \text{OH}^-$ ,  $\text{Cl}^-$ ,  $\text{CO}_3^{2-}$ ,  $\text{SO}_4^{2-}$  systems (IUPAC Technical Report): Pure and Applied Chemistry, v. 85, no. 12, p. 2249-2311.
- PQ Corporation, 2009, Metso (R) sodium metasilicate: a soluble silicate for institutional and industrial cleaning: Amersfoort, PQ Corporation, p. 7.  
<https://www.zhuongrong.com.tw/userfiles/files/20211222115710834.pdf>
- Pradip, 1981, The surface properties and flotation of rare-earth minerals PhD Thesis: University of California, Berkeley, Department of Materials Science and Mineral Engineering, p. 422.
- Pradip, and Fuerstenau, D. W., 1991, The role of inorganic and organic reagents in the flotation separation of rare-earth ores: International Journal of Mineral Processing, v. 32, no. 1-2, p. 1-22.
- Prestidge, C. A., and Ralston, J., 1995, Contact angle studies of galena particles: Journal of Colloid And Interface Science, v. 172, no. 2, p. 302-310.
- Princen, H., and Kiss, A., 1989, Rheology of foams and highly concentrated emulsions: Journal of Colloid and Interface Science, v. 128, no. 1, p. 176-187.
- Pugh, R. J., 2016, Bubble size measurements and foam test methods, in Bubble and Foam Chemistry, Cambridge University Press, Cambridge, UK, p. 372-404.
- Puigdomènech, I., Rard, J. A., Plyasunov, A. V., and Grenthe, I., 1999, Temperature corrections to thermodynamic data and enthalpy calculations, OECD Publishing, Paris, France, p. 96.

- Quinn, J. J., Kracht, W., Gomez, C. O., Gagnon, C., and Finch, J. A., 2007, Comparing the effect of salts and frother (MIBC) on gas dispersion and froth properties: *Minerals Engineering*, v. 20, no. 14, p. 1296-1302.
- Rabinovich, V., and Havin, Z., 1978, Краткий химический справочник / Brief chemical handbook (in Russian), Leningrad, Izd. Himija, p. 71.
- Radtke, D. B., White, A. F., Davis, J. V., and Wilde, F. D., 1998, Dissolved oxygen, U.S. Geological Survey TWRI Book 9: Washington, USGS, p. 1-27.
- Rao, M., and Natarajan, K., 1988, Electrochemical aspects of grinding media-mineral interaction on sulphide flotation: *Bulletin Materials Science*, v. 10, no. 5, p. 411-422.
- Rao, S. R., 1970, Thermodynamic analysis of ethyl xanthate adsorbed at galena surface: *Surface Science*, v. 21, no. 2, p. 413-425.
- Rao, S. R., 1971, Xanthates and related compounds, New York, Marcel Dekker Inc., p. 504.
- Rao, S. R., 2004, Surface chemistry of froth flotation (2<sup>nd</sup> ed.), Springer Science + Business Media, LLC, New York, USA, v. 1, p. 744.
- Rashchi, F., Dashti, A., Arabpour-Yazdi, M., and Abdizadeh, H., 2005, Anglesite flotation: a study for lead recovery from zinc leach residue: *Minerals Engineering*, v. 18, no. 2, p. 205-212.
- Rau, M. G. S., 1961, Studies in the adsorption of xanthates on galena PhD Thesis: The University of London, Imperial College of Science and Technology, p. 161.
- Ray, H. S., Sridhar, H. S., and Abraham, K. P., 2014, Extraction of nonferrous metals, New Delhi, Affiliated East-West Press (Pvt) Ltd., v. 1, p. 532.
- Redmond, P., 2023, Irish-type Zn-Pb deposits in the context of global zinc supply, *in* Andrew, C. J., Hitzman, M. W., and Stanley, G., eds., *Irish-type Deposits around the world*: Dublin, Irish Association for Economic Geology, p. 19-34.
- Relvas, J. M. R. S., Barriga, F. J. A. S., Ferreira, A., Noiva, P. C., Pacheco, N., and Barriga, G., 2006, Hydrothermal alteration and mineralization in the Neves-Corvo volcanic-hosted massive sulfide deposit, Portugal. I. Geology, mineralogy, and geochemistry: *Economic Geology*, v. 101, p. 753-790.
- Remes, A., 2012, Advanced process monitoring and control methods in mineral processing applications PhD thesis: Aalto University, Department of Automation and Systems Technology, p. 170.

- Ren, H., and Hu, Y., 1996, 用水杨羟肟酸捕收剂从强磁中矿中选取高品位稀土精矿的研究 /Study on the selection of high grade rare-earth concentrates from high-intensity separation middlings with salicylhydroxamic acid as the collector (in Chinese): Metal Mine, no. 11, p. 20-22.
- Robb, L., 2020, Introduction to ore-forming processes, 2nd Edition, Wiley-Blackwell, p. 496.
- Roberts, J., Deredin, C., and Paulin, J.-g., Process improvement update at Brunswick mine, *in* Proceedings 40th Annual Meeting of the Canadian Mineral Processors, Ontario, Canada, January 22–24, 2008, p. 27-49.
- Robie, R. A., and Bethke, P. M., 1962, Molar volumes and densities of minerals, Washington D.C., USA, USGS, p. 10-15.
- Rötzer, N., and Schmidt, M., 2018, Decreasing metal ore grades-Is the fear of resource depletion justified?: Resources, v. 7, no. 4, 88.
- Ruan, Y., Zhang, Z., Luo, H., Xiao, C., Zhou, F., and Chi, R., 2017, Ambient temperature flotation of sedimentary phosphate ore using cottonseed oil as a collector: Minerals, v. 7, no. 5, p. 1-14.
- Rubinstein, Y. B., and Filippov, J. A., 1980, Кинетика флотации/Flotation kinetics [in Russian], Moscow, Nedra, p. 375.
- Ryabeva, E. G., and Dobrovol'skaja, N. V., 1978, Определение суммы содержаний железа и марганца в сфалерите по магнитной восприимчивости / Determination of the sum of iron and manganese contents in sphalerite by magnetic susceptibility [in Russian]: Труды минералогического музея, v. 27, p. 125-127.
- Ryan, L., and Norris, R., 2014, Chemistry coursebook, Cambridge, Cambridge University Press, v., p. 374-375.
- Salarirad, M. M., Behnamfard, A., and Veglio, F., 2021, Removal of xanthate from aqueous solutions by adsorption onto untreated and acid/base treated activated carbons: Desalination and Water Treatment, v. 212, p. 220-233.
- Samatova, L., Kienko, L., Shestovets, V., and Voronova, O., 2007, Промышленное внедрение низкотемпературно й флотации флюорита с применением Аспарала Ф и собирательных смесей на его основе в комплексе с модификатором/ Industrial testing of low-temperature fluorite flotation with Asparal F mixtures (in Russian): Горный



- информационно-аналитический бюллетень / Mining Informational and Analytical Bulletin, v. 12, p. 308-318.
- Samatova, L., Shepeta, E., and Kondratjev, S., 2015, Изучение флотационных свойств собирателя FX-6 при обогащении шеелит-сульфидных руд / Investigation of flotational properties of FX-6 collector during processing of scheelite-sulfide ores (in Russian): Физико-технические проблемы разработки полезных ископаемых / Physical and Technical Problems of Mineral Development, v. 2, p. 156-160.
- Sander, R., 1999, Compilation of Henry's law constants for inorganic and organic species of potential importance in environmental chemistry: Mainz, Max-Planck Institute of Chemistry, p. 107.
- Sarkar, B., Chandrasekhar, S., and Das, A., 2007, Advanced gravity separators - A review of state of the art technology, *in* Proceedings of National Seminar on Advanced Gravity Separator, Jamshedpur, India, 2007, p. 57-74..
- Scheludko, A., Toshev, B. V., and Bojadjev, D. T., 1976, Attachment of particles to a liquid surface (capillary theory of flotation): Journal of the Chemical Society, Faraday Transactions 1: Physical Chemistry in Condensed Phases, v. 72, no. 1, p. 2815-2828.
- Schramm, L. L., Stasiuk, E. N., Yarranton, H., Maini, B. B., and Shelfantook, B., 2003, Temperature effects from the conditioning and flotation of bitumen from oil sands in terms of oil recovery and physical properties: Journal of Canadian Petroleum Technology, v. 42, no. 8, p. 55-61.
- Schriner, D., 2016, Advanced beneficiation of bastnaesite ore through centrifugal concentration and froth flotation, Master's Thesis: Colorado School of Mines, Department of Metallurgical and Materials Engineering, p. 116.
- Schubert, H., 2008, On the optimization of hydrodynamics in fine particle flotation: Minerals Engineering, v. 21, no. 12, p. 930-936.
- Schubert, H., and Schneider, V., О роли ассоциации аполярных групп при адсорбции собирателя / On the role of non-polar groups during collector adsorption (in Russian), *in* Proceedings VIII International Mineral Processing Congress, Leningrad (St. Petersburg), 1969, Izd. Instituta Mechanobr, p. 315-524.
- Schulze, H. J., 1989, Hydrodynamics of bubble-mineral particle collisions: Mineral Processing and Extractive Metallurgy Review, v. 5, no. 1-4, p. 43-76.

- Schwarz, S., and Grano, S., 2005, Effect of particle hydrophobicity on particle and water transport across a flotation froth: *Colloids and Surfaces A: Physicochemical and Engineering Aspects*, v. 256, no. 2, p. 157-164.
- Shaffer, L., and von Wandruszka, R., 2015, Temperature induced aggregation and clouding in humic acid solutions: *Advances in Environmental Chemistry*, v. 2015, no. 1, 543614.
- Shaw, D. J., 1992, *Introduction to colloid and surface chemistry*, 4<sup>th</sup> ed., Oxford, Elsevier Science, p. 320.
- Shean, B., Hadler, K., and Cilliers, J. J., 2017, A flotation control system to optimise performance using peak air recovery: *Chemical Engineering Research and Design*, v. 117, p. 57-65.
- Sheikh, N., 1972, The chemical stability of heavy metal xanthates, PhD Thesis: University of British Columbia, Mining Engineering, p. 153.
- Shen, Y., Nagaraj, D. R., Farinato, R., and Somasundaran, P., 2016, Study of xanthate decomposition in aqueous solutions: *Minerals Engineering*, v. 93, p. 10-15.
- Sheng, J. J., 2013, Chapter 11 - Foams and their applications in enhancing oil recovery, *in* Sheng, J. J., ed., *Enhanced Oil Recovery Field Case Studies*: Boston, Gulf Professional Publishing, p. 251-280.
- Sheridan, G. E., and Griswold, G. G., 1922, Concentration of ores by flotation, U.S. Patent Office, Patent No. 1,421,585: U.S.
- Shi, F. N., and Zheng, X. F., 2003, The rheology of flotation froths: *International Journal of Mineral Processing*, v. 69, no. 1-4, p. 115-128.
- Shumskaya, E. N., Poperechnikova, O. Y., and Kuptsova, A. V., 2016, Особенности переработки полиметаллических руд / Features of complex ore processing technology [in Russian]: *Gornyj Zhurnal / Mining Journal*, v. 11, p. 39-48.
- Shun-Ming, D., and Jian-Tao, L., Preferential flotation of a refractory Cu-Pb-Zn polymetallic Ore, *in* *Proceedings Proceedings of the 2017 3rd International Forum on Energy, Environment Science and Materials (IFEESM 2017)* 2018/02 2018, Atlantis Press, p. 1967-1971.
- Sidorov, A., Volkov, A., and Savva, N., 2015, Вулканизм и эпитеpмальные месторождения / Volcanism and epithermal deposits [in Russian]: *Вулканология и сейсмология*, v. 2015, no. 1, p. 3-12.
- Sillitoe, R. H., Steele, G. B., Thompson, J. F. H., and Lang, J. R., 1998, Advanced argillic lithocaps in the Bolivian tin-silver belt: *Mineralium Deposita*, v. 33, p. 539-546.

- Silverman, D., and Roseveare, W. E., 1932, An equation relating viscosity and surface tension: *Journal of the American Chemical Society*, v. 54, no. 11, p. 4460-4460.
- Simmons, S. F., White, N., and John, D., 2005, Geological characteristics of epithermal precious and base metal deposits: *Economic Geology 100th Anniversary Volume*, p. 485-522.
- Singer, D., 1986a, Descriptive model of Cyprus massive sulfide: *Mineral deposit models: US Geological Survey Bulletin*, v. 1693, p. 131.
- Singer, D., 1986b, Descriptive model of kuroko massive sulfide, *in* Cox, D. P., and Singer, D. A., eds., *Mineral deposit models: U.S. Geological Survey Bulletin 1693*: Washington, USGS, p. 189-194.
- Siva Reddy, G., and Konda Reddy, C., 1988, The chemistry of activation of sphalerite-a review: *Mineral Processing and Extractive Metallurgy Review*, v. 4, no. 1-2, p. 1-38.
- Siwek, B., Zembala, M., and Pomianowski, A., 1981, A method for determination of fine-particle flotability: *International Journal of Mineral Processing*, v. 8, no. 1, p. 85-88.
- Smith, T., Lin, D., Lacouture, B., and Anderson, G., Removal of organic carbon with Jameson cell at Red Dog mine, *in* *Proceedings 40th Annual Meeting of the Canadian Mineral Processors*, Ottawa, Ontario, Canada, January 22–24, 2008, p. 334-346.
- Smolko-Schvarzmayer, N., Klingberg, A., and Nordberg, H., 2017, Use of branched alcohols and alkoxylates thereof as secondary collectors, *US Patent Office*, Patent No. US 10,376,901 B2: USA.
- State Commission for Mineral Reserves, 2007, Свинцовые и цинковые руды/Lead and Zinc Ores [in Russian]: ФГУ ГКЗ, Moscow, p. 41.
- Stén, P., Parvinen, P., Miettinen, M., Luukkanen, S., Kaskiniemi, V., and Aaltonen, J., 2003, On-line analysis of flotation process waters at Siilinjärvi (Finland) apatite concentrating plant: *Minerals Engineering*, v. 16, no. 3, p. 229-236.
- Stevenson, P., 2005, Remarks on the shear viscosity of surfaces stabilised with soluble surfactants: *Journal of Colloid Interface Science*, v. 290, no. 2, p. 603-606.
- Stevenson, P., and Stevanov, C., 2004, Effect of rheology and interfacial rigidity on liquid recovery from rising froth: *Industrial & Engineering Chemistry Research*, v. 43, no. 19, p. 6187-6194.
- Stringer, C., Wang, T., Michaelos, M., and Pachitariu, M., 2021, Cellpose: a generalist algorithm for cellular segmentation: *Nature Methods*, v. 18, no. 1, p. 100-106.

- Strong, A., Yan, D., and Dunne, R., The detection of xanthate in solution and on sulfide surfaces to help understand and improve mineral separation on industrial plants, *in* Proceedings Centenary of Flotation Symposium, Brisbane, Australia, 6–9 June 2005, Australasian Institute of Mining and Metallurgy, p. 619-624.
- Su, F., Hanumantha Rao, K., Forssberg, K. S. E., and Samskog, P. O., 1998, The influence of temperature on the kinetics of apatite flotation from magnetite fines: *International Journal of Mineral Processing*, v. 54, no. 3-4, p. 131-145.
- Sun, S., and Chao, T., Hypothesis for the effect of temperature on coal flotation, *in* Proceedings SME Annual Meeting of the American Institute of Mining, Metallurgical, and Petroleum Engineers, New York, 1966, p. 13.
- Sun, S. C., 1952, Frothing characteristics of pine oils in flotation: *Transactions of the American Institute of Mining and Metallurgical Engineers*, v. 193, no. 1, p. 65-71.
- Sun, X., Huang, L., Wu, D., Tong, X., Yang, S., and Hu, B., 2022, The selective depression effect of dextrin on pyrite during the Zn–Fe sulfides flotation under low alkaline conditions: *Colloids and Surfaces A: Physicochemical and Engineering Aspects*, v. 650, p. 129573.
- Sutherland, D., Skayman, P., Keogh, C., McKinley, S., and Uludag, E., 2019, Technical report. Olympias mine. Greece, Vancouver, Eldorado Gold Corporation, p. 195.
- Sutherland, K. L., and Wark, I. W., 1955, *Principles of flotation*, Australasian Institute of Mining and Metallurgy Melbourne, p. 489.
- Sverdrup, H. U., Olafsdottir, A. H., and Ragnarsdottir, K. V., 2019, On the long-term sustainability of copper, zinc and lead supply, using a system dynamics model: *Resources, Conservation & Recycling: X*, v. 4, 100007.
- Taggart, A., 1945, *Handbook of mineral dressing*, New York, John Wiley & Sons Ltd., p. 12-99.
- Taggart, A. F., Taylor, T. C., and Knoll, A. F., Chemical reactions in flotation, *in* Proceedings AIME, New York, 1930, American Institute of Mining and Metallurgical Engineers, p. 3-33.
- Tajadod, J., 1998, Flotation chemistry of enargite and chalcopyrite using potassium amyl xanthate and depressants, PhD Thesis: Queen's University, Department of Mining Engineering, p. 275.
- Talbot, D., and Talbot, J., 1998, *Corrosion science and technology*, Boca Raton, CRC Press, p. 406.

- Tan, S. N., Jiang, A., Liau, J. J., Grano, S. R., and Horn, R. G., 2009, The surface dilational viscosity of polypropylene glycol solutions and its influence on water flow and foam behavior: *International Journal of Mineral Processing*, v. 93, no. 2, p. 194-203.
- Tane, J.-L., 2012, A simplified interpretation of the basic thermodynamic equations: *The General Science Journal*, December 11, p. 12.
- Taylor, C. D., Zierenberg, R. A., Goldfarb, R. J., Kilburn, J. E., and Seal, R. R., 1996, Volcanic-associated massive sulfide (VMS) deposits range from lens shaped to sheet-like bodies of sulfide-mineral- rich rock spatially associated with volcanic rocks ranging in composition from basalt to rhyolite, *in* Edward A. du Bray ed. Preliminary compilation of descriptive geoenvironmental mineral deposit models, USGS, Denver, CO, USA, p. 137-144.
- The Mining Association of Canada, 2019, Facts and Figures 2019. The state of Canada's mining industry, p. 104. [https://mining.ca/wp-content/uploads/dlm\\_uploads/2021/04/FF-English-Web-1.pdf](https://mining.ca/wp-content/uploads/dlm_uploads/2021/04/FF-English-Web-1.pdf)
- Thompson, M., 2006, Base metals handbook, 1<sup>st</sup> ed., Cambridge, England, Woodhead Publishing, p. 466.
- Tolcin, A. C., 2022, 2018 Minerals yearbook. Zinc: USGS, Washington, p. 13. <https://pubs.usgs.gov/myb/vol1/2018/myb1-2018-zinc.pdf>
- Townsend, H. E., 1970, Potential-pH diagrams at elevated temperature for the system Fe-H<sub>2</sub>O: *Corrosion Science*, v. 10, no. 5, p. 343-358.
- Turko, M., Dormeshkin, O., Miskov, E., and Solovjeva, L., 2014, Флотация сильвина из калийных руд при повышенных температурах / Flotation of sylvite from potash ores at elevated temperatures (in Russian): *Труды БГТУ: Химия и технология неорганических материалов и веществ*, v. 3, p. 71-77.
- Twidle, T. R., and Engelbrecht, P. C., 1984, Developments in the flotation of copper at Black Mountain: *Journal of The South African Institute of Mining and Metallurgy*, v. 84, no. 6, p. 164-178.
- Tyushkova, N. I., Marasanova, L. V., and Gorenkov, N. L., Research and developing of the technologies of oxidized Pb-Zn ores treatment, *in* Proceedings XXVI IMPC, New Dehli, India, p. 5551-5555.
- U.S. Geological Survey, 2022, 2022 Final list of critical minerals, Notice No. 87 FR 10381, USGS, Washington, p. 10381-10382

- Udaya Bhaskar, K., Govindarajan, B., Barnwal, J. P., Rao, K. K., Gupta, B. K., and Rao, T. C., 2005, Classification studies of lead–zinc ore fines using water-injection cyclone: *International Journal of Mineral Processing*, v. 77, no. 2, p. 80-94.
- Udaya Bhaskar, K., Govindarajan, B., Barnwal, J. P., Venugopal, R., Jakhu, M. R., and Rao, T. C., 2002, Performance and modeling studies of an MGS for graphite rejection in a lead concentrate: *International Journal of Mineral Processing*, v. 67, no. 1, p. 59-70.
- Ulf, G., 2017, The Arrhenius equation is still a useful tool in chemical engineering: *Nordic Pulp & Paper Research Journal*, v. 32, no. 1, p. 21-24.
- Umipig, C. V., Israel, E. E., Hutalle, G. G., and Williams, S. R., Canatuan Cu/Zn flotation metallurgy - dealing with zinc pre-activation, *in Proceedings 44th Annual Meeting of the Canadian Mineral Processors*, 2012, p. 187-195.
- Urone, P. P., and Hinrichs, R., 2022, Thermal expansion of solids and liquids, *College Physics 2e*: Houston, Texas, OpenStax, p. 537-544.
- Vahrushev, V., 2014, Повышение эффективности процессов обесшламливания и выщелачивания в технологии получения хлорида калия из сильвинитовых руд Верхнекамского месторождения / Improving sylvinite desliming and leaching (in Russian) PhD Thesis: Perm State University, Chemical technology, p. 124.
- Verburg, R., and Oliveira, M., Surface paste disposal of high-sulfide tailings at Neves-Corvo – evaluation of environmental stability and operational experience, *in Proceedings Mining Meets Water – Conflicts and Solutions*, IMWA 2016, Leipzig, July 11-15 2016: Leipzig, IMWA, p. 361-367.
- Verma, M. P., A thermodynamic assessment of dissociation constant of water, *in Proceedings Twenty-Eighth Workshop on Geothermal Reservoir Engineering*, Stanford, CA, USA, January 27-29, 2003, Stanford University.
- Vigdergauz, V., Trofimova, E., Sarkisova, L., Kutlin, B., and Schekotov, N., 2000, Низкотемпературная флотация флюорита эмульсией карбоксильного собирателя / Low-temperature fluorite flotation with carboxyl collector emulsion (in Russian): *Горный информационно-аналитический бюллетень*, v. 2, p. 235-238.
- Vikentiev, V., Стратегическое и критическое минеральное сырье в осадочных формациях: геологические взаимоотношения и проблемы генезиса / Strategic and critical mineral

- raw materials in sedimentary formations: geological relationships and problems of genesis, *in* Proceedings LITOL 2023, Moscow, 2023, Izd. GEOS, p. 27-31.
- Vinnett, L., 2021, Measurement, modeling and evaluation of the flotation rate distribution, PhD Thesis: McGill University, Department of Mining and Materials Engineering, p. 254.
- Vinnett, L., Grammatikopoulos, T., El-Menshawy, A. H., and Waters, K. E., 2022, Justifying size-by-size flotation rate distributions from size-by-association kinetic responses: Powder Technology, v. 395, p. 168-182.
- Volpe, C. D., and Siboni, S., 1997, Some reflections on acid-base solid surface free energy theories: Journal of colloid and interface science, v. 195, no. 1, p. 121-136.
- Walck, C., 2007, Handbook on statistical distributions for experimentalist, Stockholm, University of Stockholm, Internal Report SUF-PFY/96-01, p. 190.
- Wang, G. C., 2016a, 3 - Nonferrous metal extraction and nonferrous slags, *in* Wang, G. C., ed., The Utilization of Slag in Civil Infrastructure Construction, Woodhead Publishing, p. 35-61.
- Wang, H., Wang, J., Zou, Q., Liu, W., Wang, C., and Huang, W., 2018, Surface treatment using potassium ferrate for separation of polycarbonate and polystyrene waste plastics by froth flotation: Applied Surface Science, v. 448, p. 219-229.
- Wang, H., Zhang, Y., and Wang, C., 2019, Surface modification and selective flotation of waste plastics for effective recycling - a review: Separation and Purification Technology, v. 226, p. 75-94.
- Wang, L., 2016b, Entrainment of fine particles in froth flotation, PhD Thesis: The University of Queensland Australia, Sustainable Minerals Institute, p. 162.
- Wang, L., and Li, C., 2020, A brief review of pulp and froth rheology in mineral flotation: Journal of Chemistry, v. 2020, no. 1, 3894542.
- Wang, L., and Yoon, R.-H., 2006, Stability of foams and froths in the presence of ionic and non-ionic surfactants: Minerals Engineering, v. 19, no. 6-8, p. 539-547.
- Wang, T., Sun, G., Deng, J., Xu, H., Wang, G., Hu, M., Qin, Q., and Sun, X., 2023, A depressant for marmatite flotation: synthesis, characterisation and floatation performance: International Journal of Minerals Metallurgy and Materials, v. 30, no. 6, p. 1048.
- Wang, X., Miller, J. D., Cheng, F., and Cheng, H., 2014, Potash flotation practice for carnallite resources in the Qinghai Province, PRC: Minerals Engineering, v. 66, no. 2014, p. 33-39.

- Wardell Armstrong International Limited, 2007, Technical report on the Neves-Corvo mine, Southern Portugal: Wardell Armstrong International Limited, Cornwall, p. 126.  
<https://www.sec.gov/Archives/edgar/data/1377085/000120445907001642/lundintechrep1.pdf>
- Wark, I. W., and Cox, A. B., 1938, Principles of flotation, VI – influence of temperature on effect of copper sulfate, alkalies and sodium cyanide on adsorption of xanthates at mineral surfaces., New York, American Institute of Mining and Metallurgical Engineers, p. 267-301.
- Wark, W., and Cox, A., 1932, Principles of flotation: an experimental study of the effect of xanthates on contact angles at mineral surfaces: Transactions of the American Institute of Mining and Metallurgical Engineers (AIME).
- Warren, J. L., 1985, Determination of the contributions of true flotation and entrainment in batch flotation tests: International Journal of Mineral Processing, v. 14, p. 33-44.
- Weaire, D. L., and Hutzler, S., 1999, The physics of foams, Oxford, Clarendon Press, p. 246.
- Wei, Q., Dong, L., Jiao, F., Qin, W., Pan, Z., and Cui, Y., 2021, The synergistic depression of lime and sodium humate on the flotation separation of sphalerite from pyrite: Minerals Engineering, v. 163, p. 106779.
- Wei, Y., and Sandenbergh, R. F., 2007, Effects of grinding environment on the flotation of Rosh Pinah complex Pb/Zn ore: Minerals Engineering, v. 20, no. 3, p. 264-272.
- Weise, K., Schmitz, J., and Wollmann, G., 1978, Das Mineral- Anreicherungsverfahren Flotation (Ein Überblick) / The flotation mineral concentration process: an overview (in German), Karlsruhe, p. 156-157.
- Weiss, N. L., 1985, SME mineral processing handbook, Society of Mining Engineers, American Institute of Mining, Metallurgical and Petroleum Engineers, Inc., New York, NY, USA, v. 1, p. 1053.
- Wills, B. A., and Finch, J. A., 2016, Froth flotation, Amsterdam, Elsevier, Wills' Mineral Processing Technology, 8th ed., p. 512.
- Wojcik, P., 2023, Zinc supply and influences from geology, *in* Andrew, C. J., Hitzman, M. W., and Stanley, G., eds., Irish-type Zn-Pb deposits around the world: Dublin, Irish Association for Economic Geology, p. 35-44.



- Wu, W., and Nancollas, G. H., 1996, Interfacial free energies and crystallization in aqueous media: *Journal of Colloid and Interface Science*, v. 182, no. 2, p. 365-373.
- Xia, L., Hart, B., Chen, Z., Furlotte, M., Gingras, G., and Laflamme, P., 2017, A ToF-SIMS investigation on correlation between grinding environments and sphalerite surface chemistry: implications for mineral selectivity in flotation: *Surface and Interface Analysis*, v. 49, no. 13, p. 1397-1403.
- Xiang, Y., 2015, Carboxymethyl chitosan as a selective depressant in differential flotation of galena and chalcopyrite, Master's Thesis: University of Alberta, Department of Chemical and Materials Engineering, p. 83.
- Xu, J.-q., Li, F.-j., and Zeng, X.-l., 2006, 从尾矿中回收氟碳铈矿和独居石的浮选研究/Flotation of bastnaesite and monazite in dressing plant tailing (in Chinese): *Chinese Rare Earths*, v. 27, no. 5, p. 67-72.
- Xu, J., 2005, 新浦磷矿低温捕收剂的选择 /Selection of collectors in Xinpu phosphate mine at lower temperature (in Chinese): *化工矿物与加工 / IM & P*, v. 12, p. 21-23.
- Xu, L., Hu, Y., Tian, J., Wu, H., Yang, Y., Zeng, X., Wang, Z., and Wang, J., 2016a, Selective flotation separation of spodumene from feldspar using new mixed anionic/cationic collectors: *Minerals Engineering*, v. 89, no. 4, p. 84-92.
- Xu, L., Hu, Y., Wu, H., Tian, J., Liu, J., Gao, Z., and Wang, L., 2016b, Surface crystal chemistry of spodumene with different size fractions and implications for flotation: *Separation and Purification Technology*, v. 169, no. 10, p. 33-42.
- Xu, M., and Wilson, S., 2000, Investigation of seasonal metallurgical shift at Inco's Clarabelle mill: *Minerals Engineering*, v. 13, no. 12, p. 1207-1218.
- Yáñez, A., Kupka, N., Tunç, B., Suhonen, J., and Rinne, A., 2024, Fine and ultrafine flotation with the Concorde Cell™ – a journey: *Minerals Engineering*, v. 206, p. 108538.
- Yang, G.-l., 2005, 稀土浮选工艺流程优化试验/Possibility of improving flow sheet of rare earth flotation beneficiation (in Chinese): *Chinese Rare Earths*, v. 26, no. 1, p. 25-26.
- Yarar, B., 2000, in: Kirk-Othmer (Ed.), *Kirk-Othmer Encyclopedia of Chemical Technology*. John Wiley & Sons, Inc., Hoboken, NJ, USA, p. 1-26.
- Yarar, B., and Kaona, J., The critical surface tension of wetting of sulfide minerals, *in Proceedings SME-AIME Annual Meeting*, Atlanta, 1 January, 1983, p. 5.

- Ye, L., Cook, N. J., Ciobanu, C. L., Yuping, L., Qian, Z., Tiegeng, L., Wei, G., Yulong, Y., and Danyushevskiy, L., 2011, Trace and minor elements in sphalerite from base metal deposits in South China: a LA-ICPMS study: *Ore Geology Reviews*, v. 39, no. 4, p. 188-217.
- Yianatos, J., Industrial flotation process modelling, a chemical engineering approach, *in* *Proceedings Role of Chemical Engineering in Processing of Minerals and Materials*, Bhubaneswar, India, 19-22 December, 2003, Allied Publishers Pvt. Ltd., p. 34-45.
- Yin, W., Sun, H., Tang, Y., Hong, J., Yang, B., Fu, Y., and Han, H., 2019, Effect of pulp temperature on separation of magnesite from dolomite in sodium oleate flotation system: *Physicochemical Problems of Mineral Processing*, v. 55, no. 4, p. 1049-1058.
- Yoon, R. H., and Sabey, J. B., 1982, Coal flotation in inorganic salt solutions: Virginia Polytechnic Institute and State University, p. 113.
- Yörük, S., Smith, G. W., and Finch, J. A., 1987, Critical surface tension of wetting and flotation separation of hydrophobic solids: *Separation Science and Technology*, v. 22, no. 6, p. 1527-1546.
- Young, H. D., Freedman, R. A., Ford, A. L., Jain, N., and Sethia, N. K., 2019, University physics for JEE mains and advance, Pearson Education India, v. 1, p. 664.
- Yu, Wu, Zhao, Zhu, and Luo, 2019, Effect of a small amount of iron impurity in sphalerite on xanthate adsorption and flotation behavior: *Minerals*, v. 9, no. 11, 687.
- Yu, M. A., and Damodaran, S., 1991, Kinetics of protein foam destabilization: evaluation of a method using Bovine Serum Albumin: *Journal of Agricultural and Food Chemistry*, v. 39, no. 9, p. 1555-1562.
- Zanin, M., Gredelj, S., and Grano, S. R., Factors affecting froth stability in mineral flotation and implications on minerals recovery: a case study, *in* *Proceedings V International Mineral Processing Seminar*, Santiago, Chile, 2008, Gecamin, p. 197-206.
- Zanin, M., Lambert, H., and du Plessis, C. A., 2019, Lime use and functionality in sulphide mineral flotation: a review: *Minerals Engineering*, v. 143, p. 105922.
- Zhang, C., He, T., Li, H., and Bu, X., 2019, 紫外光谱法研究黄药在黄铜矿表面的吸附热力学与动力学/Adsorption thermodynamics and kinetics of xanthate at chalcopyrite surface based on ultraviolet spectrophotometry [in Chinese]: *Spectroscopy and spectral analysis*, v. 39, no. 10, p. 3172-3178.

- Zhang, S., Huang, Z., Wang, H., Liu, R., Cheng, C., Shuai, S., Hu, Y., Guo, Z., Yu, X., He, G., and Fu, W., 2021a, Flotation performance of a novel Gemini collector for kaolinite at low temperature: *International Journal of Mining Science and Technology*, v. 31, no. 6, p. 1145-1152.
- Zhang, W., 2014, Evaluation of effect of viscosity changes on bubble size in a mechanical flotation cell: *Transactions of Nonferrous Metals Society of China (English Edition)*, v. 24, no. 9, p. 2964-2968.
- Zhang, X., Shao, G., Wu, P., and Bai, X., 2003, 氧化铅锌矿石低温浮选工艺研究 / Study on the flotation of lead-zinc oxide ore at low temperature (in Chinese): *Mining and Metallurgy/矿冶*, v. 12, no. 1, p. 21-21.
- Zhang, X., Zhao, Y., Zhang, Z., and Wang, S., 2021b, Investigation of the interaction between xanthate and kaolinite based on experiments, molecular dynamics simulation, and density functional theory: *Journal of Molecular Liquids*, v. 336, p. 116298.
- Zhang, Y.-H., Wu, L.-M., Huang, P.-P., Shen, Q., and Sun, Z.-X., 2018, Determination and application of the solubility product of metal xanthate in mineral flotation and heavy metal removal in wastewater treatment: *Minerals Engineering*, v. 127, p. 67-73.
- Zhang, Y., 1995, 萤石低温浮选捕收剂的研究 / Collectors for low temperature flotation of fluorite: a study (in Chinese): *Mining and Metallurgical Engineering*, v. 15, no. 1, p. 25-27.
- Zhang, Y., 2016, Froth flotation of xenotime Master's Thesis: Colorado School of Mines, Department of Metallurgical and Materials Engineering, p. 167.
- Zhang, Y., and Li, D., 2007, Application of surfactants in low temperature flotation of phosphate ore/几种表面活性剂在磷矿低温浮选中的应用 (in Chinese): *IM & P 化工矿物与加工*, v. 4, p. 8-9.
- Zhao, M., 1991, 温度对辉钼矿浮选的影响及其改善途径 / Effect of temperature on molybdenite flotation and improvement approaches (in Chinese): *国外金属矿选矿 / Guowai Jinshukuang Xuankuang*, v. 22, p. 86-89.
- Zheng, G., Sun, T., Kou, J., Xu, S., and Li, J., 2016, 新型捕收剂EV-1的合成及其在磷矿选矿中的应用 / Synthesis of collector (EV-1) and its application in flotation of apatite ores (in Chinese): *化工矿物与加工 / IM & P*, v. 2, p. 4-8.

- Zheng, L., Du, Z., and Liu, Y.-c., 2005, 凡口矿高碱介质中闪锌矿浮选特性研究/ The study on flotation properties of sphalerite in high alkalinity medium in Fankou lead-zinc mine (in Chinese): *Mining and Metallurgical Engineering*, v. 25, no. 3, p. 37-40.
- Zheng, X., Franzidis, J. P., and Johnson, N. W., 2006, An evaluation of different models of water recovery in flotation: *Minerals Engineering*, v. 19, no. 9, p. 871-882.
- Zhou, Q., and Lu, S., 1995, 萤石浮选增效剂及其应用 / Fatty acid booster and its application in fluorite flotation (in Chinese): *化工矿山技术 / Chemical Mining Technology*, v. 24, no. 4, p. 22-25.
- Zhou, W., Wu, C., Lv, H., Zhao, B., Liu, K., and Ou, L., 2020, Nanobubbles heterogeneous nucleation induced by temperature rise and its influence on minerals flotation: *Applied Surface Science*, v. 508, p. 145282.
- Zhu, C. S., Wang, L. P., and Chen, W. B., 2009, Removal of Cu(II) from aqueous solution by agricultural by-product: peanut hull: *Journal of Hazardous Materials*, v. 168, no. 2-3, p. 739-746.
- Zhu, H., Qin, W., Chen, C., and Liu, R., 2016, Interactions between sodium oleate and polyoxyethylene ether and the application in the low-temperature flotation of scheelite at 283 K: *Journal of Surfactants and Detergents*, v. 19, no. 6, p. 1289-1295.
- Ziemniak, S. E., Palmer, D. A., Benezeth, P., and Anovitz, L. M., 2004, Solubility of litharge ( $\alpha$ -PbO) in alkaline media at elevated temperatures: Lockheed Martin Corporation, New York, p. 33.

## APPENDIXES

**APPENDIX A: Summary of recommended flotation temperatures for different minerals**

Mineral / Source of ore	Recommended flotation temperature (°C)	Inter-seasonal/ temperature effect	Reagents	References
<b>Sphalerite (ZnS):</b>				
Matagami concentrator (Canada)	-	2.5% change in Zn grade (summer-winter)	CuSO <sub>4</sub> , xanthates, MIBC	(Nesset <i>et al.</i> , 2002)
Fankou Mine (China)	25-40 (not higher than 50)	Zn recovery and grade by 0.66% and 0.4% (summer-winter)	CuSO <sub>4</sub> , buthyl xanthate	(Zheng <i>et al.</i> , 2005)
Meggen plant (Germany)	25	4% in Zn grade for 5-7 °C amplitude	Xanthates, CuSO <sub>4</sub> , ZnSO <sub>4</sub>	(Weise <i>et al.</i> , 1978)
Somincor (Portugal)	30-45 (highest losses at 60 and above)	up to 25% Zn recovery	Xanthates, CuSO <sub>4</sub> , lime	(Fernandes, 2016; Manouchehri <i>et al.</i> , 2012)
Uchalinskaja plant (Russia)	30-40	10% in Zn grade when 10 and 40 °C compared	Xanthates, CuSO <sub>4</sub>	(Arustamjan, 2004)

Mineral / Source of ore	Recommended flotation temperature (°C)	Inter-seasonal/ temperature effect	Reagents	References
Boliden concentrators (Sweden)	not lower than 12	ca. 3% in Zn grade when tests at 4 and 22 °C compared	IBX, Dowfroth 250, NaHSO <sub>3</sub> , dextrin, CuSO <sub>4</sub>	(Albrecht <i>et al.</i> , 2010; Ikumapayi <i>et al.</i> , 2012)
Brunswick Mine concentrator (Canada)	35	0.1% Zn recovery loss when temperature dropped below 35	Xanthates, CuSO <sub>4</sub> , lime	(Roberts <i>et al.</i> , 2008)
<b>Galena (PbS)</b>				
Mono-mineral lab tests	-	7% gain in Pb recovery by rising temp. from 5 to 20	MIBC, SBX	(He <i>et al.</i> , 2020)
Mono-mineral lab tests	below 60	-	n-BAF	(Kubota <i>et al.</i> , 1974)
<b>Gold</b>				
Hudson Bay Mining and Smelting (Canada)	around 20	up to 30% decrease in gold recovery	Xanthates, lime, TNC 312, KAX	(Levanaho <i>et al.</i> , 2005)

Mineral / Source of ore	Recommended flotation temperature (°C)	Inter-seasonal/ temperature effect	Reagents	References
<b>Chalcopyrite (CuFeS<sub>2</sub>)</b>				
Belousovskaja plant (Kazakhstan)	18-20	-	Cyanide, xanthates	(Abramov, 2005)
Prieska Copper Mines concentrator (South Africa)	-	loss in Cu-Zn selectivity: higher Zn content in Cu concentrates in summer	Cyanides, Cu-sulfate, IPX, DIBD, TEB	(Marais, 1980)
<b>Pentlandite ((Fe,Ni)<sub>9</sub>S<sub>8</sub>)</b>				
Clarabelle mill (Canada)	-	2% Ni loss when temperature dropped from around 20 to around 10	Xanthates, lime	(Xu and Wilson, 2000)
<b>Quartz (SiO<sub>2</sub>)</b>				
Mihajlovsky GOK (Russia)	above 10-12	Magnetite reverse flotation operation: 2-3% loss in grade and recovery of iron	amine PA-14, starch	(Ignatova and Shelepov, 2011)

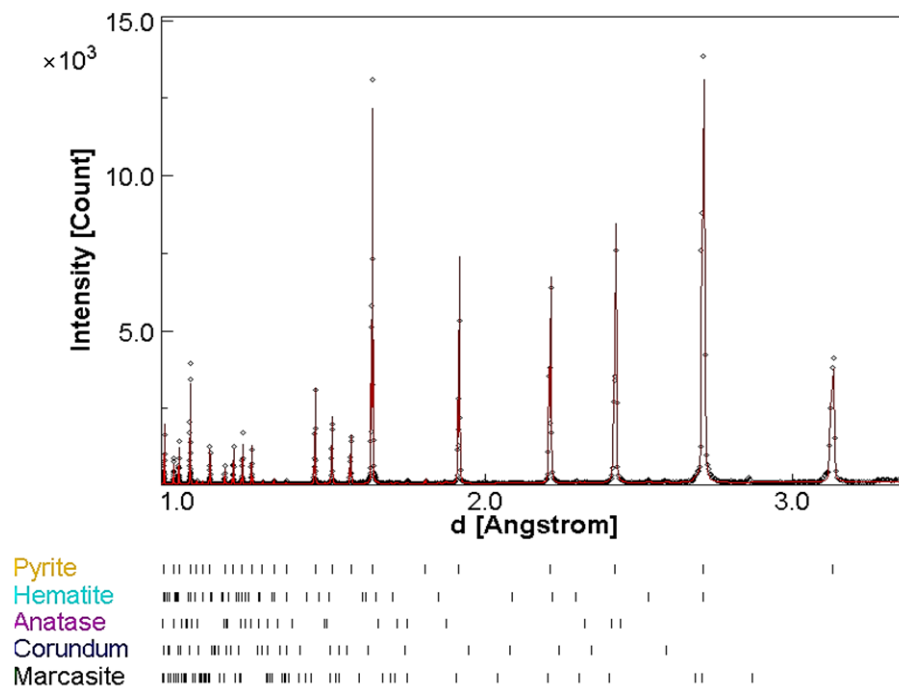
Mineral / Source of ore	Recommended flotation temperature (°C)	Inter-seasonal/ temperature effect	Reagents	References
<b>Smithsonite (ZnCO<sub>3</sub>) + Sphalerite (ZnS) (9:1)</b>				
Lanping mine (China)	25-30	-	-	(Zhang <i>et al.</i> , 2003)
<b>Alunite KAl<sub>3</sub>(SO<sub>4</sub>)<sub>2</sub>(OH)<sub>6</sub>.</b>				
Lab tests with Wah-Wah Mountains alunite ore (USA)	35 to 50		oleic acid	(Miller and Ackerman, 1980)
<b>Carnallite (KMgCl<sub>3</sub>·6(H<sub>2</sub>O))</b>				
Qarhan Salt Lake plants (China)	Room temp. – decomposition to KCl, reagent temp.: >60	November to March shutdown	Amines, CMC, alcohol frother	(Wang <i>et al.</i> , 2014)
<b>Sylvite (KCl)</b>				
Mosaic (Canada)	20-32	-	Amines, polyglycol	(Essilfie, 2014)
JSC “Sylvinites” plant (Russia)	below 35	-	Armeen HT, SKFlot FA-4, Flotigam S	(Aliferova, 2007)



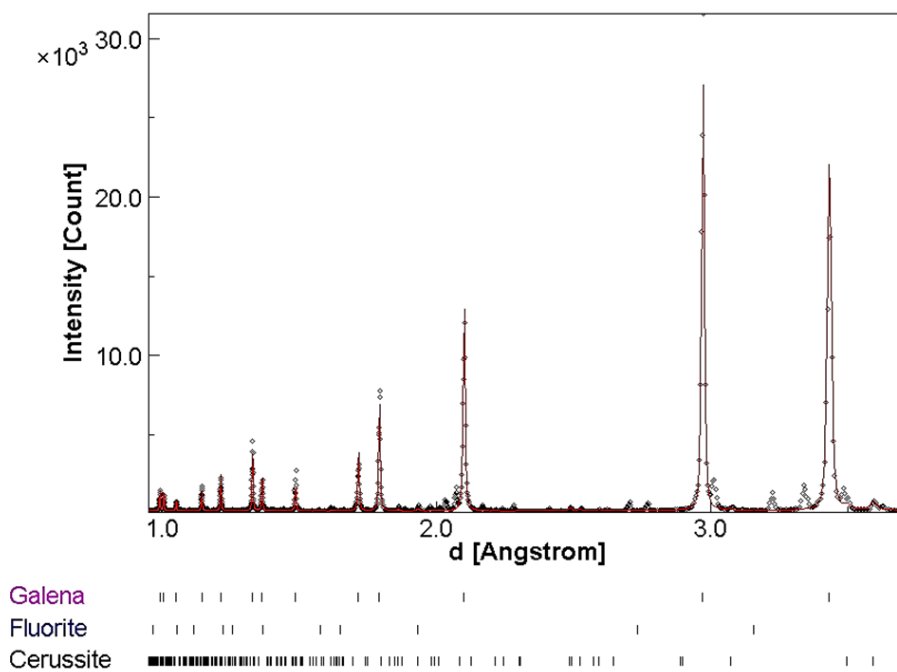
Mineral / Source of ore	Recommended flotation temperature (°C)	Inter-seasonal/ temperature effect	Reagents	References
JSC “Belaruskali” (Belarus)	below 36	-	Lutamine TH 95, Lutamine TH 95 summer, starches	(Turko <i>et al.</i> , 2014)
<b>Bastnaesite ((Y, Ce)(CO<sub>3</sub>)F)</b>				
Baotou concentrator (China)	35-45	-	Naphthyl hydroxamic acid, water glass	(Li <i>et al.</i> , 2018)
Wei Shan RE Mine (China)	40-43	-	L102, water glass, Al salt	(Zanin <i>et al.</i> , 2019)
<b>Pyrochlore ((Na, Ca)<sub>2</sub>Nb<sub>2</sub>O<sub>6</sub>(OH,F))</b>				
Niobec (Canada)	principal trigger – phosphates in water	4 % Nb recovery decrease in winter	Fatty acids	(Marois <i>et al.</i> , 2018)
<b>Scheelite (CaWO<sub>4</sub>)</b>				
Luanchuan flotation plant (China)	principal trigger – silica glass in process water	5-8% recovery drop in winter	Silica glass	(Kang <i>et al.</i> , 2017)

Mineral / Source of ore	Recommended flotation temperature (°C)	Inter-seasonal/ temperature effect	Reagents	References
<b>Coal</b>				
Karbomet Mining Coal Washing Plant (Turkey)	25-50	-	Waste vegetable oil lab testing	(Hacifazlıoğlu and Gerdan, 2016)
Milldale coal (USA)	27	Around 1% increase in recovery per 1 °C increase, best selectivity against ash content between 20 and 30 °C	Amyl alcohol lab testing	(Gayle and Eddy, 1961)
<b>Spodumene (LiAl(SiO<sub>3</sub>)<sub>2</sub>)</b>				
Vilatuxe (Spain)	33-50	-	Oleic acid, caustic soda	(Menéndez <i>et al.</i> , 2004)

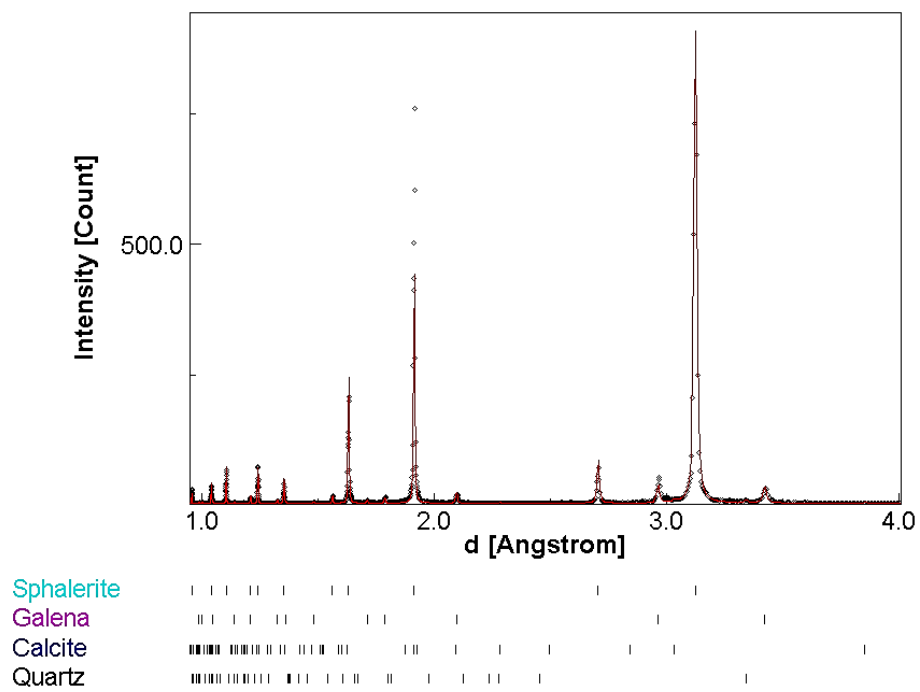
**APPENDIX B: XRD diffractograms for: pyrite (a), galena (b), sphalerite (c)**



(a)

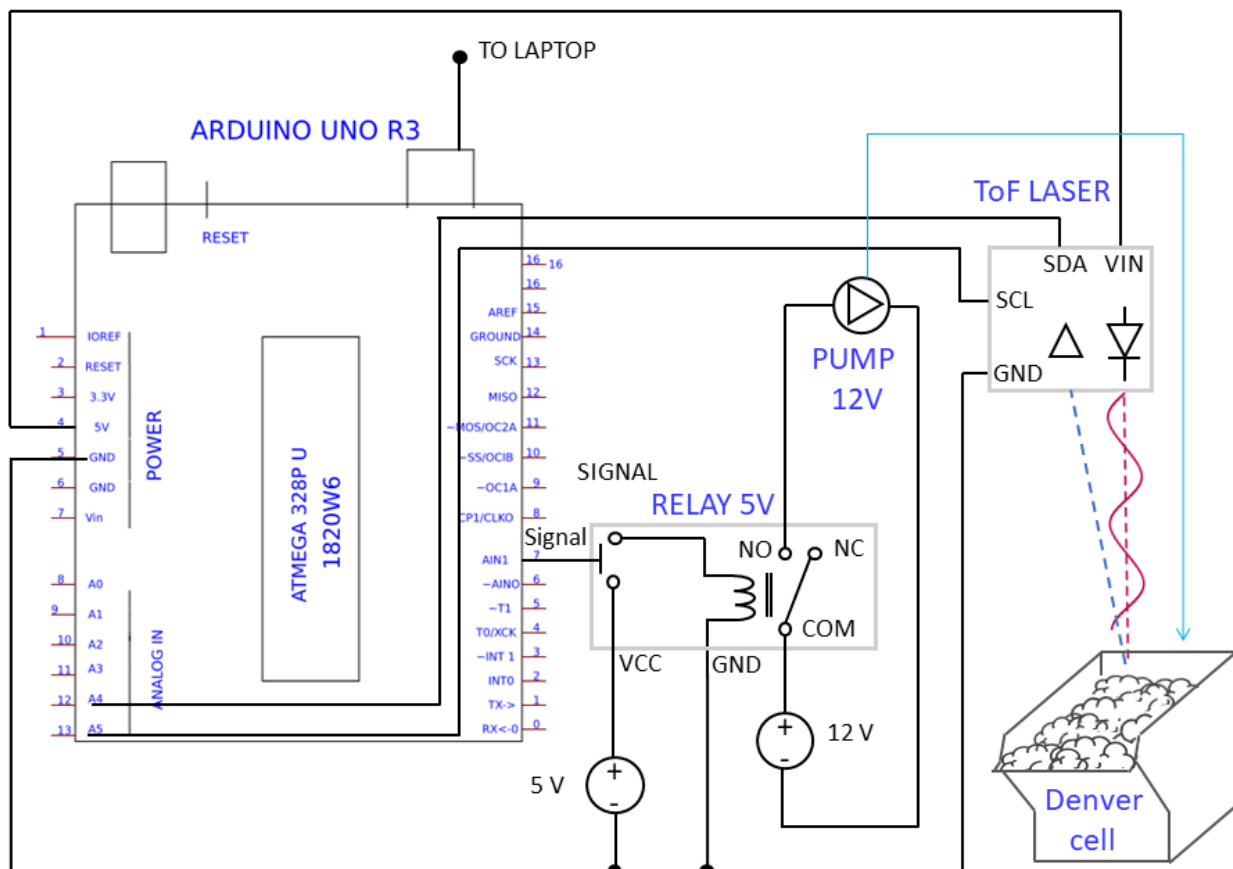


(b)



(c)

## APPENDIX C: Detailed Scheme of Denver Flotation Set-Up with Automatic Level Control



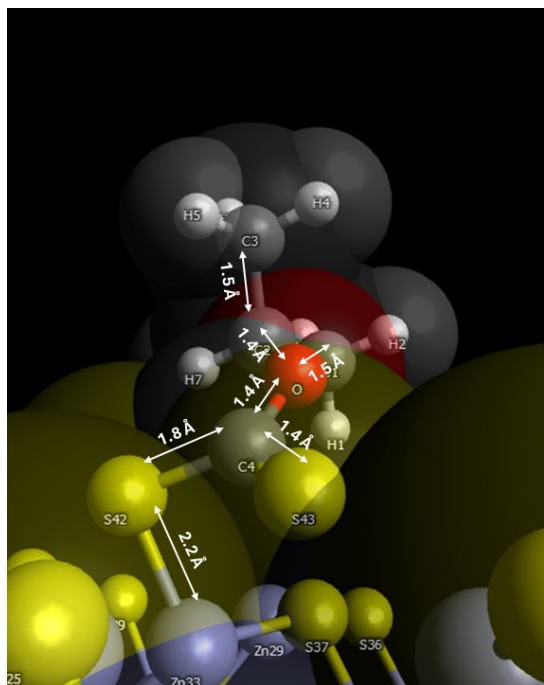
**APPENDIX D: Calculations of the moments of inertia of the atoms of iPX molecules adsorbed on galena, sphalerite, and pyrite**

Atom	x (Å)	y (Å)	z (Å)	$A_r$	$A_r \cdot X$	$A_r \cdot Y$	$A_r \cdot Z$	$A_r \cdot (\bar{X} - x)^2$	$A_r \cdot (\bar{Y} - y)^2$	$A_r \cdot (\bar{Z} - z)^2$
iPX-Galena										
Pb	-1.1	1.8	-1.5	207.2	-227.9	372.7	-320.1	182.4	42.8	117.6
C	-5.7	2.3	-0.6	12.0	-69.0	27.6	-7.5	164.7	10.9	0.3
S	-1.6	-0.3	-0.3	32.1	-51.6	-9.0	-9.8	5.9	84.7	7.6
O	-4.2	0.6	-0.1	16.0	-66.9	9.3	-2.1	73.3	9.3	7.0
C	-6.5	0.1	0.3	12.0	-77.6	0.8	3.4	235.1	19.6	13.8
C	-5.4	1.1	0.3	12.0	-64.6	13.7	3.6	133.8	0.5	14.3
C	-3.0	0.5	0.5	12.0	-36.0	5.7	6.5	11.0	9.1	21.3
S	-2.8	0.9	1.9	32.1	-90.0	30.0	60.7	19.0	5.3	230.9
$\Sigma=$				335.4	-683.4	450.9	-265.4	825.1	182.2	412.7
iPX-Sphalerite										
Zn	-2.5	0.0	-0.5	65.4	-165.7	-2.3	-35.9	127.0	164.0	8.2
C	-4.1	2.4	0.0	12.0	-48.7	28.8	-0.4	0.2	8.6	0.3
S	-2.7	2.1	-1.2	32.1	-87.6	67.4	-38.5	45.8	9.8	32.5
O	-5.3	2.2	-0.4	16.0	-85.4	34.7	-7.0	31.8	6.1	0.9
C	-7.4	3.3	-0.4	12.0	-88.9	40.2	-5.0	144.7	38.9	0.6
C	-6.5	2.3	0.3	12.0	-78.3	27.8	3.4	80.5	7.1	2.7
C	-7.2	1.0	0.4	12.0	-86.8	11.6	4.4	130.4	4.1	3.8
S	-3.7	2.9	1.3	32.1	-119.0	91.5	41.4	1.5	54.7	70.7
$\Sigma=$				193.5	-760.3	299.6	-37.7	561.9	293.3	119.8
iPX-Pyrite										
Fe	-0.9	1.8	-1.3	55.9	-52.4	97.7	-73.1	185.3	34.6	76.6
C	-5.8	2.3	-0.6	12.0	-69.4	27.6	-7.6	109.4	21.4	3.0
S	-2.8	1.0	1.8	32.1	-88.7	31.3	57.9	0.0	0.0	121.3

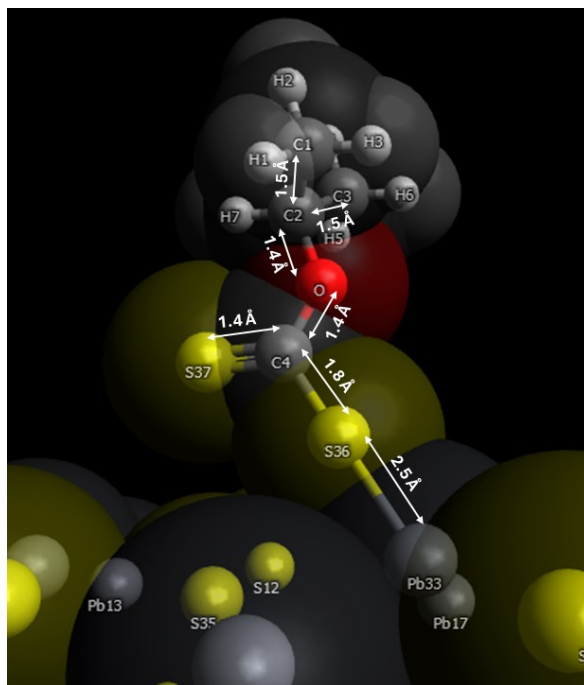
APPENDIX D: Calculations of the moments of inertia of the atoms of iPX molecules adsorbed on galena, sphalerite, and pyrite

Atom	x (Å)	y (Å)	z (Å)	$A_r$	$A_r \cdot X$	$A_r \cdot Y$	$A_r \cdot Z$	$A_r \cdot (\bar{X} - x)^2$	$A_r \cdot (\bar{Y} - y)^2$	$A_r \cdot (\bar{Z} - z)^2$
O	-4.2	0.6	-0.2	16.0	-67.1	9.4	-2.7	33.0	2.2	0.0
C	-5.3	1.2	0.3	12.0	-64.0	13.8	3.4	79.5	0.4	2.2
C	-3.0	0.5	0.5	12.0	-35.9	5.8	5.7	0.7	2.7	4.5
C	-6.6	0.1	0.3	12.0	-77.6	0.8	3.6	165.0	9.6	2.3
S	-1.6	-0.3	-0.4	32.1	-52.4	-9.4	-12.6	40.5	50.5	2.1
$\Sigma =$				184.0	-507.6	177.1	-25.4	613.3	121.4	211.8

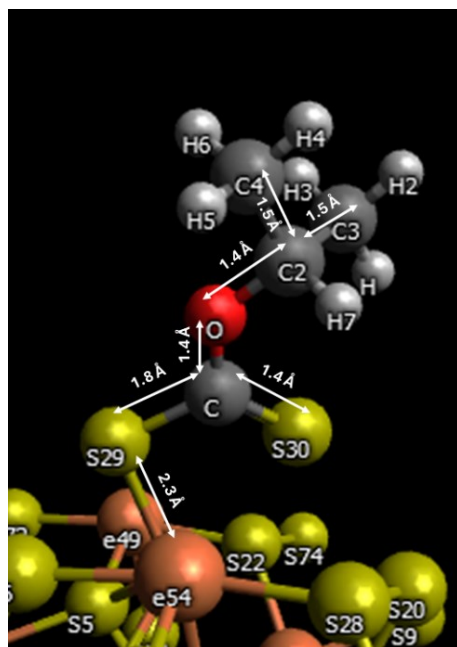
**APPENDIX E: iPX molecule on sphalerite (a), galena (b) and pyrite (c) surfaces (110)**



(a)



(b)



(c)



# APPENDIX F: Experimental results of adsorption tests for pyrite, sphalerite, and galena

Run	Uncoded variables					Py responses		Sph responses		Gn responses	
	$pH$	$T, ^\circ C$	$SIPX, \mu mol/l$	$D, \mu mol/l$	$A, \mu mol/l$	$k_a^{Py} nmol/(m^2 \cdot s)$	$q_e^{Py} \mu mol/m^2$	$k_a^{Sph} nmol/(m^2 \cdot s)$	$q_e^{Sph} \mu mol/m^2$	$k_a^{Gn} nmol/(m^2 \cdot s)$	$q_e^{Gn} \mu mol/m^2$
1	9	15	16	20	40	6.3	0.33	4.9	0.97	6.5	1.24
2	10	25	21	40	80	5.5	0.44	4.5	1.24	6.4	1.55
3	10	25	11	40	80	5.7	0.24	4.1	0.75	7.5	0.86
4	10	45	11	40	80	8.5	0.26	8.1	0.90	10.4	1.00
5	10	25	6	40	80	5.5	0.25	4.0	0.72	8.0	0.87
6	10	5	11	40	80	3.7	0.23	2.9	0.61	2.7	0.64
7	11	35	16	20	40	3.5	0.35	1.9	0.54	4.0	0.71
8	10	25	11	80	80	3.8	0.19	3.7	0.99	5.8	0.81
9	10	25	11	40	80	5.4	0.28	4.1	0.74	8.1	0.91
10	9	15	6	60	40	5.4	0.14	6.5	0.45	5.9	0.37
11	11	35	6	60	40	3.5	0.14	2.1	0.34	3.5	0.36
12	10	25	11	0	80	6.0	0.26	5.6	0.68	10.6	0.92
13	11	15	16	60	40	2.9	0.36	1.5	0.53	3.5	0.88
14	9	15	6	20	120	4.8	0.15	7.3	0.39	8.8	0.40
15	8	25	11	40	80	6.5	0.22	5.8	0.81	10.8	1.12
16	10	25	11	40	80	5.9	0.24	3.8	0.75	7.3	0.89
17	12	25	11	40	80	2.3	0.17	2.8	0.76	2.1	0.65
18	11	35	16	60	120	4.5	0.31	3.7	0.70	4.4	0.97
19	10	25	11	40	160	6.3	0.24	6.9	1.04	10.2	0.95
20	9	35	6	60	120	7.2	0.14	9.5	0.27	10.5	0.42
21	9	35	16	60	40	7.1	0.33	8.5	0.92	10.0	1.07
22	9	15	16	60	120	7.0	0.34	7.3	0.87	9.6	1.05
23	11	35	6	20	120	4.5	0.15	2.4	0.58	5.3	0.45
24	9	35	6	20	40	6.5	0.13	8.6	0.33	9.9	0.45
25	9	35	16	20	120	8.2	0.38	8.9	1.06	11.1	1.21
26	11	15	16	20	120	4.0	0.34	1.8	0.89	4.2	1.04
27	10	25	1	40	80	4.1	0.03	3.6	0.09	8.0	0.09
28	10	25	11	40	80	6.0	0.25	3.9	0.76	6.7	0.85
29	11	15	6	60	120	4.3	0.14	1.9	0.37	3.4	0.37
30	10	25	11	40	0	2.0	0.22	1.2	0.39	2.7	0.63
31	10	25	11	40	80	5.8	0.24	4.0	0.75	6.8	0.90
32	11	15	6	20	40	4.5	0.15	1.6	0.34	5.2	0.31

**APPENDIX G: Foam stability central composite design results**

Run	Coded Variables					Foam Stability Responses	
	Temperature °C	pH	MIBC (ppm)	SIPX (ppm)	Gas velocity (J <sub>g</sub> )	$H_f$ , mm	$t^{1/2}$ , s
1	-1	-1	1	1	1	33.1	2.7
2	0	0	2	0	0	15.1	2.6
3	0	0	0	0	0	12.3	1.6
4	-1	1	-1	1	1	32.3	2.7
5	0	0	0	0	0	12.5	1.6
6	0	0	-2	0	0	11.7	1.3
7	1	1	1	1	1	17.6	1.5
8	1	1	-1	-1	1	19.9	1.0
9	0	0	0	0	-2	5	0.0
10	-1	-1	-1	-1	1	30.4	2.4
11	1	-1	1	1	-1	8.9	1.1
12	1	-1	-1	1	1	13.9	1.0
13	-1	1	1	1	-1	10.8	2.2
14	2	0	0	0	0	11.1	1.0
15	1	1	-1	1	-1	7.9	1.2
16	0	0	0	0	0	11.2	1.6
17	0	2	0	0	0	17.4	1.6
18	-1	-1	1	-1	-1	9.7	2.3
19	0	0	0	0	0	13	1.6
20	0	0	0	2	0	14	1.3
21	0	-2	0	0	0	11.6	1.5
22	1	-1	-1	-1	-1	7.9	1.2
23	0	0	0	0	0	10.8	1.5
24	-1	-1	-1	1	-1	8.4	2.9

Run	Coded Variables					Foam Stability Responses	
	Temperature °C	pH	MIBC (ppm)	SIPX (ppm)	Gas velocity (J <sub>g</sub> )	$H_f$ , mm	$t^{1/2}$ , s
25	1	1	1	-1	-1	7.6	1.8
26	-1	1	1	-1	1	36	2.2
27	0	0	0	-2	0	12.9	2.0
28	-2	0	0	0	0	28.3	3.1
29	0	0	0	0	2	31	1.9
30	-1	1	-1	-1	-1	7.6	2.3
31	1	-1	1	-1	1	12.7	1.2
32	0	0	0	0	0	11.7	1.5

**APPENDIX H: Statistical significance of models of froth stability parameters in SEDEX ore flotation**

	Solids yield		Water yield		Air recovery	
	Conc 1	Conc 2	Conc 1	Conc 2	Conc 1	Conc 2
F-value	15.20	1.96	6.65	5.56	1.41	7.57
p-value	0.001	0.194	0.010	0.017	0.333	0.007
$R^2$	95.13	71.55	89.53	87.72	64.44	90.68
$R^2_{adj}$	88.87	34.97	76.06	71.94	18.71	78.70
SD	0.37	0.94	0.24	0.13	5.0	2.48

	Froth speed		Froth height over the lip		Bubble burst rate	
	Conc 1	Conc 2	Conc 1	Conc 2	Conc 1	Conc 2
F-value	3.83	4.46	1.17	7.66	3.10	5.39
p-value	0.45	0.031	0.428	0.007	0.075	0.019
$R^2$	83.12	85.14	60.06	90.78	79.96	87.40
$R^2_{adj}$	61.41	66.04	8.70	78.93	54.19	71.19
SD	0.25	0.36	2.02	0.85	0.10	0.08

**APPENDIX I: Responses of galena, pyrite, and sphalerite flotation systems under the investigated general factorial design.**

Run	Uncoded Variables		Galena Responses		Pyrite Responses		Sphalerite Responses	
	pH	T, °C	$\gamma_g$	$\gamma_g^w$	$\gamma_p$	$\gamma_p^w$	$\gamma_s$	$\gamma_s^w$
1	9.0	30.0	31.8	12.0	4.5	15.3	37.7	21.9
2	11.0	30.0	14.1	12.8	6.8	22.2	14.5	18.8
3	9.0	40.0	23.6	7.5	2.6	6.9	9.6	11.7
4	11.0	10.0	29.5	38.9	20.8	44.9	26.2	47.9
5	11.0	20.0	25.6	21.3	11.5	38.5	20	24.8
6	9.0	40.0	26.8	8.0	1.6	8.5	9	9.9
7	11.0	40.0	10.6	7.0	3.7	6.3	4.7	10.1
8	11.0	40.0	11.5	6.6	4.2	8.6	4.3	9.8
9	9.0	20.0	66.3	22.8	11.3	30.1	52.2	29.4
10	11.0	20.0	24.7	20.5	12.2	38.3	22.4	26.3
11	9.0	20.0	66.9	25.0	10.8	30.2	53.5	30.6
12	9.0	10.0	90.8	48.0	28.1	45.8	77.6	44
13	11.0	30.0	15.5	14.0	4.7	18.6	15.3	19.5
14	9.0	10.0	88.6	46.4	23.8	37.3	77	44.5
15	9.0	30.0	35.0	15.3	2.7	15.2	36.5	19.8
16	11.0	10.0	28.2	36.2	19.3	40.4	24.2	46.1

## APPENDIX J: A detailed numerical example of the thermodynamic calculations.

A sum of carbon-containing components in a water contacting with air at 25 °C can be described by the following equation:

$$C = [HCO_3^-] + [H_2CO_3] + [CO_3^{2-}] = 1 \times 10^{-5} \text{ mol/l} \quad (\text{J-1})$$

For this system the following reactions should be considered:

$$HCO_3^- \rightleftharpoons CO_3^{2-} + H^+ \therefore K_{[HCO_3^-]} = \frac{[CO_3^{2-}][H^+]}{[HCO_3^-]} \therefore [HCO_3^-] = \frac{[CO_3^{2-}][H^+]}{K_{[HCO_3^-]}} \quad (\text{J-2})$$

$$\begin{aligned} H_2CO_3 &\rightleftharpoons HCO_3^- + H^+ \therefore K_{[H_2CO_3]} = \frac{[HCO_3^-][H^+]}{[H_2CO_3]} \therefore \\ \therefore [H_2CO_3] &= \frac{[HCO_3^-][H^+]}{K_{[H_2CO_3]}} = \frac{[CO_3^{2-}][H^+]^2}{K_{[HCO_3^-]}K_{[H_2CO_3]}} \end{aligned} \quad (\text{J-3})$$

Then, by substituting the expressions from J-2 and J-3 to J-1 the following equation is derived:

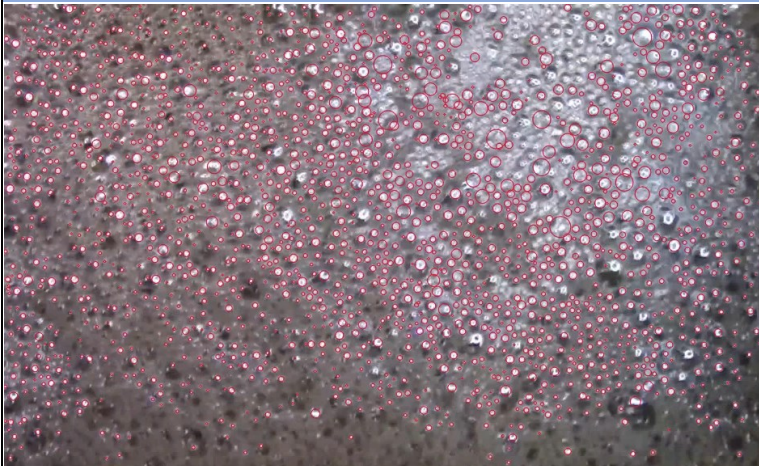
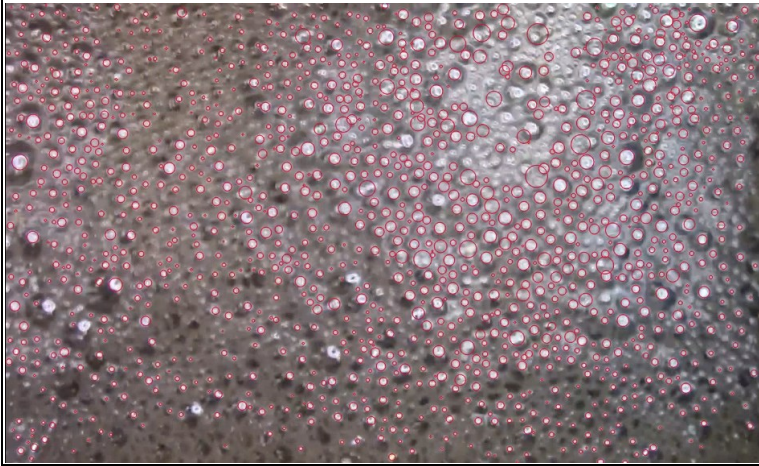

$$\begin{aligned} C &= \frac{[CO_3^{2-}][H^+]}{K_{[HCO_3^-]}} + \frac{[CO_3^{2-}][H^+]^2}{K_{[HCO_3^-]}K_{[H_2CO_3]}} + [CO_3^{2-}] = \\ &= \frac{[CO_3^{2-}](K_{[H_2CO_3]}[H^+] + [H^+]^2 + K_{[HCO_3^-]}K_{[H_2CO_3]})}{K_{[HCO_3^-]}K_{[H_2CO_3]}} \end{aligned} \quad (\text{J-4})$$

From J-4, the concentration of  $[CO_3^{2-}]$  in the system can be expressed:

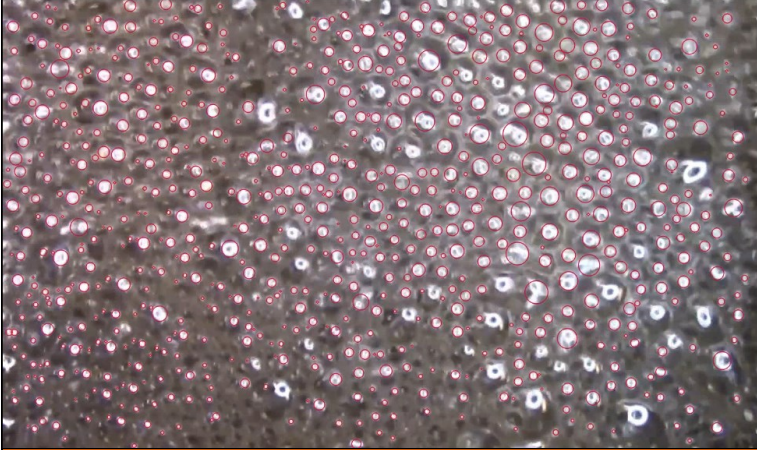

$$[CO_3^{2-}] = \frac{K_{[HCO_3^-]}K_{[H_2CO_3]}C}{K_{[H_2CO_3]}[H^+] + [H^+]^2 + K_{[HCO_3^-]}K_{[H_2CO_3]}} \quad (\text{J-5})$$

Using this substitution approach derivations of equations in Section 3.7.1 were performed.

**APPENDIX K: Bubble size on the top of the froth at different temperatures.**

8.2 °C	
	<p>Mean bubble size: 10.0 mm;  Median bubble size: 8.7 mm;  St. dev. 5.9 mm;  Bubble population: 703,690;  Frames used: 11,496</p>
15 °C	
	<p>Mean bubble size: 10.6 mm;  Median bubble size: 9.5 mm;  St. dev. 5.7 mm;  Bubble population: 2,988,863;  Frames used: 46,080</p>
25 °C	
	<p>Mean bubble size: 10.7 mm;  Median bubble size: 9.3 mm  St. dev. 6.3 mm;  Bubble population: 2,499,123;  Frames used: 45,772</p>



35 °C	
	Mean bubble size: 12.6 mm; Median bubble size: 11.5 mm St. dev. 7.0 mm; Bubble population: 1,441,097; Frames used: 43,040
41.8 °C	
	Mean bubble size: 12.8 mm; Median bubble size: 11.0 mm St. dev. 7.9 mm Bubble population: 480,528; Frames used: 11,520